Site C0022[1]

M. Strasser, B. Dugan, K. Kanagawa, G.F. Moore, S. Toczko, L. Maeda, Y. Kido, K.T. Moe, Y. Sanada, L. Esteban, O. Fabbri, J. Geersen, S. Hammerschmidt, H. Hayashi, K. Heirman, A. Hüpers, M.J. Jurado Rodriguez, K. Kameo, T. Kanamatsu, H. Kitajima, H. Masuda, K. Milliken, R. Mishra, I. Motoyama, K. Olcott, K. Oohashi, K.T. Pickering, S.G. Ramirez, H. Rashid, D. Sawyer, A. Schleicher, Y. Shan, R. Skarbek, I. Song, T. Takeshita, T. Toki, J. Tudge, S. Webb, D.J. Wilson, H.-Y. Wu, and A. Yamaguchi[2]

Chapter contents

[1] Strasser, M., Dugan, B., Kanagawa, K., Moore, G.F., Toczko, S., Maeda, L., Kido, Y., Moe, K.T., Sanada, Y., Esteban, L., Fabbri, O., Geersen, J., Hammerschmidt, S., Hayashi, H., Heirman, K., Hüpers, A., Jurado Rodriguez, M.J., Kameo, K., Kanamatsu, T., Kitajima, H., Masuda, H., Milliken, K., Mishra, R., Motoyama, I., Olcott, K., Oohashi, K., Pickering, K.T., Ramirez, S.G., Rashid, H., Sawyer, D., Schleicher, A., Shan, Y., Skarbek, R., Song, I., Takeshita, T., Toki, T., Tudge, J., Webb, S., Wilson, D.J., Wu, H.-Y., and Yamaguchi, A., 2014. Site C0022. *In* Strasser, M., Dugan, B., Kanagawa, K., Moore, G.F., Toczko, S., Maeda, L., and the Expedition 338 Scientists, *Proc. IODP,* 338: Yokohama (Integrated Ocean Drilling Program). doi:10.2204/iodp.proc.338.107.2014
[2] **Expedition 338 Scientists' addresses.**

Background and objectives

During Integrated Ocean Drilling Program (IODP) Expedition 338, logging while drilling (LWD)/measurement while drilling (MWD) and coring were conducted at IODP Site C0022, which is located in the trench slope basin previously drilled at IODP Sites C0004 and C0008 (Fig. **F1**).

During IODP Expeditions 314 and 316, LWD and coring, respectively, were conducted at Site C0004 (Expedition 314 Scientists, 2009b; Expedition 316 Scientists, 2009a). Site C0004 targeted the uppermost 400 meters below seafloor (mbsf) near the tip of the megasplay fault zone where the seaward-most branch of this fault system approaches the surface (Figs. **F1**, **F2**) (Moore et al., 2007, 2009). This megasplay fault is thought to coincide with the rupture area of the 1944 Tonankai earthquake, and its slip was likely responsible for the devastating tsunami at the time of that earthquake (Park et al., 2002; Moore et al., 2007).

Logging data obtained during Expedition 314 suggested three logging units corresponding to the slope sediment, accretionary prism, and underthrust sediment, the latter two of which are bounded by the megasplay branch fault (Expedition 314 Scientists, 2009b). The sediment cored during Expedition 316 is divided into four lithostratigraphic units: Pleistocene upper slope apron (Unit I, 0–78.06 mbsf), Pliocene accretionary complex (Unit II, 78.06–258.01 mbsf), Pliocene fault-bounded unit (Unit III, 258.01–307.52 mbsf), and Pleistocene underthrust slope basin (Unit IV, 307.52–398.79 mbsf) (Expedition 316 Scientists, 2009a). Two biostratigraphic age reversals were found within Unit III, which represents the megasplay branch fault zone. Unit III is characterized by a fractured and brecciated zone, and the fault zone within Unit III was sampled at 271 mbsf, where it consists of microbreccia and a narrow dark layer ~1 cm thick that dips at ~50° to the core vertical axis (Expedition 316 Scientists, 2009a). Analyses of this fault sample revealed evidence for frictional heat, including an increase in vitrinite reflectance, enrichment in Al and K and depletion in Ca and Sr, and an increase in illite crystallinity, implying possible propagation of seismic slips to this shallow portion of the megasplay branch fault (Yamaguchi et al., 2011; Sakaguchi et al., 2011a). In addition, the top 1 m of core contains repeated occurrences of earthquake-induced mud breccia, the uppermost of which was found by ^{210}Pb dating to have been deposited at the time of the 1944 Tonankai earthquake (Sak-

doi:10.2204/iodp.proc.338.107.2014

aguchi et al., 2011b). However, the seismic profile and reconstruction of splay fault activity through time indicate that the surface layers younger than ~1.24 Ma are not displaced by this megasplay branch fault (Fig. F2) (Expedition 316 Scientists, 2009a; Strasser et al., 2009), which implies that this fault has been inactive recently. Alternatively, Kimura et al. (2011) suggested ongoing splay fault activity may not only be inferred by stratal ages and architecture across the fault itself but also by broader and distributed deformation, manifest by deformation of the lower slope basin and erosion and redeposition of slope sediment by successive oversteepening and mass transport and accumulation of mass transport deposits overlying the fault.

Site C0008, located ~1 km seaward of Site C0004, was also drilled and cored during Expedition 316 (Expedition 316 Scientists, 2009b). Drilling objectives were to help assess the timing and relative age of past fault motions via identification of provenance and age of basin material. Seismic horizons identified in the basin sediment at Site C0004 continue laterally across the basin to Site C0008, and the lithologies are similar (Expedition 316 Scientists, 2009b).

As a contingency operation during Expedition 338, LWD and coring to 420 mbsf were conducted at Site C0022 (proposed Site NT2-13A), which is located ~350 m southeast of Site C0004 (Fig. F2). Objectives of LWD and coring at Site C0022 include collection of logging data and samples across the shallow end (~100 mbsf) of the megasplay branch fault in order to characterize fault materials and properties, search for signs of seismic rupture propagation, and constrain activity of this fault. Thus, LWD and coring at Site C0022 provide additional information on the activity of the megasplay branch fault and its bearing on the 1944 Tonankai earthquake and tsunami.

Operations

Site C0022

Hole C0022A

Operations began with dropping transponders at Site C0022 from 2030 h on 27 December 2012. The transponders were all confirmed on the seabed by 0143 h on 28 December, whereupon dynamic positioning calibration began, finishing at 0530 h. The vessel moved 1.5 nmi upcurrent from the well center, and the crew began making up and running the LWD bottom-hole assembly (BHA) into the hole from 0730 h. The LWD BHA was run to 260 m drilling depth below rig floor (DRF) by 1445 h, when time was taken to test the active heave compensator (AHC). After 30 min in standby mode, the AHC test was suspended because there was a malfunction. The cause of the malfunction could not be found. Running into the hole continued to the seabed, when Hole C0022A was spudded at 1600 h (water depth = 2675.5 meters below sea level [mbsl]) and the next 40.5 mbsf was washed down. From 1730 h, LWD commenced following the same rotation speed increase with depth plan to total depth as for IODP Holes C0018B and C0021A: 15 rotations per minute [rpm] × 0.6–2.5 kNm (40.5–45.5 mbsf), 30 rpm × 0.9–3.4 kNm (45.5–50.5 mbsf), 45 rpm × 0.5–4.7 kNm (50.5–60.5 mbsf), 60 rpm × 0.8–4.4 kNm (60.5–82.5 mbsf), 70 rpm × 1.1–7.9 kNm (82.5–111.5 mbsf), and 80 rpm × 0.9–14.1 kNm (111.5–420.5 mbsf). Kill mud was spotted from 2200 h, and the LWD BHA was pulled out of the hole to 36 mbsf for wait on weather. At 0300 h on 29 December, the LWD BHA was run down to 96 mbsf and then reamed down from 0330 h to 136.0 mbsf. Once back at 136.0 mbsf, drilling ahead with the LWD BHA resumed to total depth (420.5 mbsf), finishing at 1645 h. From 1715 h, the LWD BHA was pulled out of the hole to 2692.6 m DRF (11 m above seabed) while a damaged drill pipe joint was laid down. Pulling out of the hole continued from 1930 h and the BHA reached the surface by 0315 h on 30 December.

Hole C0022B

At 1800 h on 30 December 2012, the vessel moved 10 nmi north of Site C0022 into the low-current area to begin loading bentonite and drilling equipment. From 2130 h, the hydraulic piston coring system (HPCS)/extended shoe coring system (ESCS) BHA was made up and tested. From 0115 h, the BHA was run into the hole and the vessel began drifting toward the well center by 0300 h on 31 December. The HPCS BHA reached 2960 m DRF by 0745 h and stood by for the next 2 h while the core blowout preventer ball valve underwent maintenance. The bit was lowered to 2700 m DRF (2 m above the seabed), the sinker bar was run down at 1130 h in preparation for cutting the first core, and spud-in and shooting took place at 1245 h (seafloor = 2674 mbsl). Washing down to 19.5 mbsf ended at 1500 h, and piston coring resumed at 1600 h. By 0515 h on 1 January 2013, HPCS Core 338-C0022B-8H had been cut at 84.5 mbsf. At that point, coring operations switched from HPCS to the extended punch coring system (EPCS), cutting the first EPCS core (9T) by 0945 h to 89.5 mbsf. At 1730 h, the coring system was changed from EPCS to ESCS, cutting from 99.5 mbsf. ESCS coring continued, pausing at 1315 h on 2 January to drill ahead from 162 to 190.5 mbsf. ESCS coring from 190.5 mbsf resumed at 1715 h. ESCS coring

paused again at 0315 h on 3 January, while drilling ahead from 228.5 to 266.5 mbsf (38 m advance) was completed. ESCS Core 338-C0022B-24X was cut from 0900 h, after which coring resumed. Coring in Hole C0022B finished at 0745 h on 5 January with the recovery of Core 41X. Kill mud was spotted, and the ESCS BHA was pulled out of the hole to the surface by 2330 h. As drill pipe was laid down, the transponders were released and recovered on the surface by the watch boat. The vessel began moving to Site C0021 in preparation for coring operations.

Logging while drilling

LWD and MWD data were collected in Hole C0022A to a total depth of 420.5 mbsf, allowing continuous downhole measurements of in situ properties and downhole drilling parameters. Surface drilling parameters were also recorded. Schlumberger's TeleScope downhole MWD tool and geoVISION and arcVISION LWD tools were deployed in Hole C0022A (see Fig. **F3** in the "Methods" chapter [Strasser et al., 2014a]). Both real-time data and memory data were collected, including annular pressure, gamma ray, resistivity, and azimuthal resistivity images. Overall, data quality was good, with the exception of poor quality of the upper interval (0–49.0 mbsf) of the resistivity images because of wash down. The gamma ray and resistivity logs and resistivity images were interpreted for lithologic and structural features. Porosity and bulk density were calculated using resistivity data, and in situ stress orientations were determined from compressional borehole breakout orientations.

Data quality and processing

Data quality was checked at three points: during data acquisition by monitoring the real-time data, during data processing by validation, and through an inspection of the final, processed data. The Logging Staff Scientist and logging scientists assessed the real-time drilling parameters, rate of penetration, rotations per minute, surface weight on bit, equivalent circulating density, stick-slip, downhole weight on bit, and downhole torque using logging watchdog sheets (see the **"Methods"** chapter [Strasser et al., 2014a]). The overall quality of the processed logging data was determined to be fair, although somewhat affected by weather conditions during acquisition. No useful downhole temperature data were collected. Because of no rotation during wash down and drilling with low rotations per minute, poor quality resistivity images were recorded above 49 mbsf (2753 m DRF). Sharp horizontal lines, artifacts from ship heave and pipe vibration, were observed throughout the processed resistivity images and make identification of low-angle bedding and features problematic. Missing data because of high stick-slip (>300 cycles/min) were also observed.

The seafloor was confirmed at 2704.0 m DRF (2675.5 m mud depth below sea level [MSL]), based on the natural gamma radiation and resistivity curves extracted from the memory data.

Logging units and lithostratigraphy

Site C0022 is located near the tip of the megasplay fault drilled at Site C0004 and is upslope from Site C0008 (Expedition 314 Scientists, 2009b; Expedition 316 Scientists, 2009a, 2009b). Hole C0022A penetrated slope basin sediment into the very tip of the megasplay. For consistency with previous work (e.g., Expedition 333 Scientists, 2012c; Kimura et al., 2011; Strasser et al., 2011), only one unit composed entirely of slope basin sediment is defined as Unit I (0–420.5 mbsf) in Hole C0022A. The gamma ray log supports this classification, as its character does not change significantly through the entire drilled section and maintains a constant baseline of ~75 gAPI. However, three subunits were identified based on changes in the character of the resistivity logs (Fig. **F3**).

Subunit IA (0–74.3 mbsf)

Subunit IA extends from the seafloor to 74.3 mbsf, including the 49 mbsf wash down interval. In the upper 7 m, the gamma ray log increases to its baseline of ~75 gAPI. Through the rest of Subunit IA, gamma ray values remain constant, with minor fluctuations (±10 gAPI) around this baseline. Four small (<2 m thick) low gamma ray spikes are observed at 16.2, 40.7, 48.6, and 61.1 mbsf; in all four instances, gamma ray values drop to 59–60 gAPI (Fig. **F4**). These intervals are interpreted to be thin sand or ash horizons. From the seafloor to ~7 mbsf, resistivity increases to ~0.9 Ωm and exhibits a gradual increase to ~1.1 Ωm through the rest of Subunit IA, with frequent ±0.1 Ωm fluctuations. The base of Subunit IA is placed at 74.3 mbsf, where the character of the resistivity logs changes significantly.

Subunit IB (74.3–212.9 mbsf)

Subunit IB exhibits the most variability in the resistivity logs and contains a highly fractured zone (86.6–105.2 mbsf) identified from the resistivity images and discussed in more detail below (Fig. **F3**). Throughout Subunit IB, the gamma ray log exhibits repeated decimeter-scale coarsening- and fining-up-

ward cycles (Fig. F4). This subunit also exhibits several strong localized spikes in resistivity and, to a lesser extent, in gamma ray.

Subunit IC (212.9–420.5 mbsf)

The Subunit IB/IC boundary is placed immediately below a prominent low-resistivity spike, marking the end of the higher variability of Subunit IB. Subunit IC extends from 212.9 mbsf to the base of the hole (420.5 mbsf) and is characterized by low variability in resistivity (Fig. F4). Throughout Subunit IC, the gamma ray log exhibits small-scale variations around the baseline and resistivity maintains minor fluctuations (±0.2 Ωm) around a constant baseline (~1.2 Ωm), with the exception of a few prominent spikes. At 254.7 mbsf, resistivity drops to ~0.83 Ωm, with no corresponding change in the gamma ray log. Another resistivity low (~0.7 Ωm) at 266.5 mbsf corresponds to a very low spike (~38.9 gAPI) in the gamma ray log, tentatively interpreted as a sand bed. Between 295 and 299 mbsf, a series of high (>1.6 Ωm) and low (0.7 and 0.4 Ωm) resistivity spikes occur, with no corresponding variations in the gamma ray log. Another low resistivity of 0.69 Ωm occurs at 333.8 mbsf, coincident with a gamma ray low of ~32 gAPI, indicating another possible sand horizon. Between ~300 and 387 mbsf, resistivity exhibits decimeter-scale cycles of gradual increases and decreases around a 1.2 Ωm baseline. From ~387 mbsf to the base of the hole (420.5 mbsf), resistivity returns to a fairly constant value (1.2 Ωm), with only minor fluctuations (±0.1 Ωm), and the gamma ray log shows a gradual increase from ~60 to ≥75 gAPI.

Structural image analysis

Shallow, medium, and deep button resistivity data were used to generate both static and dynamic processed images (see the **"Methods"** chapter [Strasser et al., 2014a]). Bedding, fractures, faults, and breakouts were recorded. In the absence of a caliper measurement, the bit diameter was used as the borehole diameter and assumed to be constant.

Bedding and fractures

Despite poor quality images because of heave-induced horizontal lines, some bedding and structural features could be identified from the resistivity images. Throughout the entire section, bedding dips are consistently low angle (0°–30°) but exhibit subtle variations with depth (Fig. F3). Bedding dip changes between Subunits IB and IC. Within Subunit IB, the dominant dip direction is to the south-southeast and dip angles predominantly range between 15° and 30°. Below 212.9 mbsf (within Subunit IC), however, the dominant dip direction switches to northwest and dip angles trend shallower (<20°) (Fig. F5).

Fracture orientations are variable throughout the section but are generally high angle (>40°) and primarily dip toward the northwest (Fig. F5), particularly between 86.6 and 105.2 mbsf. This is identified as a highly fractured zone (Fig. F3) and interpreted as the region of the megasplay tip, although no clear fault can be identified. An interval between 170 and 270 mbsf corresponds to a section of particularly low quality resistivity images; therefore, the absence of fractures in this section could be related to image quality rather than to an absence of structure. Below ~320 mbsf, many high-angle resistive fractures can be identified.

Borehole breakouts

In Hole C0022A, few breakouts are observed in the upper 130 m section, with the exception of those breakouts appearing immediately following a pipe connection. Breakouts could be associated with pipe stand connections because of lower annular pressure during connections or because of some time-dependent evolution of breakouts. Breakout occurrence increases with depth, and breakouts are most prevalent in the lower section of logging Subunit IC (Fig. F3). Analyses indicate a mean breakout azimuth of 49.5° and, therefore, an azimuth of 139.5° for the maximum horizontal stress (S_{HMAX}). This northwest–southeast trend is roughly parallel to the convergent direction of the Philippine Sea plate and to the dominant S_{HMAX} determined at previous IODP Nankai Trough Seismogenic Zone Experiment (NanTroSEIZE) Sites C0001, C0004, C0006, and C0009 (Chang et al., 2010; Lin et al., 2010; Byrne et al., 2009; Kinoshita et al., 2008) and Ocean Drilling Program Site 808 (Ienaga et al., 2006; McNeill et al., 2004).

Physical properties

Estimation of porosity and bulk density from resistivity

Porosity was estimated in Hole C0022A using Archie's law (Archie, 1947), which describes an empirical relationship between measured resistivity at the bit and porosity (see the **"Methods"** chapter [Strasser et al., 2014a]). Because no temperature measurements were taken at Site C0022, seawater electrical resistivity was calculated using the temperature profile that was estimated for Hole C0008A during Expedition 316 (Expedition 316 Scientists, 2009b). Site C0008 is located ~600 m southeast of Site C0022 and penetrates lithologically similar sediment, so it should provide a reasonable estimate for tempera-

ture. The temperature at the seafloor is estimated at 2.2°C, with an average thermal gradient of 51°C/km (Expedition 316 Scientists, 2009b). Uncertainties in the quality of resistivity measurements taken on cores collected in Hole C0022B meant that data from these cores were not used to estimate the Archie parameters for Hole C0022A (see **"Physical properties"**). Insufficient data were available from nearby Sites C0004 and C0008 to make reasonable estimates of the Archie parameters. Additionally, estimates of resistivity-derived porosity at IODP Site C0010, which is also closer to Site C0022 than Site C0002, were carried out using parameters nearly identical (a = 1 and m = 2.3) to those estimated at Site C0002 (Expedition 319 Scientists, 2010). Thus, Archie parameters a = 1 and m = 2.4 estimated for Kumano Basin sediment at IODP Site C0002 during Expedition 314 were applied to Hole C0022A for consistency with previous estimations (Expedition 314 Scientists, 2009a). Bulk density was calculated from the resistivity-derived porosity using a grain density (ρ_g) value of 2.70 g/cm^3. This grain density value is an average, with a standard deviation of 0.05 g/cm^3, of all the moisture and density (MAD)–derived grain densities measured from Hole C0022B (see **"Physical properties"**).

The resistivity-derived porosity and bulk density depth trends are shown in Figure **F3.** Porosity is very high in the upper 10 m of the hole, decreasing from ~91% at the seafloor to 63% at 10 mbsf; these large values are caused by bit resistivity measurements that are very close (less than a factor of 2 larger) to the estimated values of seawater resistivity. From 10.0 to 100 mbsf, resistivity-derived porosity decreases in a generally linear fashion to 55%. Porosity remains relatively constant to ~200 mbsf, with two prominent increases in porosity at 121.2 and 187 mbsf, where porosity increases rapidly to 58% and 59%, respectively. From 202.1 mbsf to the base of Hole C0022A (420.3 mbsf), porosity decreases in an approximately linear trend to 48%.

Trends in resistivity-derived bulk density tend to mirror those described above for resistivity-derived porosity (Fig. **F3**). Generally, bulk density increases from ~1.1 g/cm^3 at the seafloor to 1.82 g/cm^3 at 121.2 mbsf. Bulk density decreases rapidly to 1.68 g/cm^3 at 125.7 mbsf before increasing again to 1.74 g/cm^3 at 154 mbsf. From 154 to 202.1 mbsf, bulk density decreases to 1.68 g/cm^3. Finally, resistivity-derived bulk density increases to 1.88 g/cm^3 at the base of the hole (420.5 mbsf).

Figure **F6** shows the resistivity-derived porosity and bulk density logs plotted for comparison along with MAD-derived measurements taken on cores from Hole C0022B. Resistivity-derived porosity and bulk density are generally within the scatter of the MAD-derived values throughout the depth of the hole. However, at ~335 mbsf, the porosity offset ($\Delta\phi = \phi_{MAD} - \phi_{resistivity}$) becomes skewed toward negative values. That is, on average the resistivity-derived values are slightly higher than the MAD-derived values near the base of the hole, although the absolute value of the offset is never greater than $|\Delta\phi| = 0.1$, excluding a few outliers.

Lithology

One lithologic unit with two lithologic subunits are recognized in Hole C0022B (Fig. **F7;** Table **T1**). Coring and logging at this site targeted a slope basin interval that was previously described at Sites C0004 and C0008 (Expedition 316 Scientists, 2009a, 2009b; Strasser et al., 2009, 2011; Kimura et al., 2011). A total of 41 cores yielded 316 sections (Table **T2**), with recovery ranging from 154% to ~20% (average = ~82%) (see **"Background and objectives"**).

Unit designations applied here are adopted with minor modification from Kimura et al. (2011). Units are differentiated based on contrasts in major and minor lithologies, grain size, mineralogy, age (see **"Biostratigraphy"** and **"Paleomagnetism"**), and log character (see **"Logging while drilling"**). Caution is required in the assessment of overall sand content and sand/mud ratios, as many of the cores, notably Cores 338-C0022B-12X through 34X, display prominent coring disturbance with heavy biscuiting and fracturing with admixing of drilling slurry. It is likely that much of the sand washed out during coring (see **"Operations"**).

Lithologic Subunit IA (slope sediment)

Interval: Sections 338-C00022B-1H-1, 0 cm, to 38X-2, 56 cm
Depth: 0–383.47 mbsf

The dominant lithology of lithologic Subunit IA is dark olive-gray silty clay (2.5GY 4/1) with variable components of calcareous nannofossils, foraminifers, siliceous biogenic debris (sponge spicules, diatoms, silicoflagellates, and radiolarians), and volcanic ash. Calcite, determined by X-ray diffraction (XRD), ranges from the detection limit (~0.5%) to ~38%, with an average of ~7%. A trend toward diminishing carbonate content with depth is observed (Fig. **F8;** Tables **T3, T4, T5**). The ratio of feldspar to quartz + feldspar trends toward larger values across the depth range of this subunit (Fig. **F8**).

Minor lithologies include sand, sandy silt, silt, and volcanic ash, which vary significantly in thickness

and frequency throughout the section (Fig. F9). A few beds with recognizable fining-upward successions are observed. Such beds typically begin with a sharp-based ~2 cm dark gray sand layer, grading upward through burrowed clayey silt into silty clay that typically contains more pelagic debris (coccoliths and siliceous skeletal elements) (Fig. F10). Many sands contain benthic foraminifers in amounts up to several volume percent (Fig. F11B). Blebs of volcanic ash (possible lapilli), discrete pumice fragments (granule to pebble size), and thin ash layers are widely distributed through most of the core sections.

Faint green color banding and mottling is present throughout most of the subunit (Fig. F10). Bioturbation is common and includes *Chondrites, Zoophycos*, possible *Trichichnus*, and other discrete burrows, many of which are pyritized. Bioturbation is especially apparent in the X-ray computed tomography (CT) images in the shallowest cores. Rare tubes of a sponge spicule agglutinating organism (possible benthic foraminifer) are observed throughout the hole.

The silt and sand fraction is dominated by quartz, feldspar, and metasedimentary lithic fragments and locally includes abundant clear volcanic glass and pumice fragments (Fig. F11E, F11F). Volcanic ash layers are distributed throughout lithologic Subunit IA (Fig. F7). Many of the sands are dark gray to nearly black, a coloration that arises from the high content of authigenic pyrite (Fig. F12) rather than from a mafic volcaniclastic component. In the most pyrite-rich sand, pyrite takes the form of microcrystalline grain coatings that greatly hinder grain identification (Fig. F12B). In other sands, pyrite is in the form of disseminated framboids (Fig. F12A), in some cases localized along burrows that survive as pyrite-cemented aggregates in smear slides (Fig. F12C).

Lithologic Subunit IB

Interval: Sections 338-C0022B-38X-2, 56 cm, through 41X-CC
Depth: 383.47–415.90 mbsf

The top of lithologic Subunit IB is placed at the first occurrence of a discrete bed of mud clast gravel (granule size) at 383.5 mbsf (Sample 338-C0022B-38X-2, 56 cm) (Fig. F13). At approximately the same depth, the gamma ray log suggests a substantial increase in sand below this level (see **"Logging while drilling"**). The upper portion of the subunit (within Core 38X) consists of a series of interbedded mud clast gravels (Figs. F7, F13), with layers of thin sand, clayey silt, and silty clay. Gravel beds range from 2 to 30 cm thick and are composed of well-rounded greenish gray to dark greenish gray slightly indurated silty clay clasts, which range in size from <1 mm to 5 cm, in an olive to greenish gray silty clay matrix (Fig. F13). The gravel is mostly unconsolidated, but within the consolidated sections gravel shows fabric variation from matrix supported within a silty clay matrix to clast supported. The great majority of clasts are rounded to subrounded, with rare subangular pieces. In smear slides, an abundance of possible sand-sized clay clasts is observed (Fig. F14).

Below Core 338-C0022B-39X, the dominant lithology within Subunit IB is dark olive-gray silty clay with significant interbeds of clayey silt and dark gray fine- to coarse-grained sandstone. Sand contains subordinate quartz, abundant plagioclase, and as much as 2% or more of dense mafic minerals (mostly brown amphibole and pyroxene) (Fig. F15) with common brown to black semiopaque grains, which could be intermediate mafic volcanic rock fragments, clay clasts, or glauconite. A notable crystal ash occurs in Sample 39X-5, 40 cm. This ash contains an abundance of clear glass with a significant component of euhedral brown hornblende, euhedral zoned plagioclase, and brown glass (Fig. F15E, F15F).

X-ray fluorescence core scanning

Section 338-C0022B-8H-4 shear bands

The sediment in Section 338-C0022B-8H-4 has distinct shear bands (see **"Structural geology"**). The section interval between 5 and 90 cm was scanned using the TATSCAN-F2 core scanner (Sakamoto et al., 2006) (Fig. F16; Tables T5, T6, T7). A scanning resolution of 0.5 cm was used with a measurement time of 200 ms per measurement. Within this section, an area 60 cm^2 (40–55 cm) was rescanned using the mapping utility of the TATSCAN-F2. A scanning resolution of 0.5 cm and a measurement time of 200 ms was used again, but this time elemental composition was measured over a 15 cm × 4 cm area.

In the line scan, we see an increase in Al_2O_3 around the shear bands (Fig. F16). The increase in Al_2O_3 is less clear in the lowest shear band at 65 cm, but this might be due to the crack present in this area, which hampers the collection of the X-ray signal. In general, K_2O is higher around the shear bands. Fe_2O_3 is rather low in the upper part of the section across the first two shear bands, except for the Fe_2O_3 peak at 20 cm, which can be linked to a patch of ash. At the shear band at 65 cm, Fe_2O_3 is high and K_2O is low.

CaO variability corresponds to the presence of patches of white coloration (Fig. F16). In areas with more prominent white coloration, CaO is higher. The increase in CaO content is even more obvious in the X-ray fluorescence (XRF) mapping (Fig. F17). CaO concentrations are clearly higher in the whiter areas, whereas SiO_2 concentrations are lower. Al_2O_3 is also lower in whiter areas. Al_2O_3 concentrations are

higher in the shear band area. This could indicate that more clay minerals are present in this area, although it could also be linked to reduced porosity (Milliken and Reed, 2011). The XRF mapping also indicates that the increase in Fe_2O_3 is not associated with the darkest coloration but, rather, is linked to areas with a green color. Possibly the green color indicates a higher glauconite or chlorite content.

Section 338-C0022B-38X-5 mud clasts

The sediment in Section 338-C0022B-38X-5 contains mud clast intervals within a clearly deformed zone (Figs. **F13C, F18**). Unfortunately, this section has a lot of drilling disturbance (biscuiting) and cracks, hampering collection of a good XRF measurement.

The interval between ~10 and 20 cm, where most of the mud clasts occur, shows higher Fe_2O_3 and K_2O values and lower Al_2O_3 values at the depth where the clasts are present (orange dashed line in Fig. **F18**). Overall, the interval shows a general increase in Al_2O_3 (yellow band in figure). Al_2O_3 also shows a decreasing trend in regions where the sediment surface has a green color (green bands in figure). The fining-upward interval between ~80 and 65 cm has rather variable Fe_2O_3 content but shows a clear increase in CaO as grain size decreases (gray band in figure). The deformed interval between ~85 and 120 cm is rather homogeneous (orange band in figure), except for the occurrence of some very small mud clasts at ~105 cm (orange dashed line in figure). At intervals where distinct burrows are visible, indicating the homogenization of the sediment by bioturbation, the XRF line scan results show very little variability (black dashed/dotted lines in figure).

Comparison to lithologic variations at Sites C0004 and C0008

The stratigraphic interval sampled in Hole C0022B was previously cored at Sites C0004 and C0008 (Expedition 316 Scientists, 2009a, 2009b) (Fig. **F19**). The slope basin interval cored at Site C0018 (Expedition 333 Scientists, 2011) is also analogous but cannot be easily correlated to Hole C0022B without biostratigraphic data because an anticlinal structure separates the stratigraphic successions at these two sites (Kimura et al., 2011). Hole C0022B, as seen in seismic sections (Fig. **F20**), penetrated Unit I as defined by Kimura et al. (2011). Based on interpretation of the seismic section, lithologic Subunit IB at Site C0022 is interpreted to be within the lower slope basin interval that onlaps onto the underlying prism, thinning in the direction of Site C0008. Age determinations (see **"Biostratigraphy"**) show that the lowermost portion of Hole C0022B (>400 m; 2.3–2.5 Ma) is approximately correlative with sediment just above the upper boundary of the accretionary prism in the lowermost portion of Subunit IB of Hole C0008A.

Mineralogical composition observed in Hole C0022B has similarities and contrasts with compositions observed at Sites C0004, C0008, and C0018. The feldspar content (Table **T3;** Fig. **F19**), together with the contents of mafic glass, heavy minerals (abundant brown hornblende and pyroxenes), and intermediate to basaltic lithic fragments, displays a trend suggesting increasing contribution of mafic volcanic material with depth that begins in the lower portion of lithologic Subunit IA, becoming quite pronounced within the coarser materials of lithologic Subunit IB. The presence of mafic material displays a similar pattern at all three sites, although a portion of the trend is missing at Site C0004, as a consequence of faulting along the megasplay.

The overall decline in carbonate content with depth in lithologic Subunit IA is not uniform across the sites. All four sites have the highest carbonate content (Fig. **F19**) in the shallowest portion of lithologic Subunit IA and display a trend of declining carbonate content with depth. The dominant form of carbonate at all three sites is coccolith debris, although calcareous benthic foraminifers are also reported as important components within sand (Expedition 316 Scientists, 2009a; Expedition 333 Scientists, 2011). At Site C0018, the decline in carbonate occurs at the Subunit IA/IB boundary. At Site C0004, carbonate is much diminished in the lower portion of Subunit IC sampled below the fault, but the transition from high to low carbonate has been removed by faulting. In Hole C0022B, the decline in carbonate occurs between ~230 and 270 mbsf (Figs. **F19, F20**), possibly corresponding to reflector "A" of Kimura et al. (2011) within the lower portion of their Subunit IC. At Site C0008, however, the carbonate content remains high until the appearance of the mud clast gravels (Fig. **F19**) (placed within Subunit IC by Kimura et al. [2011] but placed here within lithologic Subunit IB), very similar to the situation at Site C0018.

Summary

Lithologic Subunit IA is interpreted as a slope basin succession in agreement with previous work (Expedition 316 Scientists, 2009a, 2009b; Strasser et al., 2009, 2011; Kimura et al., 2011). Within this subunit, there is an overall trend of increasing siliciclastic composition, both with depth and across the sites, that is balanced by an associated decrease in the content of pelagic biogenic debris. Unit I at Site C0008 contains more carbonate overall and retains

more carbonate to a greater depth than Unit I at Sites C0004 and C0022. We tentatively propose that this trend relates to a relatively more distal depositional position at Site C0008 at the more seaward edge of the slope basin. Lithologic Subunit IB, with more and coarser sand, may represent the earliest stages of the slope basin fill.

Structural geology

Structures observed in cores retrieved from Hole C0022B fall into two categories: structures that can be observed along the entire cored section and structures observed at a specific interval within which the tip of the splay fault, initially identified on seismic profiles and subsequently drilled through at Site C0004 during Expedition 314, may be located (Expedition 314 Scientists, 2009b; Expedition 316 Scientists, 2009a; Moore et al., 2009). We first describe structures distributed along the entire cored section. Structures relevant to the inferred splay fault will be described in a separate section.

Bedding

A total of 190 bedding measurements were made on cores from Hole C0022B. Most bedding dips are between 0° and 20°, whereas bedding dips steeper than 20° (up to ~50°) are exclusively observed between 73.49 and 143.82 mbsf (Fig. **F21**). In this bedding disturbed zone (shaded section in figure), bedding dips fluctuate but, in total, progressively increase toward the bottom. From 145 mbsf downward, bedding dips remain <15°.

Bedding strike does not show any noticeable change with depth, whether above or below the bedding disturbed zone (Figs. **F21, F22B, F22D**). Bedding orientations within the bedding disturbed zone show scattered distributions (Fig. **F22C**).

Minor faults and deformation bands

Minor faults and deformation bands are common in Hole C0022B cores (Figs. **F23, F24**). Of 26 faults measured in Hole C0022B cores, 25 are clustered in two intervals: between 50 and 83 mbsf (fault Cluster 1), and between 386 and 405 mbsf (fault Cluster 2). With one exception dipping at 32°, all faults dip between 50° and 85°. Figure **F24** does not show any consistent variation of fault strike with depth. Hole C0022B faults show two preferred orientations (Fig. **F25**): north–south to N20°E trending faults and N100°E to N145°E trending faults. Separately plotting faults from fault Cluster 1 and those from fault Cluster 2 shows that the former strike around northwest–southeast (Fig. **F25B**), whereas the latter preferentially strike north–south to northeast–southwest (Fig. **F25C**). Such a difference in fault orientation suggests different stress conditions between the two fault clusters.

Among the 26 faults observed on core split surfaces, 15 show a normal component of displacement. Displacement along the remaining 11 faults cannot be established. Striations observed on 4 fault surfaces (all from the footwall) have rakes around 45°, indicating oblique slips along these faults.

Deformation bands (Ujiie et al., 2004; Milliken and Reed, 2011) appear dark and homogeneous, with thickness ranging between <0.5 and 2 mm. Boundaries with the host sediment are commonly sharp but in some instances are diffuse. Because they are never crossed by burrows, even in heavily bioturbated intervals, deformation bands likely postdate sediment bioturbation. In most cases, deformation bands occur sporadically but anastomosed networks are also observed.

A total of 61 deformation bands were observed and measured in Hole C0022B core, all in the splay fault footwall and most below 275 mbsf. Figure **F24** does not show any trend in the strike of deformation bands with depth. In contrast, sets of deformation bands can be distinguished on a stereographic projection (Fig. **F26**): N60°E to N70°E trending high-angle deformation bands, N140°E to N190°E trending high-angle deformation bands, and low-angle (<10°) deformation bands without preferred strike. In some cases, high-angle deformation bands show a component of normal displacement. Conversely, low-angle deformation bands in rare instances show reverse offsets of markers.

Megasplay fault

Three-dimensional seismic reflection studies (Moore et al., 2007, 2009) suggest that Hole C0022B may intersect the extension of the megasplay fault. In Hole C0022B, the bedding disturbed zone (73.49–143.82 mbsf) could correspond to the megasplay fault zone or flexure zone. Top and bottom depth of the bedding disturbed zone is consistent with two biostratigraphic age reversals: 76.48–84.48 and 132.38–148.46 mbsf (see **"Biostratigraphy"**).

In Hole C0022B between 93.36 and 95.36 mbsf, silty claystone exhibiting weakly marked planar fabrics was observed in intervals 338-C0022B-10T-5, 49–51 cm, 10T-CC, 19–20 cm, and 11H-1, 18–19 cm (Fig. **F27**). The planar fabrics, which could correspond to R- or P-type shear surfaces, bear faint striations. The rakes of the striations are close to 90°, suggesting dip-slip motion (pure normal slip or pure reverse slip). The above-mentioned intervals could corre-

spond to secondary branches of a first-order fault that may not have been sampled during drilling. Indeed, although Core 10T recovery is 100%, Core 11T recovery is only 17.2% (0.86 m). This implies that 82.8% (4.14 m) of the interval drilled for Core 11T remains unsampled and hence unexplored. In summary, the interval 94.272–99.5 mbsf in Hole C0022B corresponds to a possible shear zone related to the splay fault. This estimate agrees well with the LWD data obtained in Hole C0022A (see **"Logging while drilling"**), which show a low-resistivity interval at 100–101 mbsf, located in a fractured zone extending from 86.6 to 105.2 mbsf.

Summary

The recovery of the bedding disturbed zone as well as foliated claystone intervals suggest that the megasplay fault zone intersected at Site C0004 (Expedition 316 Scientists, 2009a) may extend southeastward to Site C0022. However, incomplete recovery at this site precludes a definitive conclusion. Moreover, smearing during core splitting renders observation of core surfaces difficult. Additional shore-based studies, including resin impregnation of the foliated claystone intervals and thin section making, are required to better characterize the planar fabrics observed on core surfaces.

Biostratigraphy

Preliminary biostratigraphy for Hole C0022B is based on shore-based examination of calcareous nannofossils and planktonic foraminifers. Ages constrained by calcareous nannofossils and planktonic foraminifers are consistent overall. Both nannofossils and foraminifers indicate an age of ~2.0 Ma for the sediment at the bottom of the hole and a stratigraphic reversal or reworking of older sediment at ~130 mbsf. Calcareous nannofossils indicate additional stratigraphic reversals or reworking of older sediment at ~80 and ~145 mbsf. Stratigraphic reversals are likely associated with megasplay faulting, whereas reworking of older sediment could also be explained by mass-movement processes.

Calcareous nannofossils

A total of 38 core catcher samples recovered from Samples 338-C0022B-1H-CC (6.98 mbsf) to 41X-CC (415.88 mbsf) were examined (Table **T8**). Well-preserved nannofossils occur abundantly throughout the sequence in Hole C0022B. Although reworked specimens are frequently observed in examined samples, a good biostratigraphic framework was established for the entire succession, although some stratigraphic reversals, discontinuities, or sediment reworking are observed.

The uppermost sample from Hole C0022B (Sample 338-C0022B-1H-CC) contains dominant *Emiliania huxleyi* (Table **T8**). Therefore, this sample is younger than 0.291 Ma and the interval above this sample corresponds to Zone NN21. The last occurrence (LO) of *Pseudoemiliania lacunosa* (0.436 Ma) is placed between Samples 1H-CC and 2H-CC (28.98 mbsf) because of the consistent occurrence of *P. lacunosa* below the latter sample. This event marks the base of Zone NN20. Both Samples 4H-CC (47.98 mbsf) and 5H-CC (57.48 mbsf) contain *Reticulofenestra asanoi*. Thus, the LO and first occurrence (FO) of this species are clearly recognized. The presence of *R. asanoi* along with common medium *Gephyrocapsa* spp. (≥4 µm), which has a bar parallel to the short axis of a specimen, provides a maximum age of 1.04 Ma between Samples 4H-CC and 5H-CC. The LO of the large form of *Gephyrocapsa* spp. (>5.5 µm) (1.24 Ma) is placed between Samples 6H-CC (66.98 mbsf) and 7H-CC (76.48 mbsf).

A stratigraphic reversal is observed between Samples 338-C0022B-7H-CC (76.48 mbsf) and 8H-CC (84.48 mbsf) because the latter sample can be correlated with the last consistent occurrence of *R. asanoi* and the reentrance of medium *Gephyrocapsa* spp. (≥4 µm) (0.903–1.04 Ma) (Table **T8**). Larger forms of *Gephyrocapsa* spp. (>5.5 µm) are consistently observed from Samples 9T-CC (89.48 mbsf) to 21X-CC (209.31 mbsf). The LO of *Helicosphaera sellii* (1.34 Ma) is recognized between Samples 21X-CC and 22X-CC (211.18 mbsf). Thus, the interval between 89.48 and 209.31 mbsf is younger than 1.34 Ma. However, there are some discontinuities in this interval, because Sample 16X-CC (132.38 mbsf) contains abundant *Calcidiscus macintyrei* (age of the LO is 1.6 Ma) and other older nannofossil species. Sample 17X-CC (142.70 mbsf) (1.34–1.589 Ma) is slightly older than samples below Sample 18X-CC (148.46 mbsf) because it only contains *H. sellii*, whose last occurrence corresponds to 1.34 Ma.

Gephyrocapsa spp. (≥4 µm) first appeared in Sample 338-C0022B-28X-CC (300.48 mbsf) (Table **T8**), and the FO of this species (1.67 Ma) is recognized in this horizon. The base of nannofossil Zone CN13b (NN19) is also found between Samples 28X-CC and 29X-CC (305.42 mbsf) (Fig. **F15** in the "Methods" chapter [Strasser et al., 2014a]; Table **T8**). The interval below Sample 38X-CC (390.98 mbsf) is characterized by abundant occurrences of discoasters (Table **T8**). The LO of *Discoaster brouweri* is placed between Samples 37X-CC (374.68 mbsf) and 38X-CC; thus,

this horizon (2.06 Ma) corresponds to the base of nannofossil Zone NN19. *Discoaster pentaradiatus* is only found in Sample 41X-CC (415.88 mbsf). Therefore, the Zone NN18/NN17 boundary is placed between Samples 40X-CC (406.83 mbsf) and 41X-CC.

Planktonic foraminifers

Globigerinoides ruber (pink) is found in Sample 338-C0022B-1H-CC (6.98 mbsf) (Table T9), so this sample is older than 0.12 Ma, corresponding to its LO. In addition, the LOs of *Truncorotalia tosaensis* (0.61 Ma) and *Globoturborotalita obliquus* (1.30 Ma) are recognized between Samples 1H-CC and 2H-CC (28.98 mbsf) and between Samples 8H-CC (84.48 mbsf) and 9H-CC (89.48 mbsf), respectively.

The change in the dominant coiling direction of *Pulleniatina* spp. from sinistral to dextral (1.7–1.8 Ma), occurring between Samples 338-C0022B-26X-CC (290.48 mbsf) and 28X-CC (300.48 mbsf), is consistent with the LO of *Neogloboquadrina asanoi* (1.8 Ma) between Samples 27X-CC (295.48 mbsf) and 28X-CC (Table T9). However, the change in coiling direction of *Pulleniatina* spp. is also recognized at an interval between Samples 15X-CC (123.60 mbsf) and 16X-CC (132.38 mbsf), indicating a stratigraphic reversal as recognized by calcareous nannofossils around this interval.

The FO of *Truncorotalia truncatulinoides* (1.93 Ma) is placed between Samples 338-C0022B-34X-CC (352.50 mbsf) and 35X-CC (362.48 mbsf) (Table T9).

Geochemistry

Inorganic geochemistry

Interstitial water geochemistry

Slope sediment was sampled from the seafloor to ~415.9 mbsf in Hole C0022B. Interstitial water (IW) samples from those cores were extracted using the standard squeezing method (see "Geochemistry" in the "Methods" chapter [Strasser et al., 2014a]). Only time-sensitive parameters and elements (pH, alkalinity, chlorinity, PO_4^{3-}, and NH_4^+) and chlorinity were analyzed during the expedition because of the limited time available; the rest of the parameters were measured on board the ship within 2 months after the expedition. The analytical results are listed in Table T10, and the variations with depth are in Figure F28.

The shallowest samples yield values almost similar to those of shallowest liquid in core liner (LCL) samples (Table T11), which consist of ambient seawater mixed with bentonite. Chlorinity increases to 140 mbsf and is stable with values between 630 and 650 mM below that depth. The variation with depth is similar to that observed at Site C0004, which is close to and located landward from this site (Expedition 316 Scientists, 2009a). Such an increase in chlorinity can be attributed to the hydration of sediment following diagenetic alteration of detrital minerals and volcanic glass. Chlorinity of IW at 90–130 mbsf is occasionally lower than the average values nearby. Chlorinity in this interval could be lowered by the following three mechanisms: infiltration of seawater (~550 mM chlorinity), clay mineral reactions, or upwelling of deep dehydrated water along a fault. The depth interval is almost concordant with the depth of the fracture zone of the megasplay fault tip (80–100 mbsf; see "Structural geology"). However, updip migration of deep-sourced fluid along the fault is not clear at present because other elements are not indicative of a deep-sourced fluid.

The IW geochemistry drastically changes just beneath the seafloor as a result of biochemical reactions; those changes are especially prominent in salinity, alkalinity, and PO_4^{3-}. Alkalinity and PO_4^{3-} vary in similar ways: they increase just beneath the seafloor before gradually decreasing with increasing depth. Such concentration profiles were also observed in the IW samples at Site C0002, but the peak maximum of those components appeared between 150 and 200 mbsf (Fig. F28). NH_4^+ gradually increases to 150 mbsf and then decreases with depth, which is similar to the concentration profile at Site C0002 (although the concentration is lower at this site). Compared to NH_4^+, pH shows an opposite trend with depth. The peak depth of alkalinity and PO_4^{3-} concentration of IW at Site C0022 is similar to that at Site C0004, whereas NH_4^+ concentration at Site C0004 gradually increases with depth to 250 mbsf without showing any peak unlike at Site C0022 (Expedition 316 Scientists, 2009a). Concentrations of PO_4^{3-} and NH_4^+ components are primarily controlled by in situ microbial activity. Compared to Site C0002, the lower concentrations in IW at Sites C0022 and C0004 are attributable to the lower organic matter content. Less organic matter in the sediment can be related to the increased distance from the land.

Liquid in core liner geochemistry

Mud water remaining in the core liner was sampled and measured to assess potential contamination of the interstitial water. Results of onboard analyses are listed in Table T11. Most LCL samples give chlorinity

similar to that of seawater (~550 mM), whereas occasionally it is >580 mM. The LCL samples with higher chlorinity than seawater contain higher alkalinity. This suggests some contribution from IW, which is more saline than seawater.

Organic geochemistry

Gas chemistry from cores

The gas data are shown in Tables **T12, T13,** and **T14.** In these tables, gas content, gas concentration assuming the detected gases are dissolved in IW, molecular ratios ($C_1/[C_2 + C_3]$), and carbon isotopes of methane ($\delta^{13}C$-CH_4) are listed. The $C_1/(C_2 + C_3)$ ratios range from 600 to 16,000, indicating that methane is predominant. These compositions are usually observed in the surface of deep-sea sediment. Especially, the ratios of void gas showed CH_4 enrichment, which would reflect the high volatility of methane. The $\delta^{13}C$-CH_4 ratio of void gas, however, is not so different from that of headspace gas, suggesting $\delta^{13}C$-CH_4 values are not influenced by degassing processes.

Vertical profiles of hydrocarbons are shown in Figure **F29.** CH_4 peaks are found at ~30, 100, and 400 mbsf. The CH_4 peak at ~30 mbsf is interpreted to be due to early diagenesis, which was also observed in shallow slope sediment in the Nankai accretionary prism at Sites C0004 and C0008 (Expedition 316 Scientists, 2009a, 2009b). Below the sulfate reduction zone, CH_4 is generally produced by microbes (e.g., Reeburgh, 2007). In Hole C0022B, sulfate was completely depleted below 23.4 mbsf (Table **T10**), suggesting a strongly reductive near-surface sediment. In such an environment, coupled CO_2 reduction and H_2 oxidation by methanogens generate CH_4 (e.g., Reeburgh, 2007). On the other hand, the CH_4 peaks at ~150 and 350 mbsf are accompanied with C_2H_6 peaks (Fig. **F29**), implying that the hydrocarbons are derived from a different process than microbial production. Between 87 and 105 mbsf, a fracture zone occurs (see **"Logging while drilling"**), which could account for the prominent peak in CH_4 close to 100 mbsf.

The vertical profiles of $C_1/(C_2 + C_3)$ ratios and $\delta^{13}C$-CH_4 are shown in Figure **F30.** CH_4 with $\delta^{13}C$-CH_4 less than –80‰ Vienna Peedee belemnite (VPDB) is observed at ~30 mbsf, suggesting microbial CH_4 generation is active at ~30 mbsf. $\delta^{13}C$-CH_4 values increase with depth, reach –70‰ VPDB at ~100 mbsf, and remain constant at about –70‰ VPDB below 100 mbsf. This $\delta^{13}C$-CH_4 profile could be attributed to isotopic fractionation during methanogenesis, where microbes preferentially utilize $^{12}CO_2$ to leave $^{13}CO_2$ in the CO_2 reservoir, causing ^{13}C-enrichment in CH_4 when methanogens produce CH_4 from ^{13}C-enriched CO_2. Below 100 mbsf, the $\delta^{13}C$-CH_4 values become constant, suggesting methanogenesis is less active. In addition, the $C_1/(C_2 + C_3)$ ratios decrease from 10^4 to 10^3, which also suggests that the generation process of hydrocarbon becomes different from the microbial process in the surface sediment.

The $C_1/(C_2 + C_3)$ ratios and $\delta^{13}C$-CH_4 data are plotted on a Bernard plot (Bernard et al., 1976) (Fig. **F31**). The diagram shows that most data fall into the region of microbial origin, so CH_4 is of microbial origin. Thermogenic methane, however, mixes to some extent with the microbial CH_4.

Hole C0022B is located near the surface of the Nankai accretionary prism, where slope collapse deposits are observed (Strasser et al., 2009). Expedition 316 drill Sites C0004 and C0008 are located landward and seaward of Hole C0022B, respectively (Screaton et al., 2009). Gas hydrates were recovered at Site C0008 (Expedition 316 Scientists, 2009b). During this expedition, gas hydrates were not found in core sediment, but gas-rich sediment can be inferred from observed void spaces in core liners. As mentioned by Toki et al. (2012), the input of organic matter from land into the Kumano Basin is high because of the short distance from the source region (Japanese Islands) and the dam effect of the outer Kumano Ridge. This high input leads to a high production rate of methane, resulting in accumulation of methane and formation of gas hydrates. At Sites C0004, C0008, and C0022 in the slope of the accretionary prism, NH_4^+ concentrations were lower than those at Site C0002. This suggests that early diagenesis at sites in the slope is less active than at Site C0002 in the Kumano Basin.

Anomalies related to the fracture zone near 100 mbsf (see **"Logging while drilling"** and **"Structural geology"**) are not detected in any components in interstitial water (Fig. **F28**). Close to the fracture zone, a radical reaction generates H_2, which could stimulate methanogenesis via H_2 oxidation (e.g., Stevens, 1997). In addition, if deep-sourced fluid flowed from a zone deeper than 2000 mbsf, expected fluid temperatures would be high enough to lead to the formation of thermogenic methane. The hydrocarbons show anomalies around the ~100 mbsf fracture zone (Fig. **F29**), implying active gas migration along the fracture zone. However, the lack of hydrocarbon isotopic anomalies (Fig. **F30**) suggests that the hydrocarbons do not come from a deep zone but rather from a near-surface zone.

Inorganic carbon, total carbon, total nitrogen, and total sulphate

Calcium carbonate ($CaCO_3$) and total organic carbon (TOC) concentrations and TOC/total nitrogen (TN) (C/N) and TOC/total sulfur (TS) (C/S) ratios were determined from total inorganic carbon, total carbon, TN, and TS measurements of sediment samples from 1.2 to 415.3 mbsf (Fig. **F32;** Table **T15**).

$CaCO_3$ varies from 0.3 to 21.7 wt%, with a median of 3.9 wt%, and this variance occurs within the uppermost 50 m. Below 50 mbsf, the data are still scattered but show an overall decline downhole.

TN concentration of sediment ranges from 0.03 to 0.09 wt%, with a median of 0.06 wt%. With up to 0.09 wt%, TN is slightly higher in the surface sediment and drops to 0.05 wt% within the upper 23 m. Below this depth, TN values remain almost constant downhole but show a slightly positive trend until ~270 mbsf. Deeper than 270 mbsf, concentrations decline similar to $CaCO_3$.

TOC varies between 0.2 and 0.7 wt%, with a median of 0.4 wt%, and shows a similar development with depth as $CaCO_3$ and TN. TOC starts at 0.7 wt% and drops to 0.4 wt% within the top 23 m. Between 23 and 270 mbsf, TOC scatters between 0.3 and 0.6 wt%. Below 270 mbsf, again similar to TN and $CaCO_3$, concentrations decline constantly.

TS concentration is between 0.0 and 0.9 wt%, but the median is 0.1 wt%., indicating that overall TS values remain low (i.e., <0.2 wt%). In the top 23 m, TS increases slightly in contrast to TOC, $CaCO_3$, and TN but remains trendless and uncorrelatable afterward. Clusters of elevated and scattered TS were only detected between 23 and 85 mbsf and 359 and 415 mbsf.

The C/N ratio ranges from 4.5 to 9.3, with a median of 6.6. Following TOC, TN, TS, and $CaCO_3$, a trend is visible between 0 and 23 mbsf, where C/N drops from 8.4 to 7.1. Below 23 mbsf, the C/N ratio scatters without trend between the aforementioned values. It can be assumed that the organic matter in Hole C0022B is mainly of marine origin because the C/N ratio remains below 10 (Meyers, 1997).

Physical properties

Physical properties measurements of core samples from Site C0022 provide insight into the evolution of a splay fault and associated deformation by combining results from the adjacent sites (Sites C0004 and C0008), where coring and logging were conducted during NanTroSEIZE Stage 1 Expeditions 314 and 316. Physical properties on core samples also help calibration as well as correlation with LWD data (see **"Logging while drilling"** and **"Core-log-seismic integration"**).

Whole-round multisensor core logger and split core multisensor core logger (whole-round cores and working halves)

Whole-round cores were analyzed by the whole-round multisensor core logger (MSCL-W). The results of gamma ray attenuation (GRA) density, magnetic susceptibility, natural gamma radiation (NGR), and electrical resistivity measurements (see the **"Methods"** chapter [Strasser et al., 2014a]) are summarized in Figure **F33.** GRA density increases with depth similar to bulk density of MAD measurements discussed in **"Moisture and density measurements (discrete cores)."** From the seafloor to 210 mbsf, magnetic susceptibility slightly increases; below 210 mbsf, magnetic susceptibility increases rapidly. NGR is mostly constant above 210 mbsf and starts decreasing below 210 mbsf. This boundary suggested by magnetic susceptibility and NGR is consistent with a subunit boundary defined by LWD data (see **"Logging while drilling"**). Electrical resistivity slightly decreases with depth, although resistivity measurements on working halves and discrete samples increase with depth as discussed later.

V_P measurements on whole-round cores and working halves were conducted using the MSCL-W and the split core multisensor core logger (MSCL-S), respectively. V_P measurements using the MSCL-W are shown in Figure **F34A.** V_P data are filtered by amplitude because the MSCL-W picked up some arrivals even for locations with lots of voids or poor contacts between liner and sediment core. V_P measurements using the MSCL-S were attempted for the first time in the NanTroSEIZE project on the D/V *Chikyu* to have better contact with cores, liners, and transducers. No other physical properties measurements using the MSCL-S were conducted. Although we attempted V_P measurements using the MSCL-S on a selected section of each core from Cores 338-C0022B-1H to 6H, good quality MSCL-S data were obtained only on Section 1H-4 (Fig. **F34B**).

Moisture and density measurements (discrete cores)

A total of 400 discrete samples from Hole C0022B were measured for MAD. MAD data from Hole C0022B are summarized in Table **T16** and Figure **F35.** Between 4.25 and 415.32 mbsf, bulk density ranges from 1.51 to 2.05 g/cm^3, grain density ranges from 2.46 to 2.89 g/cm^3, and porosity ranges from

40% to 69%. Bulk density and porosity show less scatter with increasing depth. Grain density values are generally constant with depth, scattered about an average value of 2.70 g/cm^3. Both bulk density and porosity generally change linearly with depth; bulk density increases and porosity decreases. Taking a closer look, porosity decreases quickly from 69% at the seafloor to 45%–55% at ~100 mbsf, and then increases to 60% at 150 mbsf. Interestingly, the minimum porosity of this trend at ~100 mbsf is close to the megasplay fault inferred in LWD data at 100.0–100.8 mbsf (see **"Logging while drilling"**). One potential cause for this trend is that sediment near the splay fault has experienced shear-enhanced compaction. Future postexpedition research, including laboratory experiments and detailed microstructural analyses, will shed light on the evolution of physical properties associated with shear deformation.

Thermal conductivity (whole-round cores and working halves)

Thermal conductivity was measured on whole-round cores from 4.4 mbsf (Core 338-C0022B-1H) to 369 mbsf (Core 36X) using a needle probe sensor and on working-half cores from 338 mbsf (Core 33X) to 414 mbsf (Core 41X) using a half-space line source probe. Thermal conductivity generally increases from ~1.01 to 1.53 W/(m·K) with depth (Fig. **F36**). Thermal conductivity measured on working-half cores is higher than that measured on whole-round cores.

Electrical resistivity and ultrasonic *P*-wave velocity (working halves and discrete cores)

A total of 353 electrical resistivity measurements were conducted on working-half cores between 0 and 370 mbsf, using the Wenner four-pin array probe. Each measurement was recorded in the dominant lithology types per section. In addition, nine cubic samples obtained between 335 and 415 mbsf were used to measure electrical resistivity and V_P.

During the measurements on working-half cores from Site C0022, the pins of the Wenner probe were incorrectly connected to current and potential ports. This could affect resistivity absolute values toward lower values. Several measurements with both correct and incorrect configurations of the four pins were conducted on several points on Sections 338-C0022B-10T-5 and 11T-CC. The obtained data show no systematic difference between the two configurations (Table **T17**). Thus, we conclude that the measured data of resistivity with incorrect configuration of four pins are valid and report them. More importantly, we found later that the correct values of standard seawater resistivity were not obtained because of the use of a small container when the measurements on cores from Sites C0002 and C0022 were conducted on the *Chikyu*. Unexpectedly low resistivity values obtained for cores at Sites C0002 and C0022 are probably due to overestimation of seawater impedance. This problem was resolved when resistivity was measured on cores from Site C0021 using a larger container of seawater (see also **"Physical properties"** in the "Site C0021" chapter [Strasser et al., 2014d]).

Electrical resistivity ranges from 0.103 to 1.738 Ωm, with an average of 0.498 Ωm, and increases with depth as expected from the progressive densification and porosity loss (Fig. **F37;** Table **T18**). Above 280 mbsf, resistivity increases from 0.1 to 0.7 Ωm, and below 280 mbsf, more scatter is present, with an average resistivity of ~0.5 Ωm.

Resistivity measured with the Wenner probe is lower than resistivity measured on cubic samples and resistivity measured with the MSCL-W at the same depth (Fig. **F38**). However, despite low resistivity values, resistivity variations with depth are similar between the MSCL-W and Wenner probe results. The MSCL-W resistivity shows a progressive increase from 0 to 280 mbsf with values between 0.5 and 1 Ωm and stays constant below 280 mbsf at ~0.8 Ωm (Figs. **F33, F38**). The results of resistivity on cubic samples from Expedition 316 Sites C0004 and C0008 are similar to the resistivity measured on cubic samples at Site C0022 but have higher resistivity than the Wenner probe in Hole C0022B (Fig. **F38**).

Resistivity results obtained using the Wenner probe from Sites C0002 and C0022 during Expedition 338 were compared with those obtained from IODP Expedition 333 Sites C0011 and C0012 that were also measured using the same Wenner probe (Fig. **F39**). Resistivity results from Expedition 338 Sites C0002 and C0022 are lower than those from Sites C0011 and C0012 at a given porosity value. As mentioned above, lower resistivity values for Sites C0002 and C0022 were possibly due to the incorrect values of standard seawater resistivity from the use of a small container. However, Archie's cementation factor (m) determined for Site C0022 (m = 2.17) from the exponent of the power law fit is similar to the values determined at Sites C0002 (m = 2.4) and C0010 (m = 2.3) during previous IODP NanTroSEIZE expeditions (Expedition 314 Scientists, 2009a; Expedition 319 Scientists, 2010) and at Site C0012 (m = 2.95) during Expedition 338 (see **"Logging while drilling"** in the "Site C0012" chapter [Strasser et al., 2014c]).

A total of nine discrete cubes were extracted from Hole C0022B (335–415 mbsf) when the sediment was too consolidated to allow Wenner probe insertion for electrical resistivity measurements. These

cubes were analyzed for electrical resistivity and V_P along three orthogonal directions (*x*, *y*, and *z*). The results of electrical resistivity and V_P are summarized in Tables T19 and T20 and Figure F40.

Electrical resistivity measured on cubes ranges from 0.44 to 1.703 Ωm. All except two samples (338-C0022B-38X-5, 32 cm, and 40X-1, 63 cm) record an anisotropy such that electrical resistivity in the vertical *z*-direction is higher than that in the horizontal *x*- or *y*-direction because of the bedding oriented within the *x*-*y* plane (Fig. F40). Resistivity is usually the lowest along the bedding plane in sedimentary rocks because of better pore connectivity. Vertical anisotropy is between 0.8% and 38.8% with negative values, except for the two cubes that probably have a bedding plane within *x*-*z* or *y*-*z* planes with anisotropy up to 113.7%. The measurements with bedding subparallel to the *x*-*y* plane present a transverse anisotropy (i.e., lineation) with a horizontal anisotropy from 2% up to 50.2%.

V_P increases with depth and ranges from 1.349 to 2.031 km/s between 335 and 415 mbsf. Horizontal and vertical anisotropies range from 0.37% to 29.7% in Hole C0022B (Fig. F40). Electrical resistivity and V_P increase with depth. This is probably related to densification and porosity reduction.

Shear strength (working halves)

Shear strength measurements using a vane shear device and a pocket penetrometer (see the "Methods" chapter [Strasser et al., 2014a]) were made on working halves from 4.24 to 306.91 mbsf. One measurement for each method was made per core. Penetrometer measurements range from 27.8 to 228.9 kPa, whereas vane shear measurements range from 3.6 to 118.7 kPa and are consistently lower than the penetrometer measurements (Fig. F41; Table T21). There is considerable scatter in the data, which increases with depth. One trend that may be observed is an increase in the maximum penetrometer values with depth. There are no definite trends in the vane shear measurements. Sediment below ~307 mbsf was too consolidated to make penetrometer and vane shear measurements; unconfined compressive strength (UCS) measurements were made on these deeper sediments (see below).

Unconfined compressive strength (discrete cores)

Unconfined compression tests (see the "Methods" chapter [Strasser et al., 2014a]) were conducted on five cubic samples (2 cm × 2 cm × 2 cm each) used for V_P and electrical resistivity measurements and two cuboid samples (1.5 cm × 1.5 cm × 3 cm each) (Table T22). A vertical load is applied along the long axis of the sample, which is parallel to the core axis. UCS (maximum force per unit area) ranges between 2.0 and 3.9 MPa, with an average of 2.8 MPa (Fig. F41; Table T22). The variability in UCS data is probably due to sample heterogeneity, sample size, control of loading rate (manual versus computer control), and sensitivity of the load cell (±0.02 kN for the load cell on the *Chikyu*).

Color spectroscopy (archive halves)

The results of color reflectance measurements using the color spectroscopy logger (MSCL-C) are summarized in Figure F42. General trends are that L* and b* decrease slightly with depth and a* is approximately constant with depth. L* ranges from 14 to 64, a* ranges from –6.2 to 8.6, and b* ranges from –2.82 to 7.21. The results in Hole C0022B are similar to those in Holes C0008A and C0008C because of the same lithologies (Expedition 316 Scientists, 2009b).

Paleomagnetism

Routine magnetic measurements were conducted with a superconducting rock magnetometer on Hole C0022B archive halves of cores. Because of time constraints, only two demagnetization steps and no discrete sample measurements were performed on samples on board the *Chikyu*. These procedures may not be sufficient to remove artificial magnetization components induced by drilling, so caution is needed when interpreting results, especially for the EPCS and the ESCS sections (below 76.5 mbsf). The initial paleomagnetic record can be totally concealed because of magnetization by the drilling slurry and cannot be adequately evaluated without discrete sample measurements (see the "Site C0002" chapter [Strasser et al., 2014b]).

Remanent magnetization of archive-half sections from Holes C0022B was measured at demagnetization levels of 0, 10, and 20 mT peak fields to identify characteristic remanent magnetization. Vector component diagrams of progressive alternating field (AF) demagnetization (Fig. F43) indicate that large downward-directed vertical components were successfully removed with 10 mT. Such a vertical component is generally considered to be imparted by the coring process, as noted in previous ocean drilling research (e.g., Gee et al., 1989).

Because Hole C0022B is located between Sites C0004 and C0008, which were cored during Expedition 316 (Expedition 316 Scientists, 2009a, 2009b), a similar paleomagnetic stratigraphic pattern is expected. Paleomagnetic data show the Brunhes/Matuyama boundary (0.78 Ma) in Hole C0004C above 20 mbsf.

The Brunhes/Matuyama boundary is unclear in Holes C0008A and C0008C, probably due to truncation of surface sediment by submarine landslides (Strasser et al., 2011).

In Hole C0022B, the interval between ~70 and ~140 mbsf is likely stratigraphically and structurally disturbed by the splay fault (see **"Background and objectives," "Logging while drilling," "Biostratigraphy,"** and **"Structural geology"**). In such disturbed environments, magnetostratigraphic interpretation is not straightforward. The inclination profile shows indistinct inclination changes from normal to negative values in the upper several tens of meters (Fig. **F44**). The signature of the profile recognized is similar to that of Hole C0008A (Expedition 316 Scientists, 2009b), but biostratigraphy data for Hole C0022B indicate that the Brunhes/Matuyama boundary (0.78 Ma) should be located shallower than 48 mbsf and the Jaramillo Subchron (0.99–1.07 Ma) should be located between 48 and 57.5 mbsf (see **"Biostratigraphy"**). Therefore, the paleomagnetic stratigraphy interpretation remains nonunique. In contrast, the interval dominated by positive inclinations between 330 and 380 mbsf in Hole C0022B may be correlated to the interval between 210 and 270 mbsf in Hole C0008A, referring to seismic reflection layers in the cross-section images along Sites C0004, C0008, and C0022 (Fig. **F2**) (Strasser et al., 2011; Kimura et al., 2011). The interval assigned to the 1.77–1.95 Ma Olduvai Subchron in Hole C0008A (Expedition 316 Scientists, 2009b) is extrapolated to Site C0022.

Core-log-seismic integration

Site C0022 is situated at the tip of the megasplay fault, ~300 m southeast of Site C0004, and ~500 m northwest of Site C0008 (Fig. **F20**). LWD data from Hole C0022A and cores from Hole C0022B document the shallow extension of the megasplay fault through the slope sediment. The Kumano 3-D prestack depth migration (PSDM) seismic volume (Moore et al., 2009) ties to Site C0022 at the intersection of In-line 2675 and Cross-line 5268. Figure **F45** presents an overview of the correlation between the LWD, seismic, and core data.

Only a single unit was defined from analysis of both core samples and LWD data (**"Lithology"** and **"Logging while drilling"**). Two subunits were identified based on core lithology, whereas three subunits were identified from the LWD data (Fig. **F45**); however, none of these boundaries are coincident.

The dominant lithology of cores from Hole C0022B is silty clay, with thin interbedded layers of sand and volcanic ash. The lithologic Subunit IA/IB boundary (383.5 mbsf) is located at the top of several layers of gravel that are not observed elsewhere in the drilled interval at this site. This boundary corresponds to a discrete decrease in gamma ray values from ~75 to 60 gAPI as well as to a low-amplitude reflection in the seismic data at ~400 mbsf (Fig. **F45**).

A positive reflection is observed at 35 msbf, and it is possible that this correlates to a sandy layer observed in the core from Hole C0022B (Fig. **F45**), although there is no clear signal in the LWD data. The logging Subunit IA/IB boundary instead correlates with the top of a package of sand layers in the core lithology, although the seismic data are reflectively transparent at this depth.

Several shear zones and microfaults were observed in cores between ~75 and 150 mbsf (see **"Structural geology"**). The lack of core recovery between 95.5 and 99.5 mbsf despite overall excellent recovery from 20 to 123 mbsf may be indicative of a highly deformed zone. The depth of this interpreted deformation zone correlates with subtle offsets in the seismic reflections at this depth (Fig. **F45**), suggesting that it may represent the updip extension of the megasplay fault. A zone of high deformation and fracturing was also identified in the LWD resistivity images between 85 and 115 mbsf, centered about a low-resistivity fracture at ~100 mbsf (Fig. **F4**).

A package of strong reflections between 150 and 220 mbsf corresponds to a zone of higher variability in resistivity and some broad intervals with locally low gamma ray values (176–182 and 192–205 mbsf) (Fig. **F45**). No cores were collected between 156.8 and 190.5 mbsf, so in this interval seismic-lithology correlation is not possible.

Finally, a strong, negative reflection at 300 mbsf may be correlated to a thick sand layer at Site C0008 and thin sand layers at Site C0004 (Kimura et al., 2011; Strasser et al., 2011). It is possible that this reflection also correlates with sand or volcanic ash layers identified in the core from Hole C0022B (Fig. **F45**). Gamma ray values show no major change, although a pair of high gamma ray spikes at 295 and 302 mbsf may correlate with two of the volcanic ash layers identified in the core.

References

Archie, G.E., 1947. Electrical resistivity—an aid in core analysis interpretation. *AAPG Bull.*, 31(2):350–366.

Bernard, B.B., Brooks, J.M., and Sackett, W.M., 1976. Natural gas seepage in the Gulf of Mexico. *Earth Planet. Sci. Lett.*, 31(1):48–54. **doi:10.1016/0012-821X(76)90095-9**

Byrne, T.B., Lin, W., Tsutsumi, A., Yamamoto, Y., Lewis, J.C., Kanagawa, K., Kitamura, Y., Yamaguchi, A., and Kimura, G., 2009. Anelastic strain recovery reveals

extension across SW Japan subduction zone. *Geophys. Res. Lett.,* 36(23):L23310. doi:10.1029/2009GL040749

Chang, C., McNeill, L.C., Moore, J.C., Lin, W., Conin, M., and Yamada, Y., 2010. In situ stress state in the Nankai accretionary wedge estimated from borehole wall failures. *Geochem., Geophys., Geosyst.,* 11:Q0AD04. doi:10.1029/2010GC003261

Expedition 314 Scientists, 2009a. Expedition 314 Site C0002. *In* Kinoshita, M., Tobin, H., Ashi, J., Kimura, G., Lallemant, S., Screaton, E.J., Curewitz, D., Masago, H., Moe, K.T., and the Expedition 314/315/316 Scientists, *Proc. IODP,* 314/315/316: Washington, DC (Integrated Ocean Drilling Program Management International, Inc.). doi:10.2204/iodp.proc.314315316.114.2009

Expedition 314 Scientists, 2009b. Expedition 314 Site C0004. *In* Kinoshita, M., Tobin, H., Ashi, J., Kimura, G., Lallemant, S., Screaton, E.J., Curewitz, D., Masago, H., Moe, K.T., and the Expedition 314/315/316 Scientists, *Proc. IODP,* 314/315/316: Washington, DC (Integrated Ocean Drilling Program Management International, Inc.). doi:10.2204/iodp.proc.314315316.116.2009

Expedition 316 Scientists, 2009a. Expedition 316 Site C0004. *In* Kinoshita, M., Tobin, H., Ashi, J., Kimura, G., Lallemant, S., Screaton, E.J., Curewitz, D., Masago, H., Moe, K.T., and the Expedition 314/315/316 Scientists, *Proc. IODP,* 314/315/316: Washington, DC (Integrated Ocean Drilling Program Management International, Inc.). doi:10.2204/iodp.proc.314315316.133.2009

Expedition 316 Scientists, 2009b. Expedition 316 Site C0008. *In* Kinoshita, M., Tobin, H., Ashi, J., Kimura, G., Lallemant, S., Screaton, E.J., Curewitz, D., Masago, H., Moe, K.T., and the Expedition 314/315/316 Scientists, *Proc. IODP,* 314/315/316: Washington, DC (Integrated Ocean Drilling Program Management International, Inc.). doi:10.2204/iodp.proc.314315316.136.2009

Expedition 319 Scientists, 2010. Site C0010. *In* Saffer, D., McNeill, L., Byrne, T., Araki, E., Toczko, S., Eguchi, N., Takahashi, K., and the Expedition 319 Scientists, *Proc. IODP,* 319: Tokyo (Integrated Ocean Drilling Program Management International, Inc.). doi:10.2204/iodp.proc.319.104.2010

Expedition 333 Scientists, 2011. NanTroSEIZE Stage 2: subduction inputs 2 and heat flow. *IODP Prel. Rept.,* 333. doi:10.2204/iodp.pr.333.2011

Expedition 333 Scientists, 2012a. Site C0011. *In* Henry, P., Kanamatsu, T., Moe, K., and the Expedition 333 Scientists, *Proc. IODP,* 333: Tokyo (Integrated Ocean Drilling Program Management International, Inc.). doi:10.2204/iodp.proc.333.104.2012

Expedition 333 Scientists, 2012b. Site C0012. *In* Henry, P., Kanamatsu, T., Moe, K., and the Expedition 333 Scientists, *Proc. IODP,* 333: Tokyo (Integrated Ocean Drilling Program Management International, Inc.). doi:10.2204/iodp.proc.333.105.2012

Expedition 333 Scientists, 2012c. Site C0018. *In* Henry, P., Kanamatsu, T., Moe, K., and the Expedition 333 Scientists, *Proc. IODP,* 333: Tokyo (Integrated Ocean Drilling Program Management International, Inc.). doi:10.2204/iodp.proc.333.103.2012

Gee, J., Staudigel, H., and Tauxe, L., 1989. Contribution of induced magnetization to magnetization of seamounts. *Nature (London, U. K.),* 342(6246):170–173. doi:10.1038/342170a0

Heki, K., 2007. Secular, transient, and seasonal crustal movements in Japan from a dense GPS array: implication for plate dynamics in convergent boundaries. *In* Dixon, T.H., and Moore, J.C. (Eds.), *The Seismogenic Zone of Subduction Thrust Faults:* New York (Columbia Univ. Press), 512–539.

Ienaga, M., McNeill, L.C., Mikada, H., Saito, S., Goldberg, D., and Moore, J.C., 2006. Borehole image analysis of the Nankai accretionary wedge, ODP Leg 196: structural and stress studies. *Tectonophysics,* 426(1–2):207–220. doi:10.1016/j.tecto.2006.02.018

Kimura, G., Moore, G.F., Strasser, M., Screaton, E., Curewitz, D., Streiff, C., and Tobin, H., 2011. Spatial and temporal evolution of the megasplay fault in the Nankai Trough. *Geochem., Geophys., Geosyst.,* 12(3):Q0A008. doi:10.1029/2010GC003335

Kinoshita, M., Tobin, H., Moe, K.T., and the Expedition 314 Scientists, 2008. NanTroSEIZE Stage 1A: NanTroSEIZE LWD transect. *IODP Prel. Rept.,* 314. doi:10.2204/iodp.pr.314.2008

Lin, W., Doan, M.-L., Moore, J.C., McNeill, L., Byrne, T.B., Ito, T., Saffer, D., Conin, M., Kinoshita, M., Sanada, Y., Moe, K.T., Araki, E., Tobin, H., Boutt, D., Kano, Y., Hayman, N.W., Flemings, P., Huftile, G.J., Cukur, D., Buret, C., Schleicher, A.M., Efimenko, N., Kawabata, K., Buchs, D.M., Jiang, S., Kameo, K., Horiguchi, K., Wiersberg, T., Kopf, A., Kitada, K., Eguchi, N., Toczko, S., Takahashi, K., and Kido, Y., 2010. Present-day principal horizontal stress orientations in the Kumano forearc basin of the southwest Japan subduction zone determined from IODP NanTroSEIZE drilling Site C0009. *Geophys. Res. Lett.,* 37:L13303. doi:10.1029/2010GL043158

McNeill, L.C., Ienaga, M., Tobin, H., Saito, S., Goldberg, D., Moore, J.C., and Mikada, H., 2004. Deformation and in situ stress in the Nankai accretionary prism from resistivity-at-bit images, ODP Leg 196. *Geophys. Res. Lett.,* 31(2):L02602. doi:10.1029/2003GL018799

Meyers, P.A., 1997. Organic geochemical proxies of paleoceanographic, paleolimnologic, and paleoclimatic processes. *Org. Geochem.,* 27(5–6):213–250. doi:10.1016/S0146-6380(97)00049-1

Milliken, K.L., and Reed, R.M., 2011. Multiple causes of diagenetic fabric anisotropy in weakly consolidated mud, Nankai accretionary prism, IODP Expedition 316. *J. Struct. Geol.,* 32(12):1887–1898. doi:10.1016/j.jsg.2010.03.008

Moore, G.F., Bangs, N.L., Taira, A., Kuramoto, S., Pangborn, E., and Tobin, H.J., 2007. Three-dimensional splay fault geometry and implications for tsunami generation. *Science,* 318(5853):1128–1131. doi:10.1126/science.1147195

Moore, G.F., Park, J.-O., Bangs, N.L., Gulick, S.P., Tobin, H.J., Nakamura, Y., Sato, S., Tsuji, T., Yoro, T., Tanaka, H., Uraki, S., Kido, Y., Sanada, Y., Kuramoto, S., and Taira, A., 2009. Structural and seismic stratigraphic framework of the NanTroSEIZE Stage 1 transect. *In*

Kinoshita, M., Tobin, H., Ashi, J., Kimura, G., Lallemant, S., Screaton, E.J., Curewitz, D., Masago, H., Moe, K.T., and the Expedition 314/315/316 Scientists, *Proc. IODP,* 314/315/316: Washington, DC (Integrated Ocean Drilling Program Management International, Inc.). **doi:10.2204/iodp.proc.314315316.102.2009**

Park, J.-O., Tsuru, T., Kodaira, S., Cummins, P.R., and Kaneda, Y., 2002. Splay fault branching along the Nankai subduction zone. *Science,* 297(5584):1157–1160. **doi:10.1126/science.1074111**

Reeburgh, W.S., 2007. Oceanic methane biogeochemistry. *Chem. Rev.,* 107(2):486–513. **doi:10.1021/cr050362v**

Sakaguchi, A., Chester, F., Curewitz, D., Fabbri, O., Goldsby, D., Kimura, G., Li, C.-F., Masaki, Y., Screaton, E.J., Tsutsumi, A., Ujiie, K., and Yamaguchi, A., 2011a. Seismic slip propagation to the updip end of plate boundary subduction interface faults: vitrinite reflectance geothermometry on Integrated Ocean Drilling Program NanTroSEIZE cores. *Geology,* 39(4):395–398. **doi:10.1130/G31642.1**

Sakaguchi, A., Kimura, G., Strasser, M., Screaton, E.J., Curewitz, D., and Murayama, M., 2011b. Episodic seafloor mud brecciation due to great subduction zone earthquakes. *Geology,* 39(10):919–922. **doi:10.1130/G32043.1**

Sakamoto, T., Kuroki, K., Sugawara, T., Aoike, K., Iijima, K., and Sugisaki, S., 2006. Non-destructive X-ray fluorescence (XRF) core-imaging scanner, TATSCAN-F2. *Sci. Drill.*, 2:37–39. **http://www.iodp.org/iodp_journals/9_Non_Destructive_X_Ray_SD2.pdf**

Screaton, E.J., Kimura, G., Curewitz, D., and the Expedition 316 Scientists, 2009. Expedition 316 summary. *In* Kinoshita, M., Tobin, H., Ashi, J., Kimura, G., Lallemant, S., Screaton, E.J., Curewitz, D., Masago, H., Moe, K.T., and the Expedition 314/315/316 Scientists, *Proc. IODP,* 314/315/316: Washington, DC (Integrated Ocean Drilling Program Management International, Inc.). **doi:10.2204/iodp.proc.314315316.131.2009**

Seno, T., Stein, S., and Gripp, A.E., 1993. A model for the motion of the Philippine Sea plate consistent with NUVEL-1 and geological data. *J. Geophys. Res.: Solid Earth,* 98(B10):17941–17948. **doi:10.1029/93JB00782**

Strasser, M., Dugan, B., Kanagawa, K., Moore, G.F., Toczko, S., Maeda, L., Kido, Y., Moe, K.T., Sanada, Y., Esteban, L., Fabbri, O., Geersen, J., Hammerschmidt, S., Hayashi, H., Heirman, K., Hüpers, A., Jurado Rodriguez, M.J., Kameo, K., Kanamatsu, T., Kitajima, H., Masuda, H., Milliken, K., Mishra, R., Motoyama, I., Olcott, K., Oohashi, K., Pickering, K.T., Ramirez, S.G., Rashid, H., Sawyer, D., Schleicher, A., Shan, Y., Skarbek, R., Song, I., Takeshita, T., Toki, T., Tudge, J., Webb, S., Wilson, D.J., Wu, H.-Y., and Yamaguchi, A., 2014a. Methods. *In* Strasser, M., Dugan, B., Kanagawa, K., Moore, G.F., Toczko, S., Maeda, L., and the Expedition 338 Scientists, *Proc. IODP,* 338: Yokohama (Integrated Ocean Drilling Program). **doi:10.2204/iodp.proc.338.102.2014**

Strasser, M., Dugan, B., Kanagawa, K., Moore, G.F., Toczko, S., Maeda, L., Kido, Y., Moe, K.T., Sanada, Y., Esteban, L., Fabbri, O., Geersen, J., Hammerschmidt, S., Hayashi, H., Heirman, K., Hüpers, A., Jurado Rodriguez, M.J., Kameo, K., Kanamatsu, T., Kitajima, H., Masuda, H., Milliken, K., Mishra, R., Motoyama, I., Olcott, K., Oohashi, K., Pickering, K.T., Ramirez, S.G., Rashid, H., Sawyer, D., Schleicher, A., Shan, Y., Skarbek, R., Song, I., Takeshita, T., Toki, T., Tudge, J., Webb, S., Wilson, D.J., Wu, H.-Y., and Yamaguchi, A., 2014b. Site C0002. *In* Strasser, M., Dugan, B., Kanagawa, K., Moore, G.F., Toczko, S., Maeda, L., and the Expedition 338 Scientists, *Proc. IODP,* 338: Yokohama (Integrated Ocean Drilling Program). **doi:10.2204/iodp.proc.338.103.2014**

Strasser, M., Dugan, B., Kanagawa, K., Moore, G.F., Toczko, S., Maeda, L., Kido, Y., Moe, K.T., Sanada, Y., Esteban, L., Fabbri, O., Geersen, J., Hammerschmidt, S., Hayashi, H., Heirman, K., Hüpers, A., Jurado Rodriguez, M.J., Kameo, K., Kanamatsu, T., Kitajima, H., Masuda, H., Milliken, K., Mishra, R., Motoyama, I., Olcott, K., Oohashi, K., Pickering, K.T., Ramirez, S.G., Rashid, H., Sawyer, D., Schleicher, A., Shan, Y., Skarbek, R., Song, I., Takeshita, T., Toki, T., Tudge, J., Webb, S., Wilson, D.J., Wu, H.-Y., and Yamaguchi, A., 2014c. Site C0012. *In* Strasser, M., Dugan, B., Kanagawa, K., Moore, G.F., Toczko, S., Maeda, L., and the Expedition 338 Scientists, *Proc. IODP,* 338: Yokohama (Integrated Ocean Drilling Program). **doi:10.2204/iodp.proc.338.104.2014**

Strasser, M., Dugan, B., Kanagawa, K., Moore, G.F., Toczko, S., Maeda, L., Kido, Y., Moe, K.T., Sanada, Y., Esteban, L., Fabbri, O., Geersen, J., Hammerschmidt, S., Hayashi, H., Heirman, K., Hüpers, A., Jurado Rodriguez, M.J., Kameo, K., Kanamatsu, T., Kitajima, H., Masuda, H., Milliken, K., Mishra, R., Motoyama, I., Olcott, K., Oohashi, K., Pickering, K.T., Ramirez, S.G., Rashid, H., Sawyer, D., Schleicher, A., Shan, Y., Skarbek, R., Song, I., Takeshita, T., Toki, T., Tudge, J., Webb, S., Wilson, D.J., Wu, H.-Y., and Yamaguchi, A., 2014d. Site C0021. *In* Strasser, M., Dugan, B., Kanagawa, K., Moore, G.F., Toczko, S., Maeda, L., and the Expedition 338 Scientists, *Proc. IODP,* 338: Yokohama (Integrated Ocean Drilling Program). **doi:10.2204/iodp.proc.338.106.2014**

Strasser, M., Moore, G.F., Kimura, G., Kitamura, Y., Kopf, A.J., Lallemant, S., Park, J.-O., Screaton, E.J., Su, X., Underwood, M.B., and Zhao, X., 2009. Origin and evolution of a splay fault in the Nankai accretionary wedge. *Nat. Geosci.,* 2(9):648–652. **doi:10.1038/ngeo609**

Strasser, M., Moore, G.F., Kimura, G., Kopf, A.J., Underwood, M.B., Guo, J., and Screaton, E.J., 2011. Slumping and mass-transport deposition in the Nankai forearc: evidence from IODP drilling and 3-D reflection seismic data. *Geochem., Geophys., Geosyst.,* 12:Q0AD13. **doi:10.1029/2010GC003431**

Stevens, T., 1997. Lithoautotrophy in the subsurface. *FEMS Microbiol. Rev.,* 20(3–4):327–337. **doi:10.1111/j.1574-6976.1997.tb00318.x**

Toki, T., Uehara, Y., Kinjo, K., Ijiri, A., Tsunogai, U., Tomaru, H., and Ashi, J., 2012. Methane production and accumulation in the Nankai accretionary prism: results from IODP Expeditions 315 and 316. *Geochem. J.,* 46(2):89–106. **http://www.terrapub.co.jp/journals/GJ/abstract/4602/46020089.html**

Ujiie, K., Maltman, A.J., and Sánchez-Gómez, M., 2004. Origin of deformation bands in argillaceous sediments at the toe of the Nankai accretionary prism, southwest Japan. *J. Struct. Geol.,* 26(2):221–231. **doi:10.1016/j.jsg.2003.06.001**

Yamaguchi, A., Sakaguchi, A., Sakamoto, T., Iijima, K., Kameda, J., Kimura, G., Ujiie, K., Chester, F.M., Fabbri, O., Goldsby, D., Tsutsumi, A., Li, C.-F., and Curewitz, D., 2011. Progressive illitization in fault gouge caused by seismic slip propagation along a megasplay fault in the Nankai Trough. *Geology,* 39(11):995–998. **doi:10.1130/G32038.1**

Publication: 13 January 2014
MS 338-107

Figure F1. Regional location map showing Site C0022 in context of the NanTroSEIZE project sites. Box = region with 3-D seismic data, red = Expedition 338 sites, blue = NanTroSEIZE Stage 1 and 2 sites, yellow arrows = estimated far-field vectors between Philippine Sea plate and Japan (Seno et al., 1993; Heki, 2007), stars = locations of 1944 and 1946 tsunamigenic earthquakes.

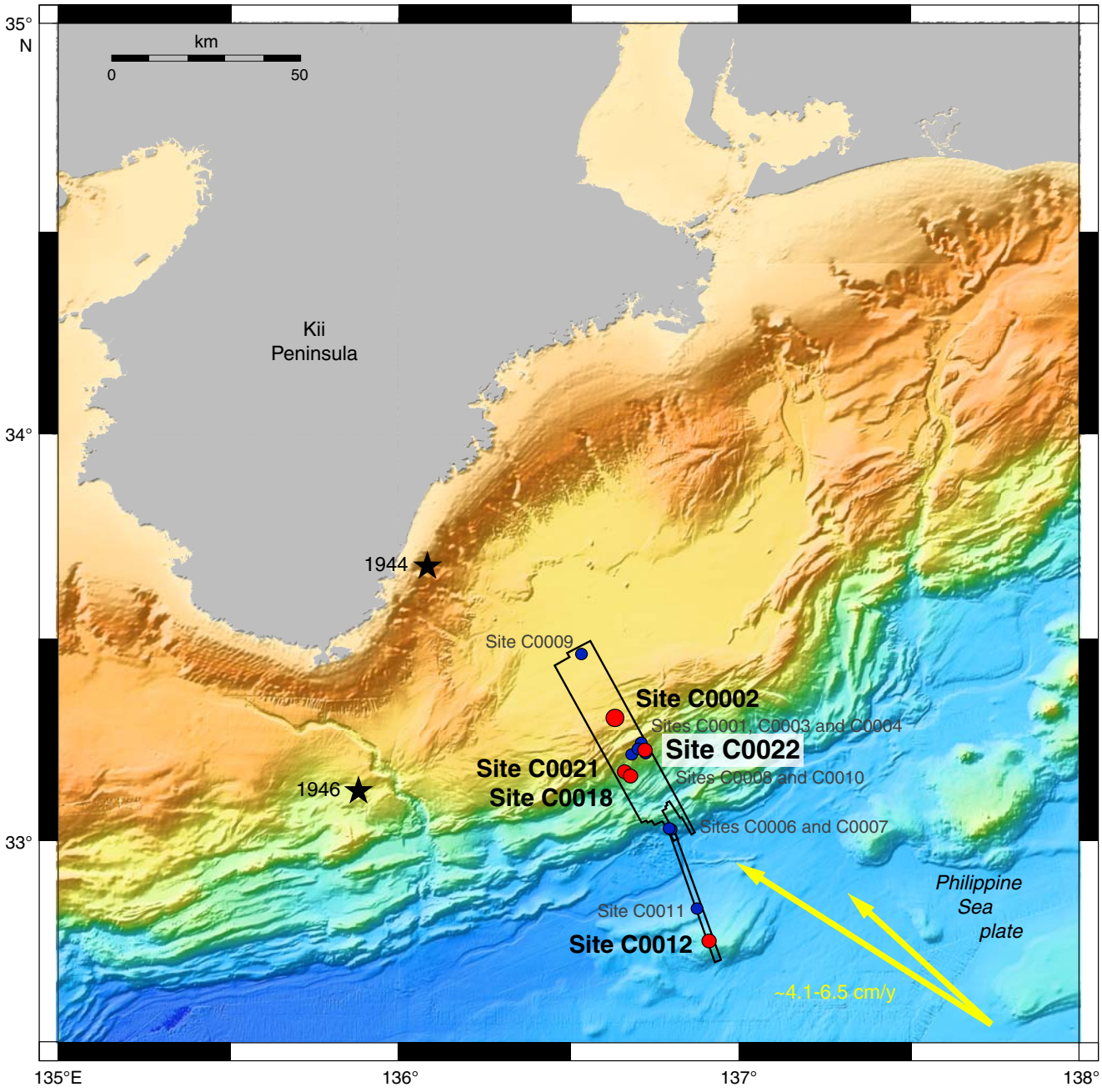

Figure F2. In-line 2675 extracted from 3-D seismic volume, showing Sites C0004, C0008, and C0022 (Moore et al., 2009). VE = vertical exaggeration.

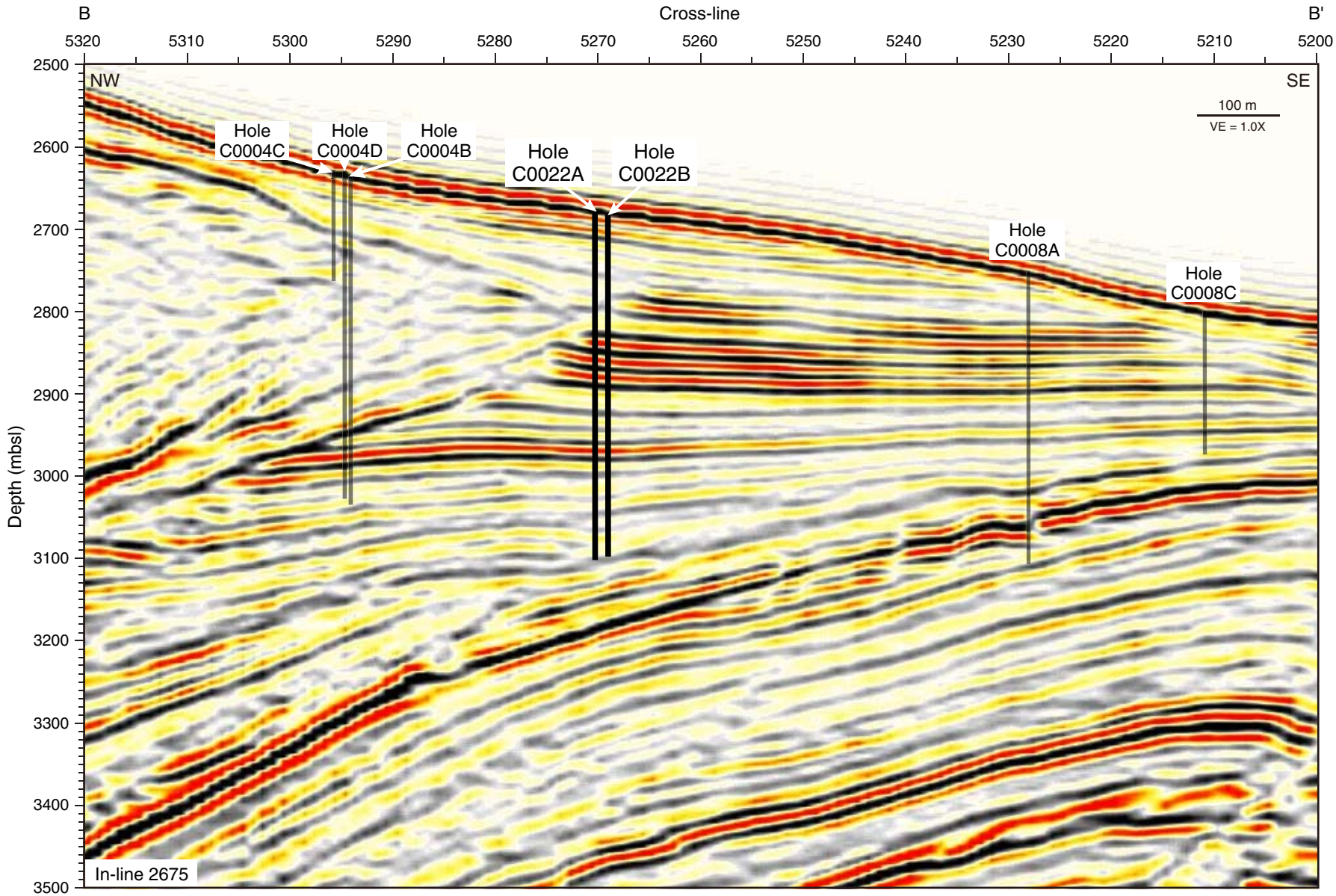

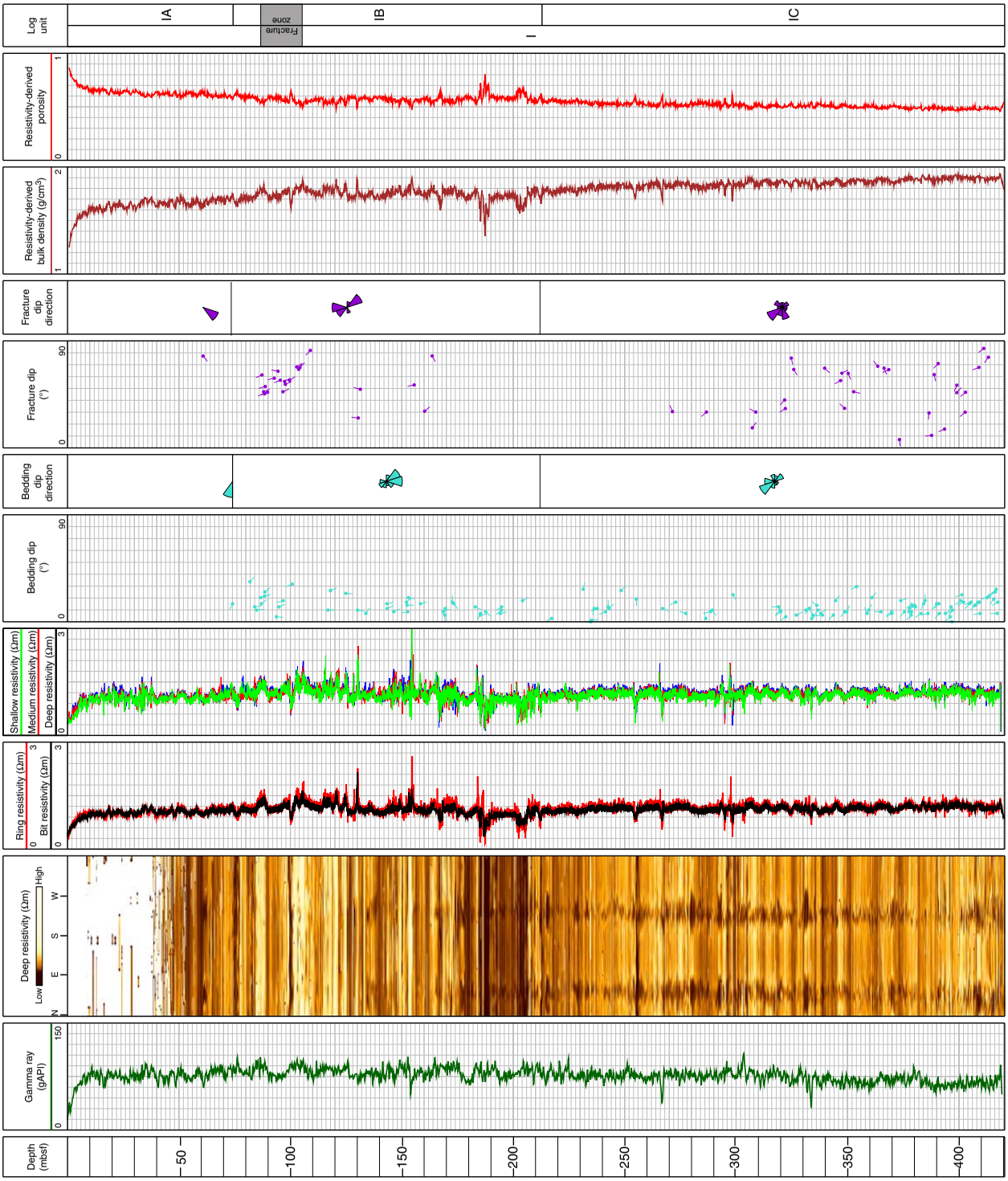

Figure F3. Overview composite plot of LWD data and deep resistivity image for Hole C0022A, with logging units, resistivity-derived porosity and bulk density, and bedding and fracture dips.

Figure F4. Composite plot of gamma ray and resistivity logs for Hole C0022A, with the observed trends and spikes highlighted. Black arrows = overall trends, red arrows = points of prominent high and low spikes.

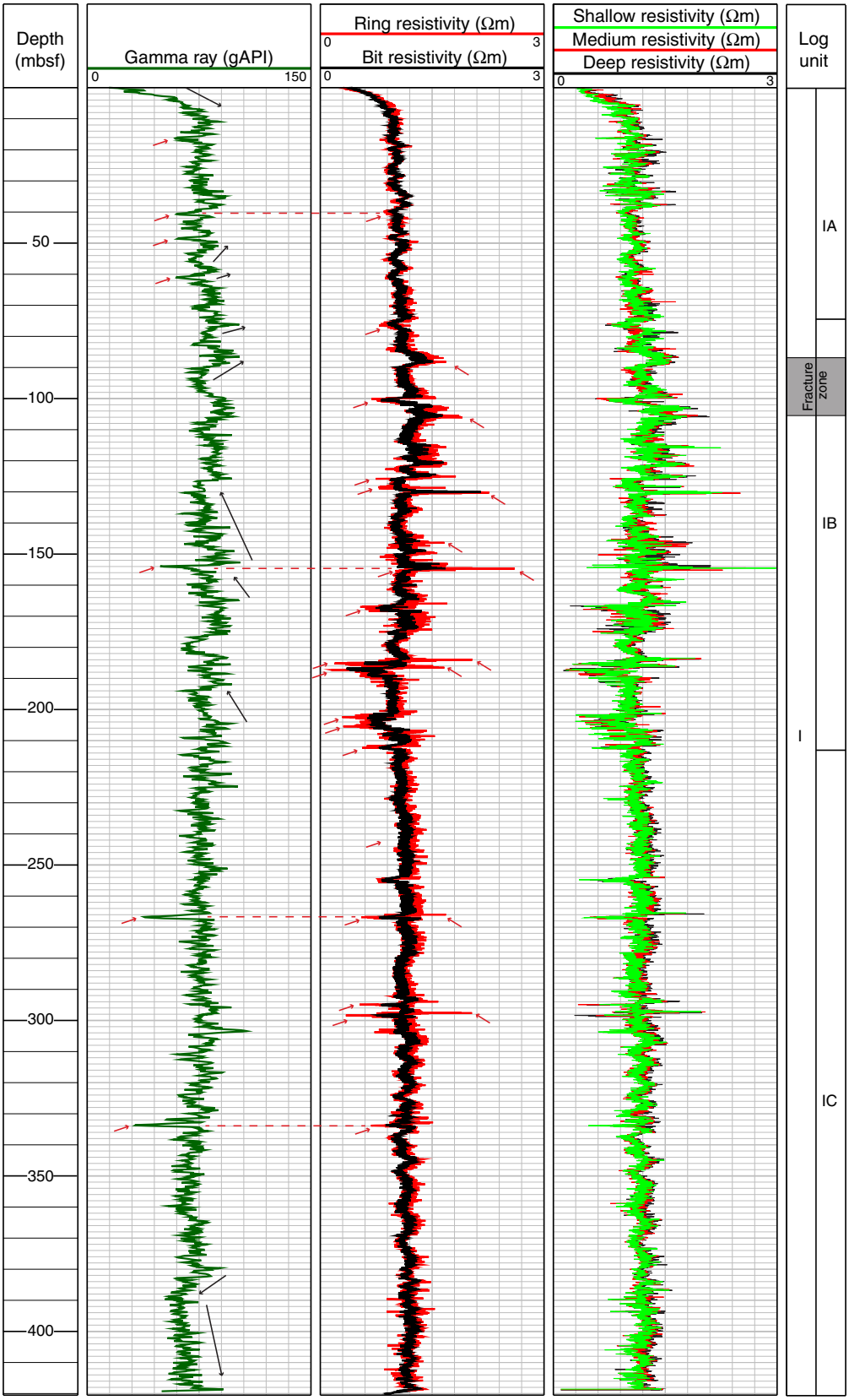

Figure F5. Stereonets and rose diagrams of the dip and azimuth of fractures and bedding in Hole C0022A, with the dips for Subunits IB and IC highlighted.

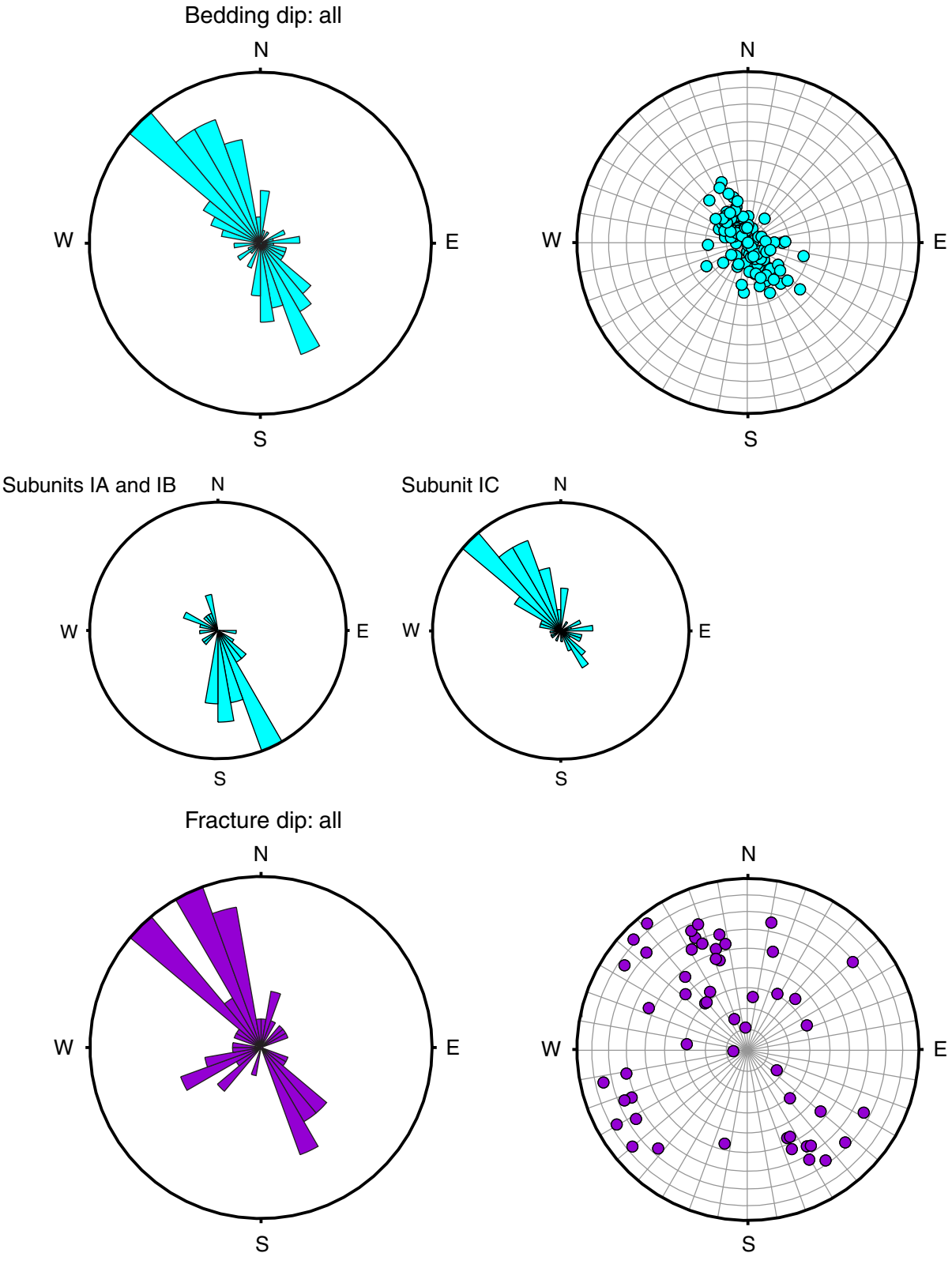

Figure F6. A. Resistivity-derived porosity (black line) plotted with MAD-derived porosity values (blue dots) from Hole C0022B. **B.** Offset ($\Delta\phi = \phi_{MAD} - \phi_{resistivity}$) between MAD-derived and resistivity-derived porosity data. **C.** Resistivity-derived bulk density (black line) plotted with MAD-derived bulk density data (blue dots). Resistivity-derived porosity and bulk density were calculated using Archie parameters of $a = 1$ and $m = 2.4$.

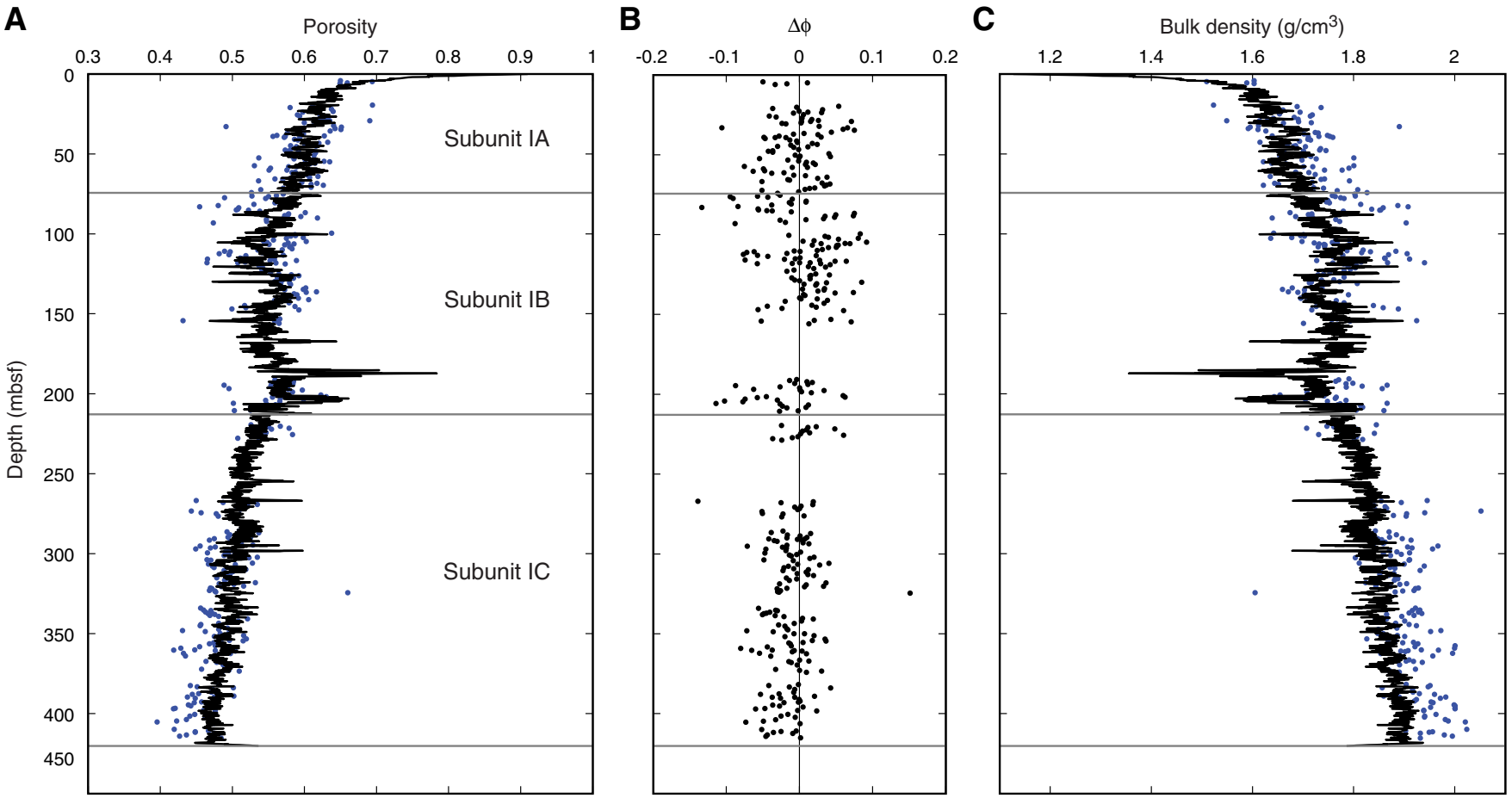

Figure F7. Core recovery and lithology of Hole C0022B.

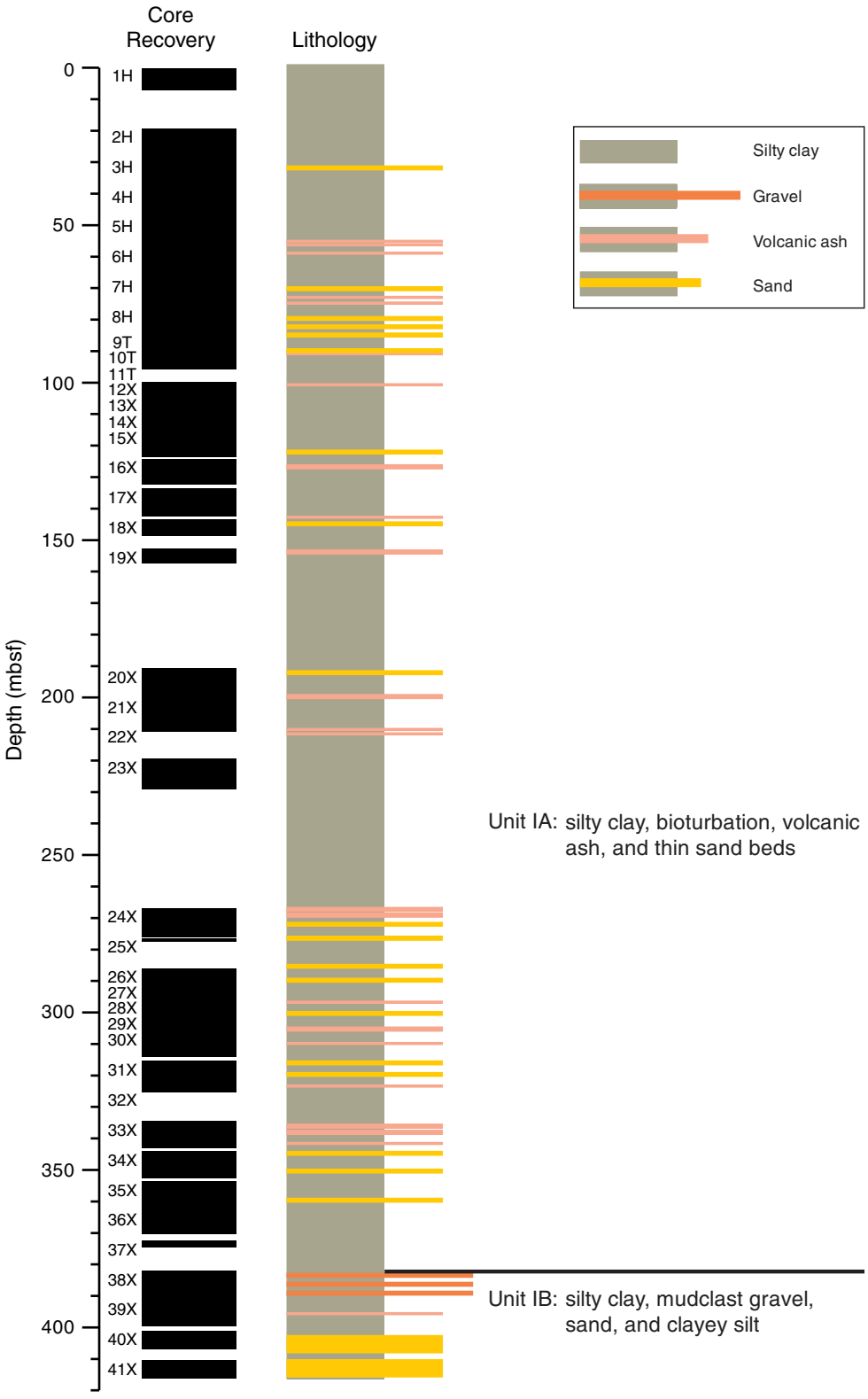

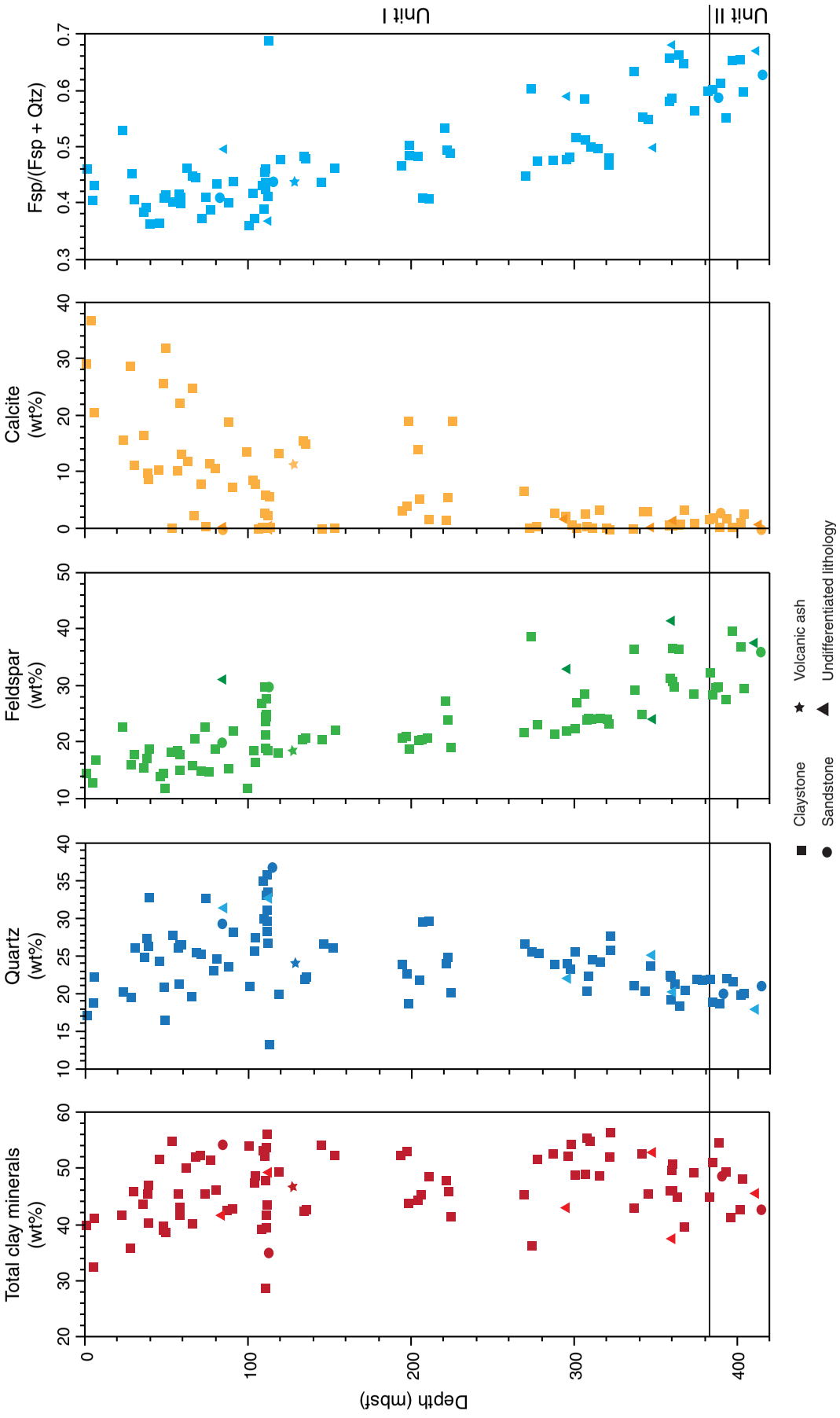

Figure F8. XRD data, Hole C0022B. Fsp = feldspar, Qtz = quartz.

Figure F9. Occurrence and thickness of sand layers and laminae, silty sand, silt, and gravel, Hole C0022B.

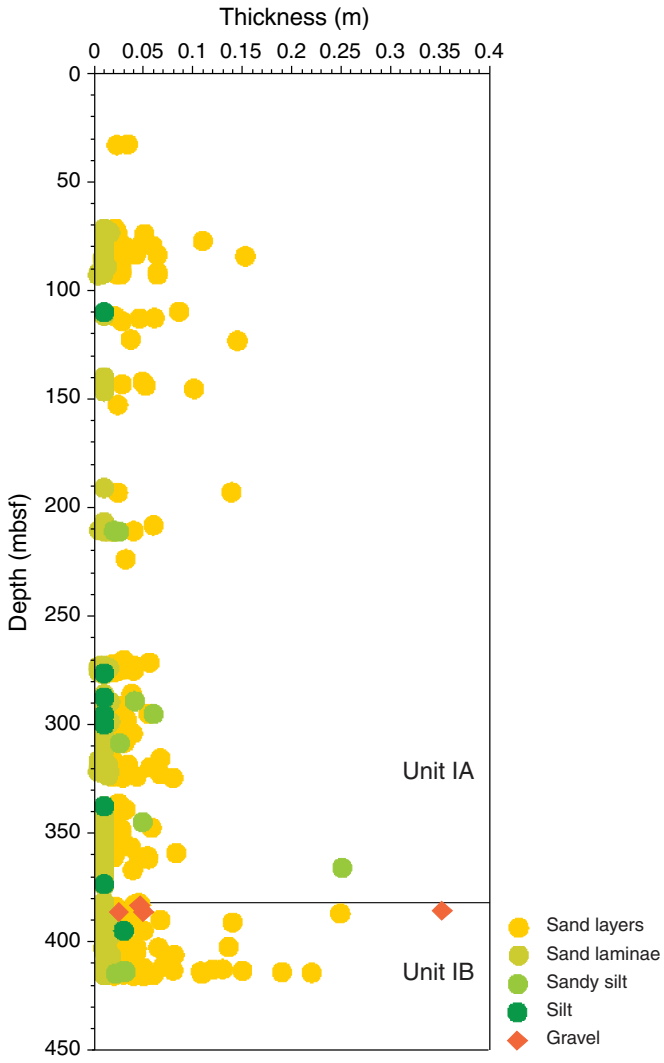

Figure F10. Images of major and minor lithologies, Hole C0022B. **A.** Fine sand in fining-upward sequences. Arrow indicates one complete sequence from fine sand above a calcareous silty clay. **B.** Greenish color banding (arrows).

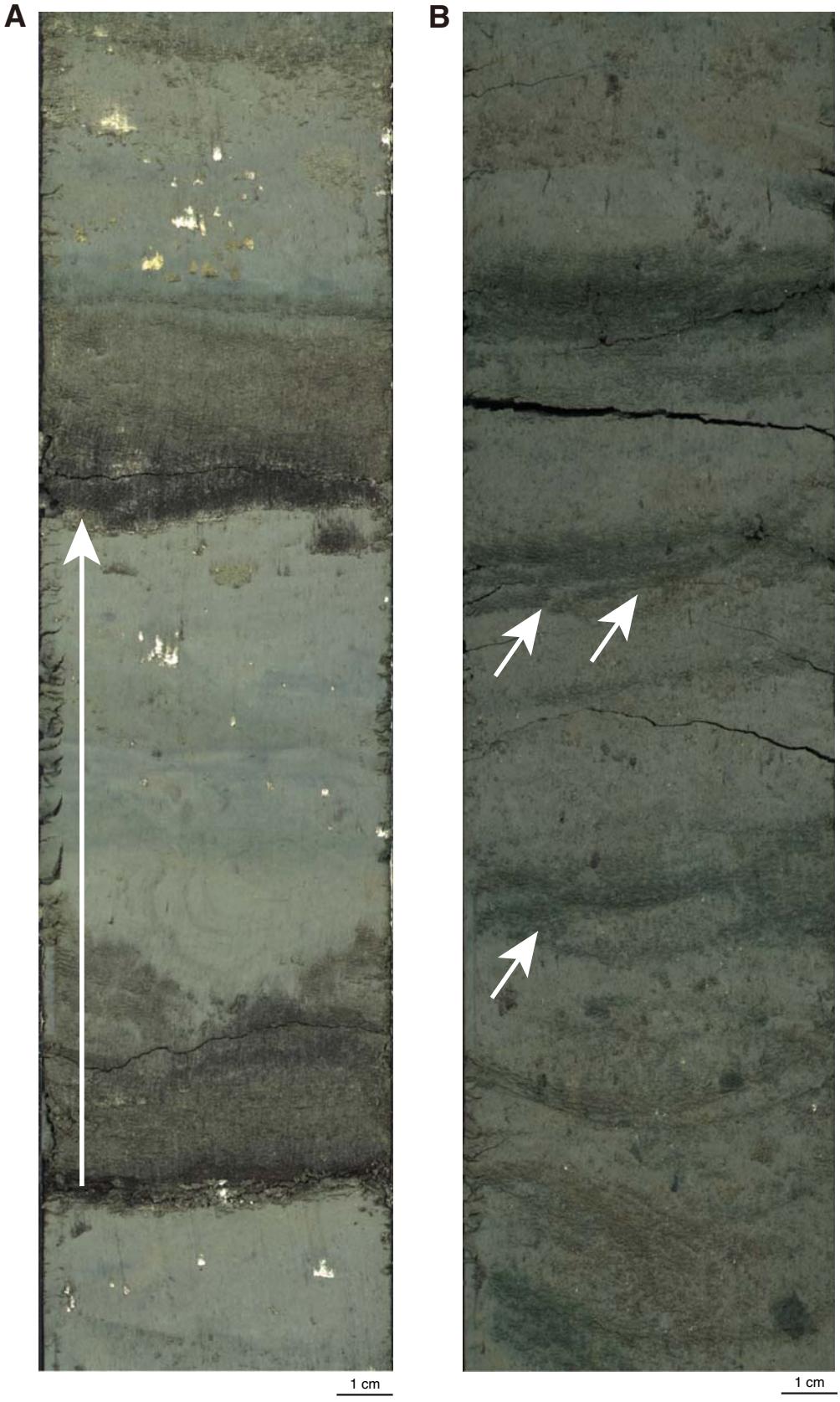

Figure F11. Images of silt and sand components common in lithologic Subunit IA, dominated by extrabasinal grains of sedimentary and metamorphic derivation with a minor admixture of pelagic biogenic debris and generally clear volcanic glass. **A.** Biosiliceous grains (diatoms, silicoflagellates, and assorted spicules) (Sample 338-C0022B-1H-1, 11 cm; plane-polarized light [PPL]). **B.** Sand-size fragments of foraminifers (Sample 338-C0022B-21X-10, 35 cm; cross-polarized light [XPL]). **C.** Chert grain (Sample 338-C0022B-3H-4, 121 cm; XPL). **D.** Polycrystalline quartz grain (Sample 338-C0022B-10T-4, 105 cm; XPL). (Continued on next page.)

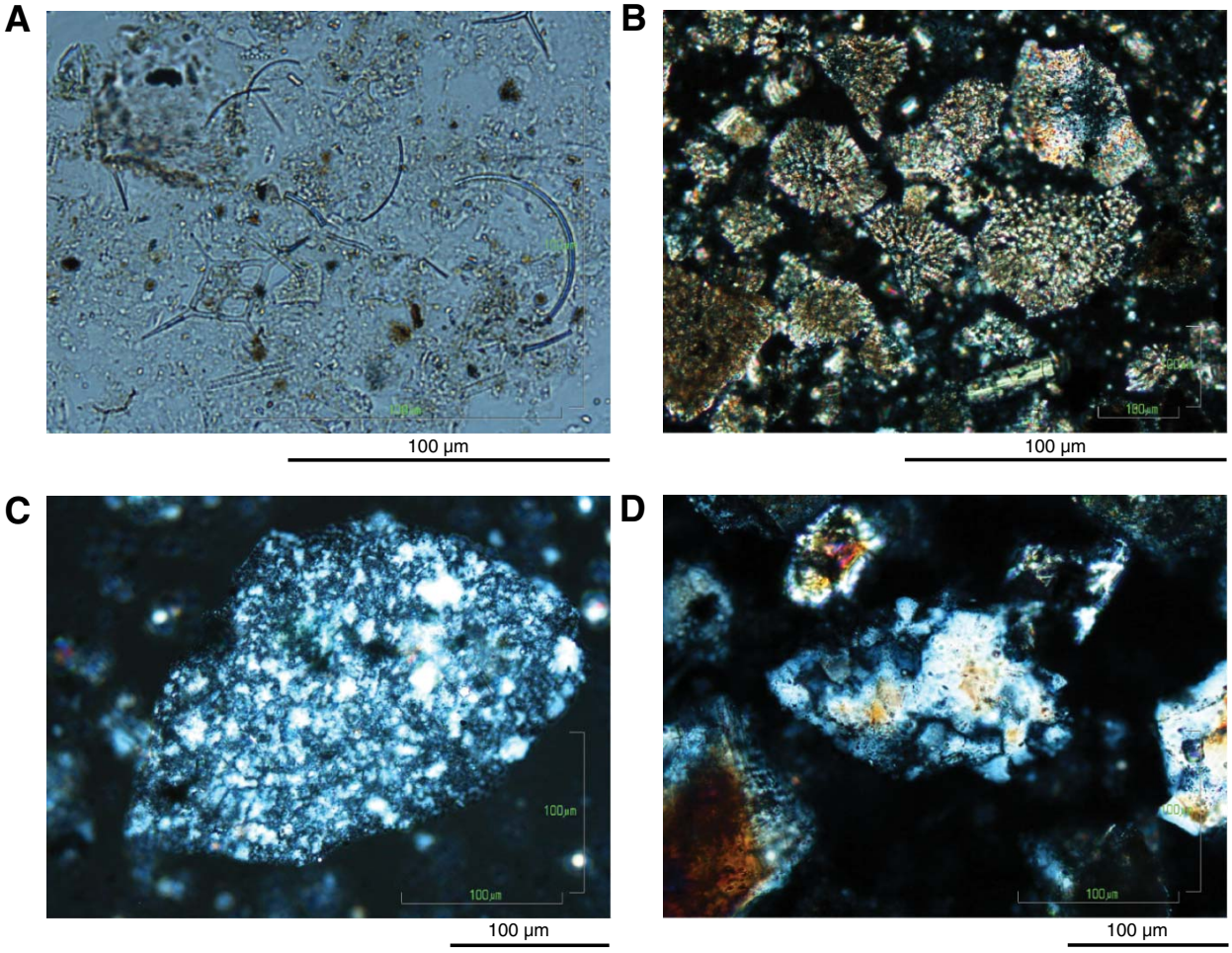

Figure F11 (continued). E. Quartz-mica phyllite with clear foliation (Sample 338-C0022B-30X-6, 120 cm; XPL). **F.** Quartz-mica phyllite with subtle evidence of foliation (Sample 338-C0022B-10T-CC, 12 cm; XPL). **G.** Orthopyroxene grain with characteristic dissolution texture (Sample 338-C0022B-29X-2, 24 cm; PPL). **H.** Clear microlitic glass (Sample 338-C0022B-30X-6, 120 cm; PPL).

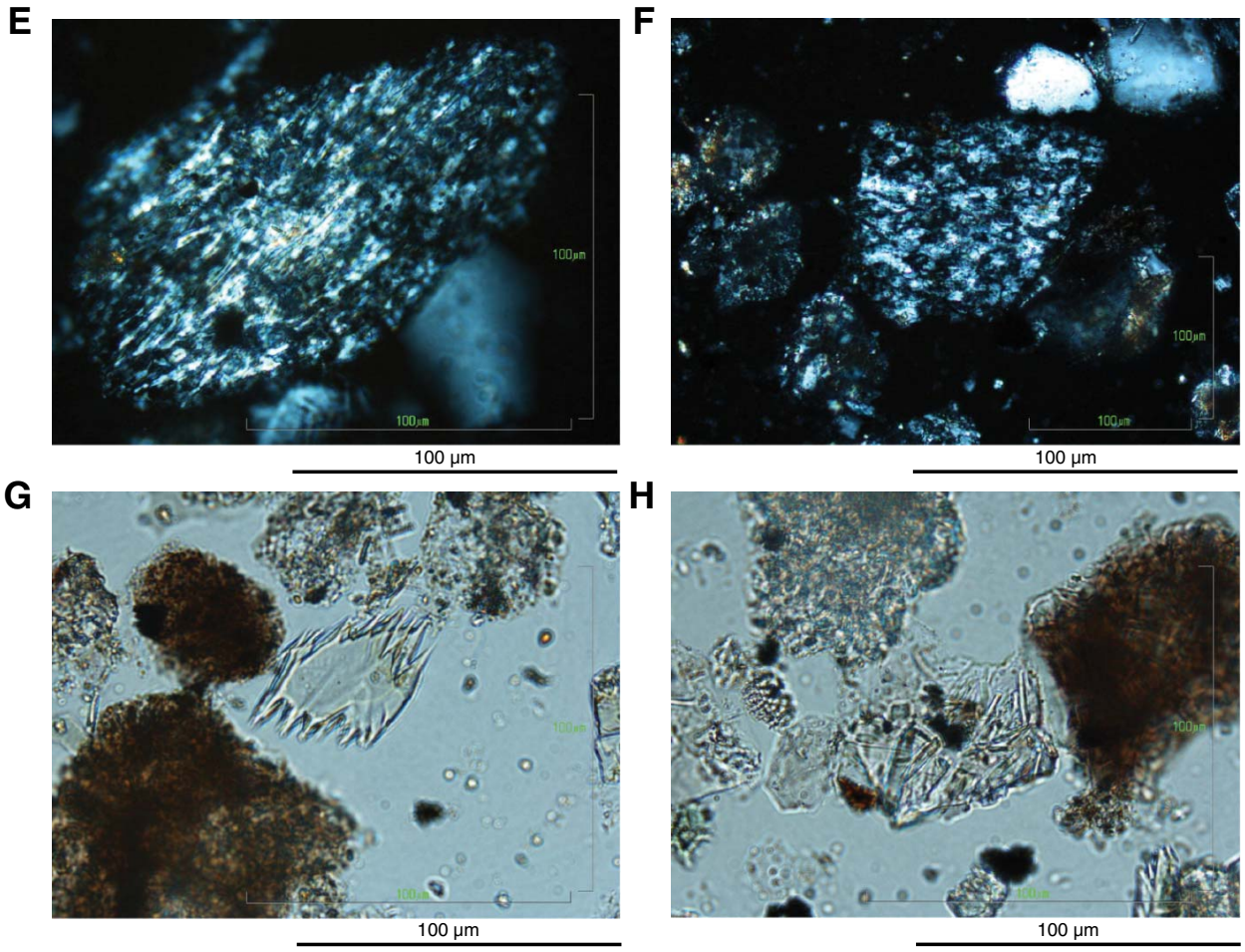

Figure F12. Images of pyrite in silty and sandy lithologies in plane-polarized light. **A.** Heavily pyritized silt with pyrite as disseminated framboids (Sample 338-C0022B-7H-2, 89 cm). **B.** Pyrite as grain coatings and minute (near clay size) framboids (Sample 338-C0022B-20X-1, 48 cm). **C.** Pyrite framboids localized along a possible burrow structure (Sample 338-C0022B-38X-1, 18 cm).

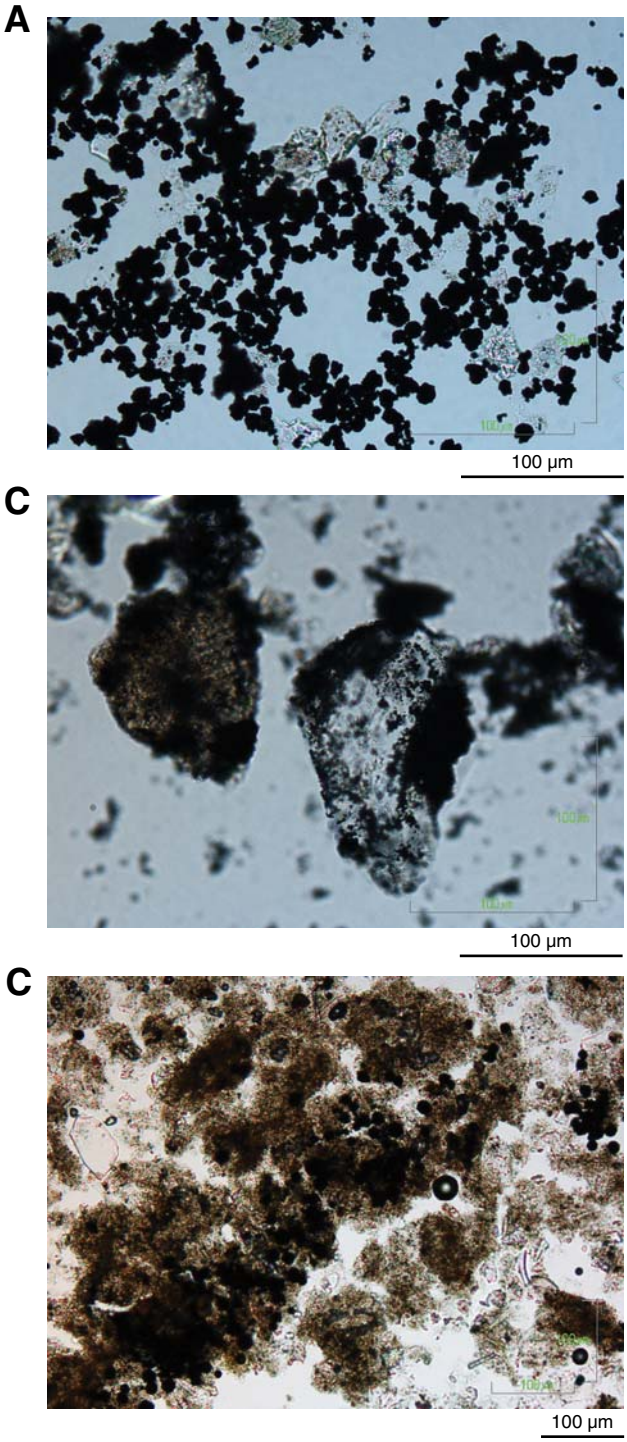

Figure F13. Photographs of textural and compositional variations of mud clast gravels in lithologic Subunit IB. **A.** Gravel of well-rounded pebble-size mud clasts with possible cobble of brownish silty clay (interval 338-C0022B-38X-4, 115.5–132.5 cm). Arrows = compactional deformation of a clast that suggests the presence of contrasting hardness among the gravel population. **B.** Granule-size mud clast gravel at top of lithologic Subunit IB (interval 338-C0022B-38X-2, 56–62 cm). **C.** Mud clast pebbles distributed along possible erosion surfaces (dashed yellow lines; possible lag layers) (interval 338-C0022B-38X-5, 8–19 cm).

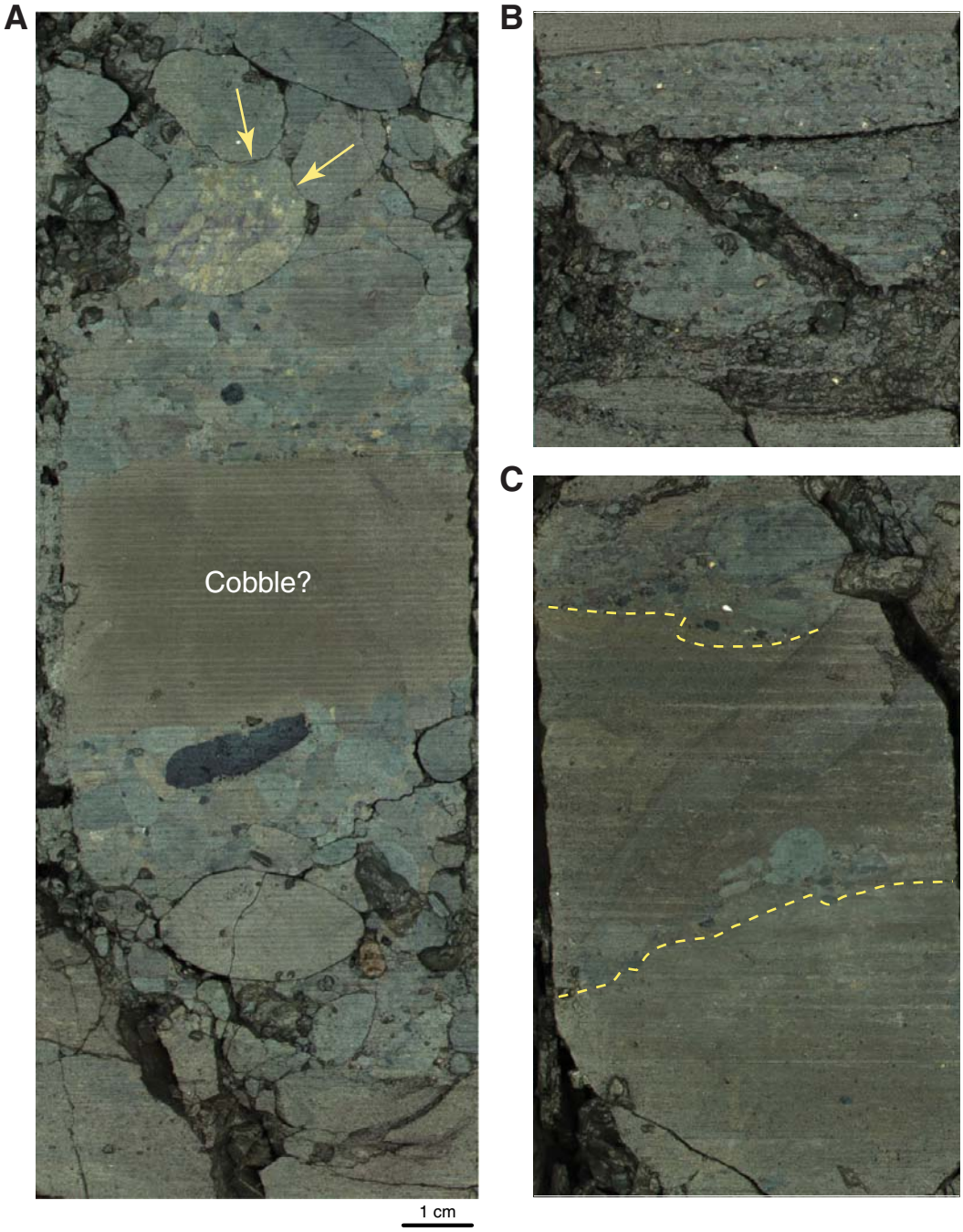

Figure F14. Images of variation of clay clasts in the gravel interval near the upper boundary of lithologic Subunit IB. Note the rounded shapes and variable color and silty/clay ratios displayed by different clasts (Sample 338-C0022B-38X-2, 72 cm). **A, B.** Red-brown clay-rich clast in (A) plane-polarized light (PPL) and (B) cross-polarized light (XPL). **C, D.** Gray-brown clast with disseminated microcrystalline pyrite in (C) PPL and (D) XPL. **E, F.** Silt-bearing clasts in (E) PPL and (F) XPL.

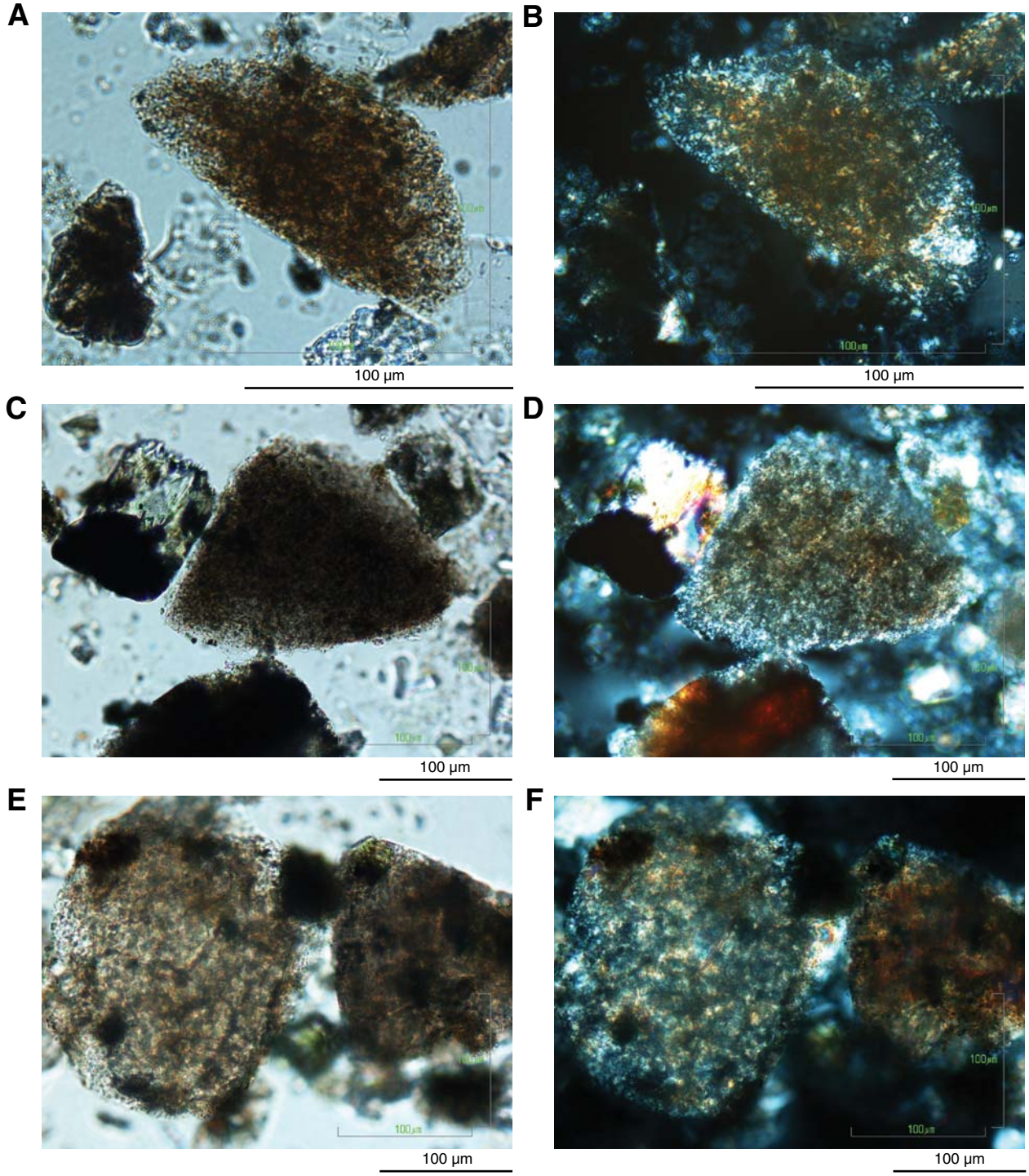

Figure F15. Images of grains of mafic volcanic derivation. Such clasts are trace to minor components in lithologic Subunit IA and common components in lithologic Subunit IB. Lathwork basaltic clasts are most abundant in the coarser sand of lithologic Subunit IB. **A, B.** Ca-plagioclase grain with included brown glass (Sample 338-C0022B-29X-2, 24 cm) in (A) plane-polarized light (PPL) and (B) cross-polarized light (XPL). **C.** Microlitic brown glass (Sample 338-C0022B-30X-6, 120 cm; PPL). **D.** Partially palagonized brown microlitc glass (Sample 338-C0022B-34X-5, 81 cm). (Continued on next page.)

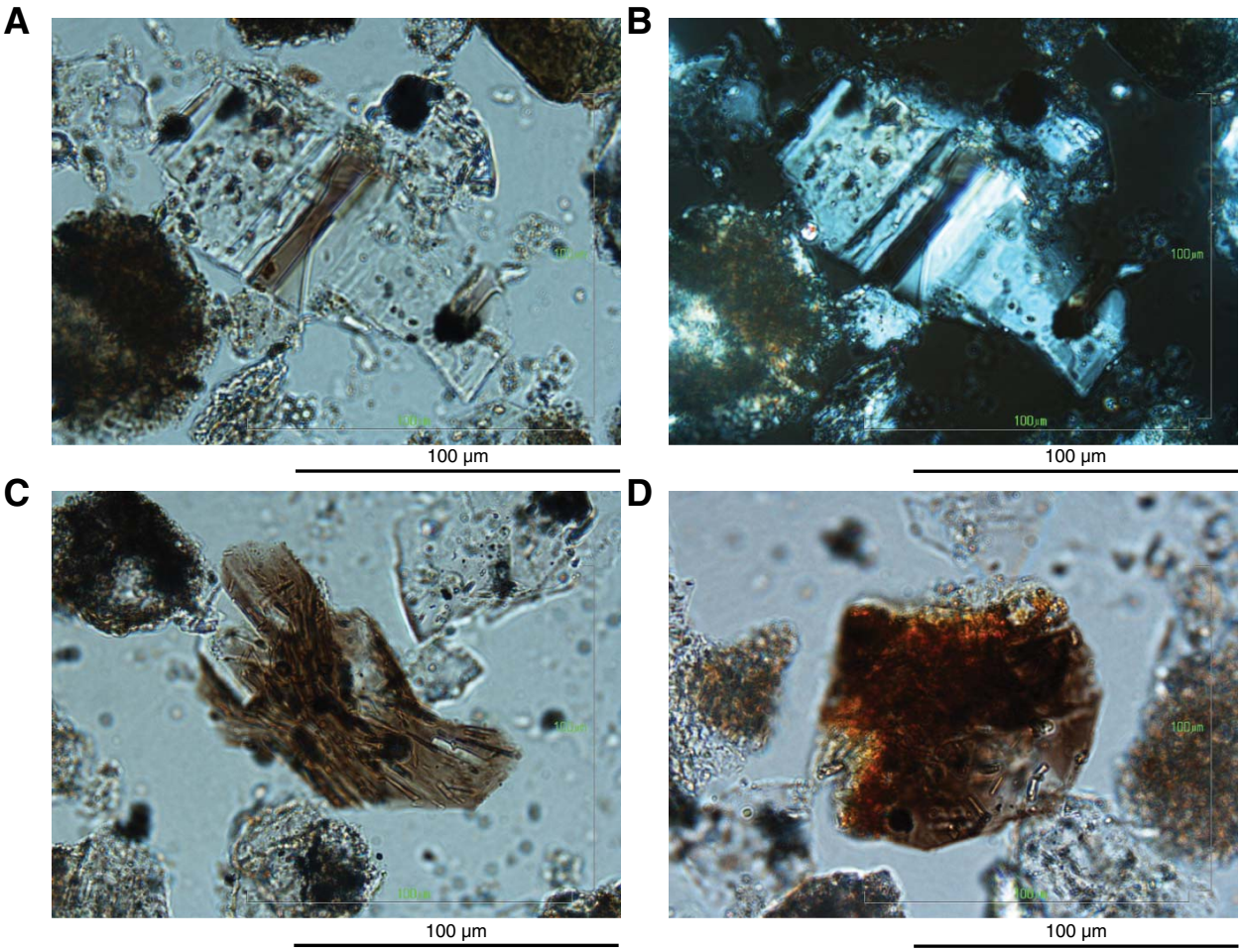

Figure F15 (continued). E, F. Vitric-crystal ash with abundant brown amphiboles (Sample 338-C0022B-39X-5, 40 cm) in (E) PPL and (F) XPL. **G.** Lathwork basaltic lithic grain (Sample 338-C0022B-40X-5, 41 cm; PPL). **H.** Two lathwork basaltic grains with minor palagonization (Sample 338-C0022B-41X-3, 120 cm; PPL).

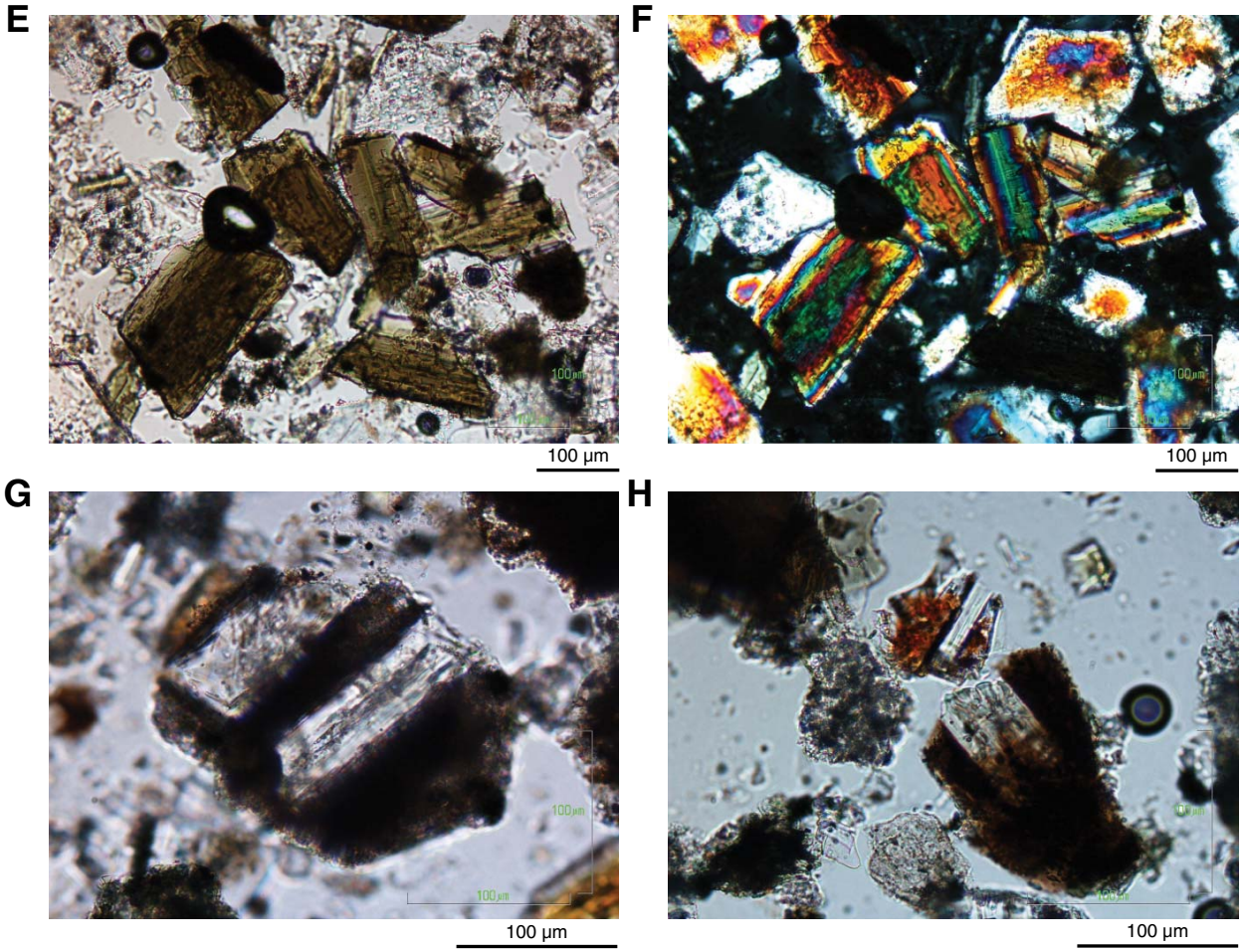

Figure F16. XRF line scan of interval 338-C0022B-8H-4, 5–90 cm. Yellow dashed lines = shear bands, arrows = points at which the scan crosses the bands, gray shading = regions of light-colored lithology that has somewhat higher carbonate content.

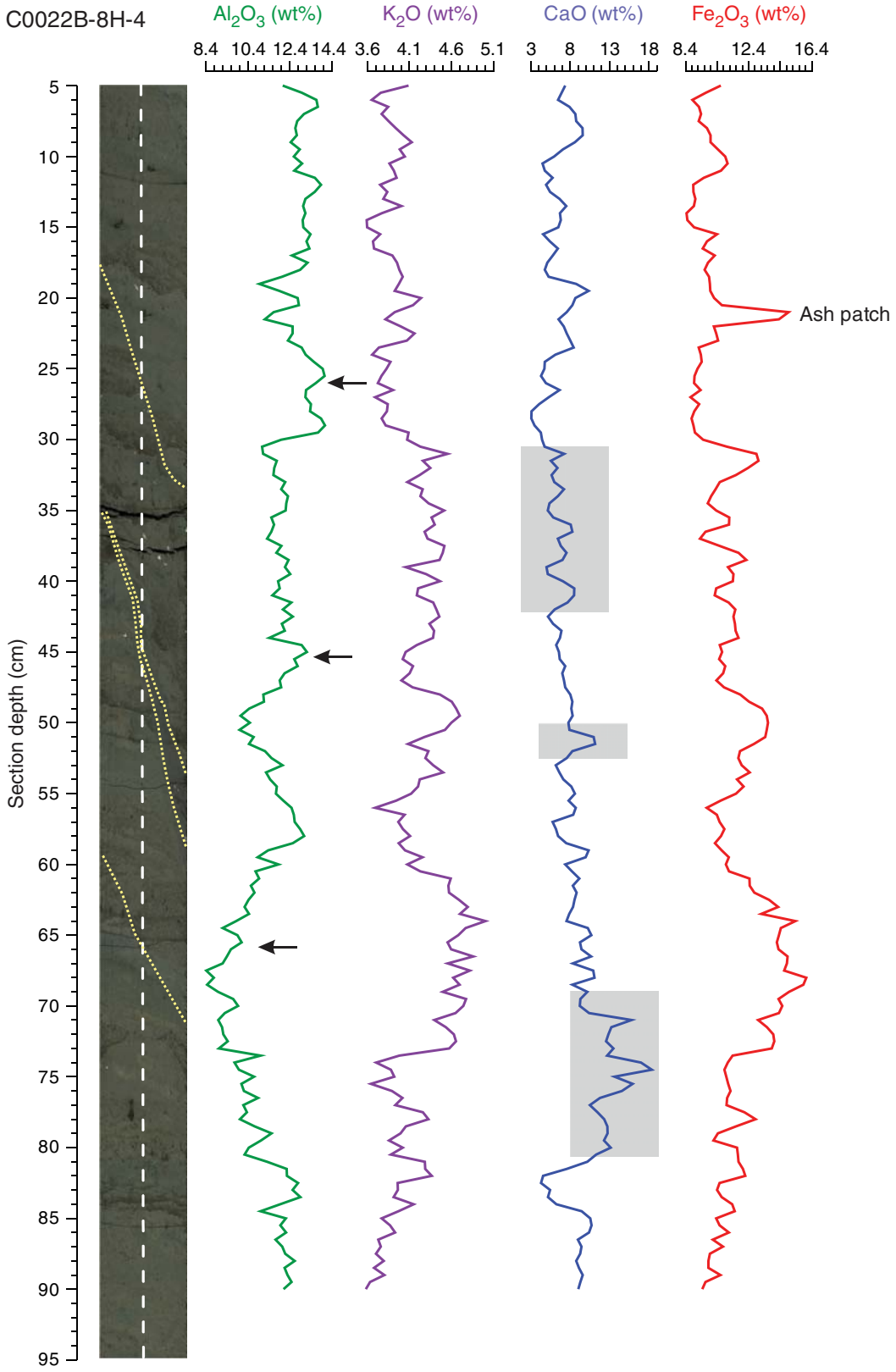

Figure F17. XRF mapping scan of interval 338-C0022B-8H-4, 40–55 cm. Black outlines = color contrasts as seen on the core surface, white lines = shear bands or possible faults.

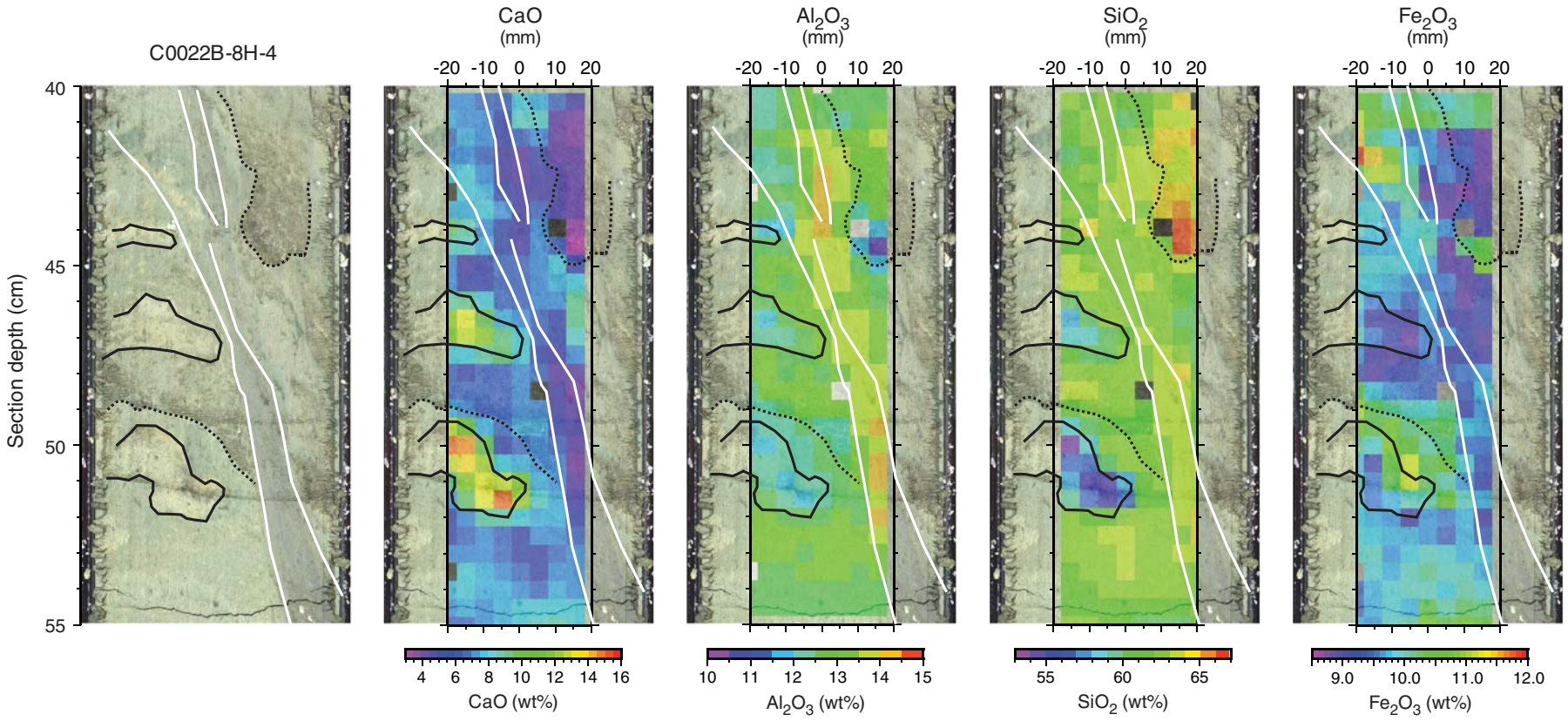

Figure F18. XRF line scan of interval 338-C0022B-38X-5, 0–142 cm. Yellow = zones rich in mud clasts, green = green color bands, black dashed line and gray shading in one intense interval = burrowed intervals, orange-shaded bands = relatively homogeneous interval other than the orange-dashed line, which is some very small mud clasts.

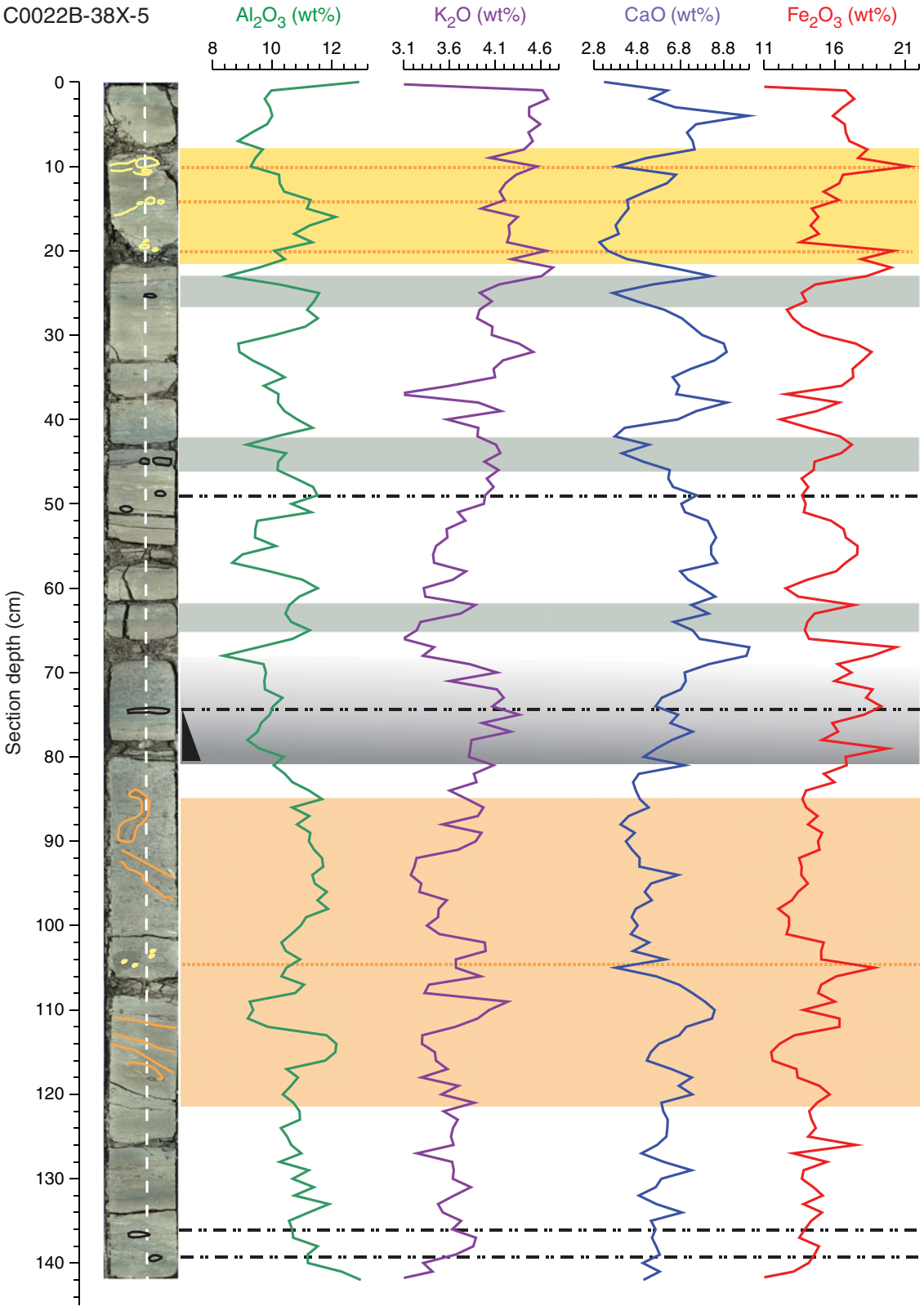

Figure F19. Comparison of lithologic and compositional variations at Sites C0004, C0008, and C0022B. Fsp = feldspar, Qtz = quartz.

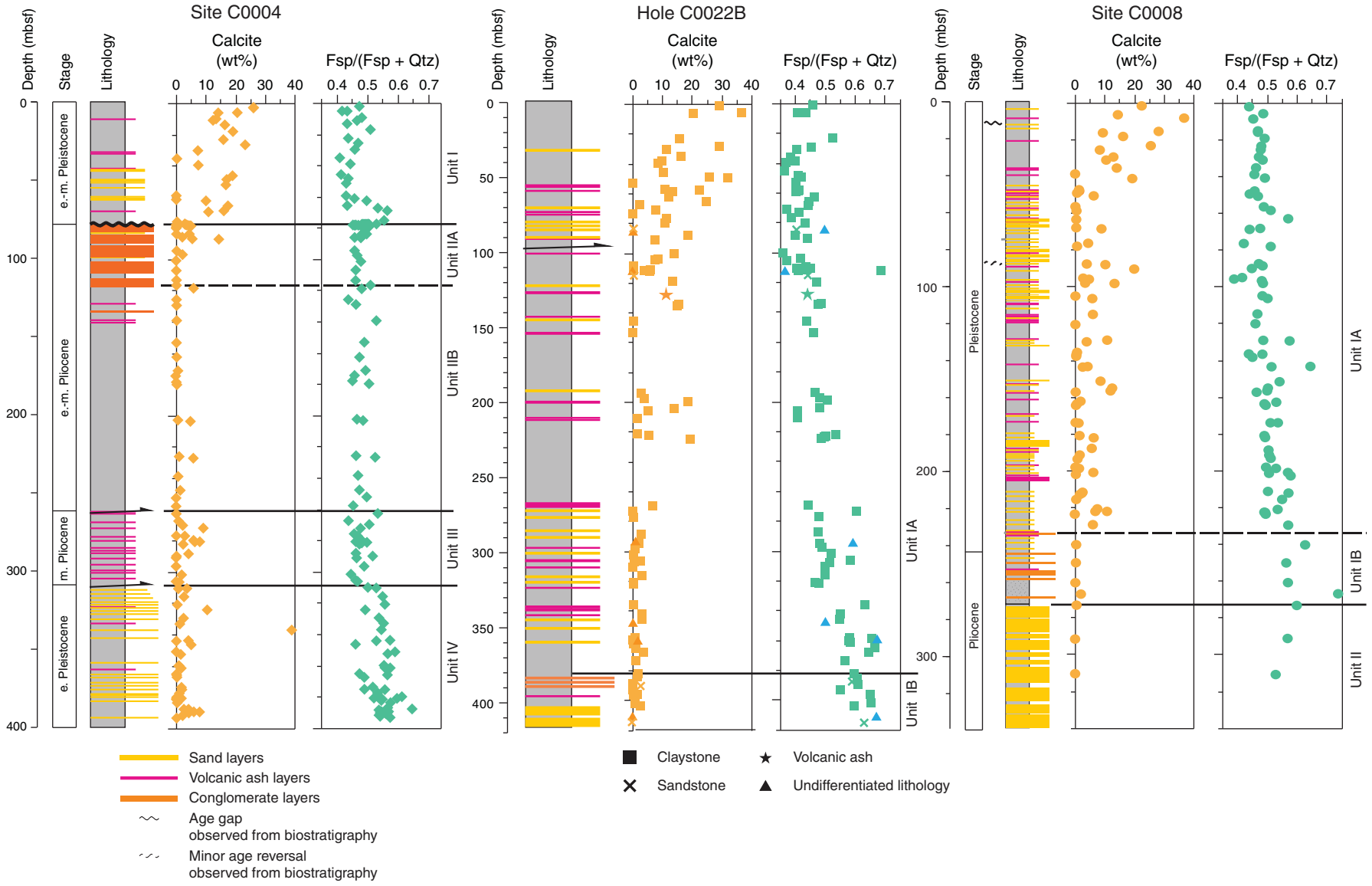

Figure F20. Interpreted seismic stratigraphy of Sites C0004 and C0008 and Hole C0022B (modified from figure 3 of Strasser et al., 2011). VE = vertical exaggeration. A, B, G, and O are regional reflections identified by Strasser et al. (2011).

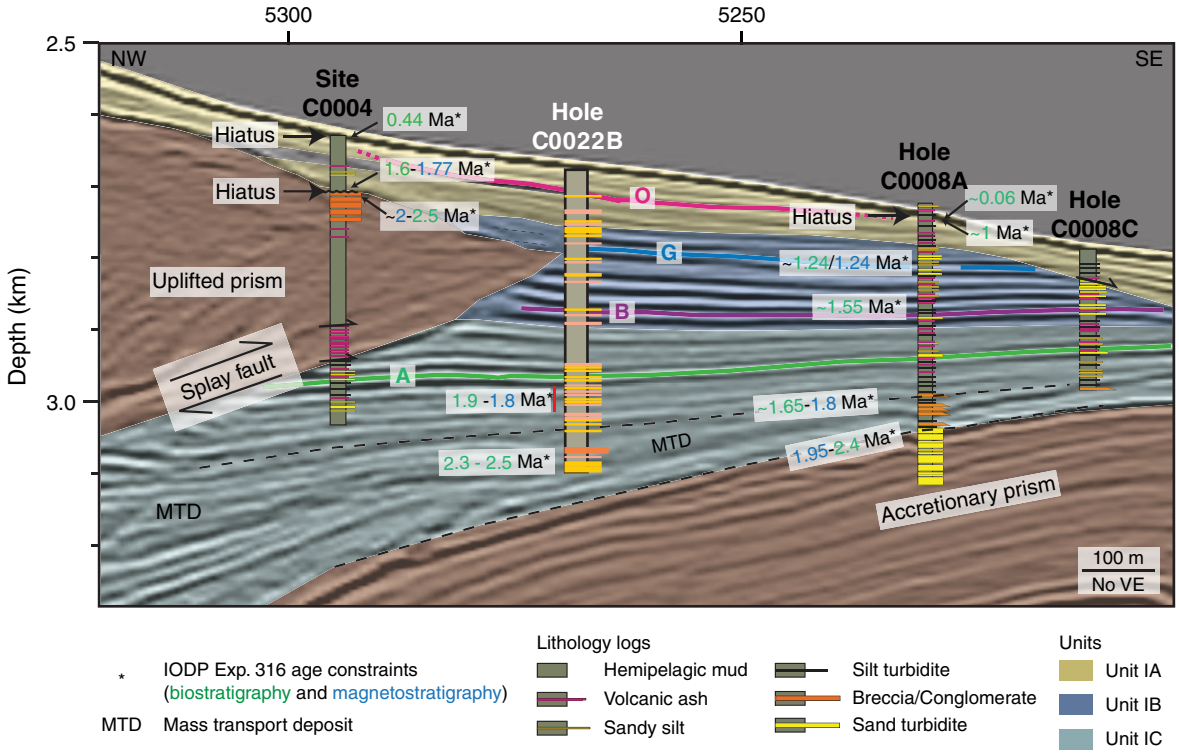

Figure F21. Bedding strike and dip variation vs. depth, Hole C0022B. Core recovery: black = cored intervals, white = uncored sections (i.e., drilled through), gray = portions of cored intervals that were not recovered. Right-hand rule (RHR) is applied for bedding strikes. Yellow line = possible location of shear zone related to the splay fault as deduced from planar fabrics in Hole C0022B. Shaded section under dip angle = bedding disturbed zone, intervals with bedding dips >20°.

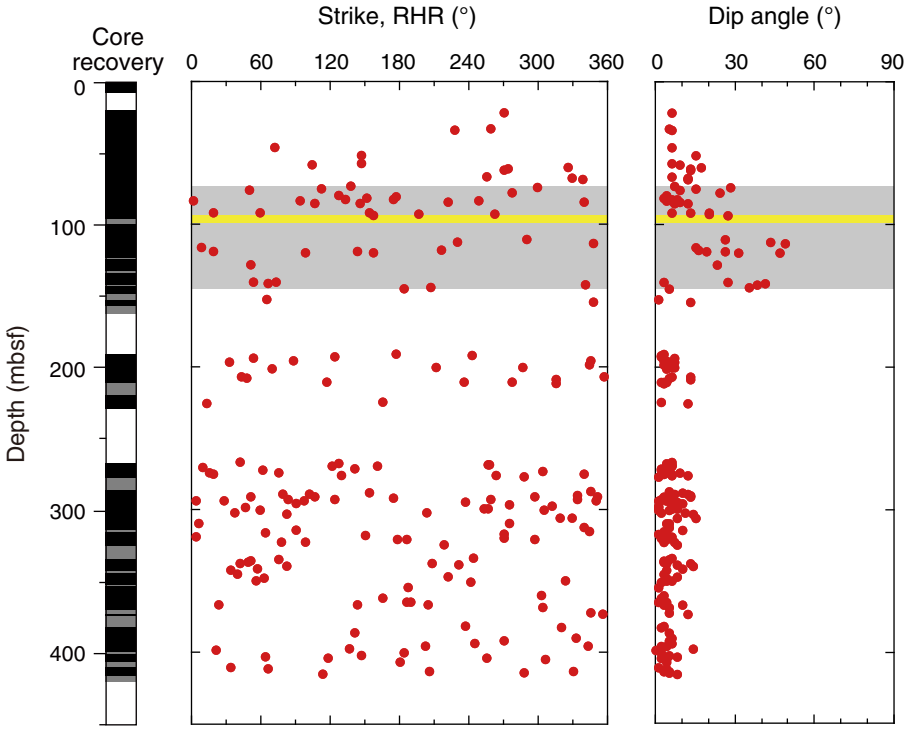

Figure F22. Lower-hemisphere equal-area projections of poles to bedding, Hole C0022B. **A.** All measurements. **B.** Above bedding disturbed zone. **C.** Within bedding disturbed zone. **D.** Below bedding disturbed zone.

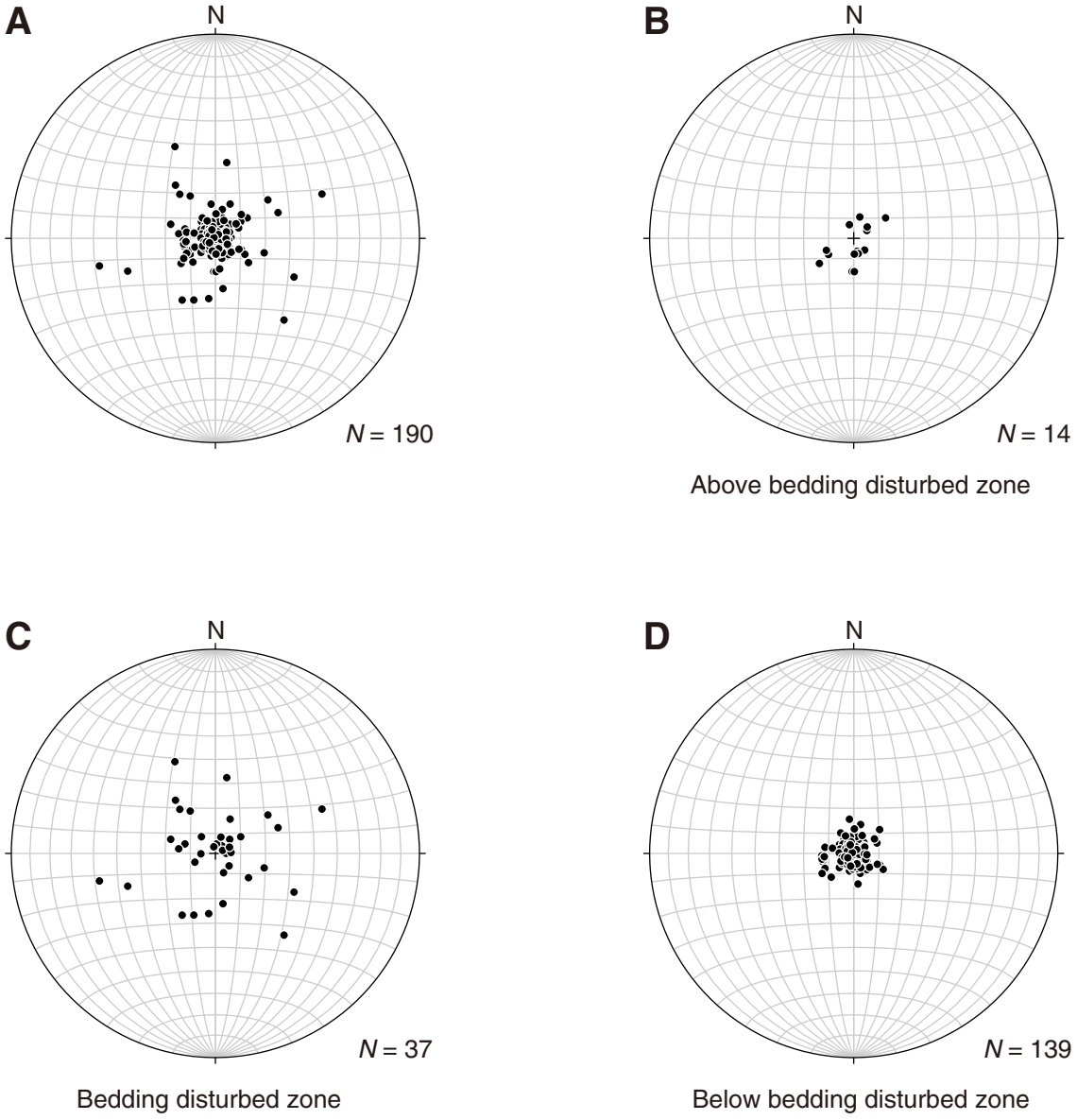

Figure F23. Examples of structures (arrows) observed on whole-round X-ray computed tomography (CT) scans and working halves of split cores. **A.** Photograph and X-ray CT scan image of split surface of normal faults showing smearing (interval 338-C0022B-8H-3, 20–60 cm). **B.** Deformation bands (interval 338-C0022B-38X-5, 9–15 cm). Offset horizontal beds indicate a normal component of displacement. **C.** Deformation bands (interval 338-C0022B-31X-8, 10–14 cm).

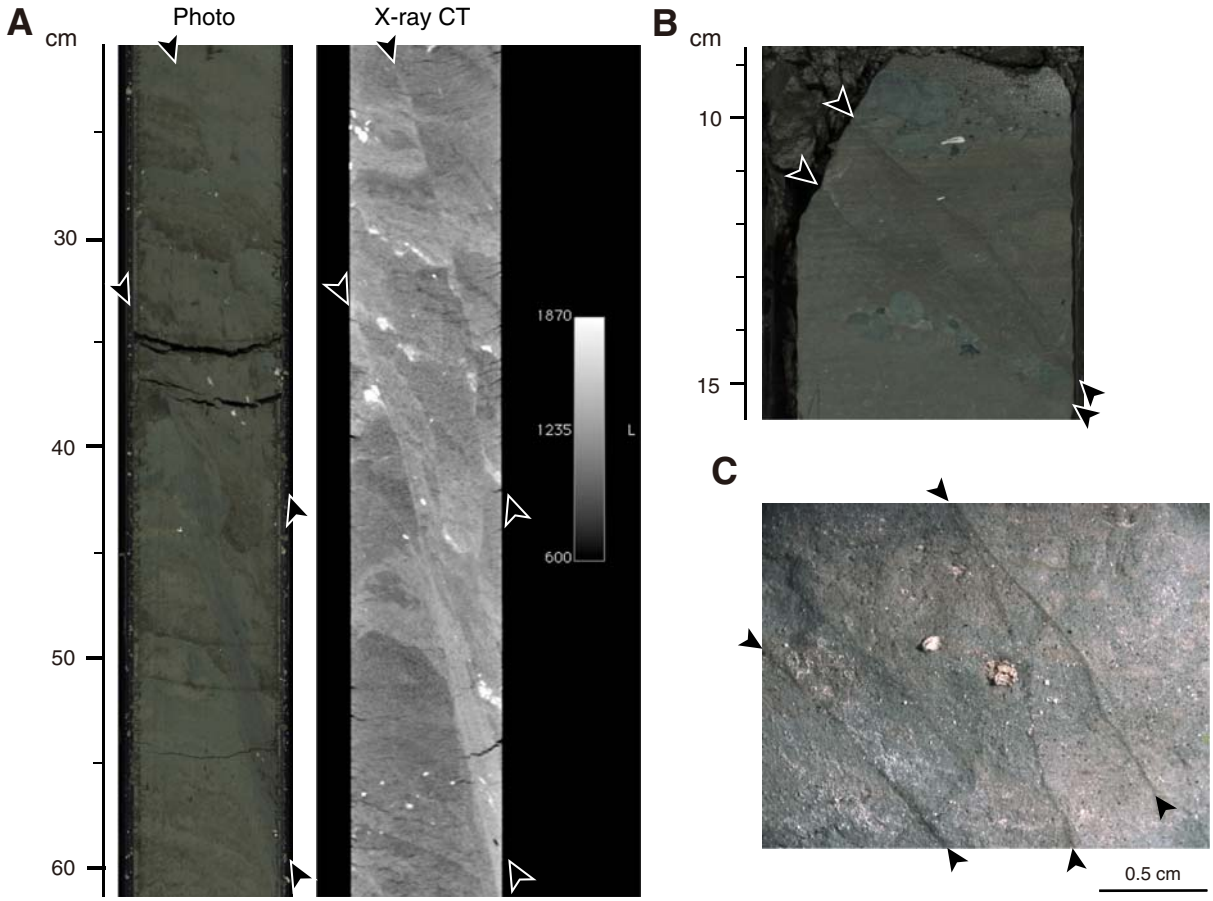

Figure F24. Fault and deformation band strike and dip variation vs. depth, Hole C0022B. Core recovery: black = cored intervals, white = uncored sections (i.e., drilled through), gray = portions of cored intervals that were not recovered. Right-hand rule (RHR) is applied for strikes. Yellow line = possible location of shear zone related to the splay fault as deduced from planar fabrics in Hole C0022B. Shaded section under dip angle = bedding disturbed zone, intervals with bedding dips >20°.

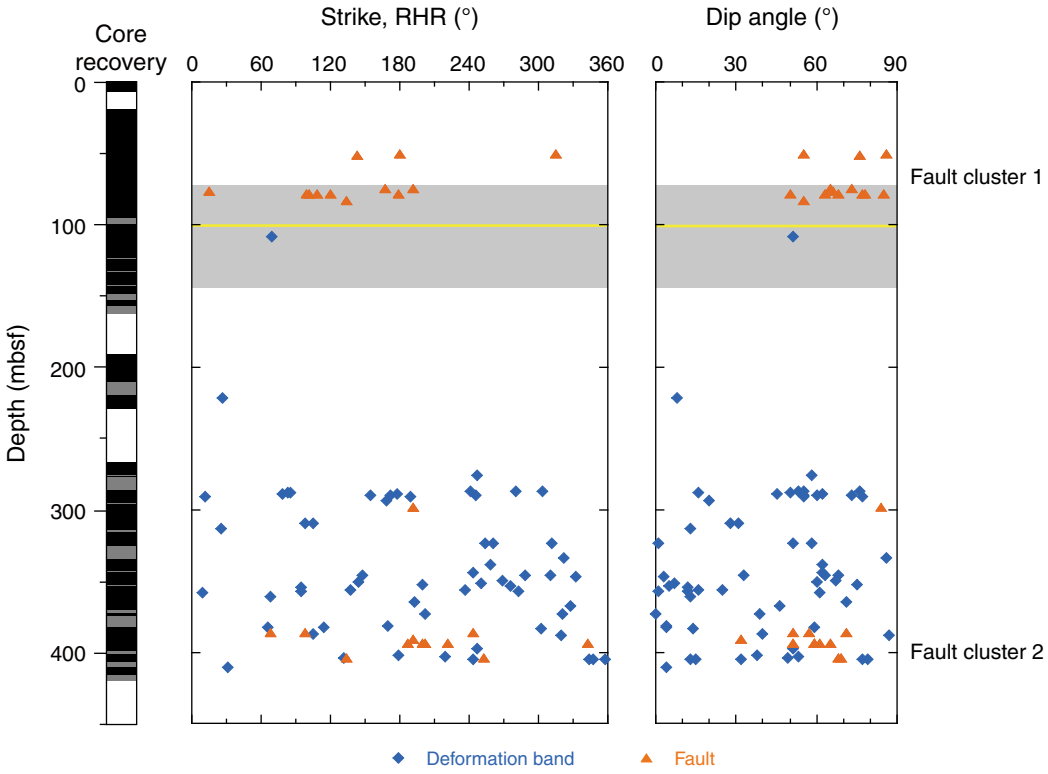

Figure F25. Lower-hemisphere equal-area projections of fault orientations in cores, Hole C0022B. Dots on great circles = striations, arrows = slip vectors of hanging wall relative to footwall. **A.** All measurements. **B.** Fault Cluster 1. **C.** Fault Cluster 2.

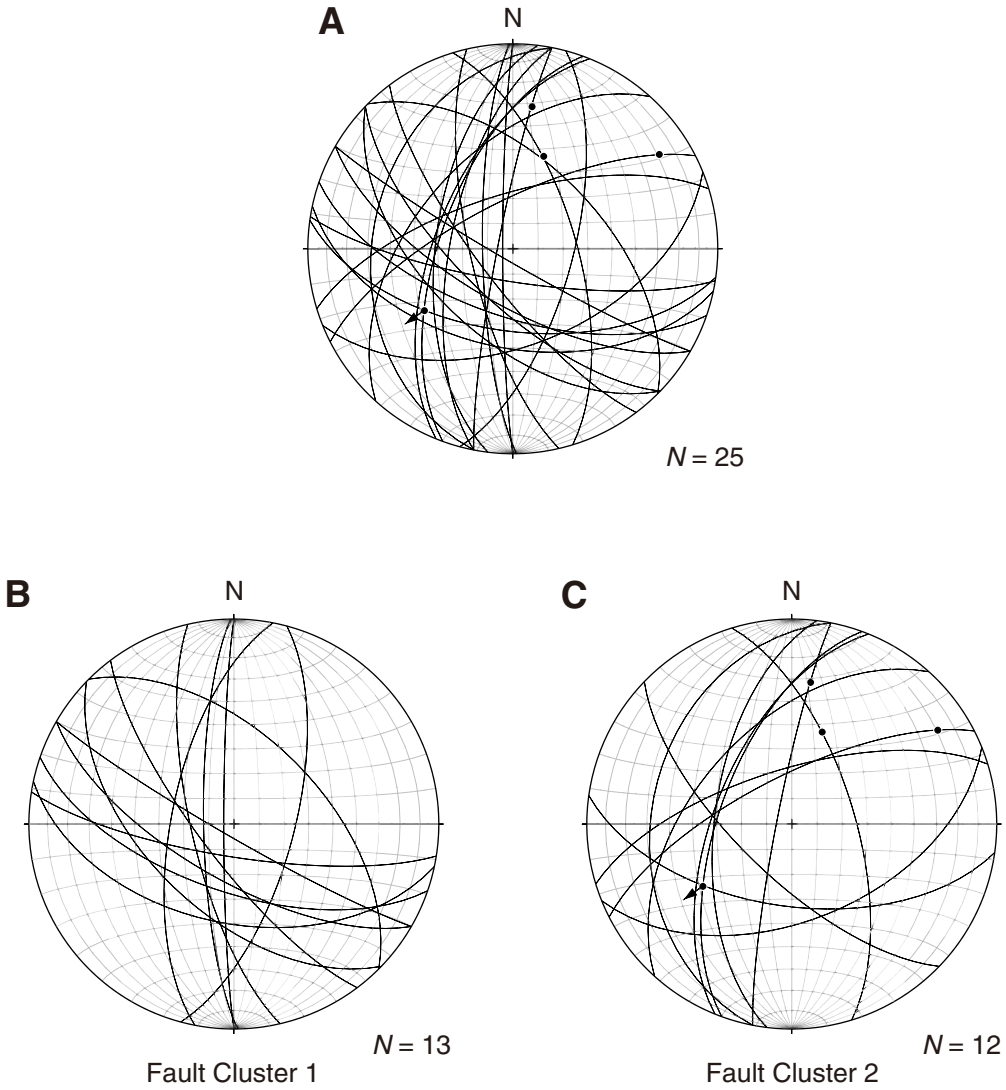

Figure F26. Lower-hemisphere equal-area projections of deformation bands (great circles and poles), Hole C0022B.

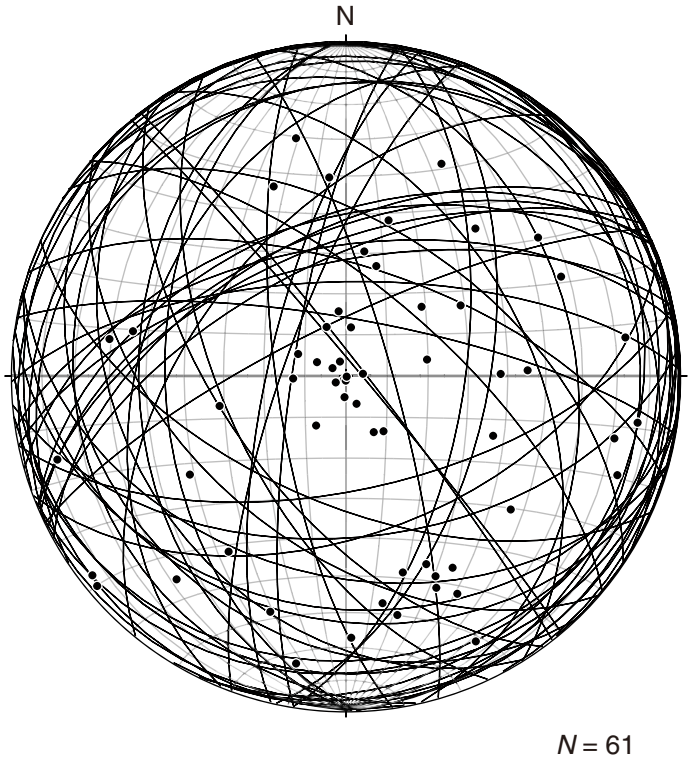

Figure F27. Examples of planar fabrics. **A.** View from bottom of the of the core catcher (interval 338-C0022B-10T-CC, 19–20 cm) looking upcore, showing claystone crossed by a series of striated planes defining a planar fabric (PF). **B.** Close-up photograph of claystone crossed by a series of striated planes defining planar fabric (interval 338-C0022B-11T-1, 18–19 cm).

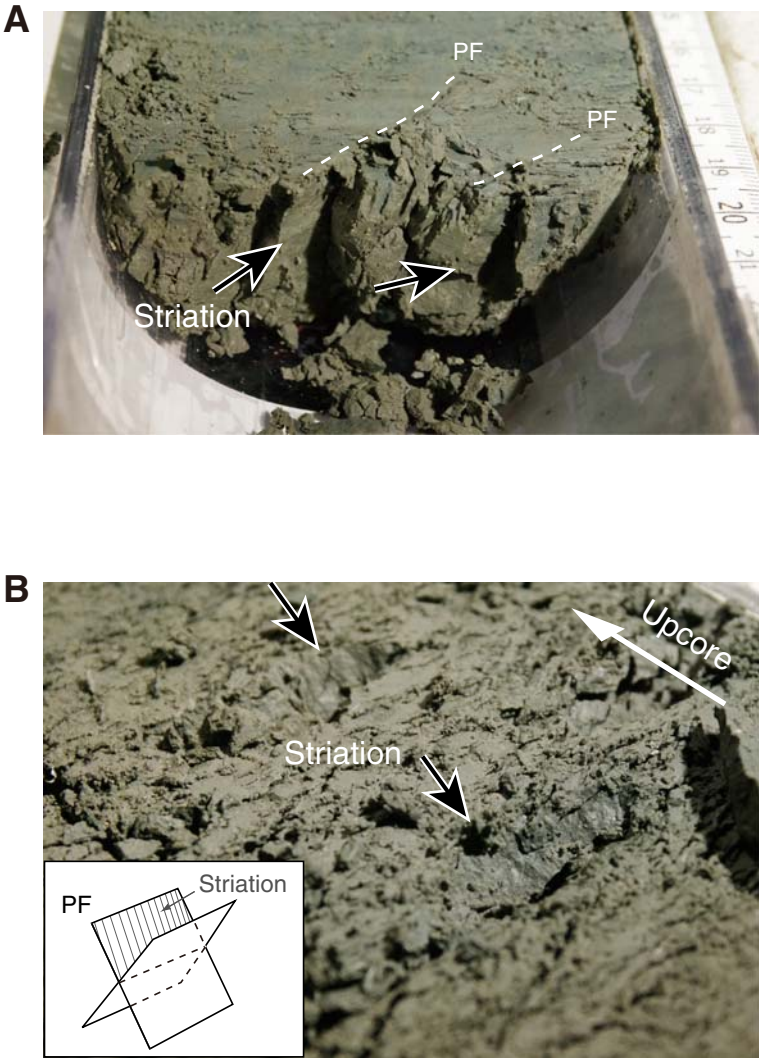

Figure F28. A. Salinity, pH, alkalinity, Cl^-, PO_4^{3-}, Br^-, SO_4^{2-}, NH_4^+, Na^+, K^+, Mg^{2+}, Ca^{2+}, Li, and B. (Continued on next page.)

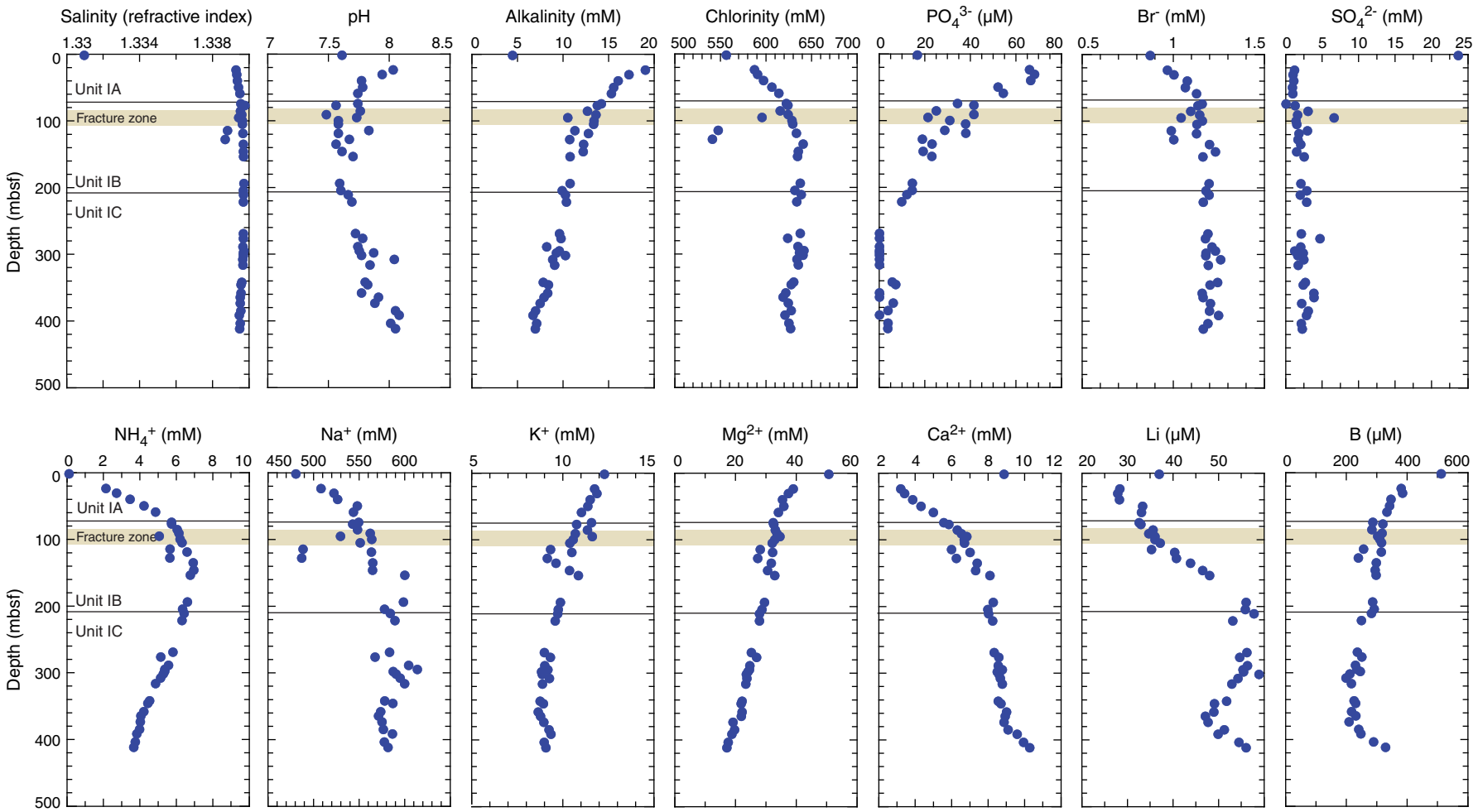

Figure F28 (continued). B. Mn, Fe, Si, Sr, Ba, V, Cu, Zn, Rb, Mo, Cs, Pb, and U. Yellow bar = heavily fractured interval. An increase in SO_4^{2-}, K^+, Mg^{2+}, Ca^{2+}, Fe, Si, Cu, Rb, Mo, Cs, Pb, and U can be observed, whereas most of the other components remain unaffected. See text for further data description and interpretations.

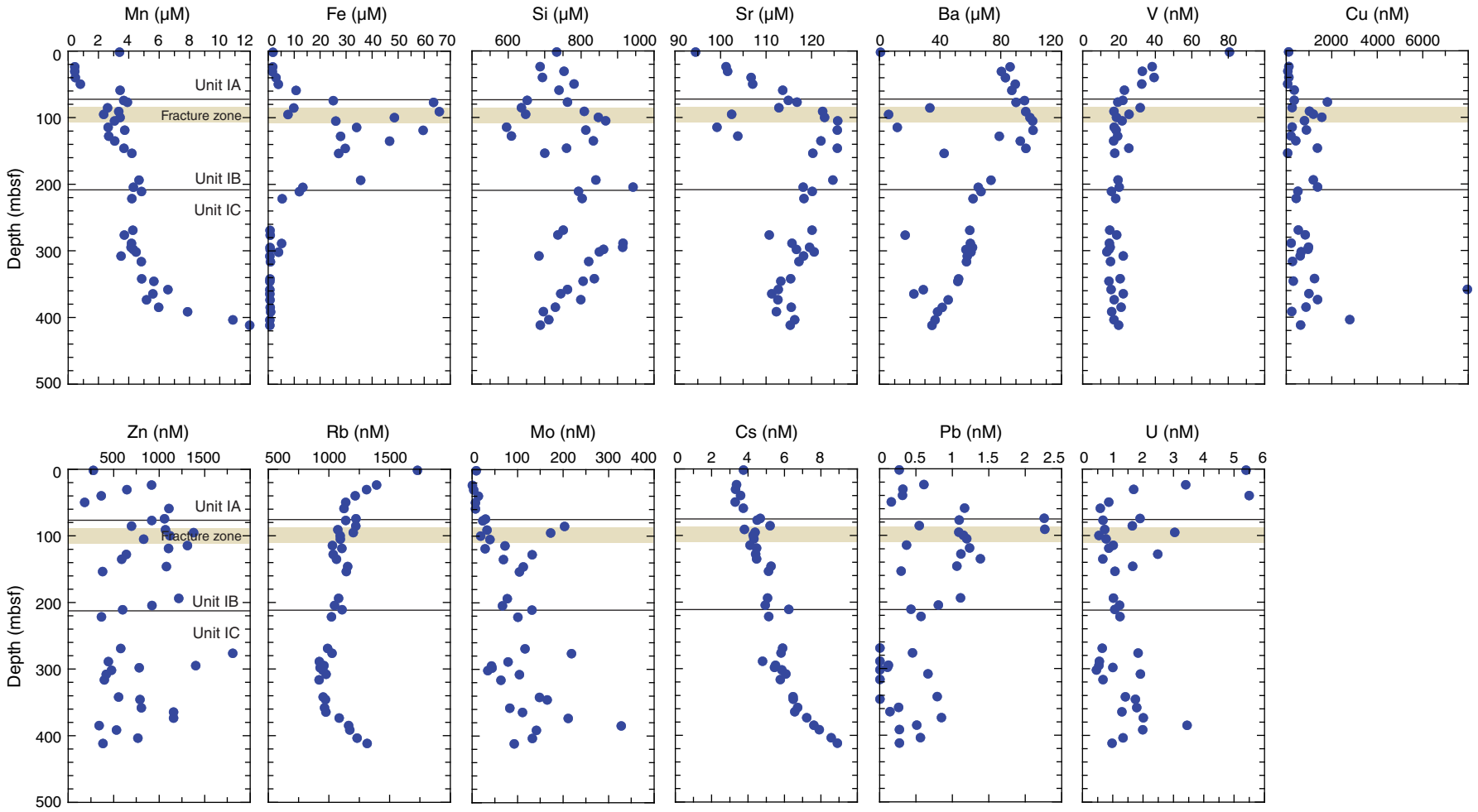

Figure F29. Vertical profiles of methane, ethane, and propane concentrations measured on headspace gas samples from Hole C0022B sediment. Data were generated using the unconventional method (adding of alkaline solution to the sample). Horizontal black lines = lithologic unit boundaries.

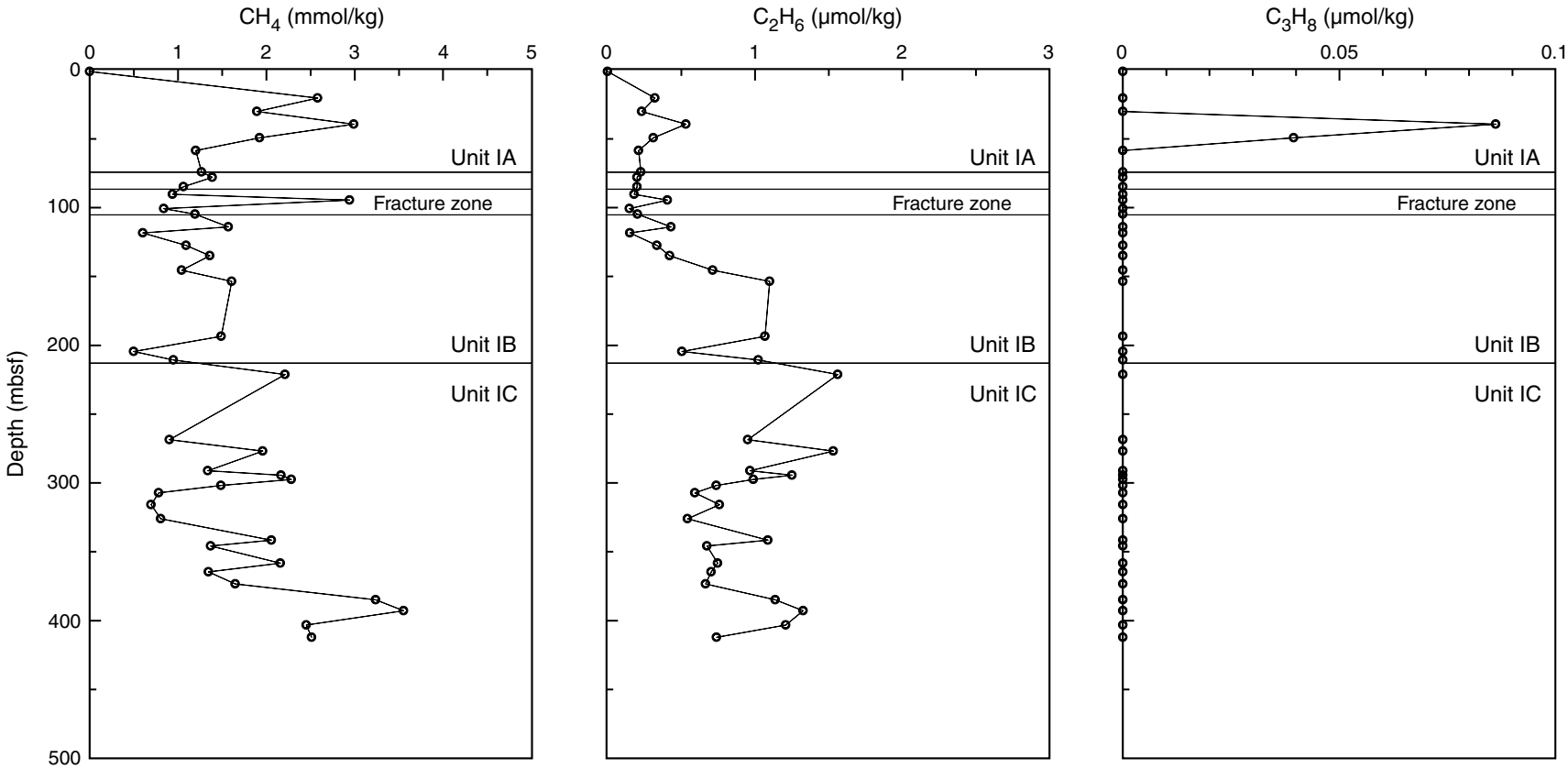

Figure F30. Vertical profiles of $C_1/(C_2 + C_3)$ ratios and $\delta^{13}C\text{-}CH_4$ calculated from headspace gas data obtained from the unconventional method (adding of alkaline solution to the sample) applied to Hole C0022B samples. VPDB = Vienna Peedee belemnite. Horizontal black lines = lithologic unit boundaries.

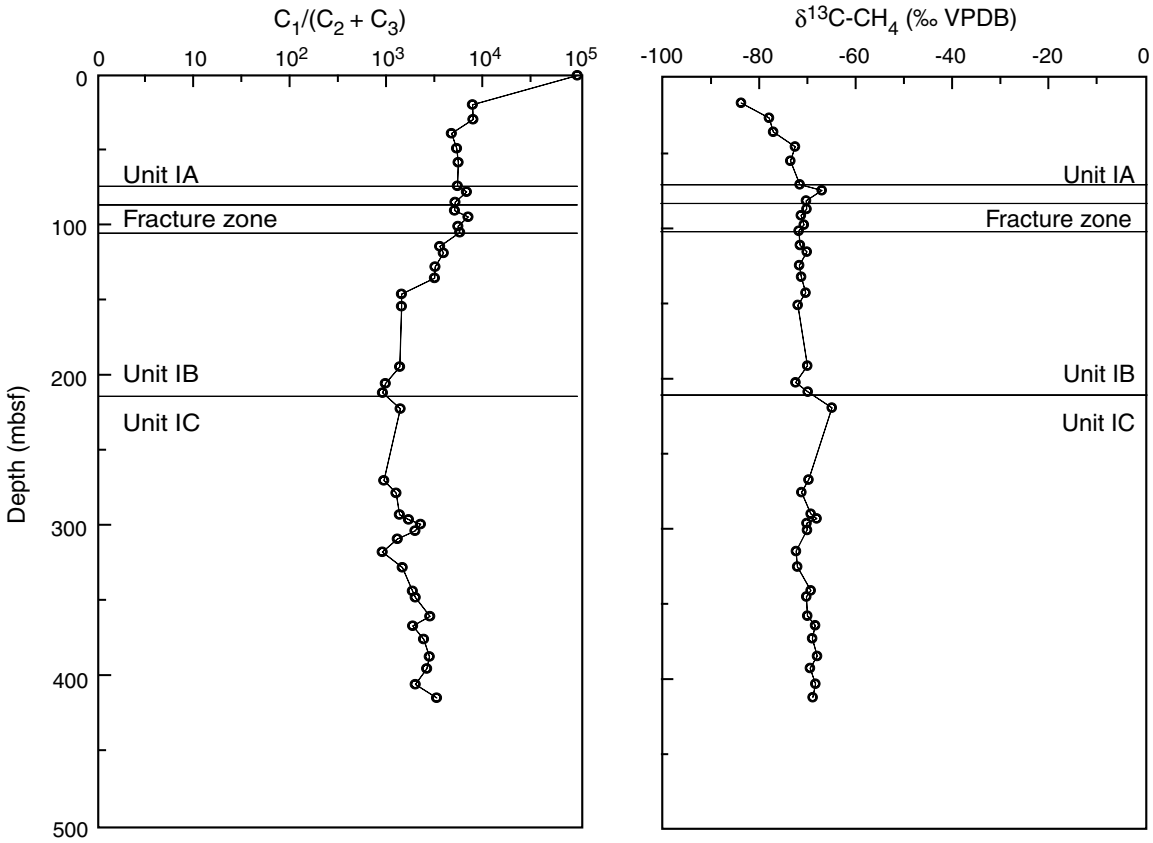

Figure F31. Relationship between $C_1/(C_2 + C_3)$ ratios and $\delta^{13}C\text{-}CH_4$ obtained from the unconventional method (adding of alkaline solution to the sample) in Hole C0022B headspace gases. VPDB = Vienna Peedee belemnite.

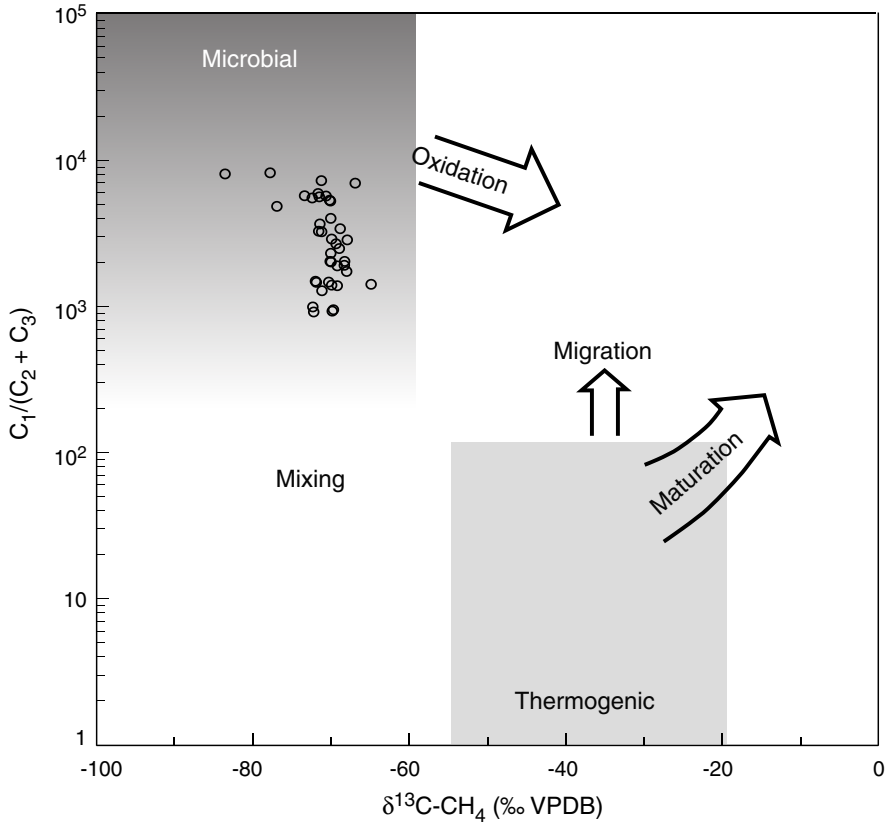

Figure F32. Solids elemental analysis. TOC = total organic carbon, TN = total nitrogen, TS = total sulfur.

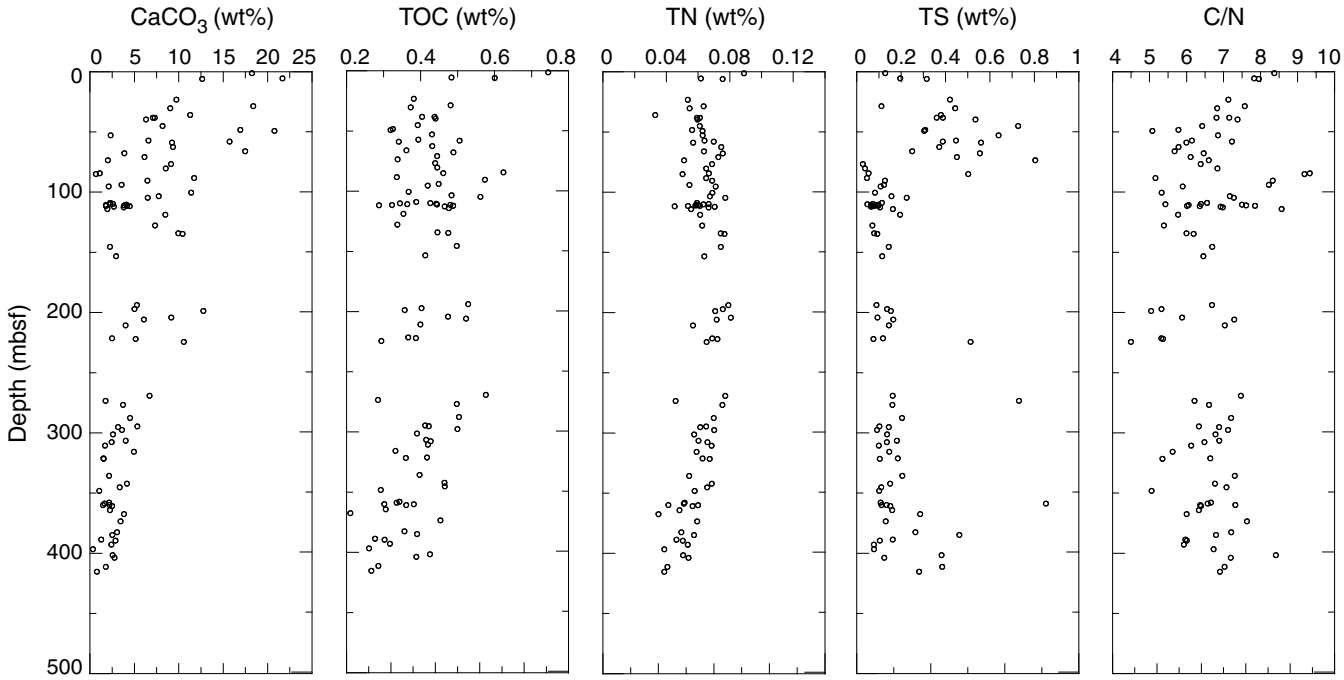

Figure F33. MSCL-W measurements, Site C0022. **A.** Gamma ray attenuation (GRA) bulk density. **B.** Magnetic susceptibility. **C.** Natural gamma radiation (NGR). cps = counts per second. **D.** Noncontact electrical resistivity.

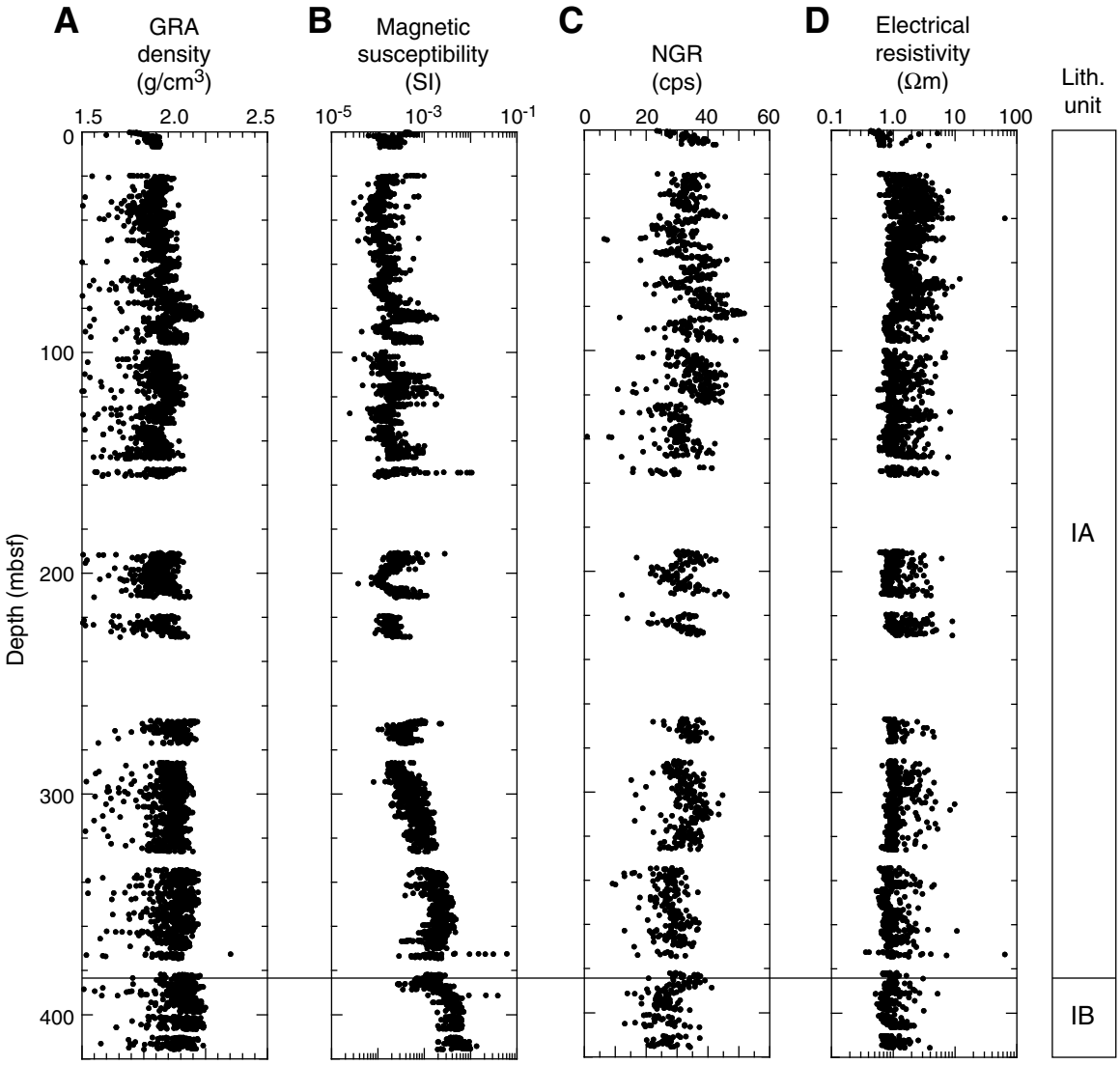

Figure F34. V_P measurements. **A.** V_P data from MSCL-W. Black = all recorded data, red = data filtered with *P*-wave amplitudes >30 mV. **B.** Comparison of V_P measurements on Core 338-C0022-1H made by MSCL-W (red) and Section 338-C0022-1H-4 made by MSCL-S (blue).

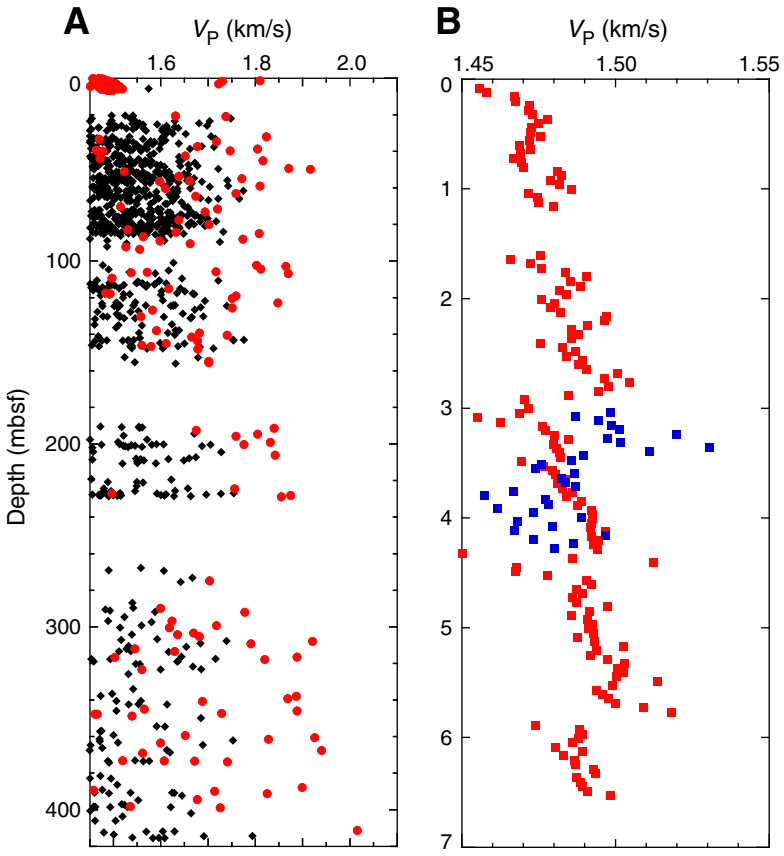

Figure F35. MAD measurements, Site C0022. **A.** Bulk density. **B.** Porosity. **C.** Grain density.

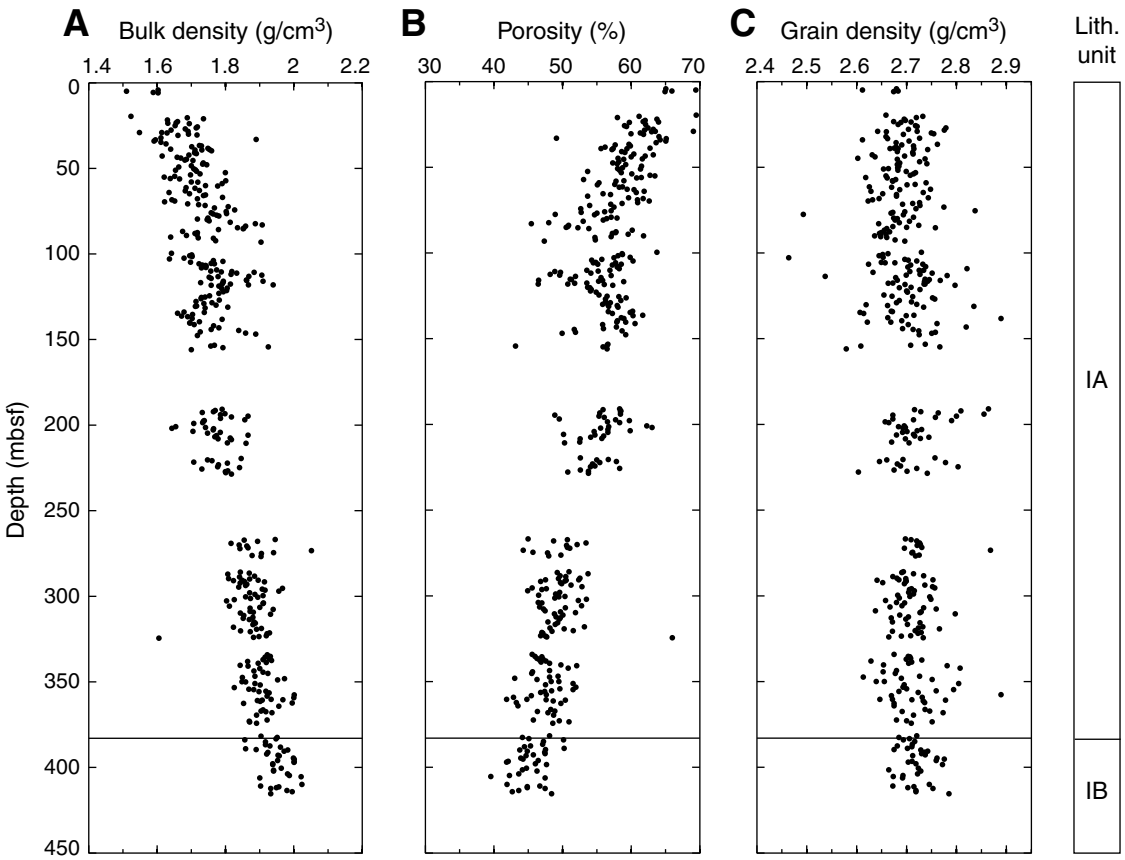

Figure F36. Thermal conductivity, Site C0022. Black = whole-round core measurements with a needle probe, red = working-half measurements with a half-space line source probe.

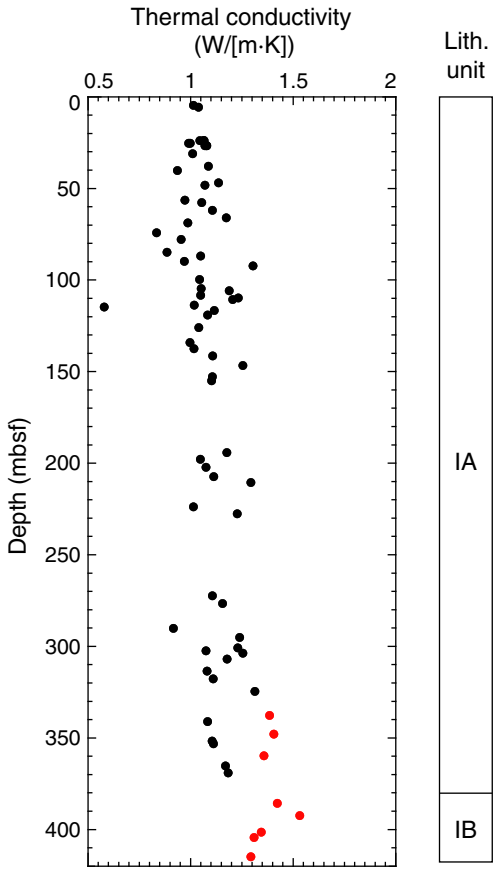

Figure F37. Wenner probe electrical resistivity measurements on unconsolidated samples in Hole C0022B.

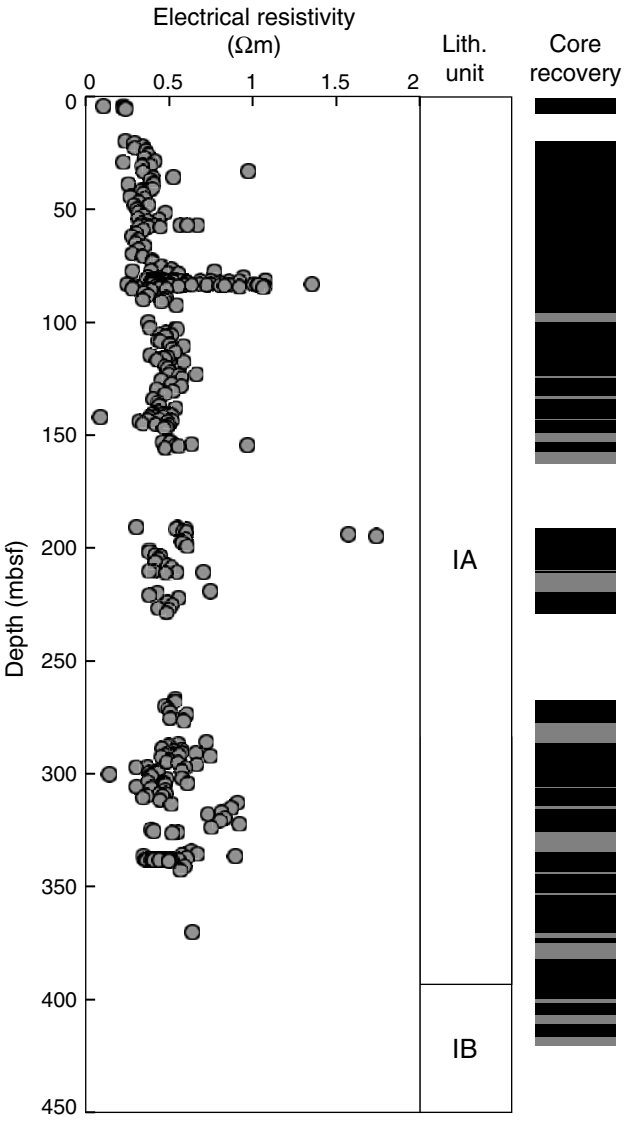

Figure F38. Comparison of electrical resistivity data. **A.** Wenner probe electrical resistivity data of Hole C0022B working-half cores together with data from cubic consolidated samples from Hole C0022B and resistivity data from Expedition 316 Holes C0004D and C0008A (Expedition 316 Scientists, 2009a, 2009b). **B.** Comparison of electrical resistivity in Hole C0022B from Wenner probe with cubic consolidated samples and whole-round multisensor core logger (MSCL-W) data.

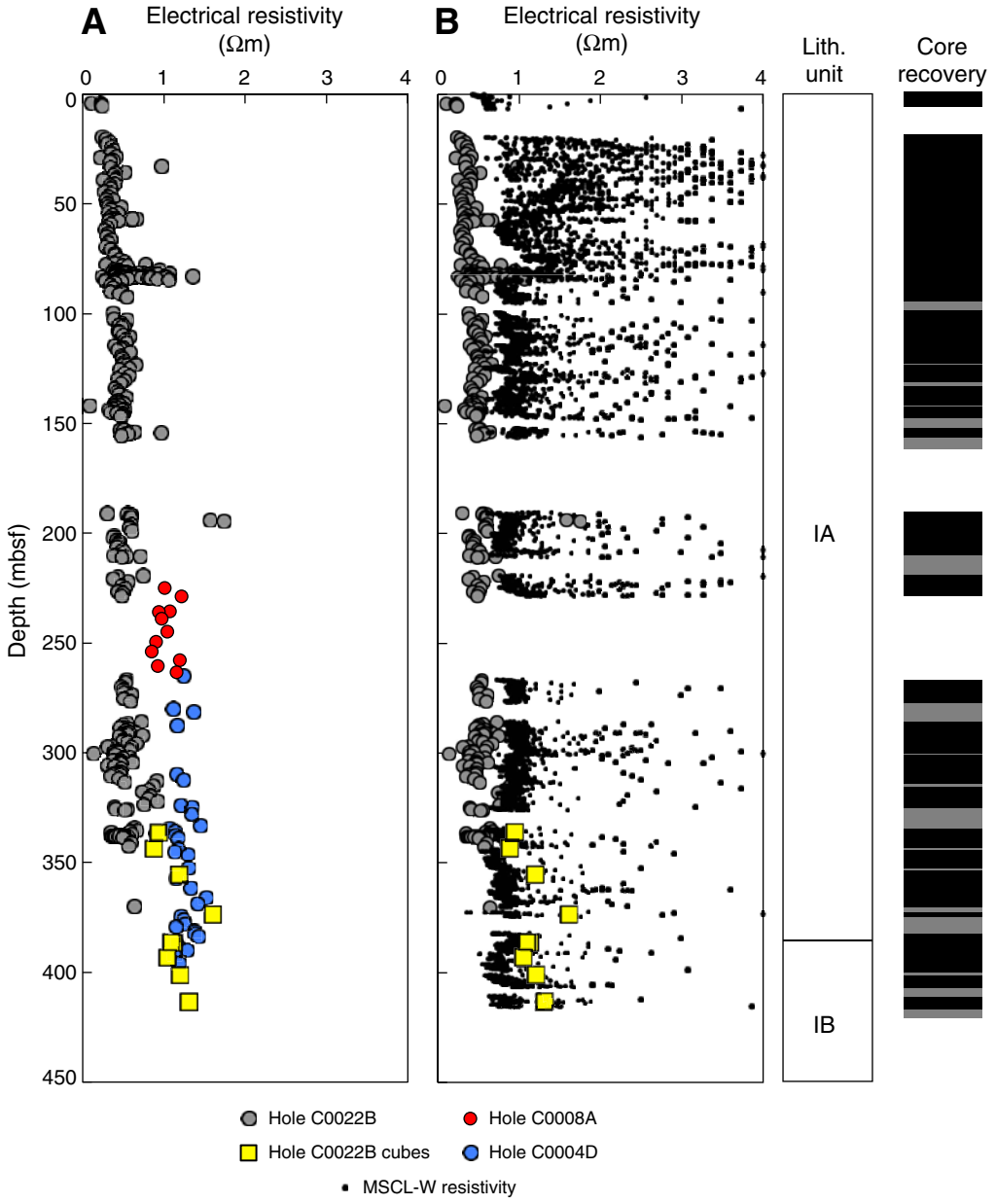

Figure F39. Relationship between electrical resistivity and porosity from Holes C0022B, C0002K, and C0002L, as well as Expedition 333 Holes C0011C–C0011D and C0012C–C0012D (Expedition 333 Scientists, 2012a, 2012b).

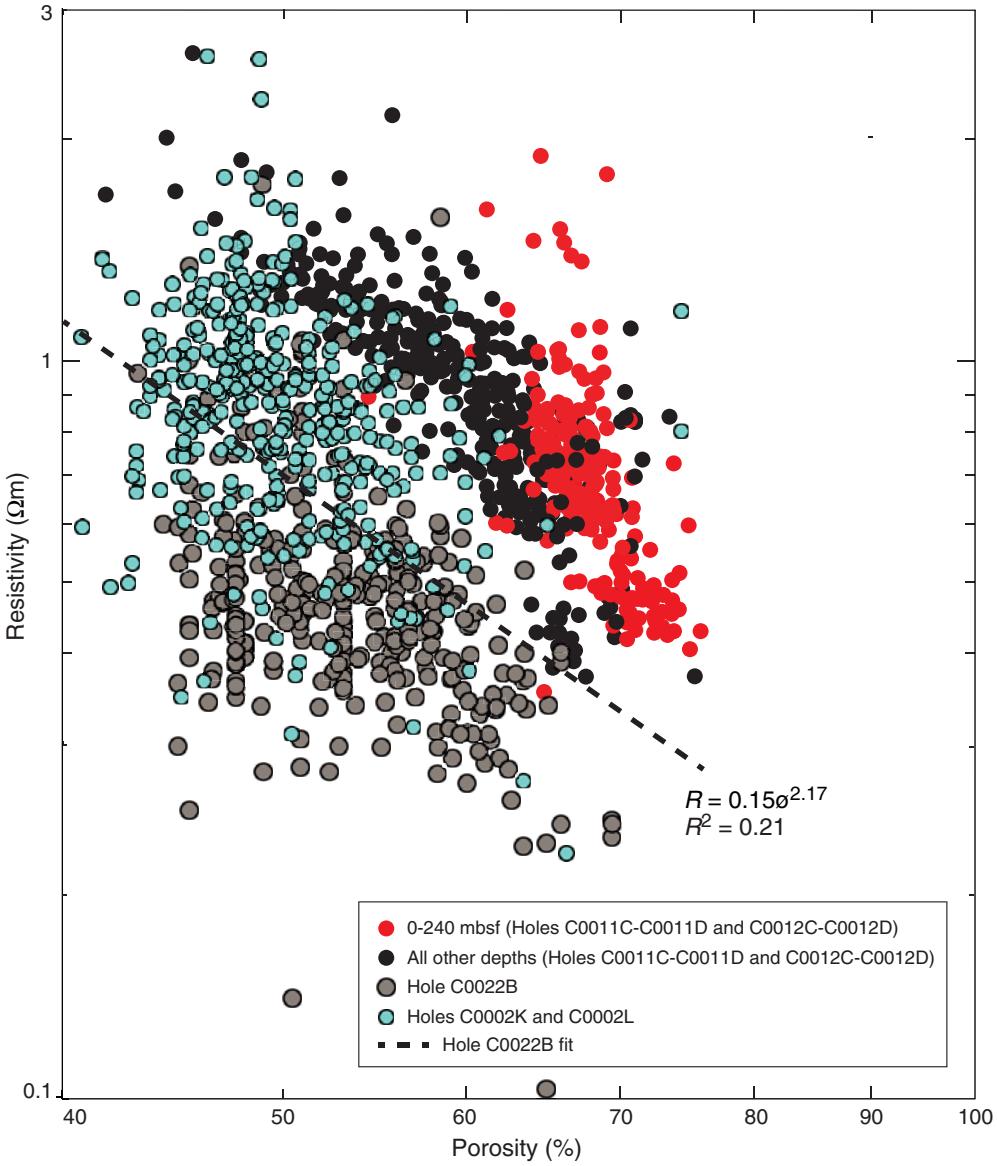

Figure F40. V_P and electrical resistivity measurements on discrete samples, Site C0022. **A.** V_P along three orthogonal axes. **B.** Electrical resistivity along three orthogonal axes. **C.** Anisotropy of V_P. **D.** Anisotropy of electrical resistivity.

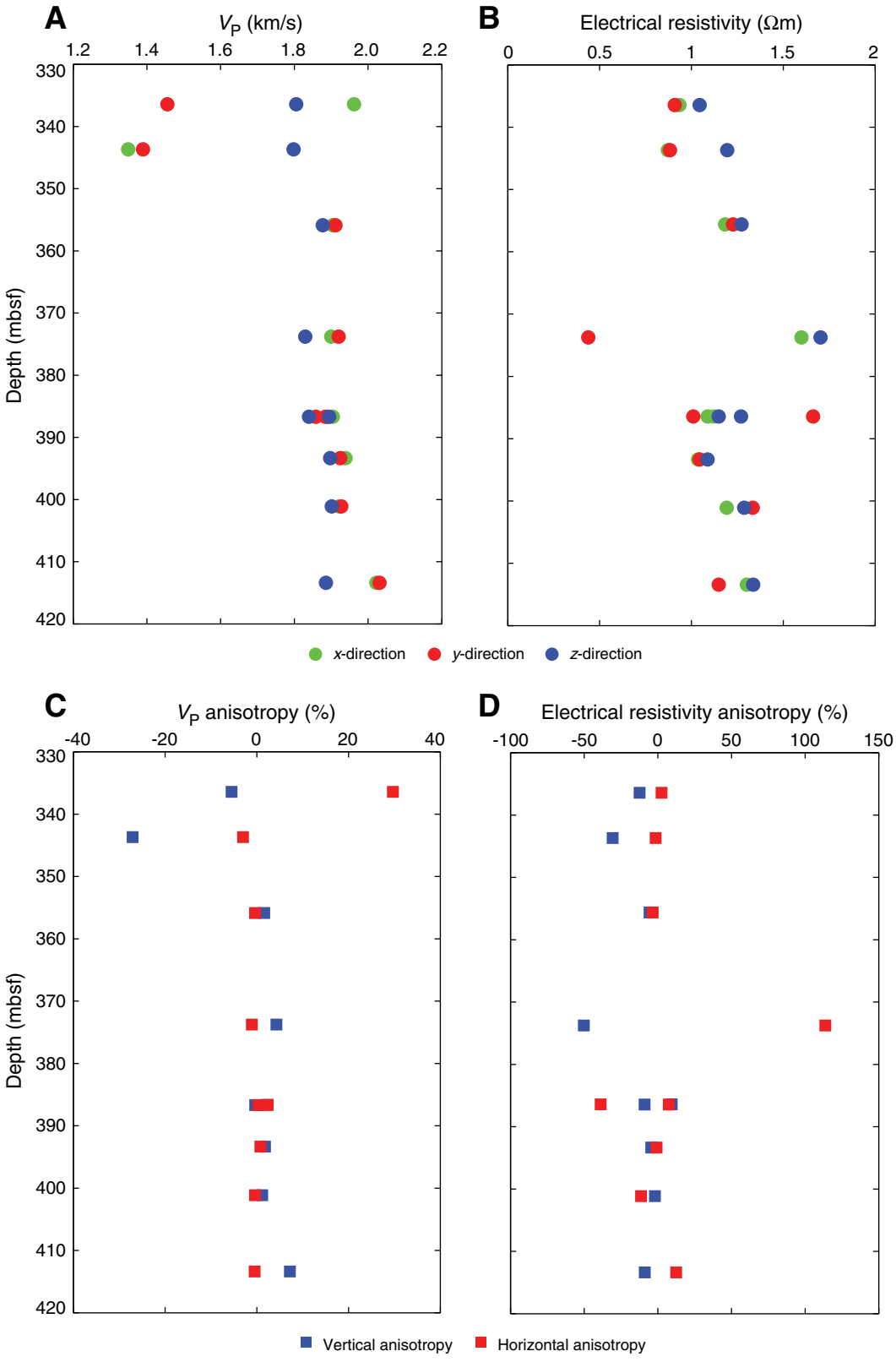

Figure F41. A. Undrained shear strength, Site C0022. **B.** Unconfined compressive strength (UCS).

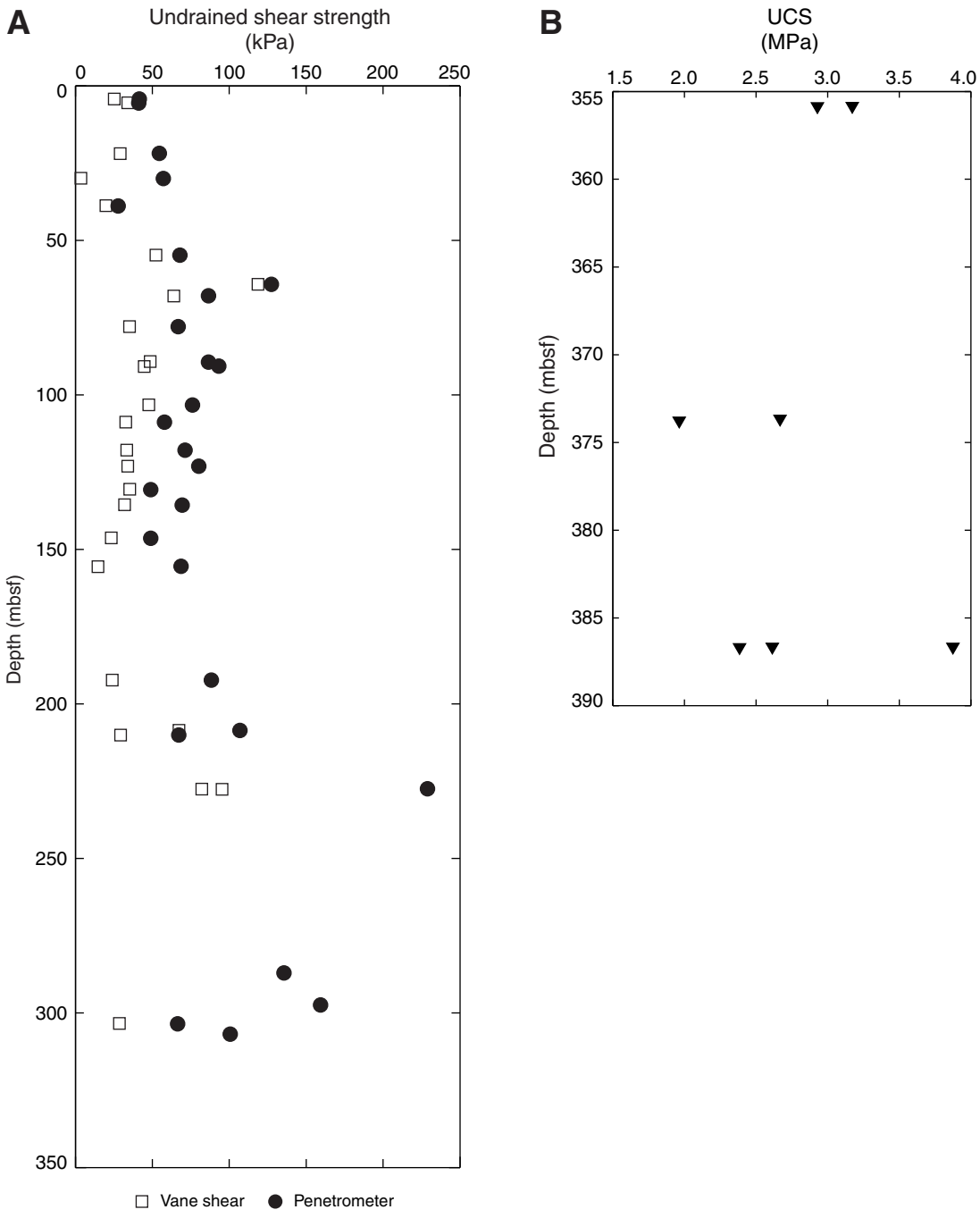

Figure F42. Color reflectance, Site C0022. **A.** L*. **B.** a*. **C.** b*.

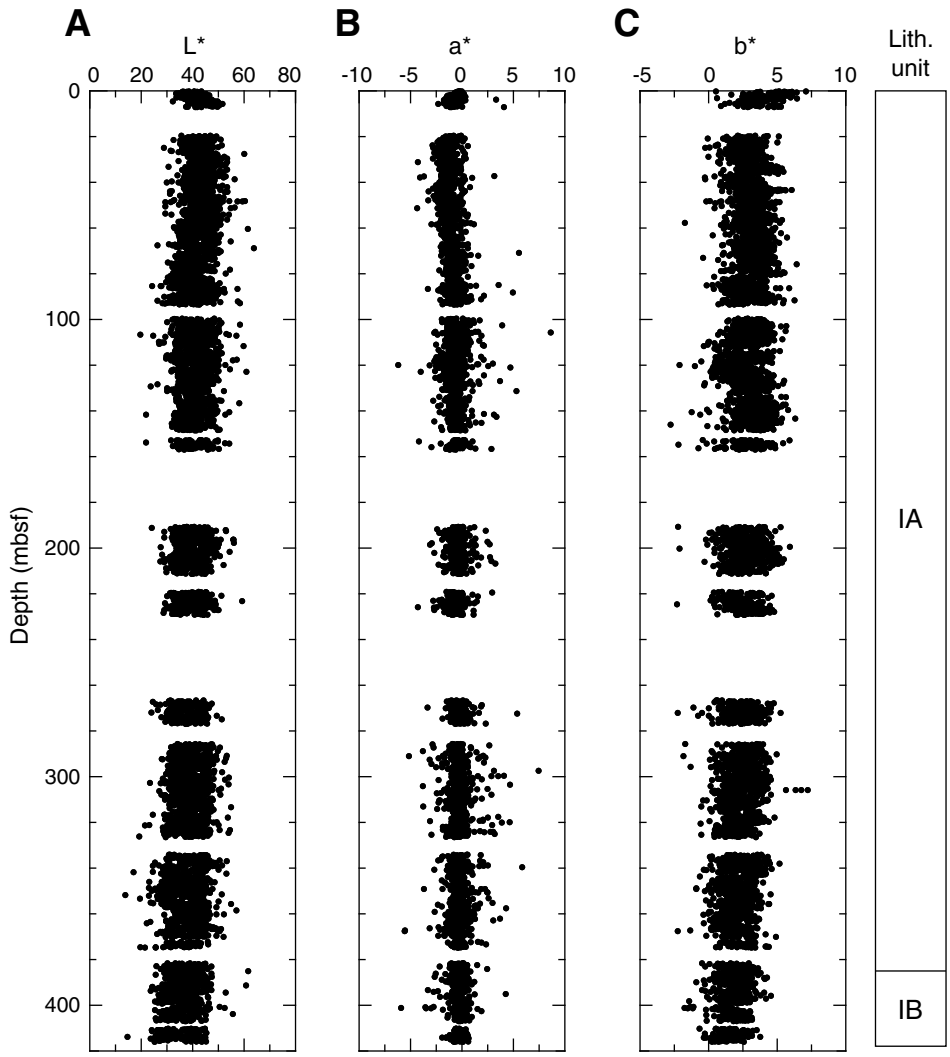

Figure F43. Vector component diagrams of progressive AF demagnetization of Samples 338-C0022B-5H-6, 32 cm, and 338-C0022B-21X-5, 40 cm. Steps are in mT for AF demagnetization. Solid squares = projection onto the horizontal plane, open squares = projection onto the vertical plane.

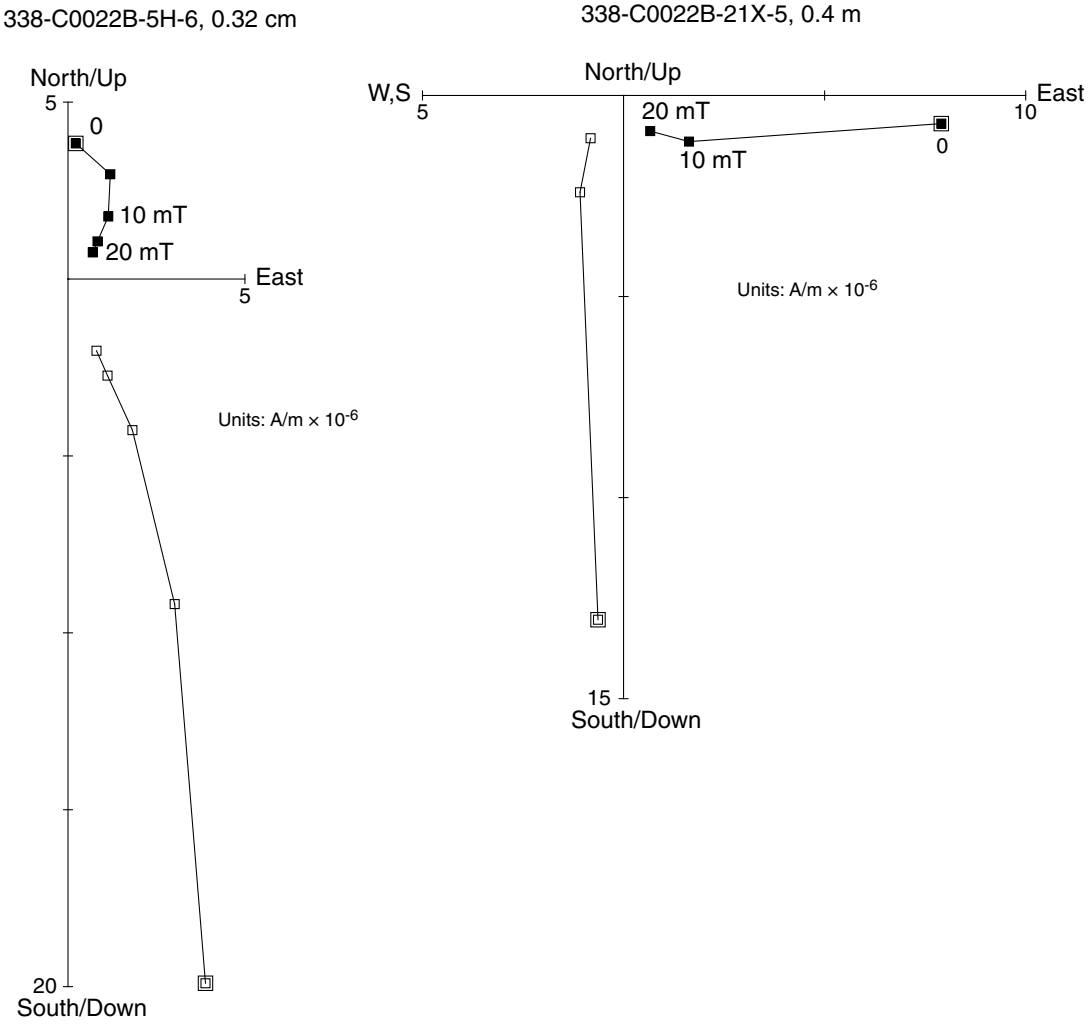

Figure F44. Inclinations after 20 mT AF demagnetization of Holes C0022B and inclinations after 40 mT AF demagnetization of Holes C0004C, C0004D, C0008A, and C0008D from Expedition 316 Scientists (2009a, 2009b). Black areas = normal polarity, white areas = reversed polarity, hatched area = mixed polarity, gray areas = no data available.

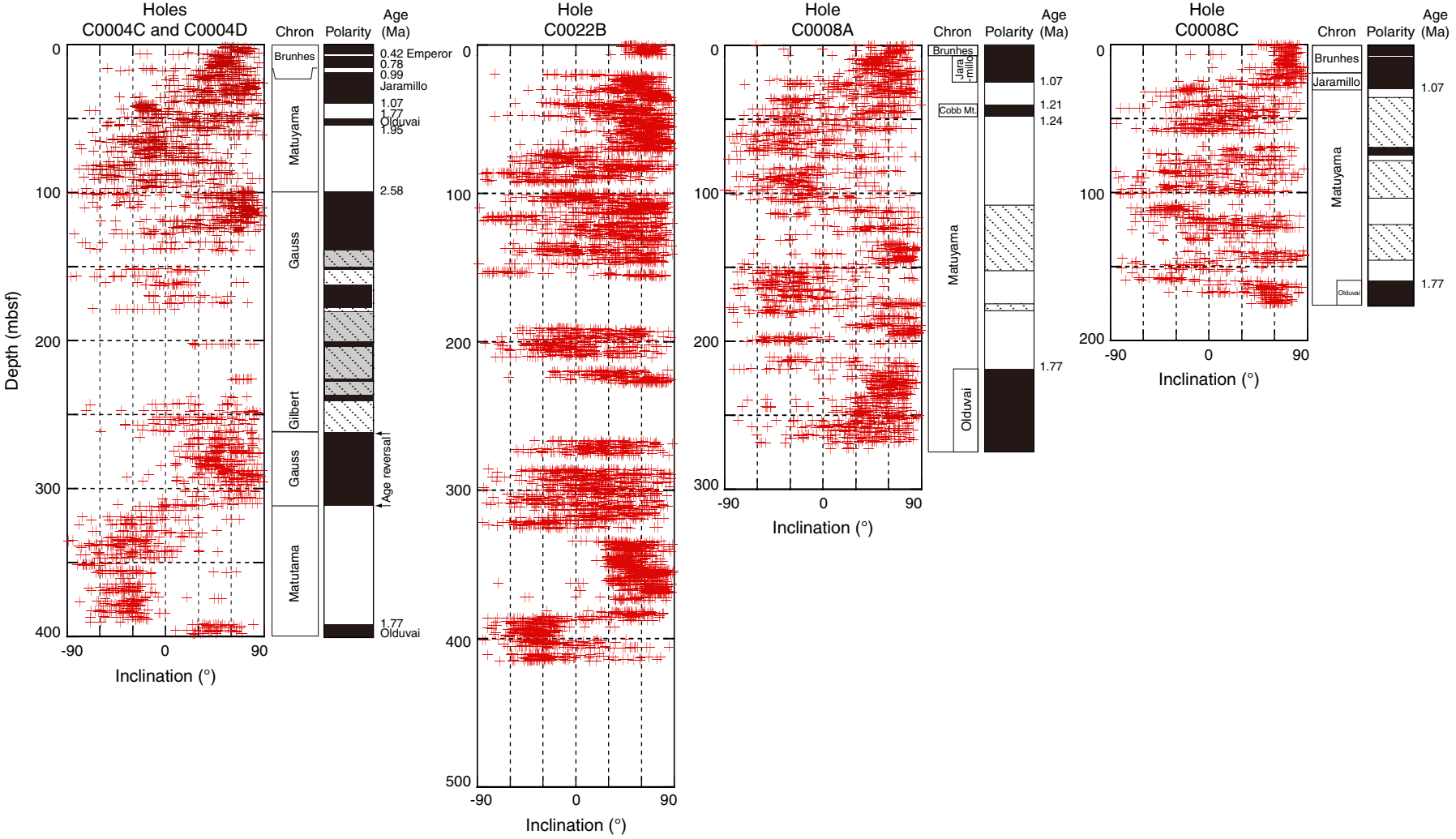

Figure F45. Core-log-seismic integration, Site C0022. LWD data from Hole C0022A, seismic data from In-line 2675 of the Kumano 3-D PSDM volume (Moore et al., 2009), core lithology from Hole C0022B (see "Lithology"), and tadpole plot of fracture dip angles and directions measured from resistivity images. Dashed black and dotted lines show correlations (? = tentative) between the different data sets. Shaded box highlights the fault zone (FZ) and wider deformation zone, as identified from fractures in resistivity images.

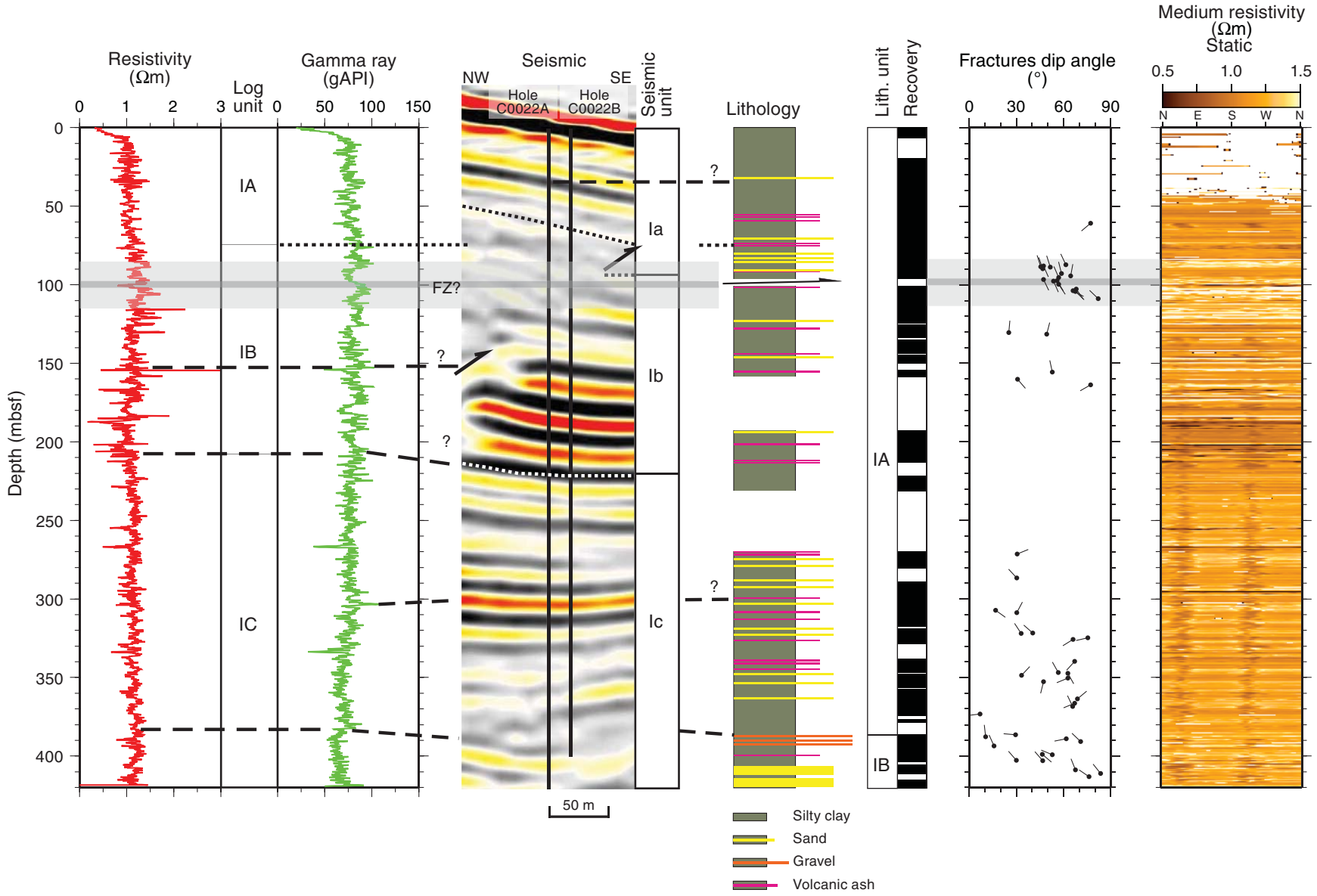

Table T1. Lithologic subunits defined in Hole C0022B.

Subunit	Core, section, interval (cm) Top	Core, section, interval (cm) Bottom	Depth (mbsf) Top	Depth (mbsf) Bottom	Thickness (m)	Stratigraphic age	Lithologic description	Process of formation	Interpretation
IA	338-C0022B-1H-1, 0	338-C0022B-38X-2, 56	0.00	383.47	383.47		Silty clay with depth-diminishing carbonate content, thin sand layers, and volcanic ash layers	Hemipelagic settling, thin-bedded turbidites, and volcanic ash fall	Slope-basin succession
IB	38X-2, 56	41X-CC, 39	383.47	415.90	32.44		Carbonate-poor silty clay, mud clast gravel layers, and significant amounts of clayey silt and fine to coarse sand	Hemipelagic settling, medium-bedded turbidites, and mass-wasting	Early stage of slope-basin fill

Table T2. Hole C0022B core depths and lengths.

Core	Depth (mbsf) Top	Depth (mbsf) Bottom	Core initial length (m)
338-C0022B-			
1H	0.00	7.01	7.01
2H	19.50	29.66	9.93
3H	29.00	39.45	10.15
4H	38.50	48.54	9.98
5H	48.00	58.29	10.23
6H	57.50	67.66	10.13
7H	67.00	77.44	10.39
8H	76.50	85.43	8.80
9T	84.50	89.92	5.40
10T	89.50	94.97	5.43
11T	94.50	95.56	1.08
12X	99.50	107.23	7.72
13X	104.50	111.60	7.04
14X	109.50	118.92	9.39
15X	114.50	123.62	9.14
16X	124.00	132.40	8.41
17X	133.50	142.72	9.19
18X	143.00	148.46	5.45
19X	152.50	156.84	4.60
20X	190.50	200.27	9.81
21X	200.00	209.33	9.47
22X	209.50	211.20	1.70
23X	219.00	229.14	10.13
24X	266.50	275.90	9.39
25X	276.00	277.12	1.13
26X	285.50	292.08	6.45
27X	290.50	295.59	5.09
28X	295.50	301.29	5.67
29X	300.50	305.45	4.93
30X	305.50	314.26	8.72
31X	315.00	324.98	9.98
32X	324.50	326.34	1.84
33X	334.00	343.01	9.14
34X	343.50	352.53	8.99
35X	353.00	363.28	10.48
36X	362.50	370.23	7.71
37X	372.00	374.70	2.65
38X	381.50	391.49	9.94
39X	391.00	399.23	8.21
40X	400.50	406.86	6.35
41X	410.00	415.90	5.90

Table T3. X-ray diffraction analysis results, Hole C0022B. (Continued on next page.)

Core, section, interval (cm)	Sample	Midpoint depth (mbsf)	Integrated peak area (total counts)				Absolute mineral abundance calculated from SVD normalization factors (wt%)					Relative abundance (wt%)			
			Total clay minerals	Quartz	Feldspar	Calcite	Total clay minerals	Quartz	Feldspar	Calcite	Sum	Total clay minerals	Quartz	Feldspar	Calcite
338-C0022B-															
1H-1, 120–124	CKY-1584910	1.22	2,323	25,773	11,612	19,501	32.0	13.8	11.6	23.2	80.7	39.7	17.1	14.4	28.8
1H-5, 117–120	CKY-1566510	5.55	1,780	26,821	9,927	22,883	25.4	14.6	9.85	28.6	78.5	32.4	18.6	12.6	36.5
1H-6, 20–23	CKY-1567410	5.99	2,329	32,512	13,226	14,627	32.5	17.7	13.3	16.2	79.7	40.8	22.2	16.7	20.4
2H-5, 9–12	CKY-1585710	23.21	2,082	28,544	16,217	11,163	31.1	15.2	16.9	11.7	74.8	41.6	20.3	22.5	15.6
2H-9, 51–53	CKY-1569610	28.60	2,053	29,500	12,997	19,696	29.7	15.9	13.2	23.7	82.5	36.0	19.3	16.0	28.7
3H-3, 0–3	CKY-1594010	30.34	2,760	39,999	14,952	10,203	37.8	21.9	15.0	9.33	83.9	45.0	26.1	17.8	11.1
3H-7, 69–71	CKY-1577910	35.92	2,500	35,208	12,192	12,201	33.7	19.3	12.0	12.6	77.7	43.4	24.8	15.5	16.3
3H-9, 54–56.5	CKY-1578910	38.20	2,637	36,368	13,006	8,386	35.4	19.9	12.9	7.12	75.3	47.0	26.4	17.1	9.45
3H-CC, 0–3	CKY-1580110	38.22	2,488	37,582	13,286	8,238	33.9	20.6	13.2	7.05	74.8	45.3	27.6	17.7	9.43
4H-3, 0–3	CKY-1600410	39.66	2,162	44,129	13,936	7,644	30.5	24.5	13.9	6.43	75.3	40.5	32.5	18.5	8.54
4H-7, 52–54	CKY-1584010	45.09	3,036	33,365	10,798	8,927	38.8	18.2	10.4	7.56	74.9	51.8	24.3	13.9	10.1
5H-1, 34–36	CKY-1595910	48.32	2,174	29,450	11,170	16,932	30.0	16.0	11.1	19.8	76.9	39.0	20.8	14.4	25.7
5H-1, 125–128	CKY-1609510	49.17	2,452	24,703	9,777	21,451	32.7	13.3	9.55	25.9	81.3	40.2	16.3	11.7	31.8
5H-5, 101–103	CKY-1595110	52.82	3,208	38,702	14,169	3,413	41.9	21.1	14.0	–0.56	76.5	54.8	27.6	18.3	T
5H-9, 48–51.5	CKY-1599010	57.16	2,348	33,862	12,955	8,221	32.2	18.5	13.0	7.29	71.0	45.4	26.0	18.3	10.3
6H-1, 53–55	CKY-1601210	58.01	2,483	31,740	12,064	16,018	33.7	17.2	12.0	18.0	81.0	41.7	21.3	14.8	22.3
6H-3, 20–23	CKY-1602010	58.89	2,349	36,294	13,209	10,122	32.4	19.9	13.2	9.86	75.4	43.0	26.4	17.5	13.1
6H-5, 128–130	CKY-1602810	62.52	3,211	32,807	15,127	11,122	43.0	17.5	15.2	10.2	85.9	50.0	20.4	17.7	11.9
6H-8, 85–87	CKY-1619810	66.05	2,321	29,092	12,511	17,086	32.3	15.7	12.6	19.8	80.3	40.2	19.5	15.7	24.6
7H-2, 54–57	CKY-1606310	67.73	2,879	35,231	15,203	4,647	39.0	19.0	15.3	1.58	74.9	52.0	25.4	20.5	2.11
7H-4, 116–118	CKY-1620410	70.85	2,973	33,703	11,239	7,570	38.2	18.4	10.9	5.72	73.2	52.2	25.1	14.9	7.81
7H-8, 0–3	CKY-1621010	73.54	2,387	44,205	16,678	2,983	34.0	24.3	16.9	–0.42	74.9	45.5	32.5	22.6	T
8H-1, 20–25	CKY-1629810	76.70	3,207	33,942	11,935	10,198	41.3	18.4	11.6	9.06	80.3	51.4	22.9	14.4	11.3
8H-5, 100–104	CKY-1627110	80.35	2,715	36,635	15,069	9,547	37.3	19.9	15.2	8.54	80.9	46.1	24.6	18.8	10.6
8H-CC, 17–19	CKY-1612510	84.35	3,116	41,296	15,305	1,968	41.4	22.6	15.3	–2.57	76.6	54.0	29.5	19.9	T
9T-3, 0–5	CKY-1629110	85.01	2,193	49,002	24,827	907	35.7	26.6	26.0	–3.52	84.9	42.1	31.4	30.7	T
9T-5, 77–81	CKY-1630610	88.31	2,379	32,295	11,765	13,099	32.3	17.6	11.7	14.1	75.7	42.7	23.3	15.4	18.7
10T-3, 0–3	CKY-1640210	90.47	2,386	41,834	17,514	7,580	34.7	22.8	17.9	5.98	81.5	42.6	28.0	22.0	7.34
12X-2, 10–14	CKY-1643210	100.49	3,504	31,675	10,229	11,847	43.8	17.2	9.62	11.1	81.7	53.6	21.0	11.8	13.6
12X-5, 135–139	CKY-1644410	103.40	2,768	37,206	14,386	8,111	37.5	20.3	14.4	6.50	78.7	47.7	25.8	18.3	8.27
13X-1, 26–29	CKY-1659210	104.69	2,832	38,677	12,822	7,713	37.4	21.2	12.6	5.91	77.1	48.5	27.5	16.3	7.66
13X-6, 30–33	CKY-1660110	108.93	2,032	52,794	21,401	2,639	32.3	29.1	22.1	–0.87	82.7	39.1	35.2	26.8	T
14X-1, 67–69	CKY-1646710	109.86	2,938	40,361	14,138	3,559	38.9	22.1	14.0	–0.08	75.0	51.9	29.5	18.7	T
14X-1, 110–112	CKY-1647610	110.09	2,582	43,583	17,765	2,255	36.7	23.8	18.1	–1.69	77.0	47.7	31.0	23.5	T
14X-2, 54–57	CKY-1648810	110.43	591	27,423	11,942	3,116	12.2	15.2	12.6	2.49	42.4	28.8	35.8	29.6	5.87
14X-2, 113–115	CKY-1649810	110.74	2,971	38,450	15,834	2,069	40.1	20.9	16.0	–2.21	74.7	53.7	28.0	21.4	T
14X-3, 30–32	CKY-1650910	111.04	1,618	38,374	14,962	3,357	24.8	21.2	15.4	1.22	62.6	39.7	33.8	24.6	1.95
14X-3, 92–94	CKY-1653310	111.37	2,093	38,307	17,120	3,934	31.2	20.9	17.7	1.37	71.1	43.9	29.4	24.9	1.93
14X-3, 109–110	CKY-1652110	111.46	1,162	25,368	10,078	1,754	17.5	14.0	10.4	0.04	41.9	41.8	33.4	24.7	0.10
14X-4, 15–18	CKY-1654210	111.71	2,073	15,688	15,839	4,859	30.7	7.65	16.8	3.26	58.4	52.6	13.1	28.8	5.58
14X-4, 90–93	CKY-1664710	112.11	3,346	38,458	14,626	3,526	43.7	20.9	14.5	–0.58	78.5	55.7	26.6	18.5	T
14X-5, 54–56	CKY-1656210	112.67	2,695	43,168	13,907	2,958	36.1	23.9	13.8	–0.68	73.0	49.4	32.7	18.8	T
14X-8, 0–2	CKY-1657110	114.08	1,409	47,514	20,180	1,900	24.9	26.2	21.1	–0.98	71.2	35.0	36.8	29.6	T
15X-4, 0–5	CKY-1672510	118.82	2,547	25,652	12,228	9,530	34.2	13.7	12.3	9.09	69.3	49.4	19.7	17.8	13.1
16X-5, 0–5	CKY-1676810	127.75	2,134	28,353	11,997	7,825	29.4	15.4	12.1	7.16	64.1	46.0	24.0	18.9	11.2
17X-1, 68–72	CKY-1666510	134.20	2,029	28,141	13,845	10,291	29.3	15.1	14.2	10.6	69.3	42.3	21.8	20.5	15.4
17X-1, 115–120	CKY-1684110	134.68	2,140	29,956	14,369	10,623	30.8	16.1	14.7	10.9	72.6	42.5	22.2	20.3	15.0

Table T3 (continued).

Core, section, interval (cm)	Sample	Midpoint depth (mbsf)	Integrated peak area (total counts)				Absolute mineral abundance calculated from SVD normalization factors (wt%)					Relative abundance (wt%)			
			Total clay minerals	Quartz	Feldspar	Calcite	Total clay minerals	Quartz	Feldspar	Calcite	Sum	Total clay minerals	Quartz	Feldspar	Calcite
18X-3, 66–69	CKY-1691010	145.47	2,907	34,931	14,497	3,093	38.8	18.9	14.6	–0.58	71.7	54.1	26.4	20.3	T
19X-1, 76–80.5	CKY-1693410	153.28	2,770	34,957	15,790	3,525	38.0	18.9	16.1	0.13	73.0	52.0	25.8	22.0	0.18
20X-5, 3–6	CKY-1696510	193.82	3,018	34,723	15,989	5,338	40.9	18.7	16.2	2.35	78.1	52.4	23.9	20.7	3.01
20X-8, 34–37	CKY-1668210	197.15	2,820	30,598	14,957	5,332	38.3	16.3	15.2	2.72	72.5	52.8	22.5	21.0	3.74
20X-10, 8–10	CKY-1669010	198.74	2,338	26,382	13,889	13,001	32.9	14.0	14.2	14.1	75.2	43.8	18.6	18.9	18.7
21X-5, 85–89	CKY-1675510	204.20	2,437	31,272	15,322	10,823	34.5	16.8	15.7	10.8	77.7	44.4	21.6	20.2	13.8
21X-7, 133–137	CKY-1703410	205.88	2,514	42,106	15,786	6,179	35.2	23.1	15.9	3.95	78.2	45.0	29.6	20.4	5.05
22X-1, 118–123	CKY-1708510	210.71	2,926	44,886	16,856	4,615	40.1	24.6	17.0	1.18	82.9	48.4	29.7	20.5	1.43
23X-5, 0–5	CKY-1709810	221.47	2,091	29,212	17,087	3,322	31.2	15.5	17.9	0.74	65.3	47.8	23.8	27.3	1.13
23X-5, 61–63	CKY-1680210	222.02	2,065	30,151	15,302	5,240	30.1	16.2	15.8	3.48	65.6	45.9	24.7	24.1	5.30
23X-7, 44–47.5	CKY-1681110	224.46	1,543	20,097	9,968	9,274	22.1	10.8	10.2	10.2	53.3	41.6	20.2	19.2	19.1
24X-4, 7–11	CKY-1717110	269.20	2,242	34,507	14,802	6,250	31.8	18.8	15.1	4.59	70.3	45.3	26.7	21.5	6.53
24X-7, 13–16	CKY-1686510	273.41	1,426	40,289	29,917	2,570	30.0	21.3	32.2	–0.31	83.2	36.1	25.6	38.7	T
25X-1, 74–78	CKY-1689010	276.76	2,753	35,010	16,738	3,546	38.3	18.8	17.1	0.14	74.3	51.5	25.3	23.0	0.19
26X-2, 136–140	CKY-1724910	287.59	2,896	33,589	16,009	4,846	39.6	18.0	16.3	1.84	75.7	52.3	23.8	21.5	2.43
27X-5, 2–6	CKY-1727110	294.62	3,100	36,050	17,433	5,067	42.5	19.3	17.8	1.79	81.4	52.2	23.7	21.8	2.20
27X-5, 63.5–68	CKY-1692210	295.23	1,903	32,389	23,038	3,565	32.0	17.0	24.5	0.98	74.5	43.0	22.8	32.9	1.31
28X-4, 2–5	CKY-1730710	297.60	2,900	31,541	15,595	3,796	39.4	16.8	15.9	0.44	72.5	54.3	23.2	21.9	0.61
29X-1, 74–77	CKY-1736910	301.26	2,645	38,045	20,840	2,780	39.0	20.3	21.7	–1.03	80.0	48.8	25.4	27.1	T
30X-1, 98.5–103	CKY-1714310	306.51	2,516	29,906	20,927	4,626	37.9	15.6	22.0	1.87	77.3	49.0	20.1	28.5	2.41
30X-4, 2–5	CKY-1741710	307.72	3,391	35,536	19,451	3,199	46.6	18.8	20.0	–1.22	84.2	55.4	22.4	23.7	T
30X-6, 6–10.5	CKY-1715110	310.59	3,056	35,207	18,116	1,967	42.2	18.8	18.6	–2.47	77.1	54.7	24.4	24.1	T
31X-1, 74–77	CKY-1744910	315.72	2,748	36,619	18,848	5,350	39.3	19.6	19.4	2.52	80.9	48.6	24.3	24.0	3.12
31X-6, 106–111	CKY-1718610	321.18	2,860	39,417	17,981	1,593	39.9	21.3	18.4	–2.85	76.7	52.0	27.8	24.0	T
31X-7, 8–12	CKY-1720110	321.57	2,852	32,840	15,582	1,305	38.7	17.6	15.9	–2.99	69.2	55.9	25.5	22.9	T
33X-2, 26.5–27.5	CKY-1739210	335.68	1,957	32,467	26,986	3,086	34.6	16.8	28.9	0.08	80.3	43.0	20.9	36.0	0.10
33X-8, 0–4	CKY-1753710	342.21	2,656	27,738	17,220	4,743	37.6	14.5	17.9	2.07	72.1	52.2	20.2	24.8	2.87
34X-2, 38–40.5	CKY-1740210	345.20	2,234	33,945	20,668	4,616	34.6	18.0	21.7	2.10	76.4	45.2	23.6	28.4	2.75
34X-5, 98.5–105	CKY-1741010	348.18	2,727	33,357	17,323	2,208	38.2	17.8	17.8	–1.67	72.2	52.9	24.7	24.7	T
35X-6, 0–5	CKY-1764910	357.94	1,973	29,322	20,154	2,966	31.4	15.4	21.3	0.25	68.4	45.9	22.5	31.2	0.37
35X-6, 88–90	CKY-1755810	358.74	2,014	28,325	25,553	2,197	34.5	14.4	27.4	–1.06	75.3	45.8	19.2	36.4	T
35X-7, 124–127	CKY-1756910	359.91	1,320	30,198	29,389	3,181	28.8	15.4	31.9	0.92	77.0	37.4	20.0	41.4	1.20
35X-8, 10–13.5	CKY-1757810	360.03	2,492	31,259	21,420	1,332	37.6	16.4	22.6	–2.73	73.8	51.0	22.2	30.6	T
35X-9, 9.5–11.5	CKY-1759110	360.76	2,173	27,133	18,812	2,736	33.0	14.2	19.8	–0.20	66.8	49.4	21.2	29.7	T
36X-2, 89–95	CKY-1768810	364.22	1,701	23,769	22,333	2,748	29.6	12.0	24.0	0.31	65.9	44.9	18.3	36.4	0.48
36X-6, 0–8	CKY-1762710	367.51	1,854	35,439	30,829	5,157	35.4	18.2	33.2	2.85	89.7	39.5	20.3	37.0	3.18
37X-3, 15–20	CKY-1775710	373.48	2,587	32,683	21,273	3,806	38.7	17.2	22.3	0.57	78.8	49.2	21.8	28.3	0.72
38X-1, 107–111	CKY-1765810	382.54	2,060	31,339	22,822	3,698	33.7	16.4	24.3	1.01	75.3	44.7	21.7	32.2	1.34
38X-4, 5–10	CKY-1778310	384.83	2,155	23,138	17,113	3,553	32.0	11.9	18.0	1.12	63.1	50.8	18.9	28.5	1.78
38X-6, 126.5–130.5	CKY-1766710	388.67	2,901	28,219	21,689	2,238	42.4	14.5	22.8	–1.90	77.7	54.5	18.6	29.4	T
38X-8, 17–21	CKY-1767910	389.52	2,186	26,391	18,920	3,992	33.2	13.7	20.0	1.54	68.4	48.6	20.0	29.1	2.26
39X-3, 1–5	CKY-1780510	392.85	2,513	31,175	19,411	3,960	37.0	16.4	20.3	0.98	74.7	49.6	22.0	27.2	1.31
39X-5, 101–104	CKY-1771810	396.66	1,728	33,736	29,692	1,646	33.3	17.4	32.0	–1.79	80.9	41.1	21.5	39.6	T
40X-1, 108.5–111.5	CKY-1772710	401.60	1,890	30,979	27,482	3,522	34.1	15.9	29.5	0.78	80.3	42.5	19.8	36.8	0.97
40X-4, 5–10	CKY-1782110	403.79	2,408	29,365	21,362	4,558	36.9	15.2	22.6	1.90	76.6	48.2	19.9	29.5	2.48
41X-2, 14–19	CKY-1783810	411.32	1,959	27,130	25,899	2,875	34.1	13.7	27.8	–0.04	75.6	45.1	18.1	36.8	T
41X-5, 80–82	CKY-1773610	415.33	1,810	30,751	25,318	2,943	32.1	15.9	27.1	0.17	75.3	42.7	21.1	36.0	0.22

Samples were taken from the working half or from whole-round samples of each core section. SVD = singular value decomposition. T = trace.

Table T4. Results of XRF analysis, Hole C0022B. (Continued on next page.)

Core, section, interval (cm)	Sample	Midpoint depth (mbsf)	Na_2O (wt%)	MgO (wt%)	Al_2O_3 (wt%)	SiO_2 (wt%)	P_2O_5 (wt%)	K_2O (wt%)	CaO (wt%)	TiO_2 (wt%)	MnO (wt%)	Fe_2O_3 (wt%)	Loss on ignition (wt%)
338-C0022B-													
1H-1, 120–124	CKY-1584810	1.20	2.97	2.32	14.1	57.8	0.11	2.32	12.9	0.58	0.06	5.05	14.1
1H-5, 117–120	CKY-1566610	5.53	2.75	1.99	13.5	55.8	0.12	2.37	15.4	0.55	0.07	4.78	14.1
1H-6, 20–23	CKY-1567510	5.97	2.95	2.15	14.2	60.1	0.11	2.85	9.06	0.59	0.07	5.02	10.2
2H-5, 9–12	CKY-1585810	23.19	3.17	1.85	14.7	62.3	0.10	2.97	7.18	0.57	0.06	4.52	8.88
2H-9, 51–53	CKY-1569710	28.59	2.80	2.13	13.9	57.9	0.11	2.54	12.9	0.61	0.06	4.90	12.8
3H-3, 0–3	CKY-1594110	30.32	2.96	2.14	14.2	63.3	0.09	2.99	6.23	0.60	0.06	5.38	8.20
3H-7, 69–71	CKY-1578010	35.91	2.69	2.36	15.1	60.9	0.11	2.94	7.67	0.65	0.06	5.30	9.29
3H-9, 54–56.5	CKY-1579010	38.19	2.91	2.21	15.3	63.1	0.10	3.11	5.12	0.62	0.06	5.13	7.65
3H-CC, 0–3	CKY-1580210	38.21	2.76	2.23	15.3	63.1	0.10	3.08	5.30	0.64	0.06	5.09	8.09
4H-3, 0–3	CKY-1600510	39.65	2.72	2.21	15.2	64.8	0.08	3.01	4.59	0.68	0.06	5.17	7.46
4H-7, 52–54	CKY-1584110	45.08	2.91	2.40	15.4	61.3	0.09	3.06	5.75	0.64	0.07	6.37	8.42
5H-1, 34–36	CKY-1596010	48.31	2.45	2.30	14.6	57.3	0.12	2.83	11.7	0.62	0.07	5.33	11.4
5H-1, 125–128	CKY-1609610	49.15	2.70	2.34	14.3	55.2	0.14	2.37	14.2	0.60	0.07	5.40	13.0
5H-5, 101–103	CKY-1595210	52.81	2.90	2.39	16.5	64.1	0.09	3.28	2.33	0.71	0.06	5.68	6.27
5H-9, 48–51.5	CKY-1599110	57.15	3.00	2.55	16.3	61.8	0.10	3.05	5.07	0.69	0.07	5.58	7.93
6H-1, 53–55	CKY-1601310	58.00	2.57	2.28	14.5	58.4	0.12	2.71	10.8	0.63	0.07	5.33	11.3
6H-3, 20–23	CKY-1602110	58.88	2.86	2.21	14.9	62.3	0.11	2.81	6.82	0.65	0.07	5.36	8.11
6H-5, 128–130	CKY-1602910	62.51	2.85	2.36	15.5	61.1	0.12	2.99	6.78	0.65	0.06	5.42	9.09
6H-8, 85–87	CKY-1619910	66.04	2.57	2.10	13.9	58.2	0.12	2.59	12.0	0.57	0.07	5.01	11.4
7H-2, 54–57	CKY-1606410	67.72	2.95	2.43	16.3	63.0	0.11	3.10	3.47	0.71	0.06	5.62	7.10
7H-4, 116–118	CKY-1620510	70.84	2.87	2.41	15.8	62.3	0.11	3.13	4.58	0.69	0.07	6.06	7.44
7H-8, 0–3	CKY-1621110	73.52	2.96	1.98	15.2	66.9	0.10	2.96	2.38	0.63	0.07	5.44	5.39
8H-1, 20–25	CKY-1629910	76.68	2.80	2.21	16.0	61.9	0.11	2.99	6.51	0.67	0.08	5.19	8.93
8H-5, 100–104	CKY-1627210	80.33	2.69	2.07	15.6	62.7	0.11	2.88	6.06	0.68	0.09	5.47	8.66
8H-CC, 17–19	CKY-1612610	84.34	2.80	2.20	16.6	65.8	0.09	3.15	1.55	0.69	0.06	5.58	5.94
9T-3, 0–5	CKY-1629210	84.99	2.87	1.75	14.9	67.9	0.07	2.82	1.46	0.66	0.07	5.53	4.67
9T-5, 77–81	CKY-1630710	88.29	2.68	2.08	15.5	60.8	0.13	2.88	8.16	0.63	0.08	5.14	10.1
10T-3, 0–3	CKY-1651010	90.46	3.04	1.89	14.7	65.3	0.09	2.79	4.51	0.62	0.08	4.99	7.55
10T-5, 100–103	CKY-1653410	93.94	2.74	1.73	15.4	67.5	0.08	2.96	2.55	0.64	0.09	4.87	5.00
11T-1, 81–84	CKY-1652210	95.31	2.78	2.21	17.6	64.2	0.09	3.25	1.97	0.73	0.06	5.78	5.00
12X-2, 10–14	CKY-1654310	100.47	2.96	2.06	15.8	60.6	0.13	2.83	7.61	0.64	0.08	5.55	9.75
12X-5, 135–139	CKY-1664810	103.39	2.80	2.07	15.7	63.5	0.09	2.93	5.09	0.64	0.08	5.68	8.61
13X-1, 26–29	CKY-1656310	104.68	2.95	2.14	15.9	64.4	0.10	2.94	4.44	0.66	0.07	5.62	7.99
13X-6, 30–33	CKY-1657210	108.92	2.67	1.89	16.0	67.3	0.08	3.11	1.69	0.66	0.08	5.26	5.26
14X-1, 67–69	CKY-1672610	109.86	2.77	2.02	16.9	65.5	0.07	3.20	1.73	0.68	0.08	5.37	5.98
14X-1, 110–112	CKY-1676910	110.08	2.73	2.22	16.5	65.2	0.10	3.13	1.74	0.69	0.08	5.49	5.51
14X-2, 54–57	CKY-1666610	110.42	2.75	1.89	15.6	67.4	0.09	3.05	2.60	0.63	0.08	5.01	6.22
14X-2, 113–115	CKY-1684210	110.74	2.74	2.01	17.0	65.4	0.08	3.20	1.52	0.69	0.07	5.39	5.84
14X-3, 30–32	CKY-1691110	111.04	2.75	1.71	15.7	67.8	0.08	3.15	2.48	0.62	0.08	4.91	6.17
14X-3, 92–94	CKY-1643310	111.37	2.84	1.72	15.6	67.0	0.08	3.13	2.55	0.62	0.09	4.98	6.48
14X-3, 109–110	CKY-1693510	111.46	2.89	1.79	16.4	66.0	0.08	3.24	1.67	0.63	0.07	4.97	5.90
14X-4, 15–18	CKY-1696610	111.70	3.57	2.07	15.4	64.4	0.14	2.48	4.27	0.60	0.10	5.28	6.75
14X-4, 90–93	CKY-1668110	112.10	2.81	2.28	17.1	63.9	0.09	3.20	1.78	0.71	0.08	5.77	6.46
14X-5, 54–56	CKY-1668910	112.66	2.59	2.00	16.6	65.2	0.09	3.17	2.17	0.71	0.09	5.50	6.43
14X-8, 0–2	CKY-1675610	114.07	2.67	1.92	15.9	67.2	0.08	2.97	1.67	0.67	0.08	5.17	5.24
15X-4, 0–5	CKY-1703510	118.79	3.12	1.99	15.3	62.5	0.11	2.88	6.39	0.59	0.08	5.39	8.66
16X-5, 0–5	CKY-1708610	127.72	3.01	1.89	15.6	63.5	0.09	2.79	5.45	0.63	0.08	5.06	8.18
17X-1, 68–72	CKY-1709910	134.18	3.01	2.09	15.4	61.9	0.12	2.77	7.30	0.64	0.07	5.30	9.17
17X-1, 115–120	CKY-1680310	134.65	2.80	2.04	15.3	61.6	0.13	2.93	7.26	0.63	0.08	5.25	9.50

Table T4 (continued).

Core, section, interval (cm)	Sample	Midpoint depth (mbsf)	Na_2O (wt%)	MgO (wt%)	Al_2O_3 (wt%)	SiO_2 (wt%)	P_2O_5 (wt%)	K_2O (wt%)	CaO (wt%)	TiO_2 (wt%)	MnO (wt%)	Fe_2O_3 (wt%)	Loss on ignition (wt%)
18X-3, 66–69	CKY-1681210	145.45	2.88	2.26	16.5	64.2	0.10	3.23	1.91	0.71	0.06	6.10	6.26
19X-1, 76–80.5	CKY-1717210	153.26	3.07	2.17	16.6	65.3	0.09	3.08	2.38	0.67	0.07	5.69	6.52
20X-5, 3–6	CKY-1686610	193.81	2.78	2.43	16.2	62.6	0.10	2.98	3.39	0.67	0.09	6.62	7.60
20X-8, 34–37	CKY-1689110	197.14	3.10	2.44	16.1	62.7	0.13	2.86	3.66	0.68	0.10	6.43	7.36
20X-10, 8–10	CKY-1692310	198.73	2.89	2.07	15.0	59.5	0.18	2.61	9.03	0.62	0.09	5.50	10.6
21X-5, 85–89	CKY-1714410	204.18	2.82	2.26	15.7	62.1	0.14	2.97	6.34	0.65	0.07	5.33	8.87
21X-7, 133–137	CKY-1715210	205.86	2.90	2.11	15.2	65.2	0.10	3.03	4.13	0.64	0.08	5.22	7.39
22X-1, 118–123	CKY-1718710	210.68	2.68	1.84	15.3	67.1	0.09	3.16	2.74	0.62	0.08	4.89	6.02
23X-5, 0–5	CKY-1720210	221.44	3.13	2.34	16.1	64.1	0.10	2.79	2.67	0.64	0.08	5.88	6.07
23X-5, 61–63	CKY-1753810	222.01	3.12	2.36	16.2	63.5	0.10	2.79	4.01	0.68	0.10	5.88	7.26
23X-7, 44–47.5	CKY-1740310	224.44	2.94	2.11	14.9	59.4	0.19	2.56	7.78	0.62	0.09	6.38	8.09
24X-4, 7–11	CKY-1739310	269.18	2.84	2.37	15.5	63.2	0.13	2.85	4.30	0.66	0.09	6.34	7.75
24X-7, 13–16	CKY-1744810	273.39	3.23	1.87	14.7	66.3	0.10	2.33	3.13	0.55	0.06	5.17	4.05
25X-1, 74–78	CKY-1737010	276.74	2.90	2.46	16.0	64.2	0.12	2.90	2.50	0.69	0.08	6.56	6.34
26X-2, 136–140	CKY-1730810	287.58	3.09	2.20	15.4	64.7	0.11	2.70	3.79	0.65	0.08	5.67	6.65
27X-5, 2–6	CKY-1727210	294.60	2.89	2.33	15.8	63.6	0.19	2.88	4.15	0.68	0.08	5.87	7.01
27X-5, 63.5–68	CKY-1725010	295.21	3.16	2.36	16.2	64.6	0.12	2.52	3.29	0.66	0.08	5.95	5.61
28X-4, 2–5	CKY-1762810	297.59	2.93	2.51	16.4	63.6	0.11	2.81	3.11	0.67	0.09	6.14	6.41
29X-1, 74–77	CKY-1644510	301.24	3.15	2.22	16.2	65.5	0.11	2.77	2.89	0.68	0.09	5.56	5.41
30X-1, 98.5–103	CKY-1759210	306.49	3.18	2.29	16.2	64.2	0.13	2.55	3.88	0.66	0.09	5.94	6.11
30X-4, 2–5	CKY-1768910	307.70	3.03	2.25	16.2	64.5	0.11	2.77	2.62	0.69	0.07	5.91	5.36
30X-6, 6–10.5	CKY-1765010	310.57	2.95	2.49	16.6	63.9	0.11	2.88	2.16	0.71	0.07	6.28	5.42
31X-1, 74–77	CKY-1741110	315.71	2.86	2.28	15.6	63.6	0.18	2.70	4.37	0.67	0.08	6.01	6.35
31X-6, 106–111	CKY-1775810	321.15	2.77	2.45	16.4	65.0	0.10	3.03	1.69	0.70	0.09	6.11	5.14
31X-7, 8–12	CKY-1755910	321.55	2.88	2.60	16.9	62.9	0.11	2.93	1.85	0.72	0.10	6.60	5.56
33X-2, 26.5–27.5	CKY-1757010	335.67	3.23	2.27	16.0	63.9	0.12	2.38	3.62	0.66	0.09	5.80	5.29
33X-8, 0–4	CKY-1640310	342.19	3.02	2.35	16.2	63.1	0.12	2.54	4.17	0.67	0.08	5.94	6.58
34X-2, 38–40.5	CKY-1659310	345.19	2.99	2.24	16.0	64.9	0.11	2.70	3.51	0.66	0.08	5.48	5.87
34X-5, 98.5–105	CKY-1660210	348.15	2.95	2.33	16.2	64.2	0.11	2.65	2.25	0.71	0.07	6.36	4.79
35X-6, 0–5	CKY-1646810	357.92	3.00	2.34	16.4	64.0	0.12	2.52	3.48	0.68	0.08	5.98	5.32
35X-6, 88–90	CKY-1647710	358.73	3.15	2.20	16.0	63.8	0.12	2.46	3.31	0.65	0.08	6.30	5.11
35X-7, 124–127	CKY-1648910	359.89	3.11	2.19	15.9	63.9	0.13	2.27	4.22	0.63	0.09	5.37	4.45
35X-8, 10–13.5	CKY-1649910	360.01	3.15	2.40	16.4	64.1	0.12	2.67	2.43	0.68	0.08	6.35	5.13
35X-9, 9.5–11.5	CKY-1757910	360.75	3.13	2.41	16.5	64.0	0.13	2.53	3.44	0.67	0.08	6.23	5.32
36X-2, 89–95	CKY-1741810	364.19	3.22	2.38	16.5	64.1	0.12	2.24	4.13	0.64	0.09	5.87	5.01
36X-6, 0–8	CKY-1765910	367.47	3.02	2.09	15.2	64.4	0.10	2.23	5.32	0.61	0.08	5.33	7.81
37X-3, 15–20	CKY-1778410	373.46	3.20	2.42	16.1	63.3	0.11	2.60	3.65	0.71	0.08	6.11	6.25
38X-1, 107–111	CKY-1766810	382.52	3.09	2.36	15.9	63.5	0.11	2.40	3.80	0.65	0.08	6.01	5.39
38X-4, 5–10	CKY-1768010	384.81	3.12	2.27	16.1	63.6	0.12	2.48	3.63	0.66	0.07	5.99	5.26
38X-6, 126.5–130.5	CKY-1780610	388.65	3.34	2.28	15.9	64.0	0.11	2.43	3.08	0.65	0.07	5.81	4.51
38X-8, 17–21	CKY-1771910	389.50	3.08	2.42	15.9	62.9	0.10	2.39	3.92	0.68	0.07	6.45	5.33
39X-3, 1–5	CKY-1772810	392.83	2.89	2.57	16.4	63.4	0.11	2.50	3.51	0.71	0.08	6.09	5.10
39X-5, 101–104	CKY-1782210	396.65	3.22	2.25	16.3	63.7	0.11	2.18	3.44	0.68	0.08	5.91	3.41
40X-1, 108.5–111.5	CKY-1783910	401.59	3.28	2.35	16.1	63.3	0.14	2.28	4.01	0.67	0.10	6.17	5.11
40X-4, 5–10	CKY-1773710	403.76	2.87	2.50	16.4	62.9	0.11	2.55	3.61	0.70	0.10	6.18	5.26
41X-2, 14–19	CKY-1834010	411.29	3.15	2.36	16.0	63.1	0.11	2.30	3.83	0.69	0.09	6.33	4.50
41X-5, 80–82	CKY-1833710	415.32	3.24	2.24	15.8	64.2	0.10	2.30	3.18	0.64	0.08	5.94	3.99

Table T5. XRF core scanning results (resolution of 0.5 cm, measurement time of 200 ms for a vertical line scan of interval 338-C0022B-8H-4, 5–90 cm. (Continued on next two pages.)

Core, section, interval (cm)	Midpoint depth (mbsf)	Na_2O (wt%)	MgO (wt%)	Al_2O_3 (wt%)	SiO_2 (wt%)	P_2O_5 (wt%)	K_2O (wt%)	CaO (wt%)	TiO_2 (wt%)	MnO (wt%)	Fe_2O_3 (wt%)
338-C0022B-											
8H-4, 5	78.19	2.67	0.93	12.2	60.2	0.35	4.11	7.57	1.10	0.17	10.7
8H-4, 5.5	78.25	0.60	1.07	13.1	62.9	0.50	3.78	7.13	1.02	0.15	9.78
8H-4, 6	78.25	2.50	1.57	13.8	61.4	0.36	3.67	6.68	0.94	0.16	8.93
8H-4, 6.5	78.26	0.66	1.71	13.8	60.9	0.42	3.87	8.11	1.02	0.20	9.35
8H-4, 7	78.26	0.62	0.97	13.2	61.6	0.27	3.79	8.86	1.04	0.18	9.48
8H-4, 7.5	78.27	1.11	1.33	12.8	61.0	0.37	3.87	8.96	1.03	0.17	9.34
8H-4, 8	78.27	0.81	1.52	12.8	60.0	0.14	3.96	9.78	1.07	0.17	9.85
8H-4, 8.5	78.28		1.18	12.8	60.5	0.34	4.05	9.79	1.07	0.17	10.1
8H-4, 9	78.28	0.09	1.10	12.5	61.8	0.22	4.15	8.81	1.11	0.15	10.1
8H-4, 9.5	78.29	0.41	1.38	13.0	61.7	0.43	4.01	7.30	1.14	0.17	10.5
8H-4, 10	78.29	0.62	0.92	12.7	62.8	0.56	4.07	6.17	1.02	0.15	11.0
8H-4, 10.5	78.30	1.55	1.79	13.1	62.2	0.51	3.88	4.70	1.06	0.13	11.2
8H-4, 11	78.30	2.86	0.98	12.7	62.2	0.37	3.94	4.99	1.02	0.14	10.7
8H-4, 11.5	78.31		2.10	13.7	63.0	0.42	3.97	5.99	1.06	0.17	9.65
8H-4, 12	78.31	1.59	1.25	14.0	63.7	0.38	3.77	5.16	1.04	0.15	8.98
8H-4, 12.5	78.32	0.10	1.22	13.7	65.0	0.35	3.86	5.67	0.97	0.18	9.00
8H-4, 13	78.32	1.33	0.57	13.2	63.7	0.25	3.81	6.86	1.02	0.17	9.12
8H-4, 13.5	78.33		0.79	13.1	63.8	0.34	4.03	7.71	1.05	0.17	9.03
8H-4, 14	78.33	1.24	1.05	13.2	63.8	0.28	3.79	6.92	0.98	0.15	8.55
8H-4, 14.5	78.34	2.15	1.46	13.1	62.6	0.29	3.61	7.03	0.94	0.15	8.61
8H-4, 15	78.34	3.28	1.75	13.1	61.0	0.34	3.62	6.70	0.97	0.15	9.04
8H-4, 15.5	78.35	1.40	1.56	13.5	62.9	0.40	3.77	4.76	1.07	0.14	10.5
8H-4, 16	78.35	3.18	1.26	13.3	61.6	0.44	3.69	5.64	0.96	0.15	9.85
8H-4, 16.5	78.36	1.82	1.35	13.4	61.9	0.39	3.70	6.66	1.02	0.16	9.58
8H-4, 17	78.36	1.41	1.45	12.6	62.5	0.50	3.92	6.00	1.10	0.17	10.3
8H-4, 17.5	78.37	1.03	1.68	13.3	63.0	0.45	3.97	5.32	1.10	0.18	9.92
8H-4, 18	78.37	1.77	1.75	13.0	63.0	0.54	4.00	5.00	1.09	0.17	9.70
8H-4, 18.5	78.38	3.46	1.44	12.1	61.9	0.42	4.04	5.47	1.04	0.18	9.98
8H-4, 19	78.38	1.75	1.63	11.1	61.0	0.38	4.00	8.96	0.99	0.20	10.0
8H-4, 19.5	78.39	1.21	1.46	12.0	59.2	0.36	3.95	10.6	1.08	0.17	10.1
8H-4, 20	78.39		0.94	12.9	60.9	0.42	4.26	8.87	1.22	0.17	10.3
8H-4, 20.5	78.40		1.05	12.9	60.9	0.32	4.16	8.49	1.13	0.19	10.8
8H-4, 21	78.40	0.83	0.83	11.7	57.7	0.97	3.95	7.77	1.06	0.19	15.0
8H-4, 21.5	78.41	2.57	1.36	11.3	57.7	0.81	3.84	6.74	1.08	0.15	14.4
8H-4, 22	78.41	3.52	0.90	12.6	59.6	0.34	4.02	7.40	1.13	0.15	10.3
8H-4, 22.5	78.42	1.10	1.53	12.6	60.9	0.17	4.18	7.77	1.11	0.18	10.4
8H-4, 23	78.42	1.76	1.05	12.4	60.2	0.44	4.09	8.21	1.11	0.18	10.6
8H-4, 23.5	78.43	1.86	1.68	13.1	60.2	0.34	3.76	8.65	0.99	0.15	9.33
8H-4, 24	78.43	3.46	1.15	13.2	61.4	0.19	3.68	6.34	0.97	0.14	9.46
8H-4, 24.5	78.44	1.45	1.32	13.6	63.6	0.38	3.90	5.00	1.02	0.16	9.51
8H-4, 25	78.44	0.31	2.51	14.1	63.7	0.24	3.85	4.93	1.04	0.14	9.25
8H-4, 25.5	78.45	2.12	1.71	14.2	63.1	0.45	3.79	4.51	0.97	0.14	9.07
8H-4, 26	78.45	3.27	1.59	13.7	62.1	0.29	3.75	5.13	0.97	0.12	9.03
8H-4, 26.5	78.46	0.55	1.40	13.3	63.1	0.30	3.93	6.86	0.97	0.18	9.45
8H-4, 27	78.46	2.64	1.94	13.2	62.7	0.36	3.71	5.49	0.93	0.14	8.81
8H-4, 27.5	78.47	1.51	1.08	13.5	65.1	0.20	3.86	4.28	0.99	0.15	9.36
8H-4, 28	78.47	0.61	1.58	13.5	66.8	0.25	3.85	3.31	0.99	0.13	9.04
8H-4, 28.5	78.48	2.77	1.24	14.0	64.7	0.27	3.79	3.28	0.99	0.15	8.87
8H-4, 29	78.48	1.05	1.01	14.2	65.8	0.31	3.84	3.68	0.98	0.18	8.99
8H-4, 29.5	78.49	0.47	1.07	13.8	65.4	0.32	4.11	4.49	1.05	0.16	9.09
8H-4, 30	78.49	3.50	1.44	12.1	62.8	0.60	4.09	4.63	1.04	0.16	9.61
8H-4, 30.5	78.50	3.86	1.18	11.2	61.4	0.82	4.25	4.97	1.05	0.16	11.1
8H-4, 31	78.50		1.05	11.2	60.8	0.56	4.57	7.44	1.18	0.20	13.0
8H-4, 31.5	78.51	0.18	1.16	11.9	61.7	0.62	4.28	5.78	1.10	0.17	13.1
8H-4, 32	78.51	0.76	1.22	11.8	61.1	0.42	4.37	6.58	1.13	0.17	12.5
8H-4, 32.5	78.52	0.97	1.16	11.7	62.8	0.30	4.24	5.85	1.15	0.16	11.7
8H-4, 33	78.52	3.14	1.28	12.3	60.6	0.53	4.10	6.20	1.09	0.13	10.7
8H-4, 33.5	78.53	3.02	1.27	12.1	60.1	0.20	4.28	7.41	1.08	0.19	10.4
8H-4, 34	78.53	2.48	1.13	12.4	61.3	0.39	4.25	6.66	1.05	0.18	10.1
8H-4, 34.5	78.54	3.02	1.01	12.3	62.1	0.37	4.35	5.58	1.11	0.18	9.91
8H-4, 35	78.54	0.19	1.38	12.3	64.1	0.47	4.54	5.36	1.09	0.14	10.4
8H-4, 35.5	78.55	2.02	2.11	11.6	61.0	0.27	4.38	6.05	1.12	0.15	11.3
8H-4, 36	78.55	0.36	0.93	11.8	61.3	0.38	4.42	8.27	1.13	0.20	11.3
8H-4, 36.5	78.56	2.09	0.85	11.6	61.3	0.29	4.30	8.49	1.06	0.20	9.76
8H-4, 37	78.56	3.10	1.05	11.4	62.6	0.31	4.34	6.63	0.99	0.14	9.41
8H-4, 37.5	78.57	0.46	0.95	12.1	62.6	0.32	4.54	7.02	1.16	0.17	10.7

Table T5 (continued). (Continued on next page.)

Core, section, interval (cm)	Midpoint depth (mbsf)	Na_2O (wt%)	MgO (wt%)	Al_2O_3 (wt%)	SiO_2 (wt%)	P_2O_5 (wt%)	K_2O (wt%)	CaO (wt%)	TiO_2 (wt%)	MnO (wt%)	Fe_2O_3 (wt%)
8H-4, 38	78.57	1.12	0.90	11.9	60.3	0.30	4.52	7.75	1.23	0.16	11.9
8H-4, 38.5	78.58		1.03	12.4	60.6	0.48	4.48	7.23	1.19	0.18	12.4
8H-4, 39	78.58	3.12	0.97	12.3	61.6	0.29	4.08	5.21	1.10	0.15	11.2
8H-4, 39.5	78.59	0.12	1.18	12.5	63.3	0.29	4.32	5.37	1.21	0.17	11.5
8H-4, 40	78.59		1.13	11.9	61.8	0.49	4.48	7.28	1.16	0.20	11.5
8H-4, 40.5	78.60	1.80	1.11	12.0	60.0	0.43	4.22	8.72	1.09	0.19	10.4
8H-4, 41	78.60	3.75	1.04	11.7	58.7	0.30	4.21	8.71	1.13	0.16	10.3
8H-4, 41.5	78.61		1.19	12.6	61.0	0.32	4.40	7.86	1.27	0.19	11.2
8H-4, 42	78.61		1.29	12.2	62.4	0.38	4.44	6.25	1.21	0.18	11.7
8H-4, 42.5	78.62	1.01	1.28	12.6	62.0	0.42	4.48	5.39	1.15	0.16	11.5
8H-4, 43	78.62	0.86	0.88	12.1	62.3	0.48	4.36	6.04	1.20	0.15	11.6
8H-4, 43.5	78.63		1.03	12.3	61.8	0.33	4.41	7.11	1.23	0.19	11.7
8H-4, 44	78.63	1.70	0.65	11.5	61.2	0.37	4.40	6.92	1.19	0.18	11.9
8H-4, 44.5	78.64	0.50	1.29	13.1	62.1	0.33	4.21	6.43	1.21	0.17	10.7
8H-4, 45	78.64		1.08	13.3	62.2	0.38	4.08	6.77	1.20	0.16	10.8
8H-4, 45.5	78.65	1.97	1.14	12.7	60.9	0.42	4.04	6.88	1.11	0.19	10.6
8H-4, 46	78.65		1.10	12.9	61.6	0.36	4.16	7.57	1.17	0.16	11.0
8H-4, 46.5	78.66	2.23	0.91	12.2	60.7	0.38	4.12	7.20	1.11	0.20	10.9
8H-4, 47	78.66	4.40	1.11	12.0	58.9	0.45	4.03	7.41	1.06	0.17	10.5
8H-4, 47.5	78.67	2.02	0.61	12.1	60.9	0.41	4.16	7.59	1.12	0.20	10.9
8H-4, 48	78.67	2.72	0.91	11.2	58.5	0.50	4.48	8.22	1.28	0.20	12.0
8H-4, 48.5	78.68		1.34	11.3	59.9	0.32	4.62	8.48	1.34	0.22	12.5
8H-4, 49	78.68	1.13	1.14	10.6	58.7	0.51	4.68	8.35	1.37	0.23	13.3
8H-4, 49.5	78.69	1.35	1.98	10.1	57.7	0.41	4.72	8.51	1.32	0.21	13.6
8H-4, 50	78.69		1.21	10.6	59.8	0.52	4.62	7.99	1.37	0.23	13.7
8H-4, 50.5	78.70	1.50	0.97	10.1	59.1	0.46	4.54	8.13	1.32	0.21	13.6
8H-4, 51	78.70		1.60	10.8	56.8	0.39	4.30	11.2	1.25	0.20	13.5
8H-4, 51.5	78.71	2.32	1.46	10.6	55.5	0.38	4.10	11.4	1.22	0.21	12.8
8H-4, 52	78.71		1.41	11.3	60.7	0.35	4.35	8.50	1.26	0.17	11.9
8H-4, 52.5	78.72	0.36	1.40	11.6	61.0	0.28	4.31	7.78	1.20	0.19	11.8
8H-4, 53	78.72		1.49	12.1	61.9	0.25	4.40	6.38	1.22	0.16	12.1
8H-4, 53.5	78.73		0.71	11.4	62.3	0.25	4.52	6.84	1.28	0.19	12.6
8H-4, 54	78.73	1.44	1.63	11.6	60.1	0.41	4.25	7.34	1.29	0.19	11.8
8H-4, 54.5	78.74		0.97	11.9	60.6	0.43	4.22	8.34	1.20	0.20	12.2
8H-4, 55	78.74		0.90	11.8	60.8	0.48	4.14	8.80	1.13	0.18	11.7
8H-4, 55.5	78.75	2.17	1.13	12.2	60.2	0.32	3.96	8.01	1.09	0.17	10.7
8H-4, 56	78.75	2.03	1.78	12.6	59.5	0.37	3.71	8.92	1.08	0.15	9.84
8H-4, 56.5	78.76		0.93	12.7	61.5	0.40	4.06	8.59	1.14	0.18	10.5
8H-4, 57	78.76	2.17	1.14	12.7	61.7	0.39	3.99	5.98	1.08	0.19	10.6
8H-4, 57.5	78.77	1.12	0.99	13.0	61.7	0.52	4.04	6.41	1.07	0.18	11.0
8H-4, 58	78.77		1.10	13.2	62.5	0.29	4.13	6.66	1.17	0.19	10.7
8H-4, 58.5	78.78	1.74	1.64	12.6	60.1	0.52	3.99	7.70	1.14	0.17	10.4
8H-4, 59	78.78	1.34	1.61	11.5	58.5	0.27	4.07	10.5	1.22	0.21	10.8
8H-4, 59.5	78.79	1.90	0.79	11.0	58.9	0.36	4.28	10.2	1.17	0.22	11.2
8H-4, 60	78.79	3.55	1.13	11.9	58.9	0.45	4.10	7.57	1.13	0.19	11.0
8H-4, 60.5	78.80	5.28	0.75	10.9	57.3	0.37	4.25	8.45	1.26	0.21	11.3
8H-4, 61	78.80		0.89	11.0	59.5	0.56	4.61	9.38	1.31	0.22	12.5
8H-4, 61.5	78.81	1.94	0.79	10.6	58.9	0.44	4.58	8.53	1.36	0.26	12.6
8H-4, 62	78.81	1.31	1.16	10.8	58.2	0.50	4.59	9.02	1.33	0.26	12.9
8H-4, 62.5	78.82	1.36	0.49	10.5	58.4	0.47	4.71	8.74	1.30	0.24	13.8
8H-4, 63	78.82	0.33	1.43	10.3	58.0	0.47	4.82	8.56	1.41	0.32	14.4
8H-4, 63.5	78.83	3.32	0.80	10.6	57.0	0.56	4.72	8.09	1.41	0.23	13.3
8H-4, 64	78.83		1.15	9.94	58.5	0.39	5.03	7.75	1.47	0.35	15.5
8H-4, 64.5	78.84	0.84	1.00	9.30	56.9	0.44	4.79	10.4	1.46	0.27	14.5
8H-4, 65	78.84		0.55	10.0	57.1	0.58	4.70	10.9	1.50	0.32	14.4
8H-4, 65.5	78.85	2.38	1.38	10.2	55.6	0.53	4.57	9.45	1.37	0.26	14.3
8H-4, 66	78.85		1.52	9.69	57.8	0.61	4.62	9.65	1.42	0.27	14.4
8H-4, 66.5	78.86		1.40	9.50	55.9	0.69	4.88	10.9	1.45	0.34	15.0
8H-4, 67	78.86	0.72	0.73	9.30	59.1	0.53	4.58	8.53	1.34	0.22	14.9
8H-4, 67.5	78.87	0.92	0.82	8.52	56.9	0.49	4.84	11.1	1.40	0.22	14.7
8H-4, 68	78.87	0.77	0.55	8.88	55.6	0.59	4.64	11.3	1.34	0.22	16.1
8H-4, 68.5	78.88		0.94	8.56	59.0	0.77	4.72	8.48	1.39	0.20	16.0
8H-4, 69	78.88		0.62	9.08	58.1	0.58	4.52	10.4	1.41	0.20	15.1
8H-4, 69.5	78.89		0.35	9.80	59.2	0.49	4.80	9.49	1.26	0.22	14.4
8H-4, 70	78.89		0.46	10.0	58.6	0.50	4.76	9.43	1.35	0.21	14.6
8H-4, 70.5	78.90		0.88	9.40	57.9	0.52	4.67	10.6	1.43	0.23	14.4
8H-4, 71	78.90	1.79	0.72	9.09	52.7	0.65	4.42	16.0	1.27	0.29	13.1
8H-4, 71.5	78.91		1.17	9.27	55.7	0.67	4.55	13.4	1.31	0.27	13.6
8H-4, 72	78.91		0.53	9.33	56.2	0.55	4.65	13.0	1.38	0.25	14.0

Table T5 (continued).

Core, section, interval (cm)	Midpoint depth (mbsf)	Na_2O (wt%)	MgO (wt%)	Al_2O_3 (wt%)	SiO_2 (wt%)	P_2O_5 (wt%)	K_2O (wt%)	CaO (wt%)	TiO_2 (wt%)	MnO (wt%)	Fe_2O_3 (wt%)
8H-4, 72.5	78.92		0.46	9.55	56.2	0.61	4.67	12.7	1.39	0.24	14.1
8H-4, 73	78.92		1.27	9.12	55.2	0.53	4.59	13.7	1.34	0.27	14.0
8H-4, 73.5	78.93		1.02	11.1	57.9	0.27	4.00	12.9	1.12	0.25	11.5
8H-4, 74	78.93	2.21	1.40	9.86	52.6	0.43	3.73	17.2	1.12	0.25	11.2
8H-4, 74.5	78.94	1.60	0.50	10.1	52.7	0.35	3.90	18.5	1.05	0.30	11.0
8H-4, 75	78.94	1.15	1.15	10.8	56.4	0.31	3.94	13.8	1.14	0.22	11.1
8H-4, 75.5	78.95	2.76	1.30	10.2	52.9	0.50	3.66	16.1	1.08	0.26	11.2
8H-4, 76	78.95	2.19	0.87	10.3	55.0	0.31	3.91	14.8	1.10	0.23	11.3
8H-4, 76.5	78.96	1.06	0.96	11.0	58.1	0.32	4.04	12.0	1.19	0.20	11.1
8H-4, 77	78.96	3.69	1.26	10.3	57.4	0.26	3.95	10.7	1.13	0.22	11.1
8H-4, 77.5	78.97	0.78	1.25	10.5	57.5	0.48	4.28	11.7	1.20	0.20	12.2
8H-4, 78	78.97	0.41	0.86	10.1	56.9	0.46	4.35	12.5	1.19	0.26	12.9
8H-4, 78.5	78.98	2.33	1.28	10.8	55.1	0.42	4.08	12.9	1.13	0.21	11.7
8H-4, 79	78.98	0.74	1.17	11.6	57.4	0.26	4.02	12.9	1.09	0.20	10.5
8H-4, 79.5	78.99	3.12	1.16	11.1	56.4	0.33	3.88	12.5	1.04	0.21	10.3
8H-4, 80	78.99		0.56	10.5	57.9	0.48	4.04	13.3	1.18	0.22	11.8
8H-4, 80.5	79.00	3.54	1.61	10.3	55.5	0.46	3.90	11.5	1.14	0.21	11.8
8H-4, 81	79.00		1.00	11.4	59.4	0.32	4.30	10.4	1.16	0.19	11.8
8H-4, 81.5	79.01		0.99	12.3	60.6	0.50	4.31	7.77	1.22	0.16	12.1
8H-4, 82	79.01		1.28	12.4	63.2	0.33	4.39	4.79	1.24	0.17	12.3
8H-4, 82.5	79.02	1.68	1.45	12.9	63.2	0.36	3.98	4.51	1.12	0.15	10.7
8H-4, 83	79.02	2.18	0.82	12.6	62.6	0.28	3.98	5.65	1.17	0.15	10.5
8H-4, 83.5	79.03	2.54	1.55	13.0	61.2	0.32	3.93	5.38	1.12	0.19	10.8
8H-4, 84	79.03	1.61	1.35	12.0	61.2	0.35	4.17	6.47	1.17	0.23	11.5
8H-4, 84.5	79.04	0.72	2.01	11.1	59.1	0.44	3.99	9.65	1.18	0.23	11.6
8H-4, 85	79.04	1.34	0.84	12.3	59.0	0.28	3.79	10.8	1.04	0.21	10.4
8H-4, 85.5	79.05	0.74	0.96	12.0	59.1	0.35	3.89	10.9	1.08	0.22	10.7
8H-4, 86	79.05		1.31	12.3	58.9	0.37	3.95	10.6	1.08	0.23	11.2
8H-4, 86.5	79.06	2.19	1.51	11.8	59.7	0.40	3.75	9.17	1.08	0.16	10.2
8H-4, 87	79.06		1.49	12.1	60.5	0.31	3.78	9.62	1.09	0.19	10.9
8H-4, 87.5	79.07	2.52	1.11	12.3	59.2	0.43	3.72	9.47	1.04	0.17	10.0
8H-4, 88	79.07	0.73	1.42	12.7	60.9	0.28	3.82	8.97	1.02	0.22	9.94
8H-4, 88.5	79.08	1.75	1.41	12.2	60.1	0.35	3.7	9.31	0.97	0.17	9.95
8H-4, 89	79.08		0.73	12.4	60.9	0.42	3.82	9.80	1.04	0.21	10.7
8H-4, 89.5	79.09	2.66	1.21	12.6	59.0	0.47	3.65	9.51	0.98	0.17	9.76
8H-4, 90	79.09	4.01	1.56	12.2	58.3	0.41	3.60	9.23	0.95	0.17	9.56

Table T6. XRF core scanning results (resolution of 0.5 cm, measurement time of 200 ms for a mapping scan of interval 338-C0022B-8H-4, 40–55 cm, over a width of 4 cm). For the section width, the center of the core is considered to be at 0 cm. (Continued on next four pages.)

Core, section, interval (cm)	Section width (cm)	Midpoint depth (mbsf)	Na_2O (wt%)	MgO (wt%)	Al_2O_3 (wt%)	SiO_2 (wt%)	P_2O_5 (wt%)	K_2O (wt%)	CaO (wt%)	TiO_2 (wt%)	MnO (wt%)	Fe_2O_3 (wt%)
338-C0022B-												
8H-4, 40	2	78.54	0.85	1.46	12.6	62.0	0.38	4.55	6.12	1.14	0.14	10.8
8H-4, 40.5	2	78.55		1.23	12.8	63.4	0.36	4.52	5.51	1.17	0.14	10.9
8H-4, 41	2	78.55	0.15	1.04	13.0	64.0	0.41	4.48	4.56	1.19	0.15	11.1
8H-4, 41.5	2	78.56	1.04	1.12	13.4	65.1	0.40	4.04	4.27	1.08	0.15	9.40
8H-4, 42	2	78.56	1.57	1.39	13.4	64.7	0.39	4.01	4.38	1.05	0.15	9.02
8H-4, 42.5	2	78.57	1.64	1.06	13.4	64.1	0.38	4.22	4.83	1.05	0.17	9.17
8H-4, 43	2	78.57	1.51	1.38	13.8	63.8	0.36	4.15	4.92	1.01	0.17	9.00
8H-4, 43.5	2	78.58	1.91	1.09	13.5	63.6	0.43	4.17	5.16	1.02	0.16	8.96
8H-4, 44	2	78.58	0.73	1.33	13.0	65.2	0.41	4.32	4.87	1.06	0.16	8.86
8H-4, 44.5	2	78.59	1.69	1.07	12.3	65.7	0.58	4.24	4.09	1.05	0.15	9.14
8H-4, 45	2	78.59	0.77	1.11	12.5	63.6	0.63	4.05	6.17	1.03	0.16	9.94
8H-4, 45.5	2	78.60	0.64	1.32	13.0	61.4	0.41	3.89	8.76	1.01	0.19	9.37
8H-4, 46	2	78.60	1.94	1.30	12.7	60.3	0.33	3.81	9.30	1.01	0.18	9.21
8H-4, 46.5	2	78.61	1.89	1.46	12.7	60.4	0.33	3.84	8.59	1.01	0.17	9.56
8H-4, 47	2	78.61	1.40	1.28	12.9	60.9	0.28	3.87	8.44	1.03	0.17	9.75
8H-4, 47.5	2	78.62	1.67	1.16	13.2	60.7	0.34	3.89	8.73	1.00	0.16	9.12
8H-4, 48	2	78.62	1.26	1.28	13.1	61.8	0.41	3.90	7.64	1.02	0.16	9.47
8H-4, 48.5	2	78.63	1.70	1.43	13.3	62.2	0.39	3.94	6.18	1.04	0.14	9.79
8H-4, 49	2	78.63	1.47	1.30	13.3	62.0	0.34	3.89	7.01	1.04	0.17	9.54
8H-4, 49.5	2	78.64	1.40	1.26	13.5	61.2	0.38	3.90	7.51	1.06	0.17	9.64
8H-4, 50	2	78.64	1.38	1.49	13.5	62.8	0.34	3.87	5.90	1.06	0.15	9.59

Table T6 (continued). (Continued on next page.)

Core, section, interval (cm)	Section width (cm)	Midpoint depth (mbsf)	Na_2O (wt%)	MgO (wt%)	Al_2O_3 (wt%)	SiO_2 (wt%)	P_2O_5 (wt%)	K_2O (wt%)	CaO (wt%)	TiO_2 (wt%)	MnO (wt%)	Fe_2O_3 (wt%)
8H-4, 50.5	2	78.65	1.43	1.31	13.8	63.6	0.36	3.91	4.46	1.05	0.15	9.93
8H-4, 51	2	78.65	1.39	1.51	13.8	63.1	0.47	3.90	4.80	1.04	0.14	9.83
8H-4, 51.5	2	78.66	0.57	1.35	14.0	63.3	0.49	4.05	4.83	1.12	0.16	10.1
8H-4, 52	2	78.66	0.87	1.41	14.5	64.4	0.31	3.97	4.22	1.05	0.13	9.16
8H-4, 52.5	2	78.67	1.03	1.47	14.7	64.4	0.36	4.00	3.89	1.05	0.13	8.95
8H-4, 53	2	78.67	1.44	1.19	14.1	63.9	0.40	3.99	4.48	1.05	0.13	9.27
8H-4, 53.5	2	78.68	1.92	1.31	13.9	62.8	0.43	3.95	5.08	1.04	0.14	9.37
8H-4, 54	2	78.68	1.38	1.24	13.7	62.8	0.49	3.96	5.76	1.03	0.15	9.48
8H-4, 54.5	2	78.69	1.92	1.28	12.8	62.2	0.45	4.02	6.12	1.07	0.16	9.94
8H-4, 55	2	78.69	2.23	1.23	12.7	61.5	0.32	4.06	6.45	1.06	0.17	10.3
8H-4, 40	1.5	78.54	0.96	1.54	12.6	63.5	0.37	4.31	5.15	1.09	0.14	10.3
8H-4, 40.5	1.5	78.55	0.46	0.88	13.0	64.2	0.39	4.32	5.06	1.10	0.15	10.5
8H-4, 41	1.5	78.55	1.37	1.16	13.0	63.8	0.42	4.22	4.41	1.11	0.15	10.3
8H-4, 41.5	1.5	78.56	1.74	1.38	13.6	64.5	0.38	3.99	4.28	1.03	0.16	8.97
8H-4, 42	1.5	78.56	2.49	1.36	13.2	63.6	0.47	4.11	4.60	1.01	0.16	8.96
8H-4, 42.5	1.5	78.57	2.23	1.46	13.2	63.5	0.42	4.18	4.86	1.02	0.16	8.96
8H-4, 43	1.5	78.57	1.27	0.93	13.5	64.6	0.39	4.27	4.78	1.05	0.17	9.03
8H-4, 43.5	1.5	78.58	0.61	1.27	13.0	65.3	0.58	4.24	4.79	1.00	0.16	9.04
8H-4, 44	1.5	78.58	1.97	1.00	11.7	66.4	0.76	4.16	3.83	0.96	0.15	9.13
8H-4, 44.5	1.5	78.59	1.67	1.08	11.0	66.0	1.13	4.10	3.28	0.97	0.14	10.6
8H-4, 45	1.5	78.59	1.22	1.13	11.8	63.2	0.80	4.06	5.86	1.00	0.17	10.8
8H-4, 45.5	1.5	78.60	1.86	1.26	13.0	61.6	0.38	3.83	7.79	1.01	0.17	9.13
8H-4, 46	1.5	78.60	0.66	1.39	12.7	61.2	0.31	3.86	9.43	1.03	0.18	9.23
8H-4, 46.5	1.5	78.61	0.96	1.25	13.0	60.8	0.34	3.87	9.34	1.03	0.17	9.26
8H-4, 47	1.5	78.61	1.66	1.40	13.1	61.3	0.35	3.79	8.26	0.99	0.16	9.01
8H-4, 47.5	1.5	78.62	1.29	1.23	13.5	62.6	0.33	3.84	6.99	1.04	0.15	9.12
8H-4, 48	1.5	78.62	1.86	1.11	13.6	64.0	0.35	3.81	4.51	1.04	0.15	9.55
8H-4, 48.5	1.5	78.63	1.86	1.37	13.7	63.9	0.35	3.84	4.05	1.01	0.15	9.75
8H-4, 49	1.5	78.63	1.43	1.68	13.8	63.3	0.38	3.90	4.77	1.02	0.15	9.53
8H-4, 49.5	1.5	78.64	0.92	1.25	14.1	63.4	0.38	4.01	5.02	1.07	0.15	9.68
8H-4, 50	1.5	78.64	2.10	1.39	13.8	63.1	0.39	3.94	4.62	1.02	0.14	9.44
8H-4, 50.5	1.5	78.65	1.19	1.42	14.3	63.6	0.38	3.98	4.47	1.06	0.14	9.39
8H-4, 51	1.5	78.65	0.76	1.42	14.4	64.0	0.34	3.87	4.76	1.06	0.14	9.30
8H-4, 51.5	1.5	78.66	1.08	1.48	13.7	63.4	0.33	3.96	5.19	1.07	0.16	9.61
8H-4, 52	1.5	78.66	1.29	1.35	14.1	63.2	0.40	3.80	5.50	1.00	0.15	9.15
8H-4, 52.5	1.5	78.67	1.37	1.28	13.7	63.0	0.40	3.79	6.01	1.02	0.16	9.33
8H-4, 53	1.5	78.67	0.08	1.36	13.4	63.1	0.38	3.91	6.72	1.06	0.16	9.77
8H-4, 53.5	1.5	78.68	1.53	1.30	13.2	62.3	0.36	3.79	6.67	1.01	0.16	9.66
8H-4, 54	1.5	78.68	1.37	1.27	12.9	62.4	0.36	3.89	6.69	1.06	0.17	9.83
8H-4, 54.5	1.5	78.69	1.27	1.35	12.6	61.4	0.36	3.99	7.61	1.06	0.18	10.3
8H-4, 55	1.5	78.69	1.58	1.37	12.2	60.9	0.35	3.98	7.73	1.11	0.17	10.6
8H-4, 40	1	78.54	0.87	0.98	12.8	64.3	0.35	4.22	4.54	1.13	0.14	10.7
8H-4, 40.5	1	78.55	0.79	1.09	13.0	62.9	0.42	4.23	6.07	1.11	0.18	10.2
8H-4, 41	1	78.55	1.58	1.11	12.9	63.6	0.42	4.22	4.79	1.14	0.17	10.1
8H-4, 41.5	1	78.56	1.20	1.04	13.5	64.8	0.35	4.08	4.52	1.05	0.17	9.27
8H-4, 42	1	78.56	1.10	1.30	13.4	64.1	0.39	4.22	4.93	1.04	0.17	9.39
8H-4, 42.5	1	78.57	1.39	1.18	13.5	63.7	0.41	4.12	5.28	1.00	0.16	9.27
8H-4, 43	1	78.57	1.86	1.00	13.1	64.2	0.45	4.01	5.35	0.98	0.17	8.88
8H-4, 43.5	1	78.58	1.11	1.07	12.5	64.7	0.64	4.11	5.40	0.98	0.16	9.36
8H-4, 44	1	78.58		1.23	11.3	65.9	0.88	4.15	4.63	0.94	0.15	10.9
8H-4, 44.5	1	78.59	1.66	1.23	11.7	62.9	0.68	4.07	6.37	0.97	0.18	10.2
8H-4, 45	1	78.59	1.50	1.45	12.6	62.2	0.40	4.01	7.54	1.00	0.18	9.07
8H-4, 45.5	1	78.60	1.59	1.09	13.2	62.3	0.36	3.85	7.42	0.98	0.16	9.03
8H-4, 46	1	78.60	1.77	1.25	13.3	62.6	0.34	3.79	6.93	1.02	0.16	8.95
8H-4, 46.5	1	78.61	1.87	1.34	13.6	62.9	0.28	3.76	5.91	1.00	0.15	9.19
8H-4, 47	1	78.61	1.82	1.27	13.7	62.9	0.38	3.76	5.76	0.98	0.16	9.28
8H-4, 47.5	1	78.62	1.38	1.32	13.7	63.9	0.34	3.85	5.12	1.05	0.16	9.27
8H-4, 48	1	78.62	1.45	1.19	13.8	63.7	0.39	3.85	4.94	1.03	0.15	9.45
8H-4, 48.5	1	78.63	1.60	1.36	13.7	63.4	0.39	3.88	5.12	1.04	0.16	9.36
8H-4, 49	1	78.63	2.09	1.22	13.8	63.0	0.37	3.81	5.34	1.01	0.16	9.23
8H-4, 49.5	1	78.64	0.48	1.18	13.6	63.5	0.37	3.96	5.92	1.07	0.17	9.78
8H-4, 50	1	78.64	1.91	1.29	13.4	62.4	0.42	3.86	6.07	1.05	0.16	9.47
8H-4, 50.5	1	78.65	0.66	1.30	13.2	62.5	0.37	3.94	6.91	1.09	0.19	9.83
8H-4, 51	1	78.65	1.28	1.35	13.3	62.2	0.32	3.84	7.00	1.00	0.18	9.55
8H-4, 51.5	1	78.66	1.22	1.45	13.0	61.6	0.41	3.80	7.40	1.04	0.17	10.0
8H-4, 52	1	78.66	1.86	1.30	12.9	62.1	0.31	3.75	7.05	0.99	0.17	9.61
8H-4, 52.5	1	78.67	1.42	1.43	13.2	62.4	0.38	3.82	6.51	1.00	0.17	9.63
8H-4, 53	1	78.67	1.56	1.35	13.2	62.9	0.31	3.82	6.02	1.03	0.17	9.69
8H-4, 53.5	1	78.68	1.82	1.00	12.7	62.6	0.28	3.87	6.56	1.03	0.16	9.92

Table T6 (continued). (Continued on next page.)

Core, section, interval (cm)	Section width (cm)	Midpoint depth (mbsf)	Na_2O (wt%)	MgO (wt%)	Al_2O_3 (wt%)	SiO_2 (wt%)	P_2O_5 (wt%)	K_2O (wt%)	CaO (wt%)	TiO_2 (wt%)	MnO (wt%)	Fe_2O_3 (wt%)
8H-4, 54	1	78.68	0.79	1.38	12.9	62.1	0.37	3.91	7.28	1.07	0.17	10.0
8H-4, 54.5	1	78.69	0.92	1.01	12.7	61.6	0.45	3.98	7.79	1.09	0.18	10.4
8H-4, 55	1	78.69	1.64	1.13	11.9	60.0	0.53	3.94	8.96	1.07	0.18	10.6
8H-4, 40	0.5	78.54	1.45	0.88	12.9	62.9	0.44	4.12	5.69	1.10	0.16	10.4
8H-4, 40.5	0.5	78.55	1.69	1.17	12.6	61.5	0.40	4.15	7.42	1.07	0.18	9.83
8H-4, 41	0.5	78.55	0.55	1.06	12.4	61.7	0.38	4.31	8.13	1.12	0.18	10.2
8H-4, 41.5	0.5	78.56	1.95	1.37	13.2	62.3	0.34	3.97	6.79	0.99	0.16	8.93
8H-4, 42	0.5	78.56	1.13	1.32	13.7	63.1	0.36	3.96	5.82	1.02	0.16	9.37
8H-4, 42.5	0.5	78.57	1.54	1.33	13.7	63.6	0.26	3.86	5.16	1.01	0.14	9.47
8H-4, 43	0.5	78.57	1.85	1.42	14.0	63.5	0.29	3.75	5.03	0.99	0.14	9.08
8H-4, 43.5	0.5	78.58	2.27	1.40	13.4	62.7	0.30	3.79	6.06	0.98	0.16	8.98
8H-4, 44	0.5	78.58	0.56	1.22	13.2	63.4	0.30	3.92	6.72	1.03	0.18	9.50
8H-4, 44.5	0.5	78.59	1.72	1.15	13.5	62.7	0.34	3.80	6.64	1.01	0.16	8.98
8H-4, 45	0.5	78.59	2.11	1.20	13.6	62.3	0.33	3.77	6.59	1.01	0.16	9.01
8H-4, 45.5	0.5	78.60	0.40	1.17	13.8	63.1	0.30	3.83	6.84	1.02	0.17	9.45
8H-4, 46	0.5	78.60	1.04	1.41	13.5	62.6	0.27	3.78	6.86	1.01	0.17	9.38
8H-4, 46.5	0.5	78.61	1.83	1.36	13.7	62.5	0.36	3.73	6.14	1.02	0.16	9.23
8H-4, 47	0.5	78.61	0.66	1.32	13.7	63.2	0.35	3.79	6.21	1.02	0.16	9.53
8H-4, 47.5	0.5	78.62	2.10	1.37	13.7	62.6	0.38	3.73	5.85	1.02	0.16	9.13
8H-4, 48	0.5	78.62	1.52	1.26	13.4	62.8	0.40	3.78	6.27	1.06	0.17	9.33
8H-4, 48.5	0.5	78.63		1.42	13.6	63.1	0.33	3.98	6.58	1.06	0.19	9.74
8H-4, 49	0.5	78.63	1.41	1.16	13.0	61.8	0.40	4.03	6.73	1.08	0.18	10.2
8H-4, 49.5	0.5	78.64	1.89	1.65	12.3	61.1	0.36	3.95	7.05	1.12	0.21	10.4
8H-4, 50	0.5	78.64	1.72	1.38	12.1	62.3	0.46	3.96	6.63	1.08	0.18	10.2
8H-4, 50.5	0.5	78.65	0.56	1.15	12.6	62.4	0.55	3.99	6.93	1.09	0.18	10.6
8H-4, 51	0.5	78.65	1.89	1.24	12.8	61.4	0.32	3.80	7.27	0.98	0.17	10.1
8H-4, 51.5	0.5	78.66	0.84	1.23	12.6	61.1	0.26	3.78	8.32	1.05	0.18	10.6
8H-4, 52	0.5	78.66	1.63	1.44	13.1	62.0	0.31	3.68	7.23	1.00	0.15	9.49
8H-4, 52.5	0.5	78.67	1.40	1.49	13.2	62.5	0.41	3.75	6.72	1.03	0.16	9.38
8H-4, 53	0.5	78.67	1.54	1.26	13.2	63.0	0.36	3.84	5.71	1.04	0.16	9.85
8H-4, 53.5	0.5	78.68	1.48	1.27	13.3	62.8	0.34	3.89	5.83	1.02	0.16	9.93
8H-4, 54	0.5	78.68	2.11	1.35	12.9	62.1	0.32	3.82	6.44	1.03	0.16	9.72
8H-4, 54.5	0.5	78.69	1.86	1.48	12.6	61.1	0.42	3.83	7.53	1.03	0.15	10.0
8H-4, 55	0.5	78.69	2.56	1.49	11.8	60.1	0.42	3.81	8.13	1.03	0.18	10.4
8H-4, 40	0	78.54		1.29	12.3	61.5	0.45	4.25	8.58	1.12	0.19	10.3
8H-4, 40.5	0	78.55	0.67	1.44	12.6	61.2	0.46	4.20	7.97	1.10	0.17	10.2
8H-4, 41	0	78.55	0.26	1.51	12.7	60.9	0.33	4.16	8.29	1.14	0.18	10.6
8H-4, 41.5	0	78.56	0.76	1.42	13.5	62.9	0.26	3.91	6.47	1.04	0.15	9.55
8H-4, 42	0	78.56	1.15	1.29	14.0	63.7	0.35	3.91	4.92	1.04	0.15	9.52
8H-4, 42.5	0	78.57	1.61	1.53	14.1	63.3	0.39	3.81	4.92	1.01	0.15	9.19
8H-4, 43	0	78.57	1.13	1.64	14.4	63.2	0.35	3.78	5.39	0.97	0.15	8.99
8H-4, 43.5	0	78.58	0.99	1.41	14.1	63.3	0.36	3.80	5.44	1.00	0.16	9.46
8H-4, 44	0	78.58	1.28	1.53	14.0	62.6	0.39	3.80	5.27	1.02	0.15	9.94
8H-4, 44.5	0	78.59	1.19	1.27	13.8	62.9	0.35	3.81	5.49	1.04	0.16	10.0
8H-4, 45	0	78.59	1.41	1.00	13.7	62.9	0.39	3.74	6.08	1.01	0.16	9.69
8H-4, 45.5	0	78.60	1.27	1.32	13.9	62.8	0.37	3.68	6.09	1.00	0.15	9.48
8H-4, 46	0	78.60	1.50	1.23	13.6	62.4	0.37	3.69	6.45	1.01	0.17	9.63
8H-4, 46.5	0	78.61	1.53	1.56	13.5	62.0	0.32	3.68	6.69	1.02	0.17	9.54
8H-4, 47	0	78.61	0.82	1.30	13.3	61.9	0.40	3.76	7.79	1.06	0.19	9.49
8H-4, 47.5	0	78.62	0.11	1.09	13.3	62.7	0.40	3.87	7.87	1.07	0.19	9.47
8H-4, 48	0	78.62	1.19	1.48	13.0	62.4	0.42	3.87	6.98	1.06	0.19	9.38
8H-4, 48.5	0	78.63	1.81	1.33	13.1	62.4	0.43	3.84	6.55	1.05	0.18	9.34
8H-4, 49	0	78.63	1.42	1.25	13.0	62.2	0.39	3.94	6.66	1.10	0.20	9.86
8H-4, 49.5	0	78.64	1.42	1.39	12.5	61.6	0.34	4.04	7.06	1.13	0.20	10.4
8H-4, 50	0	78.64	1.43	1.41	12.6	62.7	0.31	3.89	6.43	1.09	0.15	10.0
8H-4, 50.5	0	78.65	0.67	1.42	12.6	62.0	0.36	3.82	7.42	1.05	0.15	10.5
8H-4, 51	0	78.65	2.06	1.33	12.4	57.7	0.34	3.66	11.0	0.99	0.19	10.4
8H-4, 51.5	0	78.66	1.62	1.36	12.2	56.9	0.42	3.71	12.4	1.04	0.23	10.1
8H-4, 52	0	78.66	1.00	1.11	13.0	62.5	0.40	3.79	7.56	1.02	0.16	9.51
8H-4, 52.5	0	78.67	1.22	1.28	13.4	63.4	0.42	3.83	5.70	1.02	0.16	9.58
8H-4, 53	0	78.67	1.21	1.37	13.2	63.3	0.32	3.84	5.72	1.02	0.16	9.92
8H-4, 53.5	0	78.68	0.66	0.98	13.0	63.5	0.31	3.95	6.29	1.06	0.16	10.1
8H-4, 54	0	78.68	1.48	1.40	12.9	62.1	0.47	3.80	6.78	1.02	0.15	9.95
8H-4, 54.5	0	78.69	1.19	1.34	12.5	61.2	0.74	3.85	7.50	1.04	0.15	10.5
8H-4, 55	0	78.69	1.07	1.42	12.3	61.2	0.62	3.81	7.58	1.05	0.16	10.8
8H-4, 40	–0.5	78.54	0.74	1.35	13.0	61.3	0.40	4.23	7.41	1.11	0.17	10.3
8H-4, 40.5	–0.5	78.55	1.02	1.22	13.0	62.4	0.41	4.20	6.04	1.09	0.16	10.4
8H-4, 41	–0.5	78.55	0.49	1.28	13.1	62.7	0.40	4.16	5.95	1.11	0.15	10.7
8H-4, 41.5	–0.5	78.56	2.00	1.42	13.7	62.5	0.41	3.80	5.54	0.99	0.15	9.49

Table T6 (continued). (Continued on next page.)

Core, section, interval (cm)	Section width (cm)	Midpoint depth (mbsf)	Na_2O (wt%)	MgO (wt%)	Al_2O_3 (wt%)	SiO_2 (wt%)	P_2O_5 (wt%)	K_2O (wt%)	CaO (wt%)	TiO_2 (wt%)	MnO (wt%)	Fe_2O_3 (wt%)
8H-4, 42	–0.5	78.56	2.30	1.34	13.5	62.5	0.40	3.85	5.17	1.03	0.14	9.74
8H-4, 42.5	–0.5	78.57	1.64	1.35	13.5	62.7	0.44	3.83	5.23	1.01	0.15	10.1
8H-4, 43	–0.5	78.57	1.10	1.29	13.4	63.1	0.43	3.76	5.70	0.99	0.15	10.1
8H-4, 43.5	–0.5	78.58	1.00	1.46	13.4	62.2	0.30	3.75	6.74	0.97	0.17	10.0
8H-4, 44	–0.5	78.58	1.68	1.29	13.6	62.4	0.36	3.69	5.98	1.00	0.15	9.90
8H-4, 44.5	–0.5	78.59	1.30	1.61	13.5	62.7	0.39	3.66	5.86	1.00	0.15	9.78
8H-4, 45	–0.5	78.59	1.21	1.69	13.4	62.5	0.41	3.63	6.27	0.99	0.17	9.70
8H-4, 45.5	–0.5	78.60	1.65	1.35	13.2	62.7	0.31	3.78	6.28	1.01	0.18	9.52
8H-4, 46	–0.5	78.60	2.19	1.58	13.2	62.0	0.38	3.76	6.37	0.99	0.19	9.33
8H-4, 46.5	–0.5	78.61	1.80	1.52	13.0	62.2	0.32	3.71	7.09	1.01	0.19	9.15
8H-4, 47	–0.5	78.61	1.86	1.36	12.9	60.5	0.33	3.63	9.32	0.98	0.20	8.98
8H-4, 47.5	–0.5	78.62	1.31	1.49	12.7	60.6	0.35	3.74	9.51	1.04	0.19	9.12
8H-4, 48	–0.5	78.62	1.29	1.57	13.3	62.8	0.37	3.85	6.31	1.06	0.17	9.26
8H-4, 48.5	–0.5	78.63	1.57	1.52	13.2	62.7	0.39	3.89	6.06	1.05	0.18	9.43
8H-4, 49	–0.5	78.63	1.19	1.48	13.1	62.2	0.43	4.03	6.37	1.08	0.19	9.97
8H-4, 49.5	–0.5	78.64	2.01	1.55	12.6	62.0	0.36	3.90	6.17	1.06	0.16	10.3
8H-4, 50	–0.5	78.64	1.62	1.39	12.4	62.7	0.36	3.77	5.98	1.02	0.15	10.6
8H-4, 50.5	–0.5	78.65	1.89	1.17	12.2	60.4	0.54	3.70	7.72	0.98	0.16	11.2
8H-4, 51	–0.5	78.65	1.43	1.47	12.2	55.6	0.54	3.57	12.8	0.99	0.22	11.1
8H-4, 51.5	–0.5	78.66	0.84	1.33	11.8	55.6	0.41	3.78	15.1	1.01	0.24	9.97
8H-4, 52	–0.5	78.66	1.99	1.14	12.7	61.1	0.42	3.68	8.63	1.00	0.17	9.20
8H-4, 52.5	–0.5	78.67	1.24	1.33	13.3	63.2	0.33	3.81	6.01	1.03	0.16	9.63
8H-4, 53	–0.5	78.67	1.56	1.24	13.0	62.6	0.38	3.82	6.48	1.04	0.17	9.76
8H-4, 53.5	–0.5	78.68	0.92	1.39	13.0	62.5	0.36	3.90	6.83	1.04	0.16	9.90
8H-4, 54	–0.5	78.68	1.03	1.26	12.8	62.2	0.33	3.87	7.40	1.02	0.16	9.91
8H-4, 54.5	–0.5	78.69	2.35	1.48	12.6	61.3	0.38	3.84	7.27	0.99	0.15	9.64
8H-4, 55	–0.5	78.69	1.27	1.40	12.6	61.7	0.43	3.84	7.49	1.05	0.17	10.1
8H-4, 40	–1	78.54	1.20	1.05	13.0	62.3	0.40	4.06	6.57	1.11	0.16	10.2
8H-4, 40.5	–1	78.55	2.06	1.24	12.8	61.8	0.43	3.98	6.36	1.08	0.17	10.1
8H-4, 41	–1	78.55	1.00	1.18	12.7	62.1	0.43	4.12	6.75	1.11	0.17	10.5
8H-4, 41.5	–1	78.56	1.46	1.49	13.1	62.2	0.56	3.77	6.50	0.98	0.15	9.83
8H-4, 42	–1	78.56	1.69	1.45	12.8	61.5	0.49	3.77	6.32	0.99	0.16	10.8
8H-4, 42.5	–1	78.57	1.17	1.37	12.5	62.0	0.44	3.82	6.52	1.00	0.16	11.0
8H-4, 43	–1	78.57	1.60	1.43	12.7	61.7	0.36	3.71	7.33	0.97	0.17	10.0
8H-4, 43.5	–1	78.58	2.09	1.53	12.5	61.8	0.43	3.59	7.56	0.95	0.17	9.43
8H-4, 44	–1	78.58	1.11	1.31	11.9	64.4	0.39	3.57	6.69	0.95	0.15	9.58
8H-4, 44.5	–1	78.59	2.14	1.50	12.8	61.7	0.43	3.57	7.15	0.96	0.17	9.63
8H-4, 45	–1	78.59	1.72	1.30	13.2	62.7	0.45	3.74	5.93	1.03	0.16	9.83
8H-4, 45.5	–1	78.60	2.11	1.27	12.9	63.1	0.38	3.81	5.58	1.05	0.19	9.66
8H-4, 46	–1	78.60	0.24	1.15	13.3	62.7	0.30	3.80	7.70	1.06	0.19	9.58
8H-4, 46.5	–1	78.61	1.70	1.10	12.6	60.1	0.38	3.76	10.1	1.03	0.20	9.14
8H-4, 47	–1	78.61	1.26	1.61	12.2	58.7	0.38	3.72	11.7	1.01	0.21	9.22
8H-4, 47.5	–1	78.62	1.98	1.49	12.6	60.5	0.42	3.75	8.91	1.03	0.19	9.06
8H-4, 48	–1	78.62	2.08	1.27	13.0	62.8	0.35	3.82	6.20	1.07	0.18	9.21
8H-4, 48.5	–1	78.63	1.55	0.96	13.1	63.2	0.36	3.98	6.01	1.05	0.18	9.59
8H-4, 49	–1	78.63	2.01	1.45	12.7	62.0	0.34	3.98	6.11	1.08	0.19	10.1
8H-4, 49.5	–1	78.64	1.90	1.44	12.5	60.7	0.36	3.90	7.27	1.07	0.18	10.8
8H-4, 50	–1	78.64	1.63	1.40	12.2	58.4	0.38	3.77	10.3	1.05	0.20	10.8
8H-4, 50.5	–1	78.65	1.41	1.33	12.1	57.0	0.58	3.70	12.1	1.00	0.21	10.6
8H-4, 51	–1	78.65	1.90	1.38	11.9	55.7	0.49	3.68	13.3	0.97	0.23	10.4
8H-4, 51.5	–1	78.66	1.75	1.18	12.1	56.6	0.34	3.72	13.4	1.00	0.22	9.64
8H-4, 52	–1	78.66	0.98	1.27	12.9	61.2	0.40	3.69	8.81	1.04	0.18	9.52
8H-4, 52.5	–1	78.67	1.13	1.46	13.2	62.6	0.36	3.75	6.68	1.02	0.18	9.62
8H-4, 53	–1	78.67	1.84	1.31	13.0	62.2	0.39	3.81	6.77	1.02	0.17	9.53
8H-4, 53.5	–1	78.68	1.59	1.17	12.7	62.1	0.41	3.84	7.32	1.02	0.16	9.69
8H-4, 54	–1	78.68	1.37	1.31	12.8	61.9	0.48	3.82	7.30	1.03	0.16	9.83
8H-4, 54.5	–1	78.69	1.72	1.58	12.8	61.8	0.53	3.73	6.85	1.02	0.16	9.85
8H-4, 55	–1	78.69	1.14	1.33	13.0	62.3	0.51	3.84	6.68	1.06	0.18	9.94
8H-4, 40	–1.5	78.54	1.13	1.20	12.3	62.4	0.40	4.17	6.66	1.11	0.18	10.5
8H-4, 40.5	–1.5	78.55	0.61	1.10	12.4	62.5	0.44	4.15	6.96	1.14	0.18	10.6
8H-4, 41	–1.5	78.55	1.43	1.10	12.3	61.7	0.48	4.15	6.99	1.11	0.17	10.6
8H-4, 41.5	–1.5	78.56	1.44	1.24	12.9	61.6	0.51	3.87	7.05	1.00	0.17	10.2
8H-4, 42	–1.5	78.56	2.03	1.51	12.2	60.5	0.60	3.77	6.77	1.03	0.17	11.4
8H-4, 42.5	–1.5	78.57	1.12	1.18	12.3	61.1	0.43	3.73	7.96	1.04	0.17	11.0
8H-4, 43	–1.5	78.57	1.90	1.43	12.7	61.1	0.37	3.68	7.90	0.99	0.18	9.69
8H-4, 43.5	–1.5	78.58	1.92	1.29	12.5	62.2	0.33	3.64	7.05	1.01	0.17	9.87
8H-4, 44	–1.5	78.58	1.03	1.43	11.8	62.0	0.35	3.52	8.97	0.91	0.19	9.80
8H-4, 44.5	–1.5	78.59	1.87	1.16	12.7	61.2	0.35	3.70	8.07	1.03	0.18	9.69
8H-4, 45	–1.5	78.59	1.72	1.56	13.1	63.2	0.39	3.80	5.23	1.02	0.15	9.81

Table T6 (continued).

Core, section, interval (cm)	Section width (cm)	Midpoint depth (mbsf)	Na_2O (wt%)	MgO (wt%)	Al_2O_3 (wt%)	SiO_2 (wt%)	P_2O_5 (wt%)	K_2O (wt%)	CaO (wt%)	TiO_2 (wt%)	MnO (wt%)	Fe_2O_3 (wt%)
8H-4, 45.5	–1.5	78.60	0.99	1.25	13.2	63.7	0.31	3.91	5.75	1.07	0.17	9.73
8H-4, 46	–1.5	78.60	0.90	1.32	12.8	60.9	0.34	3.74	9.44	1.00	0.19	9.40
8H-4, 46.5	–1.5	78.61	1.63	1.36	12.0	57.2	0.40	3.63	13.5	1.00	0.20	9.18
8H-4, 47	–1.5	78.61	0.79	1.20	12.2	58.1	0.40	3.76	12.8	1.04	0.21	9.47
8H-4, 47.5	–1.5	78.62	1.46	1.30	13.3	61.9	0.37	3.78	7.55	1.04	0.19	9.15
8H-4, 48	–1.5	78.62	2.30	1.49	13.3	62.8	0.40	3.77	5.76	1.04	0.18	9.04
8H-4, 48.5	–1.5	78.63	0.95	1.14	13.1	63.2	0.42	3.95	6.28	1.07	0.19	9.71
8H-4, 49	–1.5	78.63	1.66	1.46	12.4	61.8	0.35	3.94	6.77	1.07	0.17	10.4
8H-4, 49.5	–1.5	78.64	1.74	1.07	12.2	58.2	0.37	3.80	10.9	1.07	0.22	10.5
8H-4, 50	–1.5	78.64	1.91	1.41	11.9	54.8	0.36	3.70	14.8	1.03	0.23	9.87
8H-4, 50.5	–1.5	78.65	1.90	1.29	12.0	56.4	0.39	3.70	13.9	1.00	0.20	9.22
8H-4, 51	–1.5	78.65	1.86	1.51	12.5	57.5	0.36	3.68	12.0	1.01	0.21	9.49
8H-4, 51.5	–1.5	78.66	2.12	1.29	12.8	59.2	0.37	3.71	9.94	1.00	0.18	9.43
8H-4, 52	–1.5	78.66	1.45	1.37	13.2	62.3	0.34	3.80	6.75	1.00	0.16	9.67
8H-4, 52.5	–1.5	78.67	2.09	1.42	13.1	62.3	0.36	3.75	6.07	1.01	0.16	9.74
8H-4, 53	–1.5	78.67	1.07	1.23	13.0	62.5	0.38	3.86	6.78	1.04	0.17	9.96
8H-4, 53.5	–1.5	78.68	1.58	1.08	12.8	61.5	0.45	3.86	7.69	1.04	0.16	9.85
8H-4, 54	–1.5	78.68	1.61	1.08	12.9	61.9	0.46	3.78	7.50	1.04	0.16	9.62
8H-4, 54.5	–1.5	78.69	1.37	1.72	12.6	61.7	0.47	3.82	7.47	1.04	0.18	9.63
8H-4, 55	–1.5	78.69	1.80	1.40	13.3	62.4	0.41	3.74	6.35	1.00	0.17	9.50
8H-4, 40	–2	78.54	1.42	1.35	12.3	61.9	0.40	4.12	6.80	1.10	0.17	10.5
8H-4, 40.5	–2	78.55	1.45	1.31	12.2	61.5	0.45	4.16	6.88	1.12	0.18	10.7
8H-4, 41	–2	78.55	0.89	1.27	12.2	61.5	0.44	4.20	7.02	1.11	0.17	11.1
8H-4, 41.5	–2	78.56	1.12	1.27	12.5	61.6	0.51	3.92	6.35	1.06	0.17	11.4
8H-4, 42	–2	78.56	1.53	1.30	12.1	60.6	0.47	3.90	6.94	1.06	0.17	11.9
8H-4, 42.5	–2	78.57	2.36	1.52	12.4	61.0	0.32	3.78	7.12	1.00	0.18	10.3
8H-4, 43	–2	78.57		1.21	13.0	63.9	0.31	3.80	6.43	1.05	0.15	10.1
8H-4, 43.5	–2	78.58	1.47	1.47	12.9	62.0	0.32	3.71	7.22	1.00	0.17	9.80
8H-4, 44	–2	78.58	1.72	1.06	12.2	60.0	0.39	3.68	9.89	1.00	0.20	9.93
8H-4, 44.5	–2	78.59	2.09	1.27	12.5	60.9	0.34	3.65	8.39	1.01	0.18	9.69
8H-4, 45	–2	78.59	1.09	1.55	12.6	62.5	0.40	3.80	6.77	1.01	0.16	10.1
8H-4, 45.5	–2	78.60	1.67	1.61	12.9	61.8	0.35	3.79	6.94	1.04	0.18	9.74
8H-4, 46	–2	78.60	0.22	1.48	12.8	61.3	0.33	3.90	8.87	1.06	0.19	9.83
8H-4, 46.5	–2	78.61	1.10	1.50	12.4	58.3	0.52	3.73	11.6	1.03	0.20	9.65
8H-4, 47	–2	78.61	0.95	1.24	12.3	59.0	0.47	3.80	11.0	1.05	0.22	9.99
8H-4, 47.5	–2	78.62	1.08	1.17	13.1	62.1	0.37	3.87	7.58	1.06	0.19	9.55
8H-4, 48	–2	78.62	1.99	1.41	13.1	62.7	0.38	3.80	6.04	1.06	0.17	9.39
8H-4, 48.5	–2	78.63	1.52	1.48	12.4	62.1	0.42	3.93	6.34	1.09	0.18	10.5
8H-4, 49	–2	78.63	0.90	1.45	12.1	61.7	0.39	3.88	7.34	1.06	0.18	11.0
8H-4, 49.5	–2	78.64	1.45	1.44	11.7	56.6	0.42	3.78	12.6	1.04	0.23	10.8
8H-4, 50	–2	78.64	1.57	1.21	11.7	54.6	0.36	3.77	15.3	1.07	0.25	10.2
8H-4, 50.5	–2	78.65	1.44	1.30	12.4	56.9	0.40	3.79	12.9	1.05	0.20	9.60
8H-4, 51	–2	78.65	1.39	1.52	12.9	59.7	0.36	3.78	9.16	1.03	0.18	9.99
8H-4, 51.5	–2	78.66	1.50	1.41	13.0	62.3	0.37	3.81	6.51	1.03	0.16	9.90
8H-4, 52	–2	78.66	2.21	1.25	13.4	62.6	0.35	3.68	5.62	1.01	0.16	9.74
8H-4, 52.5	–2	78.67	1.88	1.27	13.2	62.6	0.37	3.76	5.90	1.01	0.16	9.83
8H-4, 53	–2	78.67	1.37	1.45	13.1	62.1	0.35	3.78	6.80	1.04	0.17	9.87
8H-4, 53.5	–2	78.68		1.28	12.8	61.9	0.37	3.91	8.43	1.11	0.17	10.1
8H-4, 54	–2	78.68	2.21	1.28	12.8	61.5	0.39	3.78	7.47	0.99	0.16	9.37
8H-4, 54.5	–2	78.69	2.81	1.83	13.0	61.2	0.38	3.65	6.65	0.99	0.16	9.35
8H-4, 55	–2	78.69	0.59	1.35	13.5	63.4	0.40	3.77	6.10	1.04	0.16	9.70

Table T7. XRF core scanning results (resolution of 1 cm, measurement time of 40 ms) for a vertical line scan of interval 338-C0022B-38X-5, 0–142 cm. The line scan was taken 1 cm to the right of the center. (Continued on next two pages.)

Core, section, interval (cm)	Midpoint depth (mbsf)	Na_2O (wt%)	MgO (wt%)	Al_2O_3 (wt%)	SiO_2 (wt%)	P_2O_5 (wt%)	K_2O (wt%)	CaO (wt%)	TiO_2 (wt%)	MnO (wt%)	Fe_2O_3 (wt%)
338-C0022B-											
38X-5, 0	386.09	3.44	3.11	12.9	66.5	3.62	2.47	3.25	1.26	0.12	3.29
38X-5, 1	386.10	1.75	1.43	9.98	57.2	0.43	4.62	6.19	1.46	0.19	16.8
38X-5, 2	386.11	0.78	1.29	9.76	58.6	0.35	4.68	5.41	1.52	0.19	17.4
38X-5, 3	386.12	1.55	1.49	9.94	57.5	0.30	4.47	6.56	1.45	0.20	16.6
38X-5, 4	386.13	0.74	1.18	10.0	55.6	0.47	4.47	9.95	1.43	0.23	15.9
38X-5, 5	386.14		1.16	9.84	58.2	0.32	4.59	7.54	1.43	0.21	16.7

Table T7 (continued). (Continued on next page.)

Core, section, interval (cm)	Midpoint depth (mbsf)	Na_2O (wt%)	MgO (wt%)	Al_2O_3 (wt%)	SiO_2 (wt%)	P_2O_5 (wt%)	K_2O (wt%)	CaO (wt%)	TiO_2 (wt%)	MnO (wt%)	Fe_2O_3 (wt%)
38X-5, 6	386.15	1.74	1.30	9.33	57.2	0.42	4.47	7.11	1.42	0.29	16.8
38X-5, 7	386.16	3.59	2.03	8.87	54.4	0.41	4.51	7.36	1.51	0.24	17.0
38X-5, 8	386.17	0.52	2.11	9.70	54.9	0.71	4.42	7.46	1.61	0.27	18.3
38X-5, 9	386.18	5.65	3.60	9.45	51.8	1.09	4.04	5.22	1.29	0.17	17.7
38X-5, 10	386.19		2.09	9.29	56.4	0.86	4.56	3.83	1.45	0.21	21.3
38X-5, 11	386.20	1.88	1.53	10.2	56.6	0.61	4.33	6.59	1.51	0.18	16.6
38X-5, 12	386.21		1.90	10.3	58.8	0.52	4.21	6.17	1.59	0.19	16.3
38X-5, 13	386.22	2.63	1.81	10.4	58.5	0.46	4.15	5.20	1.46	0.19	15.2
38X-5, 14	386.23		1.03	11.3	60.9	0.54	4.20	4.32	1.29	0.14	16.3
38X-5, 15	386.24	3.16	1.47	11.2	59.5	0.59	3.95	4.39	1.25	0.15	14.4
38X-5, 16	386.25	1.74	1.15	12.1	59.7	0.48	4.35	4.07	1.38	0.17	14.8
38X-5, 17	386.26	2.82	1.94	11.4	59.7	0.40	4.25	3.79	1.36	0.19	14.3
38X-5, 18	386.27	3.96	1.86	10.8	58.4	0.47	4.26	3.94	1.30	0.18	14.9
38X-5, 19	386.28	6.40	1.84	11.4	57.8	0.40	4.23	3.05	1.28	0.14	13.5
38X-5, 20	386.29	3.52	0.71	10.1	55.0	0.67	4.66	3.43	1.60	0.13	20.2
38X-5, 21	386.30	0.12	2.69	10.4	57.4	1.41	4.28	4.32	1.37	0.15	17.9
38X-5, 22	386.31		2.05	9.6	54.5	0.85	4.73	6.37	1.67	0.24	20.0
38X-5, 23	386.32	0.50	2.07	8.5	55.3	0.59	4.61	8.23	1.65	0.27	18.3
38X-5, 24	386.33	3.06	1.61	10.3	58.7	0.54	4.14	5.52	1.44	0.16	14.6
38X-5, 25	386.34	1.67	1.85	11.6	61.9	0.39	3.93	3.66	1.28	0.12	13.7
38X-5, 26	386.35		1.27	11.4	62.5	0.58	4.06	4.78	1.29	0.17	14.0
38X-5, 27	386.36	2.34	1.33	11.9	60.7	0.41	3.93	6.05	1.24	0.19	12.6
38X-5, 28	386.37	2.04	1.14	11.5	59.5	0.45	3.90	6.87	1.28	0.20	13.0
38X-5, 29	386.38	1.31	1.01	11.1	59.3	0.59	4.07	7.34	1.28	0.23	13.7
38X-5, 30	386.39	1.40	1.75	10.1	57.8	0.45	4.06	7.81	1.39	0.26	15.0
38X-5, 31	386.40	1.85	1.20	8.87	55.2	0.48	4.36	8.82	1.54	0.23	17.5
38X-5, 32	386.41		0.62	8.91	56.1	0.51	4.52	8.94	1.63	0.21	18.6
38X-5, 33	386.42		1.38	9.36	56.1	0.91	4.19	8.38	1.55	0.21	18.0
38X-5, 34	386.43		1.13	9.93	57.7	0.79	4.08	7.28	1.61	0.20	17.3
38X-5, 35	386.44		2.00	10.4	57.5	0.46	4.10	6.44	1.52	0.23	17.3
38X-5, 36	386.45	4.15	1.73	9.73	55.2	0.63	3.60	6.74	1.51	0.21	16.5
38X-5, 37	386.46	7.49	1.43	10.2	56.6	0.66	3.03	6.61	1.24	0.23	12.5
38X-5, 38	386.47		2.03	10.2	56.2	0.62	3.92	8.96	1.50	0.26	16.3
38X-5, 39	386.48	0.97	0.84	10.4	59.2	0.45	4.17	7.54	1.48	0.21	14.7
38X-5, 40	386.49	5.82	1.96	10.9	57.1	0.51	3.57	6.68	1.27	0.13	12.1
38X-5, 41	386.50	0.62	1.41	11.4	62.4	0.46	3.91	4.22	1.29	0.13	14.2
38X-5, 42	386.51	3.36	1.71	10.2	58.9	0.39	3.91	3.75	1.26	0.17	16.8
38X-5, 43	386.52	4.06	2.05	9.15	55.6	0.95	4.11	5.33	1.38	0.20	17.2
38X-5, 44	386.53	3.09	1.17	10.5	58.8	0.40	4.16	4.08	1.27	0.15	16.4
38X-5, 45	386.54	5.94	2.20	10.2	56.2	0.37	3.98	5.07	1.22	0.22	14.6
38X-5, 46	386.55	4.02	1.21	10.2	57.6	0.48	4.14	6.31	1.35	0.20	14.5
38X-5, 47	386.56	3.66	1.84	10.8	57.9	0.40	4.01	6.24	1.26	0.23	13.7
38X-5, 48	386.57	2.65	1.53	11.4	57.8	0.48	4.08	6.46	1.25	0.27	14.1
38X-5, 49	386.58	1.70	1.27	11.5	58.7	0.14	3.99	7.56	1.21	0.27	13.7
38X-5, 50	386.59	2.99	1.05	10.7	58.6	0.40	3.98	6.83	1.29	0.23	13.9
38X-5, 51	386.60	3.62	1.26	11.3	57.3	0.43	3.69	7.02	1.35	0.25	13.8
38X-5, 52	386.61	3.81	1.17	9.51	55.5	0.69	3.77	8.06	1.53	0.25	15.7
38X-5, 53	386.62	5.04	1.57	9.45	53.1	0.73	3.57	8.26	1.45	0.24	16.6
38X-5, 54	386.63	3.95	1.97	9.44	53.4	0.58	3.58	8.45	1.60	0.24	16.8
38X-5, 55	386.64	1.17	1.52	10.1	55.2	1.00	3.45	8.23	1.48	0.24	17.6
38X-5, 56	386.65	6.27	1.46	9.01	51.5	0.69	3.42	8.23	1.51	0.28	17.6
38X-5, 57	386.66	6.58	2.53	8.67	51.2	0.81	3.43	8.50	1.27	0.27	16.8
38X-5, 58	386.67	3.28	1.26	9.93	56.7	0.54	3.78	6.80	1.43	0.23	16.1
38X-5, 59	386.68	1.79	0.86	11.0	59.5	0.53	3.64	7.15	1.26	0.21	14.1
38X-5, 60	386.69	4.52	1.57	11.5	56.8	0.45	3.32	7.83	1.21	0.21	12.5
38X-5, 61	386.70	2.89	1.58	10.9	57.5	0.53	3.34	8.42	1.25	0.20	13.4
38X-5, 62	386.71	1.93	1.14	10.6	55.2	0.73	3.88	7.30	1.57	0.24	17.4
38X-5, 63	386.72	2.44	1.42	10.5	57.3	0.39	3.72	8.10	1.34	0.23	14.6
38X-5, 64	386.73	3.40	1.28	10.7	58.8	0.51	3.28	6.49	1.31	0.22	14.1
38X-5, 65	386.74	2.69	1.22	11.3	58.3	0.46	3.24	7.36	1.35	0.22	13.9
38X-5, 66	386.75	6.17	1.70	10.7	54.1	0.87	3.09	7.69	1.30	0.23	14.2
38X-5, 67	386.76	1.59	2.15	9.55	49.9	1.06	3.43	9.99	1.72	0.30	20.3
38X-5, 68	386.77	1.77	1.95	8.36	53.0	1.21	3.31	9.87	1.56	0.26	18.7
38X-5, 69	386.78	1.93	1.82	9.72	56.0	0.60	3.82	8.13	1.53	0.23	16.2
38X-5, 70	386.79	1.18	2.12	9.80	56.3	0.59	4.12	7.00	1.56	0.17	17.2
38X-5, 71	386.80	5.84	1.15	9.75	54.3	0.53	3.60	7.05	1.56	0.21	16.0
38X-5, 72	386.81		1.49	9.77	56.8	0.58	4.12	6.82	1.59	0.18	18.7
38X-5, 73	386.82	2.14	0.75	10.4	56.1	0.64	4.19	5.93	1.50	0.17	18.2
38X-5, 74	386.83	0.41	0.16	10.0	58.3	0.58	4.07	5.65	1.40	0.12	19.3

Table T7 (continued).

Core, section, interval (cm)	Midpoint depth (mbsf)	Na_2O (wt%)	MgO (wt%)	Al_2O_3 (wt%)	SiO_2 (wt%)	P_2O_5 (wt%)	K_2O (wt%)	CaO (wt%)	TiO_2 (wt%)	MnO (wt%)	Fe_2O_3 (wt%)
38X-5, 75	386.84		1.03	9.93	57.6	0.54	4.36	6.69	1.63	0.17	18.1
38X-5, 76	386.85	4.84	2.19	9.64	55.0	0.60	3.96	6.34	1.38	0.19	15.8
38X-5, 77	386.86	4.82	2.12	9.52	53.6	0.50	4.27	7.36	1.39	0.22	16.2
38X-5, 78	386.87	7.45	2.87	9.18	52.7	1.07	3.84	6.42	1.22	0.19	15.1
38X-5, 79	386.88	4.11	2.90	9.58	52.0	0.59	3.83	5.68	1.37	0.25	19.7
38X-5, 80	386.89	3.89	2.80	10.4	54.9	0.82	3.81	5.10	1.28	0.21	16.8
38X-5, 81	386.90	0.76	1.35	10.1	57.4	0.80	4.08	7.01	1.53	0.19	16.8
38X-5, 82	386.91	4.06	2.12	10.4	57.3	0.68	3.87	4.87	1.33	0.14	15.2
38X-5, 83	386.92	2.29	1.78	10.7	58.7	0.60	3.90	4.60	1.35	0.15	16.0
38X-5, 84	386.93	3.62	1.65	11.3	59.1	0.68	3.60	4.73	1.23	0.16	14.0
38X-5, 85	386.94	3.06	1.43	11.7	59.3	0.65	3.79	4.92	1.25	0.19	13.7
38X-5, 86	386.95	2.25	1.93	10.7	59.8	0.56	3.97	5.33	1.35	0.20	14.0
38X-5, 87	386.96	2.53	1.33	11.3	59.7	0.68	3.91	4.40	1.26	0.18	14.8
38X-5, 88	386.97	4.37	1.50	10.8	59.6	0.62	3.52	4.03	1.23	0.15	14.1
38X-5, 89	386.98		1.19	11.3	61.5	0.81	3.95	4.68	1.29	0.20	15.1
38X-5, 90	386.99	1.80	1.53	11.2	60.3	0.59	3.89	4.27	1.35	0.21	14.8
38X-5, 91	387.00	1.25	1.48	11.4	60.4	0.81	3.70	4.56	1.30	0.19	14.9
38X-5, 92	387.01	4.61	1.47	11.7	58.5	0.80	3.24	4.91	1.11	0.19	13.5
38X-5, 93	387.02	2.79	1.64	11.7	59.7	1.08	3.21	4.90	1.14	0.18	13.6
38X-5, 94	387.03	3.33	1.57	11.4	57.9	0.97	3.18	6.70	1.13	0.23	13.6
38X-5, 95	387.04	1.73	1.72	11.4	59.9	0.90	3.29	5.43	1.29	0.20	14.1
38X-5, 96	387.05	3.43	0.73	11.8	60.0	0.90	3.27	5.15	1.09	0.20	13.4
38X-5, 97	387.06	2.11	1.39	11.5	61.0	0.58	3.57	5.47	1.17	0.19	13.0
38X-5, 98	387.07	4.06	1.64	11.9	60.4	0.45	3.48	4.73	1.21	0.17	12.0
38X-5, 99	387.08	4.81	2.01	11.2	59.2	0.63	3.47	4.54	1.22	0.19	12.8
38X-5, 100	387.09	6.18	1.87	11.0	58.3	0.43	3.35	4.81	1.13	0.16	12.8
38X-5, 101	387.10	5.79	1.71	10.7	59.1	0.77	3.49	4.50	1.23	0.22	12.6
38X-5, 102	387.11	2.63	1.14	10.3	59.3	0.47	3.99	5.34	1.42	0.19	15.2
38X-5, 103	387.12	2.91	1.31	10.5	59.4	0.65	4.00	4.60	1.42	0.18	15.0
38X-5, 104	387.13	0.95	2.07	10.9	58.8	0.87	3.67	6.10	1.38	0.19	15.1
38X-5, 105	387.14	2.99	1.86	10.5	55.6	1.45	3.67	3.79	1.15	0.17	18.8
38X-5, 106	387.15	0.92	1.99	10.3	58.8	0.76	3.94	5.67	1.31	0.18	16.1
38X-5, 107	387.16	2.04	2.06	11.1	57.4	0.71	3.37	6.73	1.33	0.21	15.0
38X-5, 108	387.17	2.25	2.00	10.8	57.3	0.63	3.33	7.36	1.28	0.25	14.8
38X-5, 109	387.18	1.72	2.12	9.26	56.1	0.83	4.24	7.93	1.52	0.20	16.0
38X-5, 110	387.19	3.82	2.74	9.38	55.6	0.76	4.04	8.39	1.31	0.20	13.8
38X-5, 111	387.20		1.46	9.19	58.3	0.83	3.91	8.27	1.48	0.24	16.3
38X-5, 112	387.21	2.15	1.89	9.87	56.8	0.68	3.66	7.07	1.36	0.23	16.3
38X-5, 113	387.22	0.57	1.38	11.8	61.1	0.52	3.30	6.74	1.22	0.20	13.1
38X-5, 114	387.23	3.23	1.10	12.2	60.6	0.37	3.30	5.80	1.15	0.20	12.1
38X-5, 115	387.24	3.36	2.08	12.1	60.3	0.39	3.44	5.43	1.16	0.17	11.5
38X-5, 116	387.25	4.73	1.59	11.8	59.9	0.42	3.45	5.24	1.11	0.16	11.6
38X-5, 117	387.26	3.43	1.71	10.5	59.3	0.40	3.58	6.39	1.21	0.19	13.3
38X-5, 118	387.27	5.09	1.64	10.9	56.5	0.59	3.29	7.33	1.16	0.19	13.4
38X-5, 119	387.28	1.92	0.63	10.6	59.3	0.62	3.7	6.73	1.34	0.17	14.9
38X-5, 120	387.29	2.64	0.81	10.4	57.6	0.49	3.51	7.35	1.40	0.20	15.6
38X-5, 121	387.30	0.87	0.99	10.7	60.8	0.46	3.87	5.91	1.43	0.19	14.7
38X-5, 122	387.31	2.74	1.05	10.9	59.6	0.41	3.54	6.01	1.30	0.19	14.2
38X-5, 123	387.32		1.77	10.9	61.0	0.46	3.69	6.21	1.34	0.25	14.4
38X-5, 124	387.33	2.29	2.10	10.3	58.7	0.55	3.64	6.19	1.40	0.18	14.7
38X-5, 125	387.34	4.96	1.40	10.5	57.1	0.65	3.62	6.15	1.30	0.20	14.1
38X-5, 126	387.35		2.00	10.6	57.8	0.79	3.64	5.72	1.60	0.24	17.5
38X-5, 127	387.36	6.12	1.41	11.0	58.4	0.39	3.24	4.99	1.23	0.17	13.0
38X-5, 128	387.37	2.15	0.77	10.3	59.5	0.51	3.63	6.03	1.51	0.17	15.4
38X-5, 129	387.38		2.79	11.2	58.9	0.72	3.65	7.32	1.37	0.18	13.8
38X-5, 130	387.39	2.01	1.05	10.7	61.1	0.50	3.64	5.92	1.28	0.16	13.7
38X-5, 131	387.40		0.64	11.4	61.9	0.51	3.84	5.65	1.37	0.16	14.5
38X-5, 132	387.41	0.44	1.50	10.8	61.6	0.59	3.65	4.87	1.31	0.16	15.1
38X-5, 133	387.42	0.62	1.34	11.9	61.1	0.48	3.48	5.68	1.37	0.20	13.8
38X-5, 134	387.43		1.64	11.2	59.3	0.73	3.53	6.87	1.44	0.21	15.1
38X-5, 135	387.44	3.48	2.01	10.6	58.3	0.60	3.73	5.43	1.39	0.15	14.3
38X-5, 136	387.45	2.53	1.77	10.7	59.9	0.58	3.63	5.65	1.28	0.15	13.9
38X-5, 137	387.46	4.30	1.93	10.7	58.0	0.64	3.89	5.48	1.36	0.16	13.5
38X-5, 138	387.47	0.50	1.01	11.5	60.6	0.38	3.86	5.68	1.37	0.17	14.9
38X-5, 139	387.48	1.11	1.37	11.2	60.4	0.40	3.66	5.84	1.31	0.18	14.6
38X-5, 140	387.49	2.86	2.29	11.2	59.3	0.44	3.31	5.06	1.20	0.18	14.1
38X-5, 141	387.50	0.61	1.48	12.3	61.3	0.44	3.41	5.84	1.29	0.21	13.1
38X-5, 142	387.51		2.13	13.0	63.7	1.82	3.01	5.08	1.06	0.13	10.1

Table T8. Calcareous nannofossils, Hole C0022B. (Continued on next page.)

Age (Ma)	Core, section, interval (cm)	Average depth (mbsf)	Abundance	Preservation	*Calcidiscus leptoporus*	*Calcidiscus macintyrei*	*Calciosolenia murrayi*	*Catinaster coalitus*	*Ceratolithus cristatus*	*Coccolithus pelagicus*	*Discoaster brouweri*	*Discoaster pentaradiatus*	*Discoaster quinqueramus*	*Discoaster surculus*	*Discoaster triradiatus*	*Discoaster variabilis*	*Discosphaera tubifera*	*Emiliania huxleyi*	*Florisphaera profunda*	*Gephyrocapsa* spp. large (>5.5 µm)	*Gephyrocapsa* spp. medium (4–5.5 µm)	*Gephyrocapsa* spp. small (<4 µm)	*Helicosphaera carteri*	*Helicosphaera inversa*	*Helicosphaera sellii*	*Helicosphaera wallichii*	*Oolithotus antillarum*	*Pontosphaera japonica*	*Ponstosphaera* spp.	*Pseudoemiliania lacunosa*	*Reticulofenestra asanoi*	*Reticulofenestra pseudoumbilicus*	*Reticulofenestra* spp.	*Rhabdosphaera clavigera*	*Sphenolithus abies*	*Syracosphaera pulchra*	*Umbellosphaera irregularis*	*Umbilicosphaera rotula*	*Umbilicosphaera sibogae*
	338-C0022B-																																						
<0.291	1H-CC, 25.5–30.5	6.98	V	VG	+		+				re							+	+	+	+	+					+			+				+				+		+
0.436–0.903	2H-CC, 26.5–31.5	28.98	V	G	+					+									+			+	+					+			+				+				+		+
	3H-CC, 27.0–32.0	38.48	A	G	+	re	+			+									+	+	+	+	+				+	+		+				+				+		+
0.903–1.04	4H-CC, 30.0–35.0	47.98	A	G	+		+												+		+	+	+					+		+	+			+				+		+
1.04–1.107	5H-CC, 30.0–35.0	57.48	A	G	+		+			+									+			+	+			+	+	+		+				+				+		+
1.107–1.24	6H-CC, 35.0–40.0	66.98	C	M	+														+	re?			+					+		+			+	+				+		+
1.24–1.34	7H-CC, 45.0–50.0	76.48	C	P	+														+	+	+							+					+							
0.903–1.04	8H-CC, 30.0–35.0	84.48	A	G	+		+		+	+									+		+	+	+					+	+	+			+	+						+
1.24–1.34	9T-CC, 25.0–30.0	89.48	A	G	+		+			+	re								+	+	+	+	+			+		+		+				+			+			+
	10T-CC, 20.0–25.0	94.48	C	P	+	re		re		+									+	+	+	+	+					+	+	+										+
	11T-CC, 14.5–19.5	95.53	A	G	+					+									+	+	+	+	+					+	+	+				+						+
	12X-CC, 31.0–36.0	104.48	A	M	+	re			+	+	re	re	re						+	+		+	+					+	+	+		re		+						+
	13X-CC, 15.5–20.5	109.48	A	M	+		+			+						re			+	+	+	+	+					+	+	+				+				+		
	14X-CC, 30.5–35.5	114.49	V	M	+					+			re						+	+	+	+	+					+	+	+				+						+
	15X-CC, 25.0–30.0	123.60	A	M	+														+	+	+	+						+		+										
1.67–2.06	16X-CC, 39.0–44.0	132.38	A	M	+	+			+	+	re	re							+			+	+					+		+		re	+	+						+
1.34–1.589	17X-CC, 54.0–59.0	142.70	V	G	+	re			+	+		re	re				+		+	+	+	+	+		+	+		+	+	+		re		+						+
1.24–1.34	18X-CC, 45.0–50.0	148.46	A	M	+					+				re					+	+	+	+	+					+		+											+
	19X-CC, 66.5–71.5	156.82	V	M	+	re				+									+	+	+	+	+					+													+
	20X-CC, 75.5–80.5	199.98	V	G	+	re	+			+	re	re	re	re					+	+	+	+	+					+		+					+						
	21X-CC, 23.5–28.5	209.31	C	M	+														+	+	+	+	+					+													+
1.34–1.589	22X-CC, 31.0–36.0	211.18	A	M	+	re				+	re	re	re			re			+	+	+	+	+		+			+				re									+
1.589–1.67	23X-CC, 37.0–43.0	228.47	A	M	+				+				re			re			+		+	+	+						+						+	+					+
	24X-CC, 31.0–36.0	275.88	A	G	+	re													+		+	+	+		+				+						+	+					+
	26X-CC, 30.5–35.5	290.48	A	G	+	+				+	re								+			+	+		+			+						+	+					+
	27X-CC, 20.5–25.5	295.48	A	G	+	+			+	+									+		+	+	+		+			+	+			re		+	+					+
	28X-CC, 14.0–19.0	300.48	A	G	+	+				+									+		+	+	+		+				+						+	+					+
1.67–2.06	29X-CC, 35.0–40.0	305.42	A	M	+	+			+	+									+			+	+					+							+						+
	30X-CC, 20.0–25.0	314.23	A	M	+				+	+	re								+			+	+					+													
	31X-CC, 54.5–59.5	324.48	A	G	+	+				+	re								+			+	+		+				+					re	+					+
	32X-CC, 36.0–41.0	326.32	V	M	+	+			+	+	re		re						+			+	+		+				+					re						+
	33X-CC, 29.5–34.5	342.98	V	M	+	+				+						re			+			+	+		+				+			re		+	+					+
	34X-CC, 20.5–25.5	352.50	V	G	+	+				+			re						+			+	+		+			+	+												+
	36X-CC, 33.5–38.5	370.21	A	M	+	+			+	+		re				re			+						+						re			re							
	37X-CC, 36.0–41.0	374.68	C	P		+				+	re								+			+									+										

Table T8 (continued).

Age (Ma)	Core, section, interval (cm)	Average depth (mbsf)	Abundance	Preservation	*Calcidiscus leptoporus*	*Calcidiscus macintyrei*	*Calciosolenia murrayi*	*Catinaster coalitus*	*Ceratolithus cristatus*	*Coccolithus pelagicus*	*Discoaster brouweri*	*Discoaster pentaradiatus*	*Discoaster quinqueramus*	*Discoaster surculus*	*Discoaster triradiatus*	*Discoaster variabilis*	*Discosphaera tubifera*	*Emiliania huxleyi*	*Florisphaera profunda*	*Gephyrocapsa* spp. large (>5.5 µm)	*Gephyrocapsa* spp. medium (4–5.5 µm)	*Gephyrocapsa* spp. small (<4 µm)	*Helicosphaera carteri*	*Helicosphaera inversa*	*Helicosphaera sellii*	*Helicosphaera wallichii*	*Oolithotus antillarum*	*Pontosphaera japonica*	*Ponstosphaera* spp.	*Pseudoemiliania lacunosa*	*Reticulofenestra asanoi*	*Reticulofenestra pseudoumbilicus*	*Reticulofenestra* spp.	*Rhabdosphaera clavigera*	*Sphenolithus abies*	*Syracosphaera pulchra*	*Umbellosphaera irregularis*	*Umbilicosphaera rotula*	*Umbilicosphaera sibogae*
2.06–2.393	38X-CC, 37.5–42.5	390.98	V	M	+	+				+	+				+				+					+					+	+							
	40X-CC, 35.0–40.0	406.83	V	M	+	+				+	+								+					+					+								
>2.393	41X-CC, 34.0–39.0	415.88	A	M	+	+					+	+		+					+			+		+					+			+					+

Abundance: V = very abundant, A = abundant, C = common. Preservation: VG = very good, G = good, M = moderate, P = poor. re = reworked, + = present, ? = uncertain. Median numerical ages for the last consistent occurrence and first consistent occurrence of *Reticulofenestra asanoi* and the first occurrence of large *Gephyrocapsa* are shown.

Table T9. Planktonic foraminifers, Hole C0022B. (Continued on next page.)

Age (Ma)	Core, section, interval (cm)	Average depth (mbsf)	Abundance	Preservation	*Globigerina bulloides*	*Globigerina falconensis*	*Globigerina calida*	*Globigerinella siphonifera*	*Globigerinita glutinata*	*Globigerinita uvula*	*Globigerinoides conglobatus*	*Globigerinoides ruber* (white)	*Globigerinoides ruber* (pink)	*Globigerinoides sacculifer*	*Globoconella inflata* modern form	*Globoconella inflata* transitional form	*Globoconella puncticulata*	*Globorotalia tumida*	*Globoturborotalita obliquus*	*Globoturborotalita rubescens*	*Globoturborotalita tenella*	*Globoturborotalita woodi*	*Hirsutella hirsuta*	*Hirsutella scitula*	*Menardella menardii*	*Neogloboquadrina asanoi*	*Neogloboquadrina* cf. *asanoi*	*Neogloboquadrina dutertrei*	*Neogloboquadrina humerosa*	*Neogloboquadrina incompta*	*Neogloboquadrina inglei*	*Neogloboquadrina kagaensis*	*Neogloboquadrina pachyderma* dextral form	*Neogloboquadrina pachyderma* sinistral form	*Neogloboquadrina praehumerosa*	*Orbulina suturalis*	*Orbulina universa*	*Pulleniatina obliquiloculata* dextral form	*Pulleniatina obliquiloculata* sinistral form	*Sphaeroidinella dehiscens*	*Sphaeroidinellopsis subdehiscens*	*Truncorotalia crassaformis*	*Truncorotalia tosaensis*	*Truncorotalia truncatulinoides*	*Turborotalita quinqueloba*
	338-C0022B-																																							
>0.12	1H-CC, 25.5–30.5	6.98	V	G	+	+			+					+	+	+				+			+	+					+											
>0.61	2H-CC, 26.5–31.5	28.98	V	G	+	+			+		+			+	+	+				+			+	+					+											
	3H-CC, 27.0–32.0	38.48	V	G	+	+		+	+		+	+		+	+	+				+			+	+					+											
	4H-CC, 30.0–35.0	47.98	V	G	+	+	+	+	+		+	+	+	+	+	+		+		+	+		+	+					+											
	5H-CC, 30.0–35.0	57.48	V	G	+	+	+	+			+	+		+	+	+		+		+			+	+					+											
	6H-CC, 35.0–40.0	66.98	C	M	+	+	+		+			+		+	+	+				+			+	+					+											
	7H-CC, 45.0–50.0	76.48	A	M	+	+						+		+	+	+				+			+	+					+											
<1.3	8H-CC, 30.0–35.0	84.48	C	G	+	+						+		+	+	+				+			+	+					+											
>1.3	9T-CC, 25.0–30.0	89.48	A	G	+	+		+	+		+	+		+	+	+		+	+	+																				
	10T-CC, 20.0–25.0	94.48	R	P		+			+		+	+			+																										

Table T9 (continued).

Age (Ma)	Core, section, interval (cm)	Average depth (mbsf)	Abundance	Preservation	*Globigerina bulloides*	*Globigerina falconensis*	*Globigerina calida*	*Globigerinella siphonifera*	*Globigerinita glutinata*	*Globigerinita uvula*	*Globigerinoides conglobatus*	*Globigerinoides ruber* (white)	*Globigerinoides ruber* (pink)	*Globigerinoides sacculifer*	*Globoconella inflata* modern form	*Globoconella inflata* transitional form	*Globoconella puncticulata*	*Globorotalia tumida*	*Globoturborotalita obliquus*	*Globoturborotalita rubescens*	*Globoturborotalita tenella*	*Globoturborotalita woodi*	*Hirsutella hirsuta*	*Hirsutella scitula*	*Menardella menardii*	*Neogloboquadrina asanoi*	*Neogloboquadrina* cf. *asanoi*	*Neogloboquadrina dutertrei*	*Neogloboquadrina humerosa*	*Neogloboquadrina incompta*	*Neogloboquadrina inglei*	*Neogloboquadrina kagaensis*	*Neogloboquadrina pachyderma* dextral form	*Neogloboquadrina pachyderma* sinistral form	*Neogloboquadrina praehumerosa*	*Orbulina suturalis*	*Orbulina universa*	*Pulleniatina obliquiloculata* dextral form	*Pulleniatina obliquiloculata* sinistral form	*Sphaeroidinella dehiscens*	*Sphaeroidinellopsis subdehiscens*	*Truncorotalia crassaformis*	*Truncorotalia tosaensis*	*Truncorotalia truncatulinoides*	*Turborotalita quinqueloba*
	11T-CC, 14.5–19.5	95.53	C	P	+	+			+					+	+	+				+				+	+				+								+			+
	12X-CC, 31.0–36.0	104.48	A	M	+	+			+	+	+	+			+	+		+	+						+				+	+	+				+		+		+	+
	13X-CC, 15.5–20.5	109.48	R	P								+			+	+													+											
	14X-CC, 30.5–35.5	114.49	R	P	+	+			+			+		+	+	+				+								+	+									+	cf		+
	15X-CC, 25.0–30.0	123.60	C	P	+	+	cf							+	+	+		+										+	+									+	cf		
1.7–1.8	16X-CC, 39.0–44.0	132.38	R	P								+			+			+							+			+	+	+							re?		+		
	17X-CC, 54.0–59.0	142.70	C	M	+	+	+	+	+	+		+		+	+	+		+	+									+	+							+			+	+	+
	18X-CC, 45.0–50.0	148.46	C	M	+	+			+			+			+	+		+	+									+											+	+	
	19X-CC, 66.5–71.5	156.82	A	M					+			+		+	+	+	+	+							+			+											+	+	
	20X-CC, 75.5–80.5	199.98	C	M	+	+			+			+		+	+	+				+					+		+	+	+											+	
	21X-CC, 23.5–28.5	209.31	A	G	+	+	+		+			+		+	+	+		+	+					+	+			+	+										+	+	+
	22X-CC, 31.0–36.0	211.18	R	M	+	+			+			+			+	+										re?			+												+	
	23X-CC, 37.0–43.0	228.47	R	P	+				+			+		+	+	+	+						cf					+	+										+	+	+
	24X-CC, 31.0–36.0	275.88	R	P	+	+			+			+		+	+	+													+													
	25X-CC, 15.5–20.5	277.09	C	M		+			+			+		+	+	+				+									+													
1.7	26X-CC, 30.5–35.5	290.48	R	M	+	+			+			+		+	+	+												+	+													
<1.8	27X-CC, 20.5–25.5	295.48	R	M	+	+			+	+				+	+	+								+				+	+												+	
>1.8	28X-CC, 14.0–19.0	300.48	R	M	+	+			+			+		+	+	+		+								+		+	+			+										
	29X-CC, 35.0–40.0	305.42	C	M		+			+			+		+	+	+	+									+		+	+		+	+	+								
	30X-CC, 20.0–25.0	314.23	R	M		+			+						+	+	+									+			+													
	31X-CC, 54.5–59.5	324.48	VR	P	+							+			+	+		+							+				+													
	32X-CC, 36.0–41.0	326.32	VR	P	+							+			+	+		+							+			+	+													
	33X-CC, 29.5–34.5	342.98	VR	P	+	+			+						+	+		+										+	+			+										
<1.93	34X-CC, 20.5–25.5	352.50	R	P	+	+			+			+		+				+									+	+													
>1.93	35X-CC, 66.0–71.0	362.48	B	B																																						
	36X-CC, 33.5–38.5	370.21	VR	P								+		+			+											+													
	37X-CC, 36.0–41.0	374.68	VR	P	+	+			+			+		+	+		+	+									+	+	+											+	
	38X-CC, 37.5–42.5	390.98	VR	P					+			+		+			+							+					+													
	39X-CC, 45.0–50.0	399.20	VR	P																													+									
	40X-CC, 35.0–40.0	406.83	R	P	+	+			+			+			+						+				+	+	+	+	+	+	+	+	+									
	41X-CC, 34.0–39.0	415.88	B	B																																						

Abundance: V = very abundant, A = abundant, C = common, R = rare, VR = very rare. Preservation: G = good, M = moderate, P = poor. re = reworked, + = present, cf = compare, ? = uncertain.

Table T10. Geochemistry of interstitial water in sediment sampled from Hole C0022B. (Continued on next page.)

Core, section, interval (cm)	Depth (mbsf)	Salinity (refractive index)*	pH	Alkalinity (mM)	Chlorinity (mM)	Br^- (mM)	SO_4^{2-} (mM)	PO_4^{3-} (µM)	NH_4^+ (mM)	Na^+ (mM)	K^+ (mM)	Mg^{2+} (mM)	Ca^{2+} (mM)	Li (µM)	B (µM)	Mn (µM)
338-C0022B-																
1H-2, 0–20	1.2	1.33094	7.61	4.5	556.3	0.87	23.6	16.7	0.10	480	12.3	50.6	8.9	36.9	511	3.4
2H-5, 0–8.5	23.4	1.33927	8.03	19.0	587.2	0.97	1.2	65.9	2.12	508	11.7	39.0	3.2	28.3	380	0.4
3H-2, 0–10.5	30.3	1.33931	7.94	17.2	590.6	1.00	1.0	68.1	2.71	522	11.8	37.3	3.4	27.8	384	0.4
4H-2, 0–20	39.5	1.33935	7.77	16.0	597.2	1.07	1.1	66.4	3.45	526	11.5	35.4	3.8	28.2	346	0.5
5H-2, 0–20	49.3	1.33941	7.78	15.5	606.3	1.06	0.9	52.0	4.21	548	11.4	35.8	4.3	33.3	342	0.8
6H-2, 0–20.5	58.6	1.33948	7.74	15.3	613.8	1.13	0.9	54.4	4.84	543	11.0	34.0	5.0	33.0	333	3.4
7H-7, 12–31.5	74.0	1.33954	7.74	14.2	622.1	1.16	ND	34.3	5.73	549	11.6	32.4	5.6	32.5	286	3.7
8H-1, 0–20	76.5	1.33976	7.56	13.7	623.7	1.13	1.3	41.4	5.72	543	10.7	32.5	5.8	32.9	319	3.9
9T-2, 0–21	84.8	1.33952	7.76	12.7	615.3	1.09	3.0	24.9	6.04	548	11.3	33.0	6.3	35.5	283	2.6
10T-2, 0–21	90.3	1.33959	7.48	13.6	623.9	1.14	1.6	41.5	6.13	562	10.7	33.6	6.5	34.6	317	3.3
11T-1, 0–4	94.5	1.33942	7.73	10.5	595.4	1.04	6.6	21.3	5.05	529	11.6	34.5	6.8	36.0	302	2.3
12X-1, 120.4–140.5	99.5	1.33963	7.58	13.4	628.2	1.16	1.4	30.8	6.19	564	10.6	32.8	6.7	36.0	309	3.4
13X-1, 30–50	104.5	1.33962	7.58	13.3	629.0	1.13	1.5	37.8	6.30	551	10.4	32.0	6.7	37.2	315	3.0
14X-4, 60–80	114.1	1.33880	7.83	11.3	547.3	0.99	2.9	28.7	5.64	488	9.3	28.1	6.0	35.2	256	2.6
15X-3, 110–130	118.5	1.33965	7.58	12.8	633.3	1.13	1.8	37.9	6.57	563	10.5	32.1	7.0	40.3	314	3.7
16X-4, 0–27	127.5	1.33868	7.67	10.7	540.9	1.00	1.6	18.8	5.63	487	9.1	27.2	6.2	40.7	238	2.7
17X-2, 11–32	134.8	1.33967	7.56	12.2	640.5	1.20	2.0	23.1	6.91	565	9.6	31.7	7.4	43.8	298	3.1
18X-4, 0–21.5	145.6	1.33968	7.61	12.2	635.3	1.23	1.5	19.2	6.94	565	10.4	30.4	7.3	46.5	294	3.7
19X-2, 10–31.5	153.4	1.33969	7.70	10.7	634.5	1.16	2.5	23.0	6.75	600	10.8	32.8	8.1	48.0	297	4.2
20X-4, 0–21.5	193.6	1.33970	7.59	10.7	637.4	1.20	2.1	14.4	6.59	598	9.9	29.4	8.3	56.0	285	4.7
21X-6, 0–22	204.3	1.33968	7.60	9.9	631.3	1.18	2.9	14.4	6.33	578	9.7	28.6	8.0	55.8	291	4.3
22X-1, 98–118	210.5	1.33969	7.66	10.2	638.5	1.20	2.0	12.1	6.41	584	9.7	27.8	8.0	57.7	282	4.8
23X-4, 0–25	221.2	1.33968	7.69	10.3	633.5	1.16	2.8	9.8	6.30	589	9.6	27.8	8.2	53.1	248	4.2
24X-3, 0–30.5	268.7	1.33968	7.72	9.6	637.4	1.19	2.1	ND	5.80	583	9.0	25.1	8.3	56.2	236	4.3
25X-1, 0–7.5	276.0	1.33968	7.78	9.8	623.7	1.18	4.7	ND	5.13	567	9.3	26.8	8.6	54.6	250	3.7
26X-3, 0–30	288.3	1.33965	7.74	8.2	635.0	1.21	2.0	ND	5.56	604	9.0	24.6	8.5	56.3	229	4.2
27X-4, 0–31	294.3	1.33970	7.75	9.6	641.3	1.23	1.2	ND	5.35	614	9.2	24.5	8.8	55.3	233	4.1
28X-3, 0–35	297.4	1.33967	7.87	9.3	636.5	1.18	2.4	ND	5.34	587	8.8	24.0	8.5	55.5	245	4.3
29X-2, 0–40.5	301.3	1.33968	7.77	10.2	640.3	1.18	1.6	ND	5.27	590	8.9	23.4	8.6	58.8	210	4.5
30X-3, 0–41	307.3	1.33964	8.04	8.9	633.7	1.26	2.5	ND	5.12	595	9.2	23.7	8.7	54.2	198	3.5
31X-2, 0–39.5	315.9	1.33965	7.84	9.1	635.3	1.19	1.7	ND	4.84	600	8.9	23.3	8.8	52.8	216	4.8
33X-7, 0–40.5	341.7	1.33959	7.80	7.8	630.1	1.24	2.7	5.7	4.52	578	8.7	22.1	8.5	51.7	224	4.8
34X-3, 0–41	345.4	1.33955	7.82	8.4	627.4	1.20	2.4	7.2	4.42	587	8.9	21.7	8.7	49.1	229	5.6
35X-5, 0–40	357.8	1.33955	7.77	8.3	621.4	1.16	3.8	ND	4.20	573	8.6	22.1	9.0	48.9	216	6.6
36X-3, 0–41	364.2	1.33951	7.91	7.9	618.6	1.16	3.9	ND	4.04	571	8.8	21.8	8.9	47.0	230	5.6
37X-2, 17–39.5	373.1	1.33950	7.88	7.5	624.3	1.20	2.2	6.0	4.01	575	8.9	19.1	8.9	47.6	208	5.2
38X-3, 0–40	384.3	1.33954	8.05	7.0	627.4	1.20	3.1	3.8	3.96	576	9.2	19.6	9.1	51.2	240	6.0
39X-2, 0–41	391.0	1.33946	8.08	6.7	620.7	1.25	2.8	ND	3.82	586	9.3	18.7	9.6	49.9	247	7.9
40X-3, 0–41	403.2	1.33950	8.01	7.1	624.8	1.19	2.1	3.8	3.73	577	9.0	17.5	9.9	54.4	289	10.9
41X-2, 20–60	411.4	1.33947	8.05	6.9	626.8	1.16	2.2	3.7	3.65	582	9.1	17.0	10.3	56.0	328	12.0

* = salinity was calculated from refractive index. ND = not detected.

Table T10 (continued).

Core, section, interval (cm)	Depth (mbsf)	Fe (μM)	Si (μM)	Sr (μM)	Ba (μM)	V (nM)	Cu (nM)	Zn (nM)	Rb (nM)	Mo (nM)	Cs (nM)	Pb (nM)	U (nM)
338-C0022B-													
1H-2, 0–20	1.2	1.8	732	94	1	80.6	95	273	1728	9	3.73	0.26	5.39
2H-5, 0–8.5	23.4	1.7	687	101	86	38.0	104	915	1391	ND	3.36	0.61	3.40
3H-2, 0–10.5	30.3	1.5	753	102	80	32.6	57	642	1308	3	3.30	0.32	1.68
4H-2, 0–20	39.5	3.0	693	107	83	39.2	104	361	1215	13	3.57	0.31	5.49
5H-2, 0–20	49.3	3.8	780	107	89	32.4	52	179	1136	7	3.28	0.16	0.86
6H-2, 0–20.5	58.6	10.6	739	114	87	22.8	341	1103	1121	7	3.72	1.17	0.58
7H-7, 12–31.5	74.0	24.9	651	115	95	22.0	339	1056	1221	29	4.65	2.26	1.89
8H-1, 0–20	76.5	63.5	762	117	90	19.2	1805	916	1136	23	4.48	1.09	0.67
9T-2, 0–21	84.8	9.7	635	113	33	31.5	248	693	1220	203	5.20	0.54	1.64
10T-2, 0–21	90.3	65.7	808	122	96	17.1	1011	1066	1070	32	3.79	2.27	0.73
11T-1, 0–4	94.5	7.5	647	102	6	25.3	1180	1375	1199	172	4.37	1.09	3.03
12X-1, 120.4–140.5	99.5	48.5	847	123	99	18.5	1555	1115	1090	18	4.27	1.15	0.54
13X-1, 30–50	104.5	25.9	867	126	101	21.6	792	826	1092	39	4.30	1.19	0.77
14X-4, 60–80	114.1	33.9	595	99	12	17.2	253	1309	1026	72	4.09	0.37	1.01
15X-3, 110–130	118.5	59.5	812	126	101	18.3	875	1101	1103	28	4.46	1.23	0.86
16X-4, 0–27	127.5	27.8	608	104	79	19.2	194	635	1033	131	4.40	1.11	2.48
17X-2, 11–32	134.8	46.5	833	122	93	16.9	413	585	1060	68	4.46	1.38	0.66
18X-4, 0–21.5	145.6	29.5	759	126	96	25.2	1357	1078	1152	112	5.24	1.06	1.65
19X-2, 10–31.5	153.4	27.0	699	120	43	17.5	50	376	1141	103	5.11	0.29	1.06
20X-4, 0–21.5	193.6	35.5	840	125	73	19.3	1178	1212	1078	77	5.06	1.11	1.01
21X-6, 0–22	204.3	13.2	942	118	65	20.0	1372	920	1043	66	4.93	0.80	1.22
22X-1, 98–118	210.5	11.9	792	120	67	15.7	499	595	1106	131	6.22	0.43	1.05
23X-4, 0–25	221.2	5.3	802	118	62	18.1	427	363	1018	100	5.12	0.57	1.23
24X-3, 0–30.5	268.7	0.6	750	120	59	14.8	523	575	987	116	5.88	ND	0.65
25X-1, 0–7.5	276.0	0.7	735	111	17	18.5	828	1806	1024	218	5.79	0.45	1.82
26X-3, 0–30	288.3	5.1	914	116	60	14.6	203	438	919	79	4.78	ND	0.55
27X-4, 0–31	294.3	0.6	913	119	61	15.0	973	1399	958	42	5.49	0.12	0.54
28X-3, 0–35	297.4	0.7	861	117	57	14.4	938	779	925	43	5.43	0.10	0.99
29X-2, 0–40.5	301.3	3.9	849	121	60	13.1	642	472	947	34	5.84	ND	0.45
30X-3, 0–41	307.3	0.6	684	118	58	22.2	606	417	975	103	6.06	0.66	1.90
31X-2, 0–39.5	315.9	0.8	820	117	57	15.2	269	395	916	63	5.75	ND	0.67
33X-7, 0–40.5	341.7	0.6	836	115	52	20.5	1238	553	950	148	6.46	0.79	1.41
34X-3, 0–41	345.4	0.6	805	113	52	14.4	301	787	968	164	6.47	ND	1.74
35X-5, 0–40	357.8	0.6	762	113	29	15.5	7956	802	961	83	6.71	0.26	1.78
36X-3, 0–41	364.2	0.6	743	111	23	22.2	991	1155	973	110	6.55	0.14	1.29
37X-2, 17–39.5	373.1	0.6	798	113	45	17.3	1370	1154	1081	211	7.21	0.85	2.00
38X-3, 0–40	384.3	0.7	728	115	41	21.0	859	336	1160	327	7.60	0.51	3.44
39X-2, 0–41	391.0	0.8	696	112	38	15.8	230	527	1170	141	7.90	0.27	1.98
40X-3, 0–41	403.2	0.6	710	116	36	17.1	2781	763	1229	132	8.56	0.56	1.33
41X-2, 20–60	411.4	0.6	688	115	35	19.6	624	379	1311	92	8.89	0.27	0.97

Table T11. Geochemistry of liquid in core liner sampled from Hole C0022B. (Continued on next page.)

Core, section, interval (cm)	Depth (mbsf)	Salinity (refractive index)*	pH	Alkalinity (mM)	Chlorinity (mM)	PO_4^{3-} (μM)	NH_4^+ (mM)	Br^- (mM)	SO_4^{2-} (mM)	Na^+ (mM)	K^+ (mM)	Mg^{2+} (mM)	Ca^{2+} (mM)	Li (μM)	B (μM)	Mn (μM)
338-C0022B																
1H-1	0.0	1.33942	7.39	2.4	557.1	3.8	ND	0.8	26.6	468.3	10.6	52.3	10.3	40.3	409.9	0.8
8H-1	76.5	1.33930	7.78	3.3	552.8	12.9	1.7	0.8	23.6	469.7	11.5	47.6	9.3	37.6	359.1	3.2
9T-1	84.5	1.33932	7.60	2.2	550.9	ND	0.1	0.9	26.3	467.0	10.1	52.1	10.3	33.3	419.9	1.0
10T-1	89.5	1.33936	7.57	2.4	553.2	3.4	0.3	0.9	26.5	467.3	10.2	51.8	10.2	34.3	413.3	1.0
11T-1	94.5	1.33925	8.21	2.5	542.2	ND	0.2	0.8	26.1	460.9	11.3	50.7	10.8	32.3	394.7	0.7
12X-1	99.5	1.33935	7.32	2.0	550.9	2.6	0.5	0.8	26.0	473.9	9.7	52.4	10.4	34.5	405.3	9.0
13X-1	104.5	1.33934	7.62	2.2	546.2	ND	0.4	0.9	26.6	469.7	10.4	51.9	10.4	32.3	411.9	1.5
15X-1	114.5	1.33937	7.46	2.9	554.4	6.3	2.5	0.9	23.4	482.5	11.1	47.0	9.3	36.8	418.0	3.5
17X-5, 106	138.9	1.33952	7.79	6.0	584.1	9.0	5.3	1.0	16.4	507.5	9.8	41.8	8.6	39.6	343.7	4.2
18X-5, 66	146.6	1.33931	7.50	4.5	559.1	4.4	4.2	0.9	19.7	481.3	9.7	43.0	8.9	42.1	341.8	4.5
22X-1	209.5	1.33937	7.80	1.7	551.2	ND	0.5	0.8	26.0	467.4	9.8	51.2	10.1	35.3	408.9	1.5
24X-1	266.5	1.33942	7.94	NA	563.9	ND	2.6	0.9	21.6	495.4	9.7	44.2	9.7	41.1	337.8	4.1
25X-1	276.0	1.33940	7.94	2.2	552.7	ND	0.2	0.8	26.4	472.2	10.0	52.1	10.3	37.0	422.8	1.4
26X-1	285.5	1.33939	7.94	2.0	554.7	ND	0.7	0.8	25.9	474.8	9.7	51.1	10.3	35.3	404.7	2.0
27X-1	290.5	1.33942	7.93	2.0	553.0	ND	0.4	0.8	26.4	475.1	9.5	51.9	10.3	35.7	410.5	1.4
28X-1	295.5	1.33957	7.88	2.3	555.1	ND	0.7	0.8	25.8	478.5	9.7	50.8	10.3	37.4	398.4	1.8
29X-1	300.5	1.33940	7.49	1.9	552.7	ND	0.3	0.9	26.7	472.3	10.0	52.0	10.3	37.0	414.7	1.7
30X-1	305.5	1.33939	7.81	2.7	553.7	ND	1.1	0.9	24.5	473.5	10.1	48.5	9.9	37.9	399.8	3.4
32X-1	324.5	1.33936	7.83	2.5	550.9	2.5	1.2	0.8	25.0	483.9	10.4	49.5	10.1	37.9	392.9	2.8
33X-4	337.9	1.33951	7.61	5.0	589.5	ND	3.5	1.0	16.0	519.7	8.0	36.4	9.8	41.5	272.2	6.9
34X-1	343.5	1.33948	7.82	3.5	561.6	ND	2.0	0.9	21.5	498.4	9.2	44.1	10.0	36.7	356.4	5.5
36X-1	362.5	1.33947	7.86	1.8	554.9	ND	0.5	0.8	25.8	476.5	9.4	51.3	10.3	35.8	402.6	2.6
37X-1	372.0	1.33939	8.05	2.5	551.5	ND	0.3	0.8	26.2	476.3	10.2	51.8	10.3	35.3	403.1	1.8
38X-6	387.8	1.33943	7.63	4.6	585.0	2.7	3.1	1.0	15.6	520.9	8.2	32.9	10.1	44.7	241.3	10.6
39X-1	391.0	1.33938	7.83	2.7	557.8	ND	0.8	0.9	24.4	481.6	9.6	48.9	10.3	39.4	379.0	5.6
40X-1	400.5	1.33936	7.89	2.4	553.7	ND	0.3	0.8	26.0	473.9	9.9	51.1	10.3	36.7	407.8	4.0
41X-1	410.0	1.33940	7.88	2.3	553.5	ND	3.7	0.9	26.0	473.9	10.0	51.2	10.4	36.8	403.1	3.4

* = salinity was calculated from refractive index. NA = not analyzed. ND = not detected (PO_4^{3-} < 0.3 μM, NH_4^+ < 0.01 mM, and Pb < 0.1 nM).

Table T11 (continued).

Core, section, interval (cm)	Depth (mbsf)	Fe (µM)	Si (µM)	Sr (µM)	Ba (µM)	V (nM)	Cu (nM)	Zn (nM)	Rb (nM)	Mo (nM)	Cs (nM)	Pb (nM)	U (nM)
338-C0022B													
1H-1	0.0	0.5	346.7	95.6	0.4	237.9	107.2	180.3	1550.7	176.7	5.3	0.3	25.8
8H-1	76.5	0.6	327.6	84.8	3.7	37.1	7.2	135.2	1235.1	342.0	3.2	0.2	12.9
9T-1	84.5	0.4	37.0	88.1	2.1	16.7	6.1	2127.5	1221.2	172.5	2.0	0.2	13.2
10T-1	89.5	0.4	72.0	87.4	2.3	25.6	6.0	180.2	1219.0	178.4	1.9	0.5	13.4
11T-1	94.5	0.3	109.9	86.1	1.5	61.3	5.1	76.7	1261.1	254.1	2.7	0.4	22.9
12X-1	99.5	0.5	54.0	85.8	4.0	11.7	11.0	243.3	1153.4	761.4	1.8	0.2	11.1
13X-1	104.5	0.4	72.9	87.4	3.2	25.0	6.6	133.6	1207.3	193.6	2.4	0.8	14.3
15X-1	114.5	2.5	396.2	75.6	3.4	31.7	6.2	88.1	1265.7	1181.1	3.7	0.2	7.3
17X-5, 106	138.9	0.5	469.9	87.4	4.2	31.8	5.9	67.6	1096.9	498.9	4.3	0.4	11.1
18X-5, 66	146.6	1.1	364.3	86.2	4.5	16.4	5.2	58.3	1288.0	382.9	6.2	ND	9.6
22X-1	209.5	0.4	125.0	87.2	5.7	26.3	4.1	100.6	1199.5	259.7	2.1	0.3	13.8
24X-1	266.5	0.4	299.8	92.3	6.3	54.1	9.3	61.7	1131.6	977.0	6.2	1.2	8.9
25X-1	276.0	0.5	52.6	89.5	2.5	18.6	5.5	760.3	1200.3	247.2	2.9	0.4	12.7
26X-1	285.5	0.5	106.0	88.1	5.7	19.1	7.4	94.8	1040.6	297.6	2.3	0.5	12.3
27X-1	290.5	0.5	82.4	88.2	3.4	21.4	5.8	102.4	1101.5	207.3	2.4	0.8	12.9
28X-1	295.5	0.5	125.1	89.0	3.4	24.8	10.9	101.2	1115.4	177.1	2.9	0.5	12.8
29X-1	300.5	0.5	74.8	89.0	2.6	14.4	7.6	668.1	1157.0	189.6	2.7	0.3	12.2
30X-1	305.5	0.5	282.8	87.7	4.6	44.6	8.3	88.5	1211.3	596.8	5.2	0.8	14.8
32X-1	324.5	0.6	280.0	85.5	4.8	26.1	7.0	126.8	1111.9	275.4	3.3	0.3	9.7
33X-4	337.9	0.6	529.5	95.2	5.1	20.0	11.0	64.6	938.6	226.7	6.7	0.1	2.6
34X-1	343.5	0.6	310.8	90.2	5.8	41.9	17.6	122.9	987.1	340.9	5.5	1.0	10.4
36X-1	362.5	0.5	117.4	88.9	4.7	22.8	8.4	87.4	1091.4	241.5	3.2	0.5	12.2
37X-1	372.0	0.4	86.0	86.2	3.4	28.0	7.5	208.5	1192.4	305.4	3.5	0.5	14.6
38X-6	387.8	0.6	526.1	97.8	4.6	20.7	6.5	111.4	1307.3	333.6	9.1	ND	2.8
39X-1	391.0	0.5	185.2	90.2	5.6	34.0	14.3	133.2	1129.9	328.8	5.2	0.2	12.1
40X-1	400.5	0.5	103.6	87.8	3.3	25.8	6.6	134.6	1208.5	225.0	4.2	0.2	11.8
41X-1	410.0	0.4	90.3	89.4	2.9	23.1	10.0	114.9	1228.5	170.3	4.4	0.2	11.9

Table T12. Hydrocarbon gas composition in conventionally extracted headspace gas, Hole C0022B.

Core, section, interval (cm)	Depth (mbsf)	Headspace gas (ppmv)				Headspace gas (μM)			δ^{13}C-CH$_4$ (‰ VPDB)
		Methane	Ethane	Propane	$C_1/(C_2 + C_3)$	Methane	Ethane	Propane	
338-C0022B-									
1H-1, 120.5–124.5	1.2	6	ND	ND	—	2	ND	ND	—
2H-1, 95–99	20.5	9,489	1.7	0.4	4,465	2,843	0.5	0.1	—
3H-1, 121–125	30.2	10,952	1.6	0.3	5,777	2,727	0.4	0.1	–76.1
4H-1, 91.5–95.5	39.4	6,223	1.2	ND	5,243	2,266	0.4	ND	–68.5
5H-1, 124–128	49.2	7,996	1.3	ND	6,385	2,185	0.3	ND	–47.8
6H-1, 102.5–106.5	58.5	4,525	1.0	ND	4,747	1,311	0.3	ND	—
7H-8, 0–4	74.2	9,229	1.8	ND	5,219	2,354	0.5	ND	—
8H-2, 59–63	78.0	17,178	2.6	ND	6,646	3,236	0.5	ND	–69.5
9T-1, 28–32	84.8	9,658	2.1	0.3	4,120	2,487	0.5	0.1	–68.6
10T-1, 80–84	90.3	12,192	2.2	0.3	4,811	2,254	0.4	0.1	–63.9
11T-1, 0–4	94.5	5,569	1.0	ND	5,561	2,177	0.4	ND	—
12X-1, 116.4–120.4	100.7	5,226	1.2	ND	4,324	956	0.2	ND	–64.2
13X-1, 26–30	104.8	5,997	1.5	ND	3,962	1,250	0.3	ND	–64.4
14X-4, 56–60	114.1	5,927	2.2	ND	2,651	1,447	0.5	ND	–59.5
15X-3, 106–110	118.5	3,081	1.2	ND	2,524	838	0.3	ND	–67.8
16X-3, 72–76	127.4	10,486	2.7	ND	3,863	2,601	0.7	ND	—
17X-3, 0–4	135.0	12,967	4.0	ND	3,240	2,231	0.7	ND	–63.0
18X-3, 75–79	145.5	11,604	6.4	0.3	1,728	2,924	1.6	0.1	–61.2
19X-3, 0–4	153.6	11,195	6.9	ND	1,623	3,819	2.4	ND	–71.3
20X-3, 122–126	193.5	5,810	9.0	ND	647	1,112	1.7	ND	–61.1
21X-7, 0–4	204.5	4,429	5.6	ND	786	1,388	1.8	ND	–61.1
22X-1, 118–122	210.7	6,274	8.5	ND	736	1,451	2.0	ND	–50.2
23X-3, 44–48	221.2	10,480	7.3	ND	1,444	2,234	1.5	ND	—
24X-2, 77–81	268.7	9,972	7.8	ND	1,279	2,849	2.2	ND	–62.9
25X-CC, 0–4	276.9	7,587	5.3	ND	1,422	2,585	1.8	ND	—
26X-6, 0–4	291.1	2,802	3.8	ND	734	945	1.3	ND	—
27X-3, 99.5–103.5	294.3	11,282	9.5	ND	1,194	2,645	2.2	ND	–67.2
28X-2, 68–72	297.4	7,078	7.1	ND	994	2,292	2.3	ND	—
29X-3, 0–4	301.8	6,028	4.8	ND	1,264	1,855	1.5	ND	–55.8
30X-2, 52–56	307.2	7,459	5.5	ND	1,348	2,107	1.6	ND	–70.7
31X-1, 81–85	315.8	14,447	9.8	ND	1,467	3,281	2.2	ND	–62.1
32X-CC, 0–4	325.9	5,356	4.2	ND	1,271	1,074	0.8	ND	—
33X-6, 109.5–113.5	341.6	17,582	6.6	ND	2,651	5,483	2.1	ND	—
34X-4, 0–4	345.8	5,887	4.0	ND	1,490	2,099	1.4	ND	—
35X-6, 0–4	358.3	10,361	4.2	ND	2,461	5,457	2.2	ND	–55.0
36X-4, 0–4	364.7	7,221	6.7	ND	1,074	1,561	1.5	ND	–68.5
37X-3, 0–4	373.3	12,507	7.0	ND	1,777	2,567	1.4	ND	–49.4
38X-4, 0–4	384.9	7,649	4.7	ND	1,636	2,122	1.3	ND	–56.5
39X-3, 0–4	392.8	7,557	4.0	ND	1,911	2,294	1.2	ND	–67.5
40X-2, 126–130	403.2	6,762	4.5	ND	1,487	2,022	1.4	ND	—
41X-3, 0–4	412.2	12,230	4.7	ND	2,589	3,902	1.5	ND	—

ND = not detected. — = not enough methane to measure δ^{13}C-CH$_4$. VPDB = Vienna Peedee belemnite.

Table T13. Hydrocarbon gas composition in additionally extracted headspace gas, Hole C0022B.

Core, section, interval (cm)	Depth (mbsf)	Headspace gas (ppmv)				Headspace gas (μM)			δ^{13}C-CH$_4$ (‰ VPDB)
		Methane	Ethane	Propane	$C_1/(C_2 + C_3)$	Methane	Ethane	Propane	
338-C0022B-									
1H-1, 120.5–124.5	1.2	5	ND	ND	—	1	ND	ND	—
2H-1, 95–99	20.5	13,616	1.7	ND	8,062	2,579	0.3	ND	–83.5
3H-1, 121–125	30.2	10,252	1.3	ND	8,177	1,895	0.2	ND	–77.7
4H-1, 91.5–95.5	39.4	10,507	1.9	0.3	4,841	2,990	0.5	0.1	–76.8
5H-1, 124–128	49.2	15,028	2.4	0.3	5,501	1,923	0.3	ND	–72.4
6H-1, 102.5–106.5	58.5	5,627	1.0	ND	5,713	1,201	0.2	ND	–73.3
7H-8, 0–4	74.2	9,495	1.7	ND	5,618	1,266	0.2	ND	–71.4
8H-2, 59–63	78.0	13,011	1.9	ND	6,952	1,388	0.2	ND	–66.9
9T-1, 28–32	84.8	9,271	1.7	ND	5,311	1,063	0.2	ND	–70.1
10T-1, 80–84	90.3	8,373	1.6	ND	5,242	939	0.2	ND	–70.0
11T-1, 0–4	94.5	6,444	0.9	ND	7,249	2,941	0.4	ND	–71.2
12X-1, 116.4–120.4	100.7	5,267	0.9	ND	5,689	839	0.1	ND	–70.6
13X-1, 26–30	104.8	6,897	1.2	ND	5,911	1,193	0.2	ND	–71.6
14X-4, 56–60	114.1	10,121	2.8	ND	3,656	1,570	0.4	ND	–71.4
15X-3, 106–110	118.5	3,546	0.9	ND	3,991	602	0.2	ND	–70.0
16X-3, 72–76	127.4	6,454	2.0	ND	3,270	1,093	0.3	ND	–71.5
17X-3, 0–4	135.0	9,727	3.0	ND	3,235	1,360	0.4	ND	–71.1
18X-3, 75–79	145.5	5,246	3.6	ND	1,463	1,043	0.7	ND	–70.2
19X-3, 0–4	153.6	6,902	4.7	ND	1,462	1,607	1.1	ND	–71.8
20X-3, 122–126	193.5	9,272	6.7	ND	1,394	1,490	1.1	ND	–69.9
21X-7, 0–4	204.5	3,937	4.0	ND	991	499	0.5	ND	–72.3
22X-1, 118–122	210.7	4,284	4.6	ND	927	948	1.0	ND	–69.8
23X-3, 44–48	221.2	14,563	10.3	ND	1,415	2,211	1.6	ND	–64.8
24X-2, 77–81	268.7	4,218	4.4	ND	951	905	1.0	ND	–69.6
25X-CC, 0–4	276.9	5,719	4.5	ND	1,279	1,959	1.5	ND	–71.1
26X-6, 0–4	291.1	7,119	5.1	ND	1,384	1,338	1.0	ND	–69.2
27X-3, 99.5–103.5	294.3	13,787	8.0	ND	1,733	2,167	1.3	ND	–67.9
28X-2, 68–72	297.4	10,208	4.4	ND	2,308	2,283	1.0	ND	–70.0
29X-3, 0–4	301.8	5,748	2.9	ND	2,014	1,486	0.7	ND	–69.9
30X-2, 52–56	307.2	4,706	3.6	ND	1,317	781	0.6	ND	—
31X-1, 81–85	315.8	4,176	4.6	ND	918	696	0.8	ND	–72.2
32X-CC, 0–4	325.9	7,456	5.0	ND	1,487	806	0.5	ND	–71.9
33X-6, 109.5–113.5	341.6	8,662	4.6	ND	1,894	2,058	1.1	ND	–69.1
34X-4, 0–4	345.8	6,348	3.1	ND	2,033	1,370	0.7	ND	–70.1
35X-6, 0–4	358.3	13,064	4.5	ND	2,892	2,158	0.7	ND	–69.9
36X-4, 0–4	364.7	9,979	5.2	ND	1,913	1,345	0.7	ND	–68.2
37X-3, 0–4	373.3	9,367	3.8	ND	2,484	1,650	0.7	ND	–68.9
38X-4, 0–4	384.9	19,396	6.8	ND	2,846	3,238	1.1	ND	–67.9
39X-3, 0–4	392.8	17,855	6.7	ND	2,675	3,552	1.3	ND	–69.3
40X-2, 126–130	403.2	10,268	5.1	ND	2,027	2,451	1.2	ND	–68.2
41X-3, 0–4	412.2	7,229	2.1	ND	3,398	2,512	0.7	ND	–68.8

ND = not detected. — = not enough methane to measure δ^{13}C-CH$_4$. VPDB = Vienna Peedee belemnite.

Table T14. Hydrocarbon gas composition in void gas, Hole C0022B.

Core, section, interval (cm)	Depth (mbsf)	Headspace gas (ppmv)			$C_1/(C_2 + C_3)$	$\delta^{13}C\text{-}CH_4$ (‰ VPDB)
		Methane	Ethane	Propane		
338-C0022B-						
4H-3, 1.5	39.7	137,966	9.2	0.5	14,226	–76.1
5H-3, 7	49.7	230,640	14.0	0.8	15,578	–66.3
7H-3, 3	68.7	277,990	16.7	0.8	15,881	–67.4
8H-2	77.4	269,648	16.5	0.6	15,766	–71.4
9T-3, 18	85.2	17,097	1.4	ND	12,555	–72.0
10T-4, 73.5	92.7	32,442	3.0	ND	10,965	–71.8
12X-4	102.7	17,841	1.6	ND	11,248	–72.0
13X-3	106.7	26,108	2.1	ND	12,388	–72.8
14X-1, 120	110.7	1,826	0.5	ND	3,616	—
15X-3	117.4	329,283	33.4	0.8	9,628	–70.7
16X-5	127.7	115,354	38.0	ND	3,036	–67.6
17X-3, 69	135.7	460	ND	ND	—	—
18X-2, 122	144.7	15,696	5.4	ND	2,900	–67.4
19X-6	155.4	125,903	85.4	ND	1,474	—
20X-6	194.5	127,790	29.2	ND	4,384	–72.6
21X-5	203.3	15,950	3.9	ND	4,061	–73.7
22X-1, 95	210.5	297,749	69.5	ND	4,284	–74.3
23X-6, 34	223.3	323,953	71.7	ND	4,521	–73.8
24X-2, 37	268.3	249,119	57.6	ND	4,324	–72.4
25X-1, 36	276.4	59,624	13.7	ND	4,364	–69.8
26X-5	290.8	25,796	6.0	ND	4,265	–71.8
27X-5	294.7	83,094	20.0	ND	4,159	–63.6
28X-3	297.4	260,069	56.6	ND	4,596	–64.2
29X-3	301.8	143,380	34.4	ND	4,167	–72.6
30X-4, 32	308.0	165,044	36.6	ND	4,515	–72.5
31X-3, 113	317.5	217,385	42.4	ND	5,130	–64.9
33X-6, 74.5	341.3	125,174	20.4	ND	6,139	–72.8
34X-4, 75.5	346.5	183,589	34.8	ND	5,269	–72.3
34X-5, 132	348.5	142,556	25.9	ND	5,497	–72.3
35X-5	357.8	239,433	42.7	ND	5,607	–65.6
36X-6, 107	368.5	202,443	39.7	ND	5,095	–71.6
38X-8	389.7	268,957	40.6	ND	6,630	–71.1
39X-4, 58	394.8	210,219	34.0	ND	6,189	–71.1
40X-4, 15	403.9	68,482	11.3	ND	6,084	–71.3
41X-4, 47	414.1	283,733	44.7	ND	6,352	–70.1

ND = not detected. — = not enough methane to measure $\delta^{13}C\text{-}CH_4$. VPDB = Vienna Peedee belemnite.

Table T15. Carbonate analysis data, Hole C0022B. (Continued on next page.)

Core, section, interval (cm)	Midpoint depth (mbsf)	IC (wt%)	$CaCO_3$ (wt%)	TN (wt%)	TC (wt%)	TS (wt%)	TOC (wt%)	C/N
338-C0022B-								
1H-1, 120.0	1.198	2.2	18.2	0.09	2.9	0.1	0.7	8.4
1H-5, 117.0	5.532	2.6	21.7	0.06	3.1	0.2	0.5	7.8
1H-6, 20.0	5.972	1.5	12.6	0.08	2.1	0.3	0.6	8.0
2H-5, 9.0	23.191	1.2	9.7	0.05	1.5	0.4	0.4	7.1
2H-9, 51.0	28.588	2.2	18.4	0.06	2.7	0.1	0.5	7.6
3H-3, 0.0	30.323	1.1	9.0	0.05	1.5	0.4	0.4	6.8
3H-7, 69.0	35.909	1.4	11.3	0.03	0.9	0.4	NA	NA
3H-9, 54.0	38.186	0.9	7.1	0.06	1.3	0.4	0.4	7.2
3H-CC, 0.0	38.209	0.9	7.3	0.06	1.3	0.4	0.4	6.8
4H-3, 0.0	39.65	0.8	6.3	0.06	1.2	0.5	0.4	7.4
4H-7, 52.0	45.081	1.0	8.2	0.06	1.4	0.7	0.4	6.4
5H-1, 34.0	48.314	2.0	16.9	0.06	2.4	0.3	0.3	5.8
5H-1, 125.0	49.154	2.5	20.8	0.06	2.8	0.3	0.3	5.1
5H-5, 101.0	52.81	0.3	2.3	0.06	0.7	0.6	0.4	6.8
5H-9, 48.0	57.145	0.8	6.6	0.06	1.2	0.4	0.4	6.1
6H-1, 53.0	57.996	1.9	15.7	0.07	2.4	0.4	0.5	7.2
6H-3, 20.0	58.875	1.1	9.2	0.06	1.4	0.6	0.3	6.0
6H-5, 128.0	62.507	1.1	9.3	0.07	1.6	0.4	0.4	5.8
6H-8, 85.0	66.042	2.1	17.5	0.06	2.5	0.2	0.4	5.7
7H-2, 54.0	67.719	0.5	3.9	0.08	1.0	0.6	0.5	6.5
7H-4, 116.0	70.837	0.7	6.1	0.07	1.2	0.5	0.4	6.1
7H-8, 0.0	73.523	0.2	2.0	0.05	0.6	0.8	0.3	6.6
8H-1, 20.0	76.679	1.1	9.1	0.07	1.5	0.0	0.4	6.4
8H-5, 100.0	80.328	1.0	8.5	0.07	1.5	0.0	0.4	6.8
8H-CC, 17.0	84.339	0.1	1.1	0.07	0.8	0.1	0.6	9.3
9T-3, 0.0	84.989	0.1	0.7	0.05	0.5	0.5	0.5	9.2
9T-5, 77.0	88.287	1.4	11.7	0.07	1.7	0.0	0.3	5.2
10T-3, 0.0	90.46	0.8	6.5	0.07	1.4	0.1	0.6	8.3
10T-5, 100.0	93.942	0.4	3.6	0.05	0.9	0.1	0.4	8.2
11T-1, 81.0	95.31	0.3	2.1	0.07	0.7	0.1	0.4	5.9
12X-2, 10.0	100.474	1.4	11.4	0.07	1.7	0.1	0.4	5.3
12X-5, 135.0	103.39	0.9	7.7	0.07	1.4	0.2	0.5	7.2
13X-1, 26.0	104.683	0.8	6.5	0.08	1.3	0.2	0.6	7.3
13X-6, 30.0	108.915	0.3	2.3	0.06	0.7	0.1	0.4	6.6
14X-1, 67.0	109.856	0.3	2.6	0.07	0.7	0.1	0.4	6.4
14X-1, 110.0	110.084	0.3	2.3	0.06	0.6	0.0	0.3	5.4
14X-2, 54.0	110.424	0.5	4.1	0.06	0.9	0.1	0.4	7.5
14X-2, 113.0	110.737	0.2	1.8	0.06	0.6	0.1	0.4	6.1
14X-3, 30.0	111.039	0.5	3.9	0.06	0.9	0.1	0.4	7.6
14X-3, 92.0	111.368	0.5	4.2	0.06	1.0	0.1	0.5	7.9
14X-3, 109.0	111.459	0.2	1.8	0.05	0.5	0.1	0.3	6.0
14X-4, 15.0	111.703	0.5	4.5	0.05	0.8	0.1	0.3	6.4
14X-4, 90.0	112.101	0.3	2.7	0.07	0.8	0.1	0.5	6.9
14X-5, 54.0	112.664	0.5	3.8	0.07	0.9	0.1	0.5	7.0
14X-8, 0.0	114.07	0.2	2.0	0.06	0.7	0.2	0.5	8.6
15X-4, 0.0	118.79	1.0	8.5	0.06	1.4	0.2	0.4	5.8
16X-5, 0.0	127.72	0.9	7.3	0.06	1.2	0.1	0.3	5.4
17X-1, 68.0	134.18	1.2	9.9	0.07	1.6	0.1	0.4	6.0
17X-1, 115.0	134.65	1.3	10.4	0.08	1.7	0.1	0.5	6.2
18X-3, 66.0	145.45	0.3	2.2	0.07	0.8	0.1	0.5	6.7
19X-1, 76.0	153.26	0.4	2.9	0.06	0.8	0.1	0.4	6.5
20X-5, 3.0	193.808	0.6	5.3	0.08	1.2	0.1	0.5	6.7
20X-8, 34.0	197.14	0.6	5.0	0.08	1.0	0.1	0.4	5.3
20X-10, 8.0	198.73	1.5	12.8	0.07	1.9	0.2	0.4	5.0
21X-5, 85.0	204.18	1.1	9.2	0.08	1.6	0.1	0.5	5.9
21X-7, 133.0	205.86	0.7	6.1	0.07	1.3	0.2	0.5	7.3
22X-1, 118.0	210.68	0.5	4.0	0.06	0.9	0.1	0.4	7.0
23X-5, 0.0	221.442	0.3	2.5	0.07	0.7	0.1	0.4	5.3
23X-5, 61.0	222.014	0.6	5.1	0.07	1.0	0.1	0.4	5.4
23X-7, 44.0	224.441	1.3	10.6	0.07	1.6	0.5	0.3	4.5
24X-4, 7.0	269.175	0.8	6.7	0.08	1.4	0.2	0.6	7.5
24X-7, 13.0	273.39	0.2	1.8	0.05	0.5	0.7	0.3	6.2
25X-1, 74.0	276.74	0.4	3.7	0.08	0.9	0.2	0.5	6.6
26X-2, 136.0	287.575	0.5	4.5	0.07	1.0	0.2	0.5	7.2
27X-5, 2.0	294.601	0.6	5.3	0.07	1.1	0.1	0.4	6.3
27X-5, 63.5	295.205	0.4	3.2	0.06	0.8	0.1	0.4	6.9
28X-4, 2.0	297.587	0.4	3.6	0.07	0.9	0.1	0.5	7.1
29X-1, 74.0	301.24	0.3	2.6	0.06	0.7	0.1	0.4	6.8

Table T15 (continued).

Core, section, interval (cm)	Midpoint depth (mbsf)	IC (wt%)	$CaCO_3$ (wt%)	TN (wt%)	TC (wt%)	TS (wt%)	TOC (wt%)	C/N
30X-1, 98.5	306.485	0.5	4.0	0.06	0.9	0.2	0.4	6.9
30X-4, 2.0	307.7	0.3	2.4	0.07	0.7	0.1	0.4	6.5
30X-6, 6.0	310.57	0.2	1.7	0.07	0.6	0.1	0.4	6.1
31X-1, 74.0	315.705	0.6	4.9	0.06	0.9	0.1	0.3	5.6
31X-6, 106.0	321.152	0.2	1.5	0.06	0.6	0.2	0.4	6.6
31X-7, 8.0	321.552	0.2	1.5	0.07	0.5	0.1	0.4	5.3
33X-2, 26.5	335.67	0.3	2.2	0.05	0.7	0.2	0.4	7.3
33X-8, 0.0	342.185	0.5	4.2	0.07	1.0	0.2	0.5	6.8
34X-2, 38.0	345.185	0.4	3.3	0.07	0.9	0.1	0.5	7.1
34X-5, 98.5	348.15	0.1	1.0	0.06	0.4	0.1	0.3	5.1
35X-6, 0.0	357.916	0.3	2.2	0.05	0.6	0.1	0.3	6.7
35X-6, 88.0	358.73	0.2	1.6	0.05	0.5	0.9	0.3	6.6
35X-7, 124.0	359.894	0.3	2.2	0.04	0.6	0.1	0.3	7.3
35X-8, 10.0	360.014	0.2	1.5	0.06	0.6	0.1	0.4	6.4
35X-9, 9.5	360.749	0.3	2.5	0.06	0.7	0.2	0.4	6.4
36X-2, 89.0	364.185	0.3	2.2	0.05	0.6	0.2	0.3	6.3
36X-6, 0.0	367.465	0.5	3.8	0.04	0.7	0.3	0.2	6.0
37X-3, 15.0	373.455	0.4	3.4	0.06	0.9	0.1	0.5	7.6
38X-1, 107.0	382.518	0.4	3.0	0.05	0.7	0.3	0.4	7.2
38X-4, 5.0	384.805	0.3	2.5	0.06	0.7	0.5	0.4	6.8
38X-6, 126.5	388.646	0.2	1.3	0.05	0.4	0.2	0.3	6.0
38X-8, 17.0	389.498	0.3	2.9	0.05	0.6	0.1	0.3	6.0
39X-3, 1.0	392.825	0.3	2.4	0.05	0.6	0.1	0.3	5.9
39X-5, 101.0	396.645	0.0	0.3	0.04	0.3	0.1	0.3	6.7
40X-1, 108.5	401.585	0.3	2.6	0.05	0.7	0.4	0.4	8.4
40X-4, 5.0	403.76	0.3	2.8	0.05	0.7	0.1	0.4	7.2
41X-2, 14.0	411.29	0.2	1.8	0.04	0.5	0.4	0.3	7.0
41X-5, 80.0	415.32	0.1	0.8	0.04	0.4	0.3	0.3	6.9

IC = inorganic carbon, TN = total nitrogen, TC = total carbon, TS = total sulfur, TOC = total organic carbon.

Table T16. Moisture and density measurements, Hole C0022B. (Continued on next five pages.)

Core, section, interval (cm)	Depth (mbsf)	Density (g/cm^3)		Porosity (%)	Void ratio	Notes
		Bulk	Grain			
338-C0022B-						
1H-4, 129.0	4.25	1.60	2.68	65.02	1.8591	
1H-5, 50.0	4.87	1.51	2.61	69.39	2.2665	
1H-5, 117.0	5.54	1.59	2.68	65.94	1.9363	
1H-6, 20.0	5.98	1.60	2.67	64.92	1.8503	
2H-1, 10.0	19.6	1.52	2.66	69.45	2.2732	
2H-1, 90.0	20.4	1.69	2.73	61.13	1.5729	
2H-3, 30.0	21	1.74	2.72	58	1.3812	
2H-3, 114.0	21.84	1.63	2.70	63.73	1.7571	
2H-4, 60.0	22.615	1.66	2.70	62.01	1.6324	
2H-4, 130.0	23.315	1.66	2.67	61.73	1.6129	
2H-5, 18.0	23.535	1.63	2.71	63.97	1.7755	
2H-5, 60.0	23.955	1.69	2.69	59.75	1.4842	
2H-6, 30.0	24.98	1.65	2.68	62.08	1.6369	
2H-6, 100.0	25.68	1.72	2.72	59.04	1.4411	
2H-7, 31.0	26.34	1.71	2.72	59.34	1.4595	
2H-7, 100.0	27.03	1.68	2.78	62.46	1.6639	
2H-8, 38.0	27.78	1.64	2.70	63.23	1.7199	
2H-8, 100.0	28.4	1.69	2.78	61.95	1.6283	
2H-9, 40.0	29.105	1.61	2.64	63.52	1.7414	
2H-9, 51.0	29.215	1.63	2.66	62.98	1.7015	
3H-1, 10.0	29.1	1.55	2.72	69.08	2.2345	Soupy
3H-1, 100.0	30	1.69	2.75	61.33	1.5857	
3H-3, 0.0	30.455	1.72	2.75	59.98	1.499	
3H-3, 35.0	30.805	1.66	2.69	61.8	1.6179	
3H-4, 120.0	33.03	1.89	2.73	49.12	0.9655	Sand
3H-5, 9.0	33.265	1.60	2.66	65.13	1.8681	
3H-5, 91.0	34.085	1.59	2.61	64.24	1.7966	
3H-6, 20.0	34.73	1.61	2.70	65.06	1.8622	
3H-6, 120.0	35.73	1.63	2.68	63.61	1.7483	
3H-7, 69.0	36.6	1.72	2.76	59.7	1.4815	
3H-7, 105.0	36.96	1.73	2.69	57.64	1.3605	
3H-8, 20.0	37.455	1.70	2.71	59.88	1.4927	
3H-8, 110.0	38.355	1.75	2.68	56.21	1.2836	
3H-9, 54.0	39.105	1.75	2.67	55.61	1.2527	
3H-CC, 0.0	39.13	1.73	2.68	57.36	1.345	
4H-1, 32.0	38.82	1.64	2.68	62.74	1.6838	
4H-1, 80.0	39.3	1.71	2.71	59.38	1.4621	
4H-3, 0.0	39.715	1.76	2.74	57.22	1.3374	
4H-3, 121.0	40.925	1.71	2.68	58.63	1.4174	
4H-4, 36.0	41.385	1.71	2.71	59.08	1.4438	
4H-4, 118.0	42.205	1.69	2.71	60.39	1.5245	
4H-5, 46.0	42.785	1.62	2.63	63.23	1.7194	
4H-5, 108.0	43.405	1.66	2.70	62.01	1.6325	
4H-6, 34.0	43.97	1.67	2.64	60.01	1.5008	
4H-6, 112.0	44.75	1.69	2.60	58.07	1.3851	
4H-7, 19.0	45.125	1.68	2.74	61.63	1.6064	
4H-7, 52.0	45.455	1.71	2.68	58.92	1.4342	
4H-8, 50.0	46.74	1.74	2.73	58.22	1.3936	
4H-8, 125.0	47.49	1.73	2.69	57.33	1.3437	
4H-9, 31.0	47.86	1.75	2.74	57.98	1.3797	
5H-1, 34.0	48.34	1.70	2.68	59.18	1.4495	
5H-1, 126.0	49.26	1.66	2.68	61.52	1.5986	
5H-3, 68.0	50.265	1.71	2.68	58.76	1.425	
5H-3, 122.0	50.805	1.71	2.66	58.03	1.3829	
5H-4, 14.5	51.04	1.65	2.65	61.36	1.5878	
5H-4, 78.0	51.675	1.72	2.68	58.32	1.3991	
5H-5, 24.0	52.44	1.80	2.70	53.66	1.1581	
5H-5, 101.0	53.21	1.73	2.72	58.58	1.4142	
5H-6, 33.0	53.835	1.70	2.71	60.1	1.5065	
5H-6, 118.0	54.685	1.65	2.71	62.73	1.6834	
5H-7, 23.5	55.045	1.62	2.66	63.47	1.7372	
5H-7, 112.0	55.93	1.64	2.62	61.48	1.5962	
5H-8, 3.0	56.15	1.67	2.66	60.78	1.5495	
5H-8, 114.0	57.26	1.80	2.68	53.05	1.13	
5H-9, 48.0	57.905	1.70	2.67	58.93	1.4348	
6H-1, 53.0	58.03	1.72	2.67	57.81	1.3703	
6H-3, 20.0	58.97	1.79	2.74	55.29	1.2364	

Table T16 (continued). (Continued on next page.)

Core, section, interval (cm)	Depth (mbsf)	Density (g/cm^3)		Porosity (%)	Void ratio	Notes
		Bulk	Grain			
6H-3, 133.5	60.105	1.74	2.72	57.58	1.3571	
6H-4, 7.0	60.24	1.78	2.70	55.07	1.2258	
6H-4, 116.0	61.33	1.69	2.63	58.72	1.4227	
6H-5, 2.0	61.595	1.71	2.67	58.25	1.395	
6H-5, 128.0	62.855	1.72	2.75	59.42	1.4646	
6H-6, 8.0	63.06	1.68	2.69	60.42	1.5263	
6H-6, 105.0	64.03	1.64	2.63	61.9	1.6249	
6H-7, 38.0	64.765	1.69	2.73	60.76	1.5484	
6H-7, 115.5	65.54	1.74	2.65	55.89	1.2672	
6H-8, 12.0	65.905	1.74	2.68	56.99	1.325	
6H-8, 107.5	66.86	1.79	2.68	53.64	1.1571	
7H-2, 54.0	67.79	1.72	2.74	59.64	1.478	
7H-2, 110.0	68.35	1.64	2.64	61.76	1.6148	
7H-3, 41.0	69.055	1.65	2.63	60.93	1.5598	
7H-3, 97.0	69.615	1.62	2.62	62.6	1.6741	
7H-4, 65.0	70.705	1.69	2.73	60.94	1.56	
7H-4, 115.0	71.205	1.72	2.71	58.68	1.4202	
7H-5, 15.0	71.61	1.74	2.69	57.04	1.328	
7H-5, 91.0	72.37	1.81	2.73	53.94	1.1709	
7H-6, 24.0	73.13	1.77	2.77	57.5	1.3527	
7H-8, 0.0	74.165	1.83	2.72	52.65	1.1119	
7H-8, 110.0	75.265	1.80	2.84	57.08	1.3301	
7H-9, 35.0	75.905	1.76	2.70	56.12	1.2789	
7H-9, 79.0	76.345	1.80	2.67	52.72	1.1149	
8H-1, 20.0	76.7	1.76	2.67	55	1.2222	
8H-2, 1.0	77.39	1.77	2.49	48.93	0.9581	Sand
8H-2, 49.0	77.87	1.78	2.69	54.66	1.2054	
8H-4, 77.0	79.1	1.75	2.71	57.09	1.3307	
8H-4, 130.0	79.63	1.72	2.67	57.94	1.3774	
8H-5, 22.0	79.99	1.75	2.68	56.43	1.295	
8H-5, 100.0	80.77	1.75	2.68	55.93	1.269	
8H-6, 33.0	81.525	1.81	2.71	53	1.1275	
8H-6, 113.0	82.325	1.89	2.69	48.02	0.9238	
8H-7, 35.0	82.975	1.91	2.64	45.44	0.8329	
8H-7, 117.0	83.795	1.86	2.72	50.91	1.0372	
8H-8, 55.0	84.605	1.84	2.67	50.76	1.0307	
8H-CC, 17.0	85.245	1.85	2.76	52.25	1.0941	
9T-3, 1.0	85.04	1.85	2.70	50.52	1.021	
9T-3, 71.0	85.74	1.78	2.66	53.81	1.165	
9T-4, 28.0	86.715	1.67	2.66	60.12	1.5078	
9T-4, 114.0	87.575	1.72	2.67	57.78	1.3685	
9T-5, 27.0	88.105	1.71	2.65	57.73	1.3656	
9T-5, 77.0	88.605	1.72	2.65	57.26	1.3399	
9T-6, 27.0	89.11	1.69	2.66	59.53	1.4707	
10T-1, 55.0	90.05	1.64	2.64	61.81	1.6184	
10T-3, 0.0	90.55	1.72	2.65	57.1	1.3312	
10T-3, 39.0	90.94	1.76	2.66	54.73	1.2092	
10T-4, 37.0	92.325	1.77	2.68	54.75	1.21	
10T-4, 110.0	93.055	1.90	2.70	47.36	0.8998	
12X-1, 10.0	99.6	1.64	2.73	63.77	1.7598	
12X-1, 100.0	100.5	1.70	2.66	58.69	1.4208	
12X-2, 10.0	101.005	1.70	2.65	58.75	1.4245	
12X-2, 67.0	101.575	1.70	2.65	58.1	1.3868	
12X-3, 35.0	102.44	1.68	2.65	59.85	1.4904	
12X-4, 10.0	102.83	1.64	2.46	57.49	1.3524	
12X-4, 100.0	103.73	1.76	2.70	55.71	1.2576	
12X-5, 12.0	104.28	1.79	2.70	54.25	1.186	
12X-5, 135.0	105.51	1.76	2.65	54.82	1.2136	
12X-6, 20.0	105.765	1.77	2.66	54.48	1.197	
12X-6, 106.0	106.625	1.74	2.62	55.13	1.2286	
13X-1, 26.0	104.76	1.70	2.72	60.26	1.5162	
13X-1, 120.0	105.7	1.72	2.68	57.74	1.3662	
13X-2, 57.0	106.47	1.73	2.73	58.58	1.4142	
13X-3, 35.5	107.045	1.74	2.71	57.27	1.3404	
13X-3, 129.0	107.98	1.74	2.74	58.06	1.3843	
13X-4, 9.0	108.2	1.73	2.70	57.96	1.3784	
13X-5, 20.5	109.255	1.77	2.82	58.26	1.3957	
13X-5, 101.0	110.06	1.76	2.73	56.9	1.3204	
13X-6, 30.0	110.765	1.88	2.71	48.89	0.9566	

Table T16 (continued). (Continued on next page.)

Core, section, interval (cm)	Depth (mbsf)	Density (g/cm³)		Porosity (%)	Void ratio	Notes
		Bulk	Grain			
14X-1, 67.0	110.17	1.82	2.73	53.54	1.1523	
14X-1, 110.0	110.6	1.79	2.73	55.21	1.2326	
14X-2, 54.0	111.24	1.83	2.63	49.71	0.9886	
14X-2, 113.0	111.83	1.82	2.75	54.12	1.1795	
14X-3, 30.0	112.4	1.91	2.73	48.19	0.93	
14X-3, 92.0	113.02	1.87	2.70	49.56	0.9826	
14X-3, 109.0	113.19	1.78	2.78	57.07	1.3292	
14X-4, 15.0	113.65	1.75	2.54	51.87	1.0775	
14X-4, 90.0	114.4	1.76	2.68	55.59	1.2518	
14X-5, 54.0	115.46	1.86	2.75	51.31	1.0538	
14X-5, 97.0	115.89	1.91	2.68	46.52	0.87	
14X-6, 26.0	116.58	1.79	2.74	55.22	1.2332	
14X-6, 134.0	117.66	1.81	2.66	51.77	1.0735	
14X-7, 32.0	118.05	1.87	2.74	50.76	1.0309	
14X-8, 0.0	118.11	1.94	2.74	46.46	0.8676	
15X-1, 72.0	115.22	1.86	2.74	51.11	1.0455	
15X-2, 9.0	115.99	1.79	2.77	55.82	1.2633	
15X-2, 88.0	116.78	1.73	2.74	58.9	1.4328	
15X-3, 17.0	117.56	1.79	2.67	53.53	1.1521	
15X-3, 91.0	118.3	1.76	2.70	56.07	1.2763	
15X-4, 0.0	118.79	1.78	2.80	57.33	1.3436	
15X-4, 115.0	119.94	1.81	2.71	53.66	1.1578	
15X-5, 12.0	120.32	1.79	2.69	53.97	1.1725	
15X-5, 113.0	121.33	1.80	2.73	54.2	1.1834	
15X-6, 53.0	122.14	1.79	2.70	54.07	1.1771	
15X-7, 36.0	122.975	1.78	2.70	54.89	1.2167	
16X-1, 60.0	124.6	1.75	2.65	55.29	1.2364	
16X-1, 126.0	125.26	1.74	2.67	56.47	1.2973	
16X-2, 10.0	125.48	1.73	2.71	58.18	1.3914	
16X-2, 70.0	126.08	1.73	2.75	59.24	1.4534	
16X-3, 29.0	126.98	1.78	2.76	56.27	1.2867	
16X-5, 0.0	127.72	1.71	2.69	58.49	1.4091	
16X-5, 76.0	128.48	1.76	2.71	56.28	1.2875	
16X-6, 24.0	128.93	1.74	2.68	56.95	1.3228	
16X-6, 115.0	129.84	1.77	2.72	55.87	1.2659	
16X-7, 20.0	130.3	1.72	2.62	56.62	1.3054	
16X-7, 57.0	130.67	1.71	2.66	57.97	1.3794	
16X-8, 2.0	131.12	1.81	2.83	56.75	1.3121	
16X-8, 57.0	131.67	1.74	2.73	58.06	1.3846	
17X-1, 41.0	133.91	1.68	2.67	60.21	1.5131	
17X-1, 68.0	134.18	1.74	2.67	56.67	1.3077	
17X-1, 115.0	134.65	1.66	2.61	59.86	1.4915	
17X-3, 21.0	135.23	1.70	2.61	57.26	1.34	
17X-3, 120.0	136.22	1.67	2.71	61.7	1.6112	
17X-4, 20.0	136.63	1.69	2.70	60.25	1.516	
17X-4, 120	137.63	1.70	2.66	58.58	1.4141	
17X-5, 35.0	138.195	1.79	2.89	58.93	1.4349	
17X-6, 32.0	139.565	1.72	2.69	58	1.3812	
17X-6, 103.0	140.275	1.70	2.62	57.91	1.3761	
17X-7, 3.0	140.375	1.70	2.67	59.18	1.4497	
17X-7, 84.0	141.185	1.71	2.76	60.58	1.5368	
17X-8, 50.0	141.875	1.77	2.70	55.84	1.2643	
18X-1, 11.0	143.11	1.78	2.82	57.86	1.3728	
18X-2, 62.0	144.12	1.76	2.69	55.97	1.2712	
18X-2, 122.0	144.72	1.84	2.71	51.73	1.0717	
18X-3, 68.0	145.47	1.73	2.72	58.68	1.4202	
18X-5, 29.0	146.185	1.86	2.76	51.87	1.0776	
18X-6, 27.0	146.825	1.89	2.75	49.91	0.9963	
18X-6, 110.0	147.655	1.72	2.72	59.22	1.452	
19X-1, 78.0	153.28	1.77	2.74	56.6	1.3039	
19X-3, 9.0	153.71	1.76	2.71	56.47	1.2975	
19X-4, 17.0	154.24	1.93	2.61	43.14	0.7587	
19X-5, 13.0	154.735	1.79	2.77	55.88	1.2667	
19X-6, 56.0	155.97	1.70	2.58	56.49	1.2983	
20X-1, 32.0	190.82	1.79	2.86	58.32	1.3991	
20X-2, 13.0	191.375	1.77	2.72	55.9	1.2673	
20X-2, 93.0	192.175	1.77	2.81	58.48	1.4083	
20X-3, 32.0	192.615	1.73	2.73	58.43	1.4054	
20X-3, 106.0	193.355	1.80	2.76	55.44	1.2442	

Table T16 (continued). (Continued on next page.)

Core, section, interval (cm)	Depth (mbsf)	Density (g/cm^3)		Porosity (%)	Void ratio	Notes
		Bulk	Grain			
20X-5, 5.0	193.92	1.79	2.86	58.43	1.4054	
20X-6, 16.0	194.635	1.87	2.67	48.88	0.9562	
20X-6, 72.0	195.195	1.82	2.80	55.32	1.238	
20X-7, 44.0	196.03	1.79	2.76	56.08	1.2767	
20X-7, 122.0	196.81	1.86	2.67	49.51	0.9804	
20X-8, 34.0	197.325	1.74	2.71	57.76	1.3674	
20X-9, 16.0	197.73	1.74	2.79	59.71	1.482	
20X-9, 93.0	198.5	1.73	2.66	56.57	1.3024	
20X-10, 8.0	198.96	1.71	2.66	58.32	1.3995	
21X-2, 72.0	200.955	1.65	2.70	62.27	1.6501	
21X-2, 112.0	201.355	1.74	2.68	56.75	1.3124	
21X-3, 30.0	201.875	1.64	2.70	63.03	1.7046	
21X-4, 0.0	202.14	1.77	2.69	55.55	1.2498	
21X-4, 79.0	202.93	1.76	2.73	56.63	1.3057	
21X-5, 33.0	203.66	1.71	2.72	59.87	1.4921	
21X-5, 85.0	204.18	1.79	2.70	54.61	1.2033	
21X-7, 19.0	204.72	1.75	2.69	56.59	1.3037	
21X-7, 133.0	205.86	1.87	2.71	50.14	1.0055	
21X-8, 29.0	206.195	1.77	2.68	54.71	1.2081	
21X-8, 95.0	206.855	1.77	2.72	55.99	1.2725	
21X-9, 32.0	207.49	1.81	2.74	54.11	1.1789	
21X-10, 26.0	208.1	1.78	2.73	55.69	1.2568	
21X-10, 62.0	208.46	1.82	2.70	52.56	1.1078	
22X-1, 80.0	210.3	1.81	2.67	52.5	1.1054	
22X-1, 118.0	210.68	1.86	2.71	50.27	1.0109	
23X-2, 15.0	219.5	1.85	2.76	52.6	1.1099	
23X-2, 100.0	220.35	1.75	2.69	56.66	1.3073	
23X-3, 2.0	220.785	1.76	2.66	54.99	1.2217	
23X-5, 0.0	221.605	1.71	2.65	57.85	1.3723	
23X-5, 61.0	222.215	1.81	2.78	55.43	1.2435	
23X-6, 8.0	223.085	1.78	2.68	54.39	1.1923	
23X-6, 122.0	224.225	1.78	2.69	54.7	1.2077	
23X-7, 44.0	224.805	1.84	2.80	54.09	1.1782	
23X-8, 5.0	225.635	1.73	2.72	58.34	1.4004	
23X-8, 110.0	226.685	1.81	2.67	52.59	1.1094	
23X-9, 30.0	227.225	1.80	2.70	53.75	1.162	
23X-9, 90.0	227.825	1.80	2.60	50.76	1.0309	
23X-10, 60.0	228.605	1.82	2.74	53.76	1.1624	
24X-1, 35.0	266.85	1.95	2.70	44.96	0.8167	
24X-1, 75.0	267.25	1.85	2.71	50.69	1.0279	
24X-2, 10.0	267.98	1.89	2.72	48.71	0.9497	
24X-4, 7.0	269.175	1.82	2.73	53.44	1.148	
24X-4, 95.0	270.055	1.84	2.73	52.11	1.0881	
24X-5, 6.0	270.605	1.86	2.72	50.59	1.0237	
24X-5, 112.0	271.665	1.87	2.73	50.67	1.027	
24X-6, 33.0	272.23	1.84	2.70	51.06	1.0433	
24X-7, 13.0	273.39	2.05	2.87	44.28	0.7947	
24X-7, 129.0	274.55	1.94	2.71	45.67	0.8407	
24X-8, 31.0	274.97	1.90	2.71	47.78	0.9148	
25X-1, 14.0	276.14	1.88	2.73	49.76	0.9905	
25X-1, 74.0	276.74	1.90	2.72	48.02	0.9237	
26X-1, 33.0	285.83	1.84	2.69	50.93	1.038	
26X-1, 101.0	286.51	1.87	2.69	49.24	0.97	
26X-2, 22.0	287.09	1.81	2.71	53.69	1.1593	
26X-2, 136.0	288.23	1.89	2.73	49.65	0.986	
26X-3, 47.0	288.745	1.84	2.67	50.46	1.0187	
26X-3, 135.0	289.625	1.81	2.68	52.55	1.1076	
26X-4, 19.0	289.875	1.87	2.70	49.39	0.9758	
26X-4, 97.0	290.655	1.90	2.68	47.49	0.9043	
26X-5, 6.0	290.85	1.82	2.64	50.53	1.0215	
26X-6, 25.0	291.355	1.86	2.70	50.36	1.0146	
27X-1, 17.0	290.67	1.85	2.75	52.33	1.0979	
27X-1, 119.0	291.69	1.91	2.70	46.81	0.8802	
27X-2, 31.0	292.21	1.84	2.65	49.7	0.9882	
27X-2, 104.0	292.94	1.86	2.70	49.85	0.9942	
27X-3, 40.0	293.71	1.86	2.74	51.23	1.0506	
27X-5, 2.0	294.675	1.84	2.75	52.83	1.12	
27X-5, 63.5	295.29	1.97	2.76	45.56	0.837	
28X-1, 31.0	295.81	1.91	2.71	47.62	0.9092	

Table T16 (continued). (Continued on next page.)

Core, section, interval (cm)	Depth (mbsf)	Density (g/cm^3)		Porosity (%)	Void ratio	Notes
		Bulk	Grain			
28X-1, 93.0	296.43	1.92	2.71	46.98	0.886	
28X-2, 31.0	297.035	1.96	2.72	44.89	0.8147	
28X-4, 3.0	297.925	1.87	2.70	49.57	0.9829	
28X-4, 99.0	298.885	1.89	2.71	49.01	0.9611	
28X-5, 35.0	299.515	1.91	2.68	46.54	0.8706	
28X-5, 109.0	300.255	1.86	2.71	50.36	1.0146	
28X-6, 24.0	300.565	1.89	2.75	49.45	0.9781	
29X-1, 71.0	301.21	1.87	2.69	48.88	0.9561	
29X-3, 33.0	302.125	1.83	2.75	53.49	1.1502	
29X-3, 96.0	302.755	1.80	2.66	52.29	1.0961	
29X-4, 66.0	303.86	1.91	2.68	46.46	0.8678	
29X-5, 8.0	304.195	1.91	2.70	47.01	0.8873	
30X-1, 39.0	305.89	1.81	2.69	52.76	1.1169	
30X-1, 98.5	306.485	1.90	2.67	46.66	0.8748	
30X-2, 28.0	306.99	1.87	2.73	50.39	1.0159	
30X-4, 3.0	307.71	1.94	2.76	47.24	0.8954	
30X-4, 107.0	308.75	1.87	2.64	47.46	0.9031	
30X-5, 14.0	309.23	1.88	2.73	49.72	0.9888	
30X-5, 74.0	309.83	1.84	2.73	51.88	1.0783	
30X-6, 6.0	310.57	1.93	2.80	48.82	0.9538	
30X-6, 78.0	311.29	1.85	2.69	50.07	1.0027	
30X-7, 35.0	312.26	1.88	2.70	49.05	0.9626	
30X-7, 95.0	312.86	1.85	2.67	49.68	0.9871	
30X-8, 37.0	313.63	1.87	2.70	49.51	0.9807	
31X-1, 12.0	315.12	1.88	2.67	47.86	0.9179	
31X-1, 74.0	315.74	1.89	2.73	49.28	0.9715	
31X-3, 23.0	316.58	1.88	2.70	48.95	0.9588	
31X-4, 43.0	318.09	1.82	2.73	53.19	1.1364	
31X-4, 115.0	318.81	1.91	2.72	48.16	0.9288	
31X-5, 30.0	319.29	1.89	2.77	50.21	1.0084	
31X-5, 128.0	320.27	1.84	2.72	51.56	1.0643	
31X-6, 24.0	320.64	1.87	2.67	48.48	0.9411	
31X-6, 106.0	321.46	1.93	2.73	46.97	0.8856	
31X-7, 8.0	321.88	1.92	2.72	47.13	0.8916	
31X-7, 135.0	323.15	1.92	2.71	46.83	0.8809	Sand
31X-8, 79.0	323.97	1.88	2.66	47.69	0.9116	
32X-1, 1.0	324.51	1.61	2.73	66	1.9411	Sand
33X-1, 13.0	334.13	1.92	2.67	45.57	0.8371	
33X-1, 126.0	335.26	1.93	2.70	45.97	0.851	
33X-2, 26.5	335.67	1.92	2.71	47	0.8866	
33X-2, 106.0	336.465	1.93	2.71	46.29	0.8619	
33X-3, 27.0	337.08	1.91	2.70	47.14	0.8917	
33X-3, 61.0	337.42	1.93	2.73	46.65	0.8744	
33X-4, 20.0	338.06	1.87	2.63	47.58	0.9076	
33X-4, 86.0	338.72	1.92	2.71	46.87	0.8821	
33X-5, 11.0	339.285	1.90	2.70	48.12	0.9274	
33X-5, 118.0	340.355	1.84	2.65	49.77	0.9907	
33X-6, 28.0	340.815	1.87	2.78	52.08	1.0869	
33X-8, 0.0	342.185	1.90	2.81	50.82	1.0335	
34X-1, 17.0	343.67	1.88	2.68	48.11	0.9272	
34X-1, 84.0	344.34	1.91	2.65	45.63	0.8393	
34X-2, 38.0	345.185	1.92	2.68	45.53	0.8357	
34X-4, 103.0	346.79	1.89	2.73	49.36	0.9747	
34X-5, 27.0	347.435	1.85	2.61	48.09	0.9263	
34X-5, 98.5	348.15	1.97	2.69	43.05	0.7561	
34X-6, 20.0	348.765	1.95	2.75	46.25	0.8606	
34X-6, 135.0	349.915	1.85	2.66	49.47	0.9792	
34X-7, 7.0	350.01	1.86	2.64	48.33	0.9352	
34X-7, 115.0	351.09	1.89	2.80	51.54	1.0636	
34X-8, 45.0	351.79	1.90	2.69	47.49	0.9043	
35X-1, 30.0	353.3	1.83	2.69	51.93	1.0802	
35X-1, 130.0	354.3	1.87	2.70	49.61	0.9846	
35X-2, 21.0	354.615	1.88	2.79	51.51	1.0621	
35X-2, 100.0	355.405	1.92	2.76	48.43	0.9392	
35X-3, 17.0	355.735	1.90	2.68	47.39	0.9007	
35X-3, 81.0	356.375	1.93	2.72	46.82	0.8804	
35X-4, 75.0	357.665	2.00	2.89	47.62	0.9092	
35X-6, 0.0	358.32	1.92	2.67	45.45	0.8331	
35X-6, 88.0	359.2	2.00	2.73	42.85	0.7499	

Table T16 (continued).

Core, section, interval (cm)	Depth (mbsf)	Density (g/cm³)		Porosity (%)	Void ratio	Notes
		Bulk	Grain			
35X-7, 102.0	360.24	1.93	2.67	44.81	0.8118	
35X-7, 124.0	360.46	1.97	2.65	41.86	0.72	
35X-8, 10.0	360.59	1.91	2.71	47.6	0.9084	
35X-8, 35.0	360.84	1.89	2.78	50.43	1.0175	
35X-9, 9.5	361.385	1.90	2.73	48.65	0.9473	
35X-10, 33.0	362.36	2.00	2.74	43.25	0.7621	
36X-1, 11.0	362.61	1.85	2.67	49.76	0.9905	
36X-2, 89.0	364.185	1.96	2.67	43.5	0.77	
36X-5, 29.0	366.35	1.91	2.74	48.27	0.9332	
36X-5, 116.0	367.22	1.90	2.75	48.89	0.9564	
36X-6, 0.0	367.465	1.92	2.69	46.35	0.8639	
36X-6, 65.0	368.115	1.94	2.77	47.86	0.9179	
36X-7, 73.0	369.515	1.89	2.71	48.7	0.9494	
37X-1, 37.0	372.37	1.92	2.68	45.74	0.843	
37X-2, 3.0	372.94	1.87	2.70	49.52	0.981	
37X-3, 15.0	373.455	1.87	2.75	50.94	1.0384	
37X-3, 94.5	374.25	1.89	2.71	48.58	0.9448	
38X-1, 22.0	381.72	1.90	2.72	48.1	0.9269	
38X-1, 107.0	382.57	1.95	2.68	44.14	0.7903	
38X-2, 39.5	383.3	1.95	2.71	45.1	0.8215	
38X-2, 106.0	383.965	1.86	2.69	50.15	1.006	
38X-4, 7.0	384.995	1.92	2.72	47.24	0.8953	
38X-5, 33.0	386.66	1.92	2.71	47.08	0.8896	
38X-5, 119.0	387.52	1.93	2.68	45.33	0.8293	
38X-6, 30.0	388.05	1.96	2.71	44.47	0.801	
38X-6, 126.5	389.015	1.86	2.70	50.21	1.0085	
38X-7, 57.0	389.625	1.89	2.67	47.51	0.905	
38X-8, 17.0	389.91	1.98	2.73	43.77	0.7783	
38X-8, 80.0	390.54	1.97	2.74	44.85	0.8131	
39X-1, 20.0	391.2	1.92	2.74	47.4	0.9013	
39X-1, 109.0	392.09	1.92	2.73	47.45	0.903	
39X-3, 1.0	392.825	1.95	2.74	45.74	0.8429	
39X-3, 44.0	393.255	1.96	2.71	44.69	0.808	
39X-4, 39.0	394.61	2.00	2.76	43.89	0.7821	
39X-4, 97.0	395.19	2.00	2.78	44.23	0.793	
39X-5, 35.0	395.985	1.95	2.76	46.48	0.8684	
39X-5, 101.0	396.645	2.00	2.71	42.08	0.7265	
39X-6, 2.0	397.065	2.00	2.70	41.84	0.7195	
39X-6, 90.0	397.945	1.94	2.72	46.03	0.8528	
39X-7, 39.0	398.385	1.94	2.77	47.66	0.9106	
40X-1, 10.0	400.6	1.96	2.72	44.75	0.8098	
40X-1, 108.5	401.585	1.94	2.66	44.13	0.7897	
40X-2, 27.0	402.17	1.94	2.73	46.25	0.8604	
40X-4, 5.0	403.76	1.98	2.72	43.62	0.7736	
40X-4, 108.0	404.79	1.99	2.69	42.27	0.7321	
40X-5, 38.0	405.395	2.02	2.67	39.56	0.6546	
40X-5, 123.0	406.245	1.90	2.69	47.46	0.9034	
41X-1, 5.0	410.05	2.02	2.75	41.91	0.7216	
41X-1, 93.0	410.93	1.90	2.67	46.68	0.8756	
41X-2, 14.0	411.29	1.96	2.71	44.84	0.8129	
41X-2, 72.0	411.87	1.95	2.70	44.86	0.8135	
41X-3, 21.0	412.37	1.93	2.75	47.47	0.9038	
41X-3, 131.0	413.47	1.98	2.72	43.62	0.7736	
41X-4, 59.0	414.2	2.00	2.72	42.68	0.7447	
41X-5, 80.0	415.32	1.93	2.79	48.43	0.9391	

Table T17. Electrical resistivity testing of the Wenner probe between correct and incorrect pin configuration, Hole C0022B.

Core, section, interval (cm)	Electrical impedance of sample at 2 kHz (Ω)	Impedance phase angle of sample (°)	Electrical impedance of seawater at 2 kHz (Ω)	Impedance phase angle of seawater (°)	Resistivity (Ωm)	Pin configuration	Ratio resistivity wrong/good configuration
338-C0022B-							
10T-5, 14	10.96	–3.65	6.80	0.44	0.44	Correct	0.97
10T-5, 14	11.05	–12.43	6.53	2.25	0.46	Incorrect	
10T-5, 87	14.24	9.59	6.80	0.44	0.57	Correct	1.17
10T-5, 87	12.09	16.99	6.53	2.25	0.49	Incorrect	
11T-1, 42	4.09	15.03	6.80	0.44	0.16	Correct	0.45
11T-1, 42	8.44	–0.37	6.53	2.25	0.36	Incorrect	
11T-CC, 2	14.99	–0.75	7.49	0.65	0.55	Correct	0.94
11T-CC, 2	12.30	–7.98	5.75	0.21	0.58	Incorrect	

Table T18. Electrical resistivity measurements, Hole C0022B. (Continued on next five pages.)

Core, section, interval (cm)	Depth (mbsf)	Electrical resistivity (Ωm)	Notes
338-C0022B-			
1H-4, 122.0	4.18	0.103	Mud
1H-4, 128.0	4.24	0.222	Mud
1H-5, 71.0	5.08	0.226	Mud and glauconite
1H-5, 82.0	5.19	0.239	Mud and glauconite
1H-5, 105.0	5.42	0.236	Silty mud
2H-1, 10.0	19.6	0.236	Mud
2H-1, 90.0	20.4	0.285	Soupy mud
2H-3, 113.0	21.83	0.338	Mud
2H-4, 60.0	22.615	0.29	Mud
2H-5, 60.0	23.955	0.358	Mud
2H-6, 100.0	25.68	0.371	Mud
2H-7, 100.0	27.03	0.353	Mud
2H-8, 102.0	28.42	0.412	Mud
3H-1, 10.0	29.1	0.22	Soupy mud
3H-1, 100.0	30	0.339	Mud
3H-3, 2.0	30.475	0.384	Silty mud
3H-3, 35.0	30.805	0.337	Mud and glauconite
3H-4, 120.0	33.03	0.971	Sand
3H-5, 10.0	33.275	0.342	Mud
3H-6, 120.0	35.73	0.522	Mud
3H-6, 135.0	35.88	0.402	Silty mud
3H-7, 105.0	36.96	0.384	Mud and glauconite
3H-8, 110.0	38.355	0.403	Mud
3H-9, 20.0	38.765	0.403	Mud
4H-1, 30.0	38.8	0.254	Mud
4H-3, 120.0	40.915	0.397	Mud
4H-4, 40.0	41.425	0.333	Mud
4H-5, 50.0	42.825	0.344	Mud
4H-6, 70.0	44.33	0.268	Mud
4H-7, 23.0	45.165	0.354	Mud
4H-8, 36.0	46.6	0.315	Mud
4H-9, 55.0	48.1	0.373	Mud
5H-1, 6.0	48.06	0.29	Mud
5H-3, 5.0	49.635	0.306	Mud brown
5H-4, 29.0	51.185	0.312	Mud green
5H-4, 52.0	51.415	0.473	Ash
5H-5, 35.0	52.55	0.342	Mud
5H-6, 33.0	53.835	0.314	Mud
5H-6, 61.0	54.115	0.437	Mud
5H-7, 17.0	54.98	0.369	Mud
5H-8, 15.0	56.27	0.332	Mud
5H-8, 96.0	57.08	0.357	Mud
5H-8, 97.5	57.095	0.564	Ash top
5H-8, 98.5	57.105	0.664	Ash middle
5H-8, 100.0	57.12	0.609	Ash bottom and mud
5H-8, 105.0	57.17	0.409	Mud
5H-9, 9.0	57.515	0.378	Mud green

Table T18 (continued). (Continued on next page.)

Core, section, interval (cm)	Depth (mbsf)	Electrical resistivity (Ωm)	Notes
5H-9, 12.0	57.545	0.445	Mud brown
6H-1, 19.0	57.69	0.318	Mud
6H-3, 31.0	59.08	0.345	Mud
6H-4, 30.0	60.47	0.3	Mud
6H-5, 34.0	61.915	0.276	Mud
6H-6, 35.0	63.33	0.312	Mud
6H-7, 33.0	64.715	0.296	Mud
6H-8, 37.0	66.155	0.351	Mud
7H-2, 22.0	67.47	0.312	Mud
7H-3, 100.0	69.645	0.28	Mud
7H-4, 69.0	70.745	0.341	Mud
7H-5, 90.0	72.36	0.399	Mud
7H-6, 21.0	73.1	0.397	Mud
7H-8, 106.0	75.225	0.449	Mud
7H-9, 82.0	76.375	0.512	Mud
8H-1, 45.0	76.95	0.391	Mud
8H-1, 85.0	77.35	0.278	Soupy sandy mud
8H-2, 2.0	77.4	0.768	Sand
8H-2, 52.0	77.9	0.49	Mud
8H-3, 20.0	78.21	0.553	Mud
8H-5, 20.0	79.97	0.372	Mud
8H-5, 31.0	80.08	0.943	Sand
8H-5, 51.0	80.28	0.443	Silty mud
8H-5, 130.0	81.07	0.411	Mud
8H-6, 18.0	81.375	0.417	Mud
8H-6, 21.0	81.405	0.439	Mud sand gradient
8H-6, 22.0	81.415	0.538	Mud sand gradient
8H-6, 23.0	81.425	0.744	Mud sand gradient
8H-6, 24.0	81.435	1.071	Sand
8H-6, 25.0	81.445	0.685	Sand and mud
8H-6, 26.0	81.455	0.45	Mud
8H-6, 27.0	81.465	0.426	Mud sand gradient
8H-6, 29.0	81.485	0.373	Mud sand gradient
8H-6, 31.0	81.505	0.361	Mud sand gradient
8H-6, 33.0	81.525	0.393	Mud sand gradient
8H-6, 35.0	81.545	0.47	Mud sand gradient
8H-6, 37.0	81.565	0.516	Mud sand gradient
8H-6, 39.0	81.585	0.415	Mud sand gradient
8H-6, 41.0	81.605	0.393	Mud sand gradient
8H-6, 43.0	81.625	0.474	Mud sand gradient
8H-6, 45.0	81.645	0.496	Mud sand gradient
8H-6, 46.0	81.655	0.57	Mud sand gradient
8H-6, 47.0	81.665	0.858	Sand
8H-6, 48.0	81.675	0.919	Mud
8H-6, 49.0	81.685	0.521	Mud
8H-6, 78.0	81.975	0.603	Mud and ash
8H-6, 92.0	82.115	0.408	Mud
8H-6, 96.0	82.155	0.802	Sand
8H-6, 100.0	82.195	0.397	Mud
8H-6, 106.0	82.255	0.608	Sand
8H-6, 115.0	82.345	0.416	Mud
8H-6, 120.0	82.395	0.607	Sand
8H-6, 135.0	82.545	0.445	Mud
8H-7, 5.0	82.675	0.415	Mud
8H-7, 13.0	82.755	0.44	Ash
8H-7, 29.0	82.915	0.439	Mud and sand faulted
8H-7, 38.0	83.005	0.432	Mud
8H-7, 44.0	83.065	1.004	Sand
8H-7, 50.0	83.125	0.397	Mud
8H-7, 54.0	83.165	0.584	Mud sand gradient
8H-7, 55.0	83.175	1.35	Mud sand gradient
8H-7, 56.0	83.185	0.747	Mud sand gradient
8H-7, 57.0	83.195	0.68	Mud sand gradient
8H-7, 58.0	83.205	0.246	Mud sand gradient
8H-7, 59.0	83.215	0.507	Sand transition
8H-7, 78.0	83.405	0.457	Mud
8H-7, 79.0	83.415	0.484	Mud sand gradient
8H-7, 80.0	83.425	0.469	Mud sand gradient

Table T18 (continued). (Continued on next page.)

Core, section, interval (cm)	Depth (mbsf)	Electrical resistivity (Ωm)	Notes
8H-7, 81.0	83.435	0.497	Mud sand gradient
8H-7, 82.0	83.445	0.588	Mud sand gradient
8H-7, 83.0	83.455	0.631	Mud sand gradient
8H-7, 84.0	83.465	1.025	Mud sand gradient
8H-7, 85.0	83.475	0.856	Sand
8H-7, 86.0	83.485	1.034	Sand transition
8H-7, 87.0	83.495	0.721	Mud
8H-7, 90.0	83.525	0.5	Mud
8H-7, 94.0	83.565	0.799	Sand
8H-7, 105.0	83.675	0.505	Mud
8H-7, 113.0	83.755	0.829	Sand
8H-7, 120.0	83.825	0.495	Mud
8H-7, 134.0	83.965	0.556	Mud
8H-8, 5.0	84.105	0.419	Mud
8H-8, 12.0	84.175	1.07	Sand
8H-8, 20.0	84.255	0.453	Mud
8H-8, 29.0	84.345	0.92	Sand
8H-8, 44.0	84.495	1.058	Sand
8H-8, 50.0	84.555	0.443	Mud
8H-8, 75.0	84.805	0.432	Mud
8H-8, 85.0	84.905	0.444	Mud
9T-1, 2.0	84.52	0.308	Mud
9T-1, 18.0	84.68	0.282	Mud
9T-3, 10.0	85.13	0.278	Mud and sand
9T-3, 20.0	85.23	0.481	Mud
9T-3, 33.0	85.36	0.371	Mud
9T-3, 75.0	85.78	0.395	Mud
9T-4, 25.0	86.685	0.346	Mud
9T-5, 25.0	88.085	0.374	Mud
9T-6, 25.0	89.09	0.483	Mud
9T-CC, 20.0	89.82	0.34	Mud
10T-1, 52.0	90.02	0.469	Mud
10T-3, 36.0	90.91	0.451	Mud
10T-4, 41.0	92.365	0.54	Mud
12X-1, 32.0	99.82	0.372	Mud
12X-2, 20.0	101.105	0.463	Mud
12X-3, 35.0	102.44	0.381	Mud
12X-4, 12.0	102.85	0.533	Brown mud
12X-4, 36.0	103.09	0.545	Mud
12X-5, 28.0	104.44	0.483	Mud
12X-6, 17.0	105.735	0.5	Mud
12X-6, 20.0	105.765	0.513	Mud
13X-1, 71.0	105.21	0.444	Mud
13X-2, 9.0	105.99	0.479	Mud
13X-3, 138.0	108.07	0.431	Mud
13X-4, 27.0	108.38	0.447	Mud
13X-6, 25.0	110.715	0.58	Silty mud
14X-1, 40.0	109.9	0.499	Mud
14X-2, 97.0	111.67	0.516	Mud
14X-3, 100.0	113.1	0.536	Mud
14X-4, 119.0	114.69	0.387	Mud
14X-5, 70.0	115.62	0.462	Mud
14X-6, 66.0	116.98	0.5	Mud
15X-1, 89.0	115.39	0.492	Mud
15X-2, 2.0	115.92	0.475	Mud
15X-2, 56.0	116.46	0.424	Mud
15X-3, 18.0	117.57	0.585	Mud
15X-4, 50.0	119.29	0.473	Mud
15X-5, 13.0	120.33	0.491	Mud
15X-6, 30.0	121.91	0.504	Mud
15X-7, 37.0	122.985	0.498	Mud
15X-7, 48.0	123.095	0.56	Mud
15X-7, 62.0	123.235	0.657	Black sand
16X-1, 75.0	124.75	0.574	Mud
16X-2, 12.0	125.5	0.451	Mud
16X-3, 30.0	126.99	0.512	Mud
16X-5, 38.0	128.1	0.57	Mud
16X-6, 81.0	129.5	0.425	Mud

Table T18 (continued). (Continued on next page.)

Core, section, interval (cm)	Depth (mbsf)	Electrical resistivity (Ωm)	Notes
16X-7, 35.0	130.45	0.521	Mud
16X-8, 58.0	131.68	0.473	Mud
17X-1, 42.0	133.92	0.4	Mud
17X-3, 22.0	135.24	0.43	Mud
17X-4, 20.0	136.63	0.441	Mud
17X-5, 15.0	137.995	0.534	Mud
17X-6, 33.0	139.575	0.431	Mud
17X-7, 16.0	140.505	0.413	Mud
17X-7, 25.0	140.595	0.473	Ash
17X-7, 41.0	140.755	0.393	Mud
17X-7, 47.0	140.815	0.457	Ash and mud
17X-7, 69.0	141.035	0.513	Mud
17X-8, 37.0	141.745	0.418	Light mud
17X-8, 50.0	141.875	0.461	Dark mud
17X-8, 67.0	142.045	0.558	Black sand
17X-8, 71.0	142.085	0.381	Mud
18X-1, 7.0	143.07	0.434	Mud
18X-1, 24.0	143.24	0.37	Black sand
18X-2, 8.0	143.58	0.517	Mud
18X-2, 28.0	143.78	0.49	Black soupy mud
18X-2, 37.0	143.87	0.322	Gray soupy mud
18X-3, 3.0	144.82	0.34	Mud
18X-3, 28.0	145.07	0.418	Soupy mud
18X-3, 57.0	145.36	0.495	Black sand
18X-5, 44.0	146.335	0.485	Mud
18X-6, 21.0	146.765	0.466	Mud
19X-1, 10.0	152.6	0.462	Mud
19X-1, 21.0	152.71	0.509	Mud
19X-1, 23.0	152.73	0.459	Sand
19X-1, 30.0	152.8	0.503	Ash
19X-3, 25.0	153.87	0.631	Mud
19X-4, 20.0	154.27	0.964	Sand
19X-4, 52.0	154.59	0.535	Mud
19X-5, 15.0	154.755	0.556	Mud
19X-6, 16.0	155.57	0.475	Mud
20X-1, 31.0	190.81	0.546	Mud
20X-1, 47.0	190.97	0.3	Black sand
20X-2, 9.0	191.335	0.599	Mud
20X-2, 11.0	191.355	0.539	Soupy sand
20X-3, 17.0	192.465	0.58	Mud
20X-3, 59.0	192.885	0.599	Mud
20X-5, 6.0	193.93	1.57	Mud
20X-6, 17.0	194.645	1.738	Mud
20X-7, 46.0	196.05	0.595	Mud
20X-8, 10.0	197.085	0.575	Mud
20X-9, 17.0	197.74	0.576	Mud
20X-10, 27.0	199.15	0.604	Mud
21X-2, 70.0	200.935	0.378	Mud
21X-3, 28.0	201.855	0.377	Mud
21X-4, 77.0	202.91	0.418	Mud
21X-5, 35.0	203.68	0.448	Mud
21X-7, 18.0	204.71	0.434	Mud
21X-8, 29.0	206.195	0.416	Mud
21X-9, 31.0	207.48	0.49	Mud
21X-10, 60.0	208.44	0.511	Mud
22X-1, 59.0	210.09	0.408	Mud
22X-1, 77.0	210.27	0.38	Mud
22X-1, 128.0	210.78	0.703	Sand
22X-1, 133.0	210.83	0.542	Mud
22X-CC, 12.0	210.96	0.477	Mud
23X-1, 17.0	219.17	0.741	Mud
23X-2, 56.0	219.91	0.423	Mud
23X-3, 17.0	220.935	0.377	Mud
23X-5, 37.0	221.975	0.555	Mud
23X-6, 75.0	223.755	0.484	Mud
23X-7, 77.0	225.135	0.515	Mud
23X-8, 97.0	226.555	0.43	Mud
23X-9, 35.0	227.275	0.497	Mud

Table T18 (continued). (Continued on next page.)

Core, section, interval (cm)	Depth (mbsf)	Electrical resistivity (Ωm)	Notes
23X-10, 57.0	228.575	0.482	Mud
24X-1, 37.0	266.87	0.533	Mud
24X-2, 12.0	268	0.53	Mud
24X-4, 97.0	270.075	0.475	Mud
24X-5, 49.0	271.035	0.492	Mud
24X-6, 56.0	272.46	0.503	Mud
24X-7, 50.0	273.76	0.602	Mud
24X-8, 69.0	275.35	0.506	Mud
25X-1, 44.0	276.44	0.585	Mud
26X-1, 24.0	285.74	0.719	Mud
26X-1, 106.0	286.56	0.553	Mud
26X-2, 28.0	287.15	0.497	Mud
26X-2, 123.0	288.1	0.484	Mud
26X-3, 25.0	288.525	0.455	Mud
26X-3, 108.0	289.355	0.572	Mud
26X-4, 20.0	289.885	0.529	Mud
26X-4, 108.0	290.765	0.656	Mud
26X-5, 29.0	291.08	0.523	Mud
26X-6, 40.0	291.505	0.479	Mud
26X-CC, 16.0	291.885	0.526	Mud
26X-CC, 22.0	291.945	0.557	Mud
27X-1, 19.0	290.69	0.574	Mud
27X-1, 95.0	291.45	0.559	Mud
27X-2, 7.0	291.97	0.743	Mud
27X-2, 31.0	292.21	0.451	Light mud
27X-3, 76.0	294.07	0.499	Mud
27X-5, 5.0	294.705	0.485	Mud
27X-5, 29.0	294.945	0.55	Sandy mud
28X-1, 30.0	295.8	0.661	Mud
28X-2, 15.0	296.875	0.366	Black soupy sand
28X-2, 35.0	297.075	0.597	Mud
28X-2, 43.0	297.155	0.301	Mud
28X-4, 98.0	298.875	0.572	Mud
28X-4, 105.0	298.945	0.429	Black sand
28X-5, 34.0	299.505	0.38	Mud
28X-5, 40.0	299.565	0.433	Sand
28X-6, 1.0	300.335	0.137	Mud
29X-1, 25.0	300.75	0.381	Mud
29X-1, 28.0	300.78	0.393	Black soupy mud
29X-3, 22.0	302.015	0.573	Sand
29X-3, 50.0	302.295	0.486	Mud
29X-4, 18.0	303.38	0.371	Mud
29X-4, 35.0	303.55	0.463	Sand
29X-5, 14.0	304.255	0.471	Sand
29X-5, 26.0	304.375	0.609	Mud
29X-5, 74.0	304.855	0.473	Sand
30X-1, 14.0	305.64	0.301	Ash
30X-1, 55.0	306.05	0.389	Mud
30X-2, 30.0	307.01	0.472	Mud
30X-4, 115.0	308.83	0.437	Mud
30X-4, 117.0	308.85	0.476	Sand
30X-5, 47.0	309.56	0.368	Mud
30X-5, 49.0	309.58	0.46	Sand
30X-5, 127.0	310.36	0.341	Soupy ash
30X-6, 125.0	311.76	0.442	Mud
30X-7, 72.0	312.63	0.908	Mud
30X-8, 4.0	313.3	0.509	Mud
31X-1, 15.0	315.15	0.868	Mud
31X-3, 49.0	316.84	0.812	Mud
31X-4, 16.0	317.82	0.731	Mud
31X-5, 50.0	319.49	0.835	Mud
31X-6, 22.0	320.62	0.802	Mud
31X-7, 22.0	322.02	0.918	Mud
31X-8, 23.0	323.41	0.749	Mud
32X-1, 5.0	324.55	0.391	Soupy sand
32X-1, 88.0	325.38	0.403	Black sand and mud
32X-1, 135.0	325.85	0.547	Mud
32X-CC, 15.0	326.08	0.515	Mud

Table T18 (continued).

Core, section, interval (cm)	Depth (mbsf)	Electrical resistivity (Ωm)	Notes
33X-1, 15.0	334.15	0.63	Mud
33X-1, 130.0	335.3	0.664	Mud
33X-2, 40.0	335.805	0.579	Mud
33X-2, 99.0	336.395	0.345	Soupy ash and mud
33X-2, 105.0	336.455	0.891	Mud very consolidated
33X-3, 30.0	337.11	0.604	Mud very consolidated (broke)
33X-3, 101.0	337.82	0.479	Mud and ash
33X-3, 102.0	337.83	0.445	Soupy sand, mud, and ash?
33X-3, 103.0	337.84	0.435	Mud and ash
33X-3, 104.0	337.85	0.388	Transition ash
33X-3, 105.0	337.86	0.536	Soupy ash
33X-4, 1.0	337.87	0.557	Soupy ash edge of core
33X-4, 2.0	337.88	0.453	Soupy ash
33X-4, 3.0	337.89	0.35	Soupy ash
33X-4, 4.0	337.9	0.368	Soupy ash
33X-4, 5.0	337.91	0.363	Soupy ash
33X-4, 6.0	337.92	0.428	Soupy ash
33X-4, 7.0	337.93	0.428	Soupy ash
33X-4, 8.0	337.94	0.478	Soupy ash
33X-4, 9.0	337.95	0.391	Soupy ash
33X-4, 10.0	337.96	0.404	Soupy ash
33X-4, 11.0	337.97	0.421	Soupy ash
33X-4, 12.0	337.98	0.44	Soupy ash
33X-4, 13.0	337.99	0.449	Soupy ash
33X-4, 14.0	338	0.432	Soupy ash
33X-4, 15.0	338.01	0.406	Soupy ash
33X-4, 16.0	338.02	0.516	Soupy ash
33X-4, 17.0	338.03	0.514	Soupy ash
33X-4, 18.0	338.04	0.44	Soupy ash
33X-4, 19.0	338.05	0.5	Transition mud
33X-4, 75.0	338.61	0.498	Mud
33X-6, 30.0	340.835	0.594	Mud super consolidated (broke)
33X-8, 40.0	342.585	0.566	Mud
36X-CC, 13.0	369.975	0.634	Mud

Table T19. Resistivity results from cubic samples, Hole C0022B.

Core, section, interval (cm)	Depth (mbsf)	R_x (Ωm)	R_y (Ωm)	R_z (Ωm)	α_l (%)	α_T (%)	Notes
338-C0022B-							
33X-2, 102.0	336.425	0.934	0.91	1.044	2.6	–12.4	Broken along *x*-*y* planes
34X-1, 18.0	343.68	0.871	0.884	1.195	–1.5	–30.6	Broken along *x*-*y* planes
35X-3, 26.0	355.825	1.184	1.226	1.274	–3.5	–5.6	
37X-3, 46.0	373.765	1.6	0.44	1.703	113.7	–50.2	
38X-5, 32.0	386.65	1.123	1.664	1.269	–38.8	9.4	
38X-5, 35.0	386.68	1.088	1.01	1.147	7.4	–8.9	
39X-3, 52.0	393.335	1.037	1.045	1.088	–0.8	–4.4	Broken along *x*-*y* planes
40X-1, 63.0	401.13	1.191	1.334	1.288	–11.3	–2	
41X-3, 123.0	413.39	1.301	1.148	1.337	12.5	–8.8	

Table T20. *P*-wave velocities results from cubic samples, Hole C0022B.

Core, section, interval (cm)	Depth (mbsf)	Resonant frequency of transducers (kHz)	V_{Px} (m/s)	V_{Py} (m/s)	V_{Pz} (m/s)	α_I (%)	α_T (%)	Notes
338-C0022B-								
33X-2, 102.0	336.425	230	1962	1455	1805	–1.49	–5.49	Broken along *x*-*y* planes
34X-1, 18.0	343.68	230	1349	1390	1798	–3.22	–27.06	Broken along *x*-*y* planes
35X-3, 28.0	355.845	230	1904	1911	1877	–0.10	1.61	
37X-3, 46.0	373.765	230	1900	1920	1830	–0.94	4.28	
38X-5, 32.0	386.65	230	1904	1859	1840	–2.81	2.23	
38X-5, 35.0	386.68	230	1891	1884	1894	5.22	–0.34	
39X-3, 52.0	393.335	230	1939	1924	1897	–3.67	1.80	Broken along *x*-*y* planes
40X-1, 63.0	401.13	230	1921	1928	1902	–0.57	1.18	
41X-3, 123.0	413.39	230	2022	2031	1885	4.23	7.24	

Table T21. Penetrometer and vane shear strength measurements, Hole C0022B.

Core, section, interval (cm)	Depth (mbsf)	Undrained shear strength (kPa)	
		Penetrometer	Vane shear
338-C0022B-			
1H-4, 128.0	4.24	41.366	
1H-4, 130.0	4.26		25.281
1H-5, 110.0	5.47		33.992
1H-5, 114.0	5.51	41.039	
2H-3, 120.0	21.9	54.446	
2H-3, 122.0	21.92		29.105
3H-1, 92.0	29.92		3.612
3H-1, 96.0	29.96	57.225	
4H-1, 27.0	38.77		19.758
4H-1, 36.0	38.86	27.795	
5H-6, 123.0	54.735	68.016	
5H-6, 125.0	54.755		52.374
6H-6, 127.0	64.25		118.699
6H-6, 130.0	64.28	127.53	
7H-2, 76.0	68.01		64.002
7H-2, 79.0	68.04	86.655	
8H-2, 54.0	77.92		35.166
8H-2, 55.0	77.93	66.708	
9T-6, 41.0	89.25		48.598
9T-6, 53.0	89.37	86.655	
10T-3, 9.0	90.64	93.195	
10T-3, 26.0	90.81		44.76
12X-4, 50.0	103.23		47.639
12X-4, 56.0	103.29	76.028	
13X-4, 70.0	108.81		32.706
13X-4, 74.0	108.85	58.043	
14X-7, 12.0	117.85		33.318
14X-7, 17.0	117.9	71.123	
15X-7, 45.0	123.065	80.115	
15X-7, 48.0	123.095		33.985
16X-7, 41.0	130.51		35.319
16X-7, 47.0	130.57	49.05	
17X-3, 50.0	135.52		31.984
17X-3, 66.0	135.68	69.488	
18X-5, 41.0	146.305		23.312
18X-5, 53.0	146.425	49.05	
19X-6, 15.0	155.56	68.67	
19X-6, 18.0	155.59		14.641
20X-2, 101.0	192.255	88.29	
20X-2, 102.0	192.265		23.979
21X-10, 67.0	208.51	107.093	
21X-10, 71.0	208.55		67.337
22X-1, 56.0	210.06	67.035	
22X-1, 60.0	210.1		29.315
23X-9, 59.0	227.515	228.9	
23X-9, 62.0	227.545		82.178
23X-9, 70.0	227.625		95.352
26X-2, 20.0	287.07	135.705	
28X-2, 64.0	297.365	159.413	
29X-4, 16.0	303.36		28.648
29X-4, 22.0	303.42	66.218	
30X-2, 20.0	306.91	100.553	

Table T22. Unconfined compressive strength (UCS) measurements, Hole C0022B.

Core, section, interval (cm)	Depth (mbsf)	*x* (mm)	*y* (mm)	*z* (mm)	Area (mm^2)	Peak load (kN)	UCS (MPa)
338-C0022B-							
37X-3-WW, 46–48	373.765	14.65	14.6	14.7	213.89	0.42	1.96
35X-3-WW, 26–28	355.825	20.8	19.25	18.55	400.40	1.27	3.17
35X-3-WW, 28–30	355.845	20.45	19.7	19.7	402.87	1.18	2.93
38X-5-WW, 32–36	386.65	14.55	15.25	27.1	221.89	0.58	2.61
38X-5-WW, 32–36	386.65	16.3	18.05	20	294.22	1.14	3.87
38X-5-WW, 35–39	386.68	17.1	17.9	30.35	306.09	0.73	2.38
38X-5-WW, 35–37	386.68	16.8	17.4	16.7	292.32	0.78	2.67